SYSTEMS FOR MEASURING B CELL RECEPTOR AFFINITY MATURATION IN GERMINAL CENTRES

by

THOMAS MUELLER

A thesis submitted to the
University of Birmingham
for the degree of
DOCTOR OF PHILOSOPHY

PSIBS Centre for Doctoral Training
College of Engineering and Physical Sciences
The University of Birmingham
May 2016

UNIVERSITY OF
BIRMINGHAM

University of Birmingham Research Archive

e-theses repository

This unpublished thesis/dissertation is copyright of the author and/or third parties. The intellectual property rights of the author or third parties in respect of this work are as defined by The Copyright Designs and Patents Act 1988 or as modified by any successor legislation.

Any use made of information contained in this thesis/dissertation must be in accordance with that legislation and must be properly acknowledged. Further distribution or reproduction in any format is prohibited without the permission of the copyright holder.

“The plan is nothing,

planning is everything.”

D. D. Eisenhower

Abstract

Germinal Centres (GCs) play a central role in adaptive immunity; involving processes of cell migration, clonal expansion, hypermutation, and selection. To elucidate the role of affinity in regulating these processes, a technique for measuring B cell receptor affinity maturation in GCs *in situ* was developed. To facilitate interrogation of individual antibody-antigen interactions, atomic force microscopy (AFM) was chosen, offering nanometre positional resolution, and pico-Newton force sensitivity.

Specificity of gold-coated AFM cantilevers towards the targeted receptors was achieved via a bespoke modification scheme, using self-assembled amine-terminated alkanethiol to facilitate attachment of the receptor specific antigen NP ((4-hydroxy-3-nitrophenyl)acetyl). Influences on molecule deposition and subsequent NP addition were investigated, as were control measures facilitating identification of successful modifications (Chapter 4).

Effects of sample preparation techniques on AFM adhesion measurements were investigated (Chapter 5). Subsequently, the developed AFM technique was applied in interrogation of B cells and hybridomas – expressing receptors of varying affinity towards NP – and two GCs in tissue sections (Chapter 6). For the automated and unbiased evaluation of large amounts of varying AFM data, bespoke data analysis methods were developed.

The project finds that AFM is capable of quantifying specific antibody-antigen interactions, but was unable to measure these in tissue sections. Possible reasons preventing such measurements are discussed.

Acknowledgements

I would like to thank my supervisors Dr. Kai-Michael Toellner, Dr. James Bowen, and Dr. Hamid Dehghani, for their support and guidance throughout the project.

I want to thank all my friends and colleagues, past and present, from both the Toellner and Cunningham lab for their help and support; namely Laura García Ibánez for the preparation of tissue samples, and in particular thank you to Dr. Jennifer Marshall, and Dr. Adriana Flores-Langarica, for their invaluable support in and out of the lab.

I want to thank my friends and colleagues, past and present, from the PSIBS CDT, for many stimulating conversations and making the shared experience such a memorable one.

I want to thank Dr. Margaret Goodall for kindly allowing me to use her cell culture facilities, and thank her, and Dr. Anita Chamba, for teaching and helping me with cell culture technique.

I want to thank the many people that have given me advice, and helped me, with my MATLAB woes, namely: Christopher Meah, Peter Saxon, Dr. Alan Race, and Dr. James Andrews.

I would like to thank Zeiss representative Dr. Dominic White for his great effort and determination in sourcing compatible microscope systems for the AFM, as well as JPK representative Dr. Alex Winkel for his support of the AFM.

I want to thank all my friends and teammates, past and present, from the university ice hockey team, for making my time in Birmingham such a memorable one.

A very special expression of gratitude goes to my parents, for their continued, unconditional support through all my studies. I would not have been able to do it without you.

For funding of the AFM facilities I want to acknowledge: Birmingham Science City: Innovative Uses for Advanced Materials in the Modern World (West Midlands Centre for Advanced Materials Project 2), with support from Advantage West Midlands (AWM) and part funded by the European Regional Development Fund (ERDF).

Lastly, I would like to thank the Engineering and Physical Sciences Research Council (EPSRC) for funding of the project, through a studentship at the PSIBS Centre for Doctoral Training (EP/F50053X/1).

Contents

List of Figures

List of Equations

List of Tables

List of Abbreviations

AFM	Atomic Force Microscopy
AP	Alkaline Phosphatase
ATAT	Amine-Terminated Alkanethiol
BCR	B Cell Receptor
CS	Control Surface
DAB	3-3'-Diaminobenzidine Tetrahydrochloride
DAPI	4',6-Diamidino-2-Phenylindole
DZ	Dark Zone
EtOH	Ethanol
FA	Formaldehyde
GC	Germinal Centre
H-bond	Hdrogen Bond
HCl	Hydrochloric Acid
LZ	Light Zone
NP	(4-hydroxy-3-nitrophenyl)acetyl
NP-OSuc	(4-Hydroxy-3-nitrophenyl)acetyl-O-Succinimide Ester
PBS	Phosphate Buffered Saline
RS	Relative Set Point
SAM	Self-Assembled Monolayer
SD	Standard Deviation
SPR	Surface Plasmon Resonance
XPS	X-Ray Photoelectron Spectroscopy

Elemental species are referred to by their symbol: e.g. Gold = Au, Sulfur = S

1 Introduction

1.1 Germinal Centres

Germinal centres (GCs) are a central part of the adaptive immune system. They are transient structures [1] that form in response to the detection of antigen in the body [2,3]. The initiating antigen can be in the form of a protein or polysaccharide, and microorganisms, such as viruses and parts of bacteria.

Formation of GCs occurs in the secondary or peripheral lymphoid organs, such as lymph nodes and the spleen, where mature naïve lymphocytes are maintained. The GC is the site where B-lymphocytes proliferate, differentiate, undergo immunoglobulin gene hypermutation, and class switching, all of which ultimately leads to the production of antibodies with affinities high enough to successfully bind, and mark for destruction, the antigen that initially triggered the reaction [4].

Shown diagrammatically in Figure 1, is a GC; composed of a light zone (LZ) and a dark zone (DZ). Naïve B cells enter the DZ where they proliferate vigorously, coupled with somatic hypermutation of their immunoglobulin genes [5]. This process produces B cell populations that are expressing a wide range of B cell receptors (BCRs) on their cell surfaces with a range of affinities towards the initiating antigen. The cells exit the cell cycle and transit to the LZ of the GC [6,7], where, based on the affinity of their mutated BCRs, they reiterate further cycles of mutation and selection, or are selected to differentiate into plasma cells or memory B cells [2,3,8]. Cells that cannot present advantageous mutations of their BCRs in selection undergo apoptosis.

Cells that have differentiated into plasma cells will no longer express the BCR on the cell surface, but instead produce a soluble version that does not contain the

membrane anchor, which will be secreted into the system as mature antibody. Cells differentiated to memory B cells retain the evolved BCR and distinguish themselves through their longevity. They ensure that if the system were to be exposed to the same antigen again in the future, an accelerated response to it can be effected.

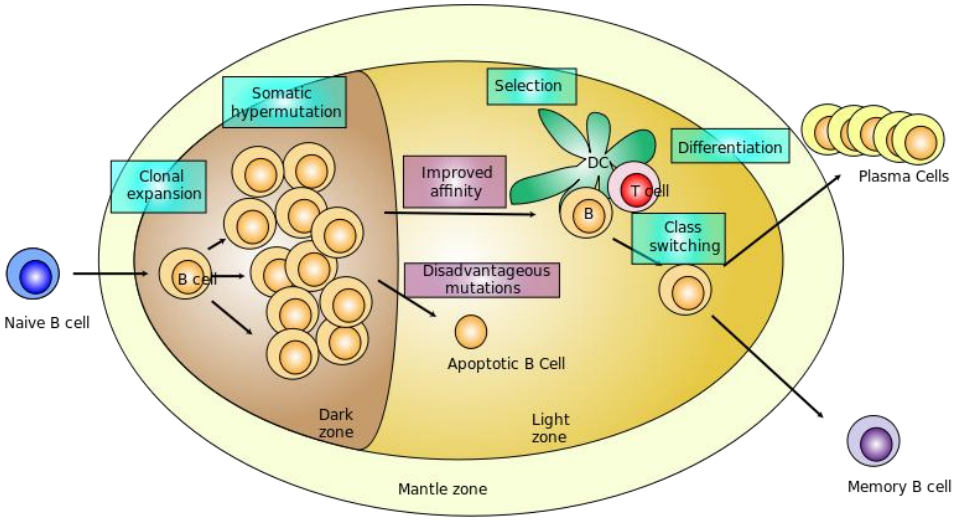

Figure 1 – Schematic of a GC.

Antigen-activated B cells are recruited to the GC and enter the DZ for proliferation and somatic hypermutation, transit to the LZ for selection and subsequent differentiation into antibody producing B cells or memory B cells. Image source: https://commons.wikimedia.org/wiki/File:Germinal_center.svg

After selection B cells can also re-enter the DZ, in a process called cyclic re-entry, for further iterations of proliferation and somatic hypermutation. Each additional iteration gives B cells the opportunity to further tune their receptors for improved affinity towards the antigen. This process ultimately leads to high affinity BCRs and represents true Darwinian evolution on a cellular level.[9]

1.2 B Cell Receptors and Antibodies

The BCR is the surface bound form of antibody, whose affinity towards the initiating antigen is developed while the cell resides in the GC. Once sufficient affinity is

demonstrated, the B cell receives instruction to leave the GC and differentiate. One of the differentiation fates is differentiation into a plasma cell, which produces, and secretes as soluble antibody, the previously surface bound BCR.

Antibody is a large, globular protein, ~150 kDa in molecular weight, which is composed of two different polypeptides called the heavy and light chain. The heavy and light chains each comprise a constant region, that is identical in amino-acid sequence from one immunoglobulin to the next, and a variable region, for which the amino-acid sequence is different from one immunoglobulin to the next.[10] Shown diagrammatically in Figure 2 is the characteristic “Y”-shape structure of an antibody, illustrating how the constituent components are held together by disulfide bonds.

Antibodies owe their functionality to their complex 3-dimensional structure; to illustrate Figure 3 shows an example of an IgG antibody, where the heavy chains are shown in blue and red, and the light chains in green and yellow. The variable regions at each tip of the “Y” are the antigen binding sites, their conformation defining specifically the antigen that an antibody can bind. The constant region of an antibody at the stem of the “Y” defines the functionality of an antibody, and, in its membrane bound form as a BCR, facilitates membrane insertion.

Membrane insertion is due to the expression of a small additional membrane targeting peptide chain in BCR molecules. The membrane bound BCR can sense antigen-binding and transmit signals into B cells.

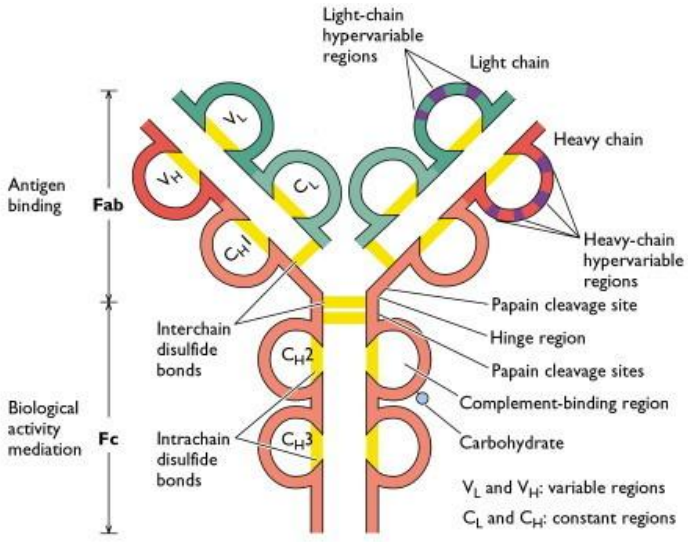

Figure 2 – Schematic of an IgG Antibody

Antibody is a large, globular protein that is composed of heavy (red) and light (green) chains, which each comprise a constant and a variable region. The constituent components are held together by disulfide bonds. Image taken from [11].

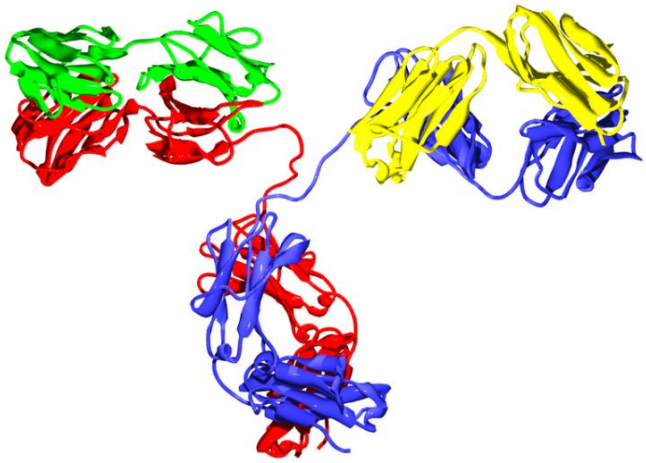

Figure 3 – 3-Dimensional Structure of an IgG Antibody

Protein structure of an IgG antibody, showing the heavy chains in red and blue, and light chains in green and yellow. PDB reference: 1IGT. Image source: https://commons.wikimedia.org/wiki/File:Antibody_IgG2.png.

The antibody schematics shown in Figure 2 and Figure 3 are examples of IgG antibody, which is one of several antibody isotypes. The structure of the antibody is determined by its isotype. IgG antibody, for example, presents in monomeric form,

where possible alternative structures are dimers and pentamers. The structures of isotypes present in mice and humans are shown in Figure 4.

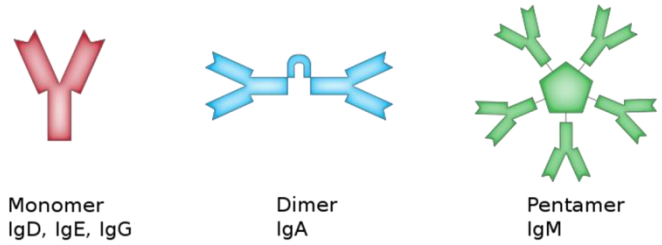

Figure 4 – Different Antibody Isotypes and Their Structures.

Different antibody isotypes present with different structures, possible variations include monomers, dimers and pentamers; with resulting numbers of antigen binding sites of 2, 4 and 10 respectively. Image source: https://commons.wikimedia.org/wiki/File:Mono-und-Polymere.svg

Antibodies can change their isotype through a process called isotype switching. This process involves the removal of a portion from the constant region of the antibody heavy chain locus, and re-joining of the gene segments surrounding the deleted portion, to retain a functional antibody gene; leaving the variable region of the heavy chain unchanged. The resultant locus now expresses a different isotype, but has retained its affinity and specificity towards the antigen.

This means that the progeny of a single B cell can produce antibodies that are all specific towards the same antigen, but with the ability to produce different effector functions appropriate to the antigenic challenge, e.g. recruitment of phagocytes for microbe destruction, or eosinophil and natural killer cell recruitment for granule release for the destruction of infected cells or parasites that are too large for phagocytosis.[4]

As an example of isotype switching, the scheme for an antibody switching from an IgM isotype to an IgG1 isotype is presented in Figure 5.

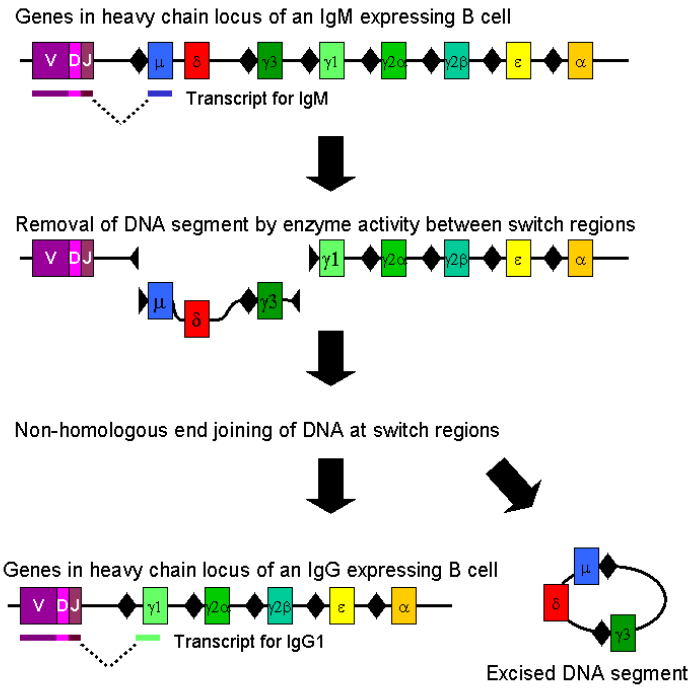

Figure 5 – Schematic for Antibody Isotype Switching

Schematic for isotype switching from IgM to IgG1. A portion from the chromosome for the constant region of the heavy chain is removed; and segments surrounding the deleted portion are re-joined to retain a functional antibody gene. Altering only the constant region of the antibody can change the effector function of the antibody, but allows it to retain its specificity and affinity.

Image source: https://commons.wikimedia.org/wiki/File:Class_switch_recombination.png.

1.3 Antibody Binding

The binding of antibody to antigen is often likened to an interaction of lock and key. It is based on non-covalent interactions being formed, such as hydrophobic, H-bonds, and van der Waal's forces, where a combination of multiples of these interactions will ensure a tight binding. As none of the interactions involved in the binding of antibody and antigen are covalent, the reaction is reversible.[12-14] Equation 1 describes the reaction, where antibody (Ab) and antigen (Ag) bind, to form an antibody-antigen

complex (AbAg). The association rate constant (k_{on}) and dissociation rate constant (k_{off}) carry units of $M^{-1}s^{-1}$ and s^{-1} respectively

$$Ab + Ag \underset{k_{off}}{\overset{k_{on}}{\rightleftharpoons}} AbAg$$

Where:

Ab	=	antibody	
Ag	=	antigen	
AbAg	=	antibody-antigen complex	
k_{on}	=	association rate constant	[$M^{-1}s^{-1}$]
k_{off}	=	dissociation rate constant	[s^{-1}]

Equation 1 – Reversible Antibody to Antigen Association

The binding of antibody (Ab) to antigen (Ag), to form an antibody-antigen complex (AbAg), is based on non-covalent interactions, such as hydrophobic, H-bonds, and van der Waal's forces, and hence is reversible. The association rate constant (k_{on}) and the dissociation rate constant (k_{off}) carry units of $M^{-1}s^{-1}$ and s^{-1} respectively.

The ratio of k_{on} and k_{off} yields the equilibrium dissociation constant K_D, as shown in Equation 2, which describes the affinity of the antibody to antigen reaction. K_D carries units of M, which denotes the concentration at which half the ligand binding sites are occupied. The lower the value of K_D, the higher the affinity.

$$K_D = \frac{k_{off}}{k_{on}}$$

Where:

K_D	=	equilibrium dissociation constant	[M]
k_{on}	=	association rate constant	[$M^{-1}s^{-1}$]
k_{off}	=	dissociation rate constant	[s^{-1}]

Equation 2 – Equilibrium Dissociation Rate Constant

The ratio of the dissociation rate constant (k_{off}) and association rate constant (k_{on}) yields the equilibrium dissociation rate constant (K_D), carrying units of M, which is a measure for the affinity of the antibody for the antigen. Its molar units denote the concentration at which half of the ligand binding sites are occupied. The lower the value of K_D, the higher the affinity.

Strictly, the affinity refers to the strength of interaction between single antigenic determinants and one antibody binding site. However, depending on the isotype, each antibody unit has at least two binding sites, and therefore multivalent binding can occur. The term used to describe the overall strength of binding due to multivalent binding is avidity. The difference between affinity and avidity is illustrated in Figure 6. The interaction shown in (A) is representative of affinity, involving only the interaction between a single antibody binding site and one antigenic determinant. The interactions shown in (B) and (C), on the other hand, are increasingly dominated by avidity. At equal affinity, the overall binding strength increases synergistically through multivalent binding. [12]

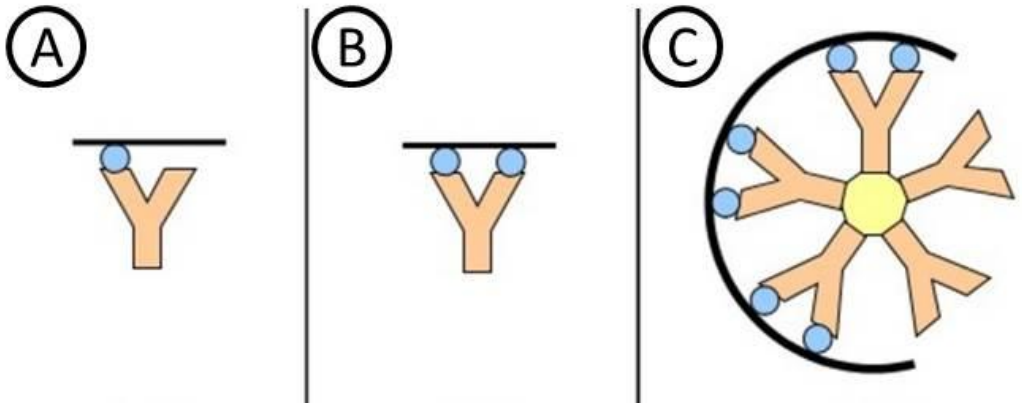

Figure 6 – Affinity vs Avidity

Affinity refers to the strength of binding between a single antibody binding site and a single antigenic determinant. Such an interaction can be seen in (A). Antibodies, however, depending on their isotype, have at least two binding sites, allowing for multivalent binding to occur. The overall strength of binding due to multivalent binding is termed avidity. Interactions which are increasingly dominated by avidity are shown in (B) and (C), where the avidity in the shown scenarios is greater than just the sum of the affinities of the individual interactions. Image taken from [12].

Techniques that assess the affinity of antibodies in solution, measure the bulk properties, which will be representative of avidity. To compensate for the multivalence of the examined antibodies, mathematical models are employed to

determine values of affinity. Currently such models are available only for the lower valence IgG antibodies that possess only two binding sites per antibody.

1.4 Imaging Germinal Centre Dynamics and B Cell Development

The GC reaction and the evolutionary path of B cells as they migrate through the GC during receptor maturation has been the focus of many research groups, and a diverse range of modalities has been employed in trying to image the development.

The approach chosen by Küppers, *et al.*, [15], was to pick individual cells from histological sections of GCs in mouse lymph nodes, and sequence their DNA using polymerase chain reaction (PCR). From this it was possible to construct genealogical trees explaining the relationship between clonally related sequences and show that somatic hypermutation is an on-going process that occurs at very high rates of one or more mutations per cell division.

There are, however, problems with the method. Due to the high sensitivity of PCR, cross contamination from individual target molecules can lead to false positives. Further, when attempting to pick out individual cells from frozen sections that are a cell diameter in thickness, it can occur that the nucleus of the picked cell is missing. This means that no information can be obtained for this cell, which is a substantial loss when considering the small number of samples that can be collected within reasonable timeframes.

Furthermore, based on the assumption that cells presenting disadvantageous mutations are steered towards an apoptosis fate, it can be tempting to infer the opposite, that highly mutated clones were expanded in the GC due to presenting

mutations that provided increased affinity. However, while the DNA sequence of an antibody variable region gene does give information on the genealogical history of the studied B cell clone, there is no information on the real affinity.

However, recently established techniques for high-throughput DNA sequencing of immunoglobulin genes may well overcome this shortcoming. Cloned immunoglobulin genes from isolated B cells can be used to express the antibody protein, allowing for its characterisation. This can alternatively also be achieved through the cloning and immortalisation of the B cell.[16] Thus, the previously collected information of the genealogical origin of clones can now be supplemented with functional information on the expressed antibodies.

A study by Hauser, *et al.*, [17], is concerned in particular with the migration patterns of GC B cells between the distinct compartments of DZ and LZ and whether the processes of differentiation and somatic hypermutation are restricted to their respective zones. Because the static nature of GC histological sections does not allow the study of the dynamics of motile cells, this study employed multiphoton microscopy in live anaesthetised mice.

Based on the findings of this study, a revised model of the migration routes of GC B cells was suggested. The traditional model for the movement of GC B cells dictates that DZ B cells transition to the LZ between iterations of division and mutation, in order to satisfy the conditions of mutation occurring in the DZ and antigen acquisition in the LZ.[18-20] The rapid rate of affinity maturation however indicates very high efficiency of selection of high affinity variants, and computer simulations suggest that selection would need to occur after every iteration for such high efficiencies to be

plausible.[21,22] Employing their own computer simulations, using experimentally determined estimates for cell division rate and time spent in each cell cycle phase, Hauser, *et al.*, [17], determined 17 % of cells to be moving across the DZ/LZ boarder each hour. The fact that far fewer such transitions were observed in experiments posed good reason to propose changes to the established model of intrazonal migration.

In the revised model according to Hauser, *et al.*, [17], GC B cells are primarily recirculating within either the DZ or LZ. The model includes infrequent transition of B cells between the zones, but it does not rely on it for multiple iterations of mutation and selection to occur.

While through the use of multiphoton microscopy the dynamics of cell migration can be observed, this is only possible for several hours before the mice finally die, allowing collection of only limited amounts of data. Further, several hours are relatively short time frames in the context of an immune response that spans two weeks, and subsequent studies did in fact suggest that the data presented by Hauser, *et al.*, [17], was insufficient to support the conclusions on intrazonal migration.[23,24]

A similar study focussing on the dynamics and migratory behaviour of GC cells was conducted by Schwickert, *et al.*, [25], who employed two-photon laser scanning microscopy for the direct visualisation of B cells in lymph node GCs in live mice.

The study found that the majority of antigen-specific B cells were, while physically restricted to the GC, motile and migrated bi-directionally between DZ and LZ. Additionally, it was found that the open structure of GCs can enhance competition by

allowing the recruitment of high affinity antigen-specific B cells to an on-going GC reaction.

Two-photon microscopy was employed by Allen, *et al.*, [6], to study GC cell migration and interaction dynamics in mouse lymph nodes. This study also found that GC B cells possessed great motility and transitioned between the DZ and LZ. GC B cells proliferated in both the DZ and the LZ, although they would only remain for short amounts of time in the LZ where antigen is displayed. The findings of the study were interpreted such that the access to helper T-cells is a limiting factor driving the selection of higher affinity B cells. Based on these conclusions a model is suggested were newly mutated high affinity GC B cells obtain and process more antigen and ultimately outcompete surrounding B cells for the attention of GC T-cells.

While the above studies have contributed to advancing our understanding of the dynamics of the GC reaction, the datasets that their conclusions were based on were limited; i.e. the data acquisition of the employed techniques was limited by either the number of samples that could be collected within reasonable time frames or the length of time over which they could be employed.

Further, the discussed studies were primarily focussed on the migration of GC B cells within the DZ, or LZ, and between the zones, but there is as of yet no established method that enables immunologists to extract information about the affinity of BCRs of GC B cells with respect to their location within the GC.

Evidence that the affinity of BCRs affects GC dynamics was shown by Zhang, *et al.*, [9]. This was shown by injecting antibodies during ongoing immune responses that were of varying affinities but with the same specificity; for the initiating antigen (4-hydroxy-3-nitrophenyl)acetyl (NP). Injection of low affinity antibody at the early stages of the response, helped accelerate affinity maturation by guiding selection pressure towards higher affinity B cell variants; as did the injection of antibodies of intermediate affinity at more mature stages of the response. Conversely, the injection of high affinity antibodies would lead to the termination of GCs as maturing BCRs could not outcompete the antibodies for access to antigen required for their survival.

Further understanding where, and when, affinities are higher in the GC, and how they increase over time, could help improve current models of the GC reaction. The only imaging modality that is suitable for making such measurements is atomic force microscopy (AFM). It provides great force sensitivity and spatial resolution, and through semi-automated data acquisition routines enables the acquisition of large amounts of data for whole GC sections that would not be feasible with techniques requiring a higher degree of supervision.

2 Aims and Objectives

Germinal centres (GCs) involve migration, and selection through cellular interactions in different microenvironments, leading to B cell differentiation. How these processes are regulated has not been studied in detail. As the differentiation of B cells in GCs depends on the affinity of the B cell receptor (BCR) [9], it would be desirable to be able to observe BCR affinity in histological specimens in order to track location and affinity of individual B cells in this environment. Developing such a method was the aim of the current project.

Proposed as novel was employing atomic force microscopy (AFM) for the interrogation of GCs, to study BCR affinities *in situ*; in order to complement specificity data, which can be obtained through the use of optical microscopy modalities, with affinity data.

To enable such investigations, the aim was to develop:

1. A bespoke scheme of modification of AFM probes for the detection of interactions specific for (4-hydroxy-3-nitrophenyl)acetyl (NP).
2. Control measures that enable the verification of successful AFM probe modification.
3. Data analysis methods for the automated and unbiased evaluation of large amounts of AFM data.

3 Atomic Force Microscopy

3.1 Atomic Force Microscopy

The atomic force microscope (AFM) is an extension to the scanning tunnelling microscope that was developed in 1982 by Binnig and Rohrer [26]; for which they were awarded the Nobel Prize in Physics in 1986 [27]. Unlike its predecessor, the AFM [28] does not require the sample to be conductive, opening up a great range of new potential applications.

The introduction of scanning probe microscopy into the biological sciences was advocated by Hansma [29], in 1988, referring to publications by Albrecht, *et al.*, [30], who published the first atomic resolution image of an insulator, and Marti, *et al.*, [31], who produced images allowing differentiation of features 0.5 nm apart in a polymerised monolayer, as demonstration that scanning probe microscopies were able to interrogate non conducting, and hence biological samples, at molecular resolution.

3.1.1 Working Principle

The generalised setup of a standard AFM is depicted diagrammatically in Figure 7. It consists of a stylus on the end of a cantilever, where the radius of the apex of the stylus tip is typically on the order of 10 nm and can be as low as 1 nm for high resolution imaging probes. The cantilever movement is controlled through piezo-electric crystals providing positional control with nanometre accuracy. A laser-photodetector pairing is used to quantify the deflection that the cantilever experiences due to contact with the sample. The laser is positioned on the top surface of the cantilever - approximately one third of the cantilever length away from

the cantilever's free end - from which the laser is reflected onto a position-sensitive photodetector. Upon deflection of the cantilever, the reflected path of the laser is altered, changing the incident position on the photodetector and hence the voltage read-out from the photodetector. Through calibration of the photodetector sensitivity against a hard surface, whose effective stiffness is orders of magnitude greater than the cantilever stiffness, the change in voltage read-out from the photodetector can be quantified as a distance of deflection of the cantilever. Subsequent determination of the cantilever specific spring constant allows for that distance to be expressed as force of deflection of the cantilever. The relationship of these parameters is shown in Equation 3, an adaptation of Hooke's Law in which the deflection is comprised of two terms: the deflection sensitivity as measured in m/V, and the deflection as measured in V.

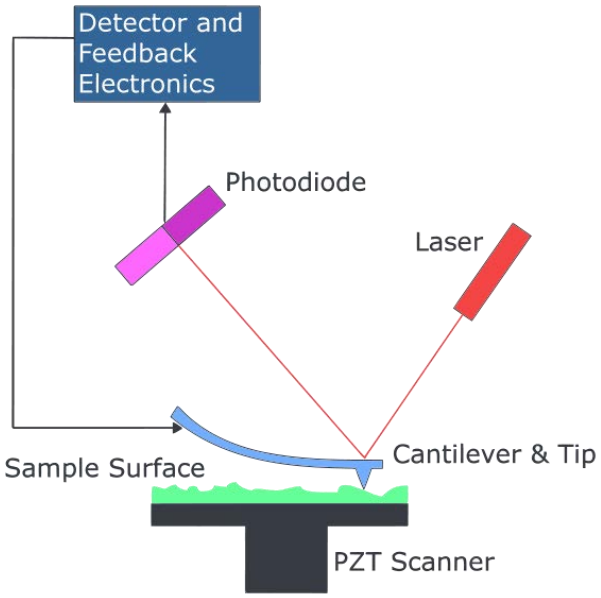

Figure 7 – Diagrammatic Depiction of an AFM Setup

The simplified set up of an AFM, comprised of a cantilever with a stylus at its free end, piezo-electric crystals for positional control of the cantilever, and a laser-photodetector pairing for quantification of cantilever deflection. Image source: https://commons.wikimedia.org/wiki/File:Atomic_force_microscope_block_diagram.svg.

$$F = k * S * \Delta x$$

Where:

F	=	force	[N]
k	=	cantilever specific spring constant	[N/m]
S	=	sensitivity of the position-sensitive photodetector	[m/V]
Δx	=	deflection	[V]

Equation 3 – Converting Measured Deflection Into Force.

In AFM measurements where the cantilever experiences deflection due to contact with the sample, the force (F), is comprised of the cantilever specific spring constant (k), the photodetector sensitivity (S), and the cantilever deflection (Δx) as quantified through the change in voltage read-out from the photodetector.

The process that the AFM will repeatedly cycle through for every point interrogation when scanning across a sample is depicted in Figure 8. The cantilever will initially be in the retracted baseline position, with sufficient distance between the cantilever and the sample for there to be no interaction between the two (A). The cantilever is then approached towards the surface, until the distance between the tip and the sample is sufficiently small for van der Waal's forces to dominate. The small interaction forces that exist between the tip and the sample at that point, cause the tip to snap into contact with the sample [32], deflecting the cantilever in the negative direction (B). The cantilever approach is continued, first relaxing the 'snap-in' cantilever deflection, then pushing into the sample, deflecting the cantilever in the positive direction. The positive cantilever deflection increases until a pre-specified set point is reached, which depending on the setup of the AFM operating software can be in either force [N] or deflection [m] (C). Upon reaching of the set point, the cantilever retraction is begun. As before, the cantilever deflection is relaxed until it reaches unstrained baseline level and then, when the tip experiences adhesion to the sample, is deflected in the negative direction (D). As the cantilever retraction continues, the cantilever deflection continuingly increases until the elastic energy built up in the

cantilever overcomes that associated with the tip-sample interaction. At this point the tip-sample connection is ruptured (E) and the cantilever returns to an unstrained position, and hence the deflection returns to the baseline value (F).

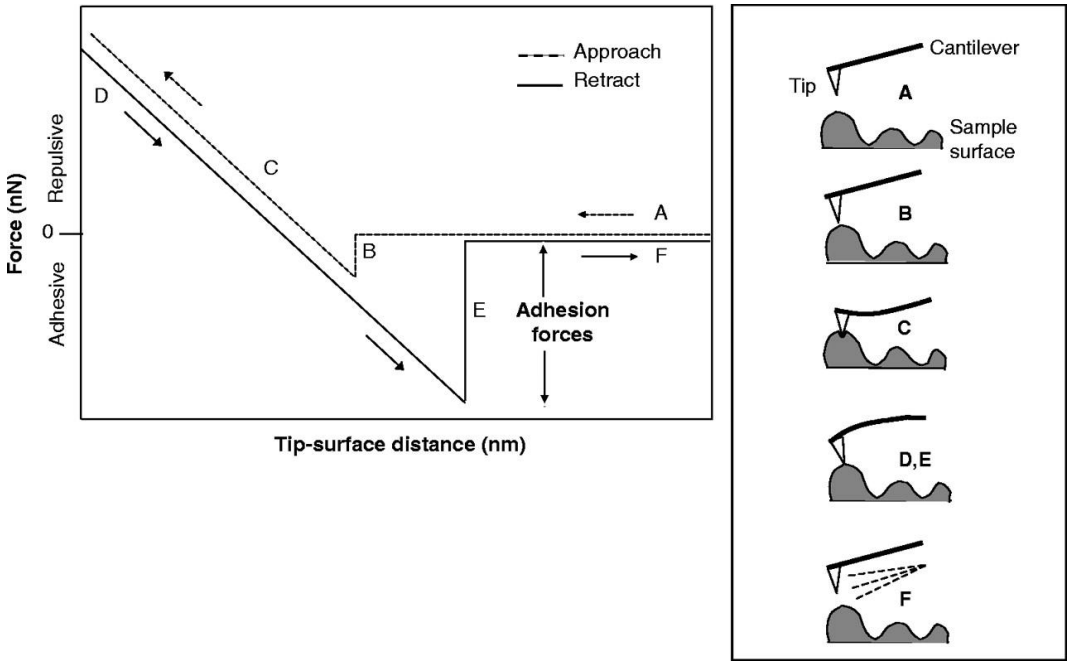

Figure 8 – Idealised Tip-Sample Interaction.

Diagrammatic description of an idealised tip-sample interaction; as drawn by Shahin, et al.,[33]. The cantilever approaches towards the sample from an initially retracted position (A), until the distance between the tip and the sample is sufficiently small for van der Waal's forces to take effect, which causes the tip to snap into contact with the sample (B). The tip is pushed into the sample until a pre-specified set point is reached (C), upon which the cantilever is retracted (D). When the tip experiences adhesion to the sample, the cantilever is increasingly deflected with continuing retraction, until the elastic energy built up in the cantilever is sufficient to overcome that associated with the tip-sample interaction (E). After rupture of the connection the cantilever returns to its unstrained baseline state (F). Scanning across the surface of the sample, this cycle is repeated for every point interrogation.

3.1.2 Cantilever Calibration

As evident from Equation 3 (p.17), the experimentally determined force of interaction, and associated interaction descriptors, depends heavily on the cantilever spring constant. This spring constant is specific to each cantilever that is used, and the nominal values that are provided by the manufacturers have been found to be by a factor of 2 in error [34]. Therefore a quick and robust method for determining the spring constant value individually for each cantilever is required to ensure accuracy of obtained results while not expending valuable instrument usage time with time-consuming calibrations.

Due to the rapid branching out of AFM into increasingly more specialised applications, an increasing number of cantilever variations are commercially available, and the field investigating methods for calibrating said cantilevers has grown accordingly. Some discourse remains over which is the most reliable method. A comprehensive review by Clifford, *et al.*, [34], identifies the three main categories of methods for cantilever calibration as (1) dimensional, (2) static experimental, and (3) dynamic experimental. Dimensional analysis requires detailed knowledge of the cantilever material composition and its geometry for use with simplified equations or finite element models to determine the spring constant. In the case of laminated cantilevers, as used here, however, the exact thickness of the different layers is not easily accessible, which makes constructing trustworthy models difficult. Static experimental methods determine the spring constant of a cantilever by applying a constant force and measuring the resulting deflection. The constant force, however, is typically applied using reference cantilevers that need to have been pre-calibrated using other more laborious methods. Lastly, dynamic experimental techniques work

by measuring the resonant frequency of a cantilever, and through the change in resonant frequency resultant from the addition of known masses can determine the cantilever spring constant. While this may produce accurate values, it is a time-consuming process and the addition of masses to the cantilever would interfere with its modification and hence its function.

The method that was employed for determining cantilever spring constants throughout this project was that described by Bowen, *et al.*, [35], that has specific application to the calibration of laminated, rectangular cantilevers. This method is in the category of dynamic experimental, using the cantilever's resonant frequency to determine its spring constant, but does so without changing the conformation of the cantilever. The method is based on the assumption that along with the resonant frequency of the cantilever, values of its width and length are easily accessible, and that the cantilever material properties are the same as the bulk properties of that material as stated in the literature.

As illustrated in Figure 9, the method achieves good correlation between the calculated and measured spring constant in the case of unlaminated rectangular cantilevers and rectangular cantilevers that had microparticles added to their apex. The spring constant of Cr and Au laminated rectangular cantilevers, however, is systematically underestimated, where the measured spring constant is typically twice the calculated spring constant.

The errors associated with the determined spring constant when using this method have been quantified to be approximately 10 %, and are comparable to other methods.[35] On account of the time and resources that are required being very limited,

however, the associated errors were deemed acceptable, and considerations for use of alternate calibration techniques were reserved for when the accuracy of the cantilever spring constant was found to detrimentally affect the obtained results.

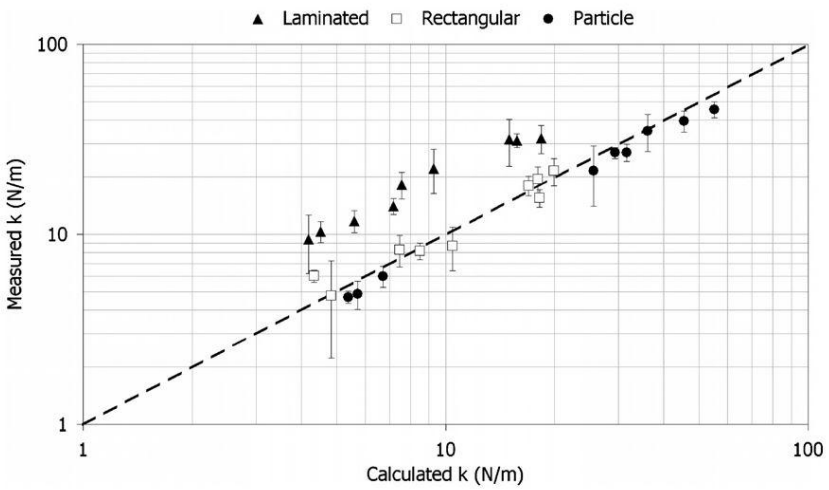

Figure 9 – Comparing Measured and Calculated Spring Constants.

The comparison of the measured and calculated spring constants for all investigated cantilevers using the method described by Bowen, *et al.*, [35], shows good correlation between calculated and measured spring constants for unlaminated rectangular cantilevers (clear squares) and rectangular cantilevers that at their apex had microparticles added (solid circles). In the case of laminated cantilevers (solid triangles) there is a systematic underestimation of the calculated spring constant; where the measured spring constant is systematically twice the calculated spring constant. Image taken from [35].

3.1.3 Atomic Force Microscopy in Biomedical Applications

The commercialisation of the AFM made the technique considerably more accessible and promoted a branching out into a variety of disciplines, including that of biomedical research. Realising AFM's capability for probing interaction forces at single molecule level, several studies were since able to elucidate biologically relevant processes by probing their associated chemical interactions.

An extensively employed interaction in biological sciences is that of streptavidin with biotin. Due to their strong binding with each other, the streptavidin-biotin interaction

also posed an accessible mechanism for interrogation via AFM. One such study by Wong, *et al.*, [36], performed direct force measurements of the interaction, looking at both long and short range adhesive interaction. Another study by Ludwig, *et al.*, [37], used the streptavidin-biotin mechanism to establish their new 'affinity imaging' method whereby the extraction of topography, adhesion, and sample elasticity can be extracted from local force scans.

Other early studies by Allen, *et al.*, [38], and Harada, *et al.*, [39], looked at the interaction between ferritin and anti-ferritin antibodies that had been immobilised onto solid substrates and found that the interaction force of that system was 49 pN and 63 pN per antibody-antigen pairing respectively. Both studies also describe the data to possess periodicity, suggesting the force of the interaction is quantised with the number of binding events occurring at each interrogation; allowing distinction between single and multiples of binding events. Such quantisation of forces associated with specific binding events was first shown by Florin, *et al.*, [40].

Vastly more specific and subtle interactions have since been interrogated via AFM. Fichtner, *et al.*, [41], investigated the adhesive functionality of E-cadherin; a calcium-dependent cell-cell adhesion molecule. Tsapikouni, *et al.*, [42], interrogated the binding forces of P-selectin with its ligand, an essential mechanism in extravasation (the recruitment of white blood cells from the vasculature), and migration of leukocytes, and Wildling, *et al.*, [43], employed AFM to determine the binding forces between serotonin transporter and a potent cocaine analogue to study antidepressant binding.

The literature far extends beyond these studies, and comprehensive reviews have been published in specialising areas of AFM in biomedical applications.

An extensive article published by Engel and Gaub, [44], in 2008, discusses the insights that AFM investigations have been able to provide into the structure and mechanics of membrane proteins. The very same topic that Baclayon, *et al.*, [45], reviewed in 2010.

Müller and Dufrêne have published separate reviews in collaboration with each other in 2009 and 2013 respectively [46,47], in which they, similarly, discuss AFM's contribution to furthering insights into how cells can interact with their environment by probing cell surface receptors and their functional states. Further, in a review by Marszalek, *et al.*, [48], published in 2012, force spectroscopy studies of polysaccharides are included alongside those focussing again on cell surface proteins, and, in a review by Allison, *et al.*, [49], the AFM's position as a very versatile imaging modality in the biological sciences is broadly reviewed. And this is just to name a few.

Lastly, another noteworthy article is that by Eifert, *et al.*, [50], discussing the further advanced insights that can be gained through the hyphenation of AFM; by which is meant the integration of AFM with complementary imaging modalities. Already, AFM is routinely integrated with optical microscopies – including super-resolution techniques such as total internal reflection fluorescence microscopy (TIRF), photoactivated localisation microscopy (PALM), and stimulated emission depletion microscopy (STED) – but has more recently also been further enhanced through integration with Raman and IR spectroscopy, electron microscopy, and, through the use of a heatable probe, even mass spectrometry.

3.1.3.1 Determining Antibody Affinity from AFM Force Measurements

Cellular adhesion is mediated by reversible bonds between specific molecules that are based on weak non-covalent interactions. The physics of such cellular adhesion interactions and their behaviour in response to applied forces, as in force spectroscopy experiments, were elucidated by Bell and Evans.[51,52] While the theoretical foundation of the stipulated principles is not easily accessible to readers unversed in fundamental physics, one consequence of their application is the ability to estimate the dissociation rate constant (k_{off}) for the interaction between specific molecules from measurements of force required to break their connection. As has already been highlighted in §1.3 (p.6), the parameter k_{off} is involved in determining the affinity of an antibody, described by K_D; to which it is directly proportional.

A study by Schwesinger, *et al.*, [53], is one example where results from AFM force measurements were used to estimate k_{off} for a range of molecular interactions. In the study, nine different single-chain Fv fragments (scFv) were investigated, determining their association and dissociation rate constants in solution, as well as the unbinding forces that they produce in AFM force measurements. The scFv are not actual fragments of an antibody, but instead the fusion of the heavy and light chain variable regions of an antibody. Even though they are missing the constant region, the proteins retain the affinity and specificity of the original antibody.

The study demonstrated a strong correlation of the unbinding forces produced by the different investigated molecules to their values of k_{off}, and showed that values of k_{off} determined from measurements of unbinding force were in good agreement with values of k_{off} determined in solution.

The study further concluded that, because k_{off} is the primary determinant of affinity, values of k_{off} determined from AFM force measurements were suitable to rank single molecules according to their affinity, and even had relevance in predicting their equilibrium behaviour in solution.

As has been pointed out in §1.3 (p.6), values of affinity describe the strength of interaction between one antibody binding site and single antigenic determinants. The forces of interaction that are measured via AFM are between such individual associations and hence directly allude to affinity. Other techniques that, for example, assess the affinity of antibodies in solution, measure bulk properties, and consequently have to compensate for the multivalence of the examined antibodies through the use of mathematical models. Such models are currently only available for the lower valence IgG antibodies that possess two binding sites per antibody.

3.2 Cantilever Modification

The studies discussed in §3.1.3 (p.21) demonstrate the versatility of AFM in biomedical research, but what they have in common is that they all rely on bespoke chemical modification of the used cantilevers, because the cantilevers are not naturally specific towards the targeted receptors. That same challenge was faced in this project. The biological systems that were interrogated in this project were all specific towards the antigen (4-hydroxy-3-nitrophenyl)acetyl (NP) and therefore it was required to develop means by which AFM cantilevers could be equipped with the NP antigen in order to interact specifically with the targeted receptors.

Several ways in which AFM cantilevers may be modified have been described in the literature [54], where the intended end application is the principal determinant for which approach is best suited. When for example the use of bare silicon tips is appropriate, functionalisation can be achieved through silanisation. Most commonly used, however, are cantilevers that are pre-coated in gold (Au). Here, functionalisation can be achieved through the use of alkanethiols, which, over the course of several hours, will form stable and densely packed self-assembled monolayers (SAMs) on the Au substrate due to the strong specific interaction of Au with sulfur (S). The SAM formation by alkanethiolate adsorption and self-assembly on Au substrates is discussed further in §4.1 (p.31).

To date, the only other study that could be identified in which NP-specific systems have been interrogated via AFM was conducted by Natkanski, *et al.*, [55]. As far as was possible to determine from the published study and its accompanying supplemental information, the cantilevers that were used in this study were pre-coated in Au, and in order to achieve specificity towards the targeted receptors were first equipped with streptavidin, which was later used for the attachment of biotinylated antigen. A detailed protocol for the functionalisation of the cantilevers, however, could not be collated from the available documentation. Personal communication with the senior author [56] of the study further revealed that the preparation of the cantilevers needed to be carried out just prior to experiments, and required cantilevers to be kept wet at all times. Consequently, this made planning and preparing experiments difficult, and in the case of failed cantilever modification could see precious samples, e.g. those obtained from animals, go to waste.

The cantilever modification scheme that was already being developed for this project at the time the study by Natkanski, *et al.*, [55], was published in 2013 overcomes these issues, as the modification scheme does not involve the use of proteins that need to be kept hydrated at all times. The advantages of having more flexibility in planning, preparing, and conducting experiments were deemed reason enough to further pursue the protocols already in place. The details of the cantilever modification scheme developed in this project are outlined in the subsequent section.

3.2.1 Proposed Cantilever Modification Scheme

The cantilever modification scheme that was developed for this project is based on the use of cantilevers pre-coated in Au. These are now routinely manufactured with good consistency and hence provide a reliable basis for reproducible preparations. The modification scheme is depicted in Figure 10, and is based on the use of an amine-terminated alkanethiol (ATAT). When cleaned cantilevers are immersed in the ATAT solution, over time, the ATAT molecules will form a SAM on the Au substrate, where the S group forms a strong covalent bond with the Au substrate, leaving the amine group exposed (A). The exposed amine group is the target for the subsequent attachment of NP, which is achieved by immersing the cantilevers in solution of (4-Hydroxy-3-nitrophenyl)acetyl-O-succinimide ester [57-59] (NP-OSuc). The NP will attach to the amine group via a bond that is also covalent. The by-products of the reaction and any excess are removed during subsequent washes (B). After completed modification, the cantilevers are dried and stored in the dark under ambient conditions.

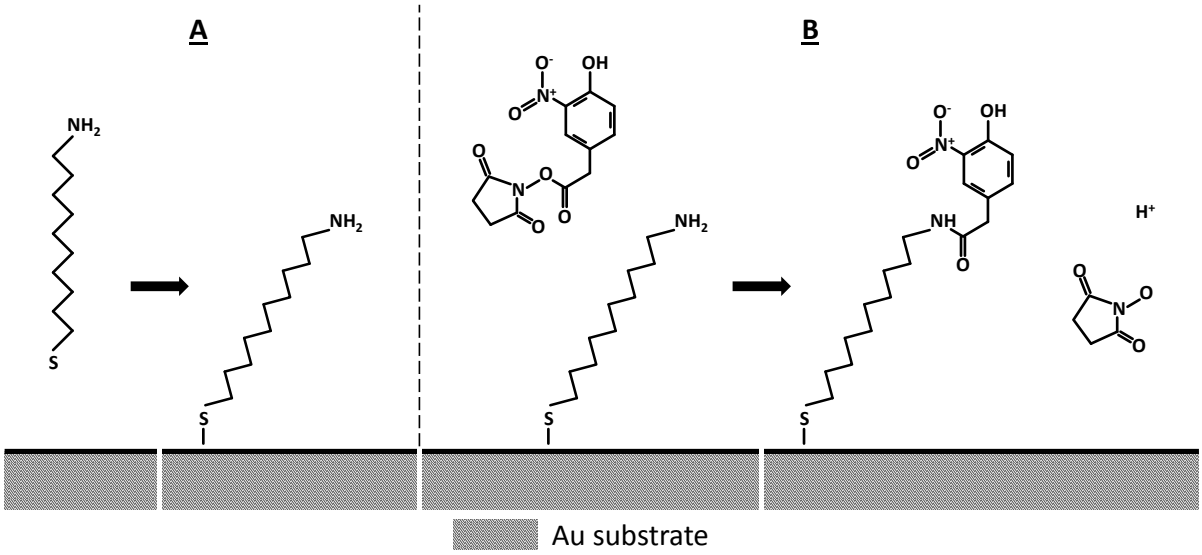

Figure 10 – Proposed Cantilever Modification Scheme

The modification scheme is based on the use cantilevers pre-coated in Au. Immersion of cleaned cantilevers in solution of ATAT will allow a SAM to form, where the S group forms a strong covalent bond with the Au substrate, leaving the amine tail group exposed (A). The exposed amine group is the target for the subsequent attachment of NP, which is achieved through immersion of the cantilevers in NP-OSuc solution. NP will attach to the amine group, forming a bond that is also covalent, and by-products of the reaction and any excess are removed in subsequent washes (B). After completed modification, cantilevers are dried and stored in the dark under ambient conditions.

The modification scheme is based on covalent bonds being formed at both modification steps, and these have been reported to require between 1-10 nN of force to be ruptured.[38,46,60,61] The magnitude of the interaction forces that are to here be investigated are expected to be on the order of no more than 100 pN, as the force of the interaction between biotin and avidin, which is considered one of the strongest interactions encountered in biological investigations, is reported to be ~250 pN.[36]

With the forces involved in the cantilever modification scheme being approximately an order of magnitude higher than the forces that are to be probed, the proposed modification scheme should provide sufficient stability to be well suited for the

planned investigations. Further, a more recent study by Teulon, *et al.*, [62], did in fact show that the routinely determined interaction forces for the (strept)avidin-biotin complex on the order of 100 pN are in fact not representative of single molecule associations, but rather are the product of multiple parallel bonds occurring. Hence, the stability of the covalent bonds that link the constituent components in the cantilever modification scheme should even more so be unaffected by the force exerted by individual interactions that are expected to be encountered.

Furthermore, the modification scheme avoids the use of proteins, which are very susceptible to damage upon dehydration.[63] This is beneficial as it avoids the need for modified tips to be kept hydrated and be used right after completed modification; allowing for more flexibility in planning, preparing, and conducting experiments.

The protocol that was developed for the preparation of the cantilevers can be found in Appendix 8.1.1 (p.206). The details of the protocol were developed in extensive investigations, which are discussed in the following chapter.

4 Confirmation of Successful Modification and Quality Control

One of the main concerns encountered in this project was that of confirming successful functionalisation of atomic force microscopy (AFM) tips with (4-hydroxy-3-nitrophenyl)acetyl (NP). The cantilever itself, and the tip especially, are too small to be interrogated directly, therefore an alternate medium was required that would provide substantial enough area on which the different chemical modification steps could be tested. For this purpose Au-coated silicon wafers (purchased from Georg Albert PVD – Beschichtungen, Silz, Germany) were chosen, because their Au coating provide the same characteristics as the Au coating on the cantilevers. Additionally, they provide a significant planar surface with minimal surface roughness (nominal RMS surface roughness < 1 nm) that enables the application of a range of techniques for the testing of the different applied chemical modifications.

The range of different surfaces that were prepared in this way is hereinafter referred to as a control surface (CS), and they are to serve a dual purpose. Firstly, they are to be used in the investigation of the individual chemical modification steps that are required in the proposed cantilever modification scheme. Secondly, they are to also serve as a robust counter-surface, with consistent chemical properties, against which the interaction with NP functionalised cantilevers can be measured in order to build up an interaction profile that can be used to easily distinguish between successfully and unsuccessfully prepared cantilevers before their use in the interrogation of biological samples for which specificity of the AFM probe is required.

4.1 Control Surfaces

The different CSs that were prepared in this project are all based on alkanethiolate molecules forming self-assembled monolayers (SAMs) on an Au substrate. The general process of SAM formation is briefly explained in Appendix 8.2 (p.214), and when considering specifically the formation of alkanethiolate SAMs on Au substrates is based on the strong interaction between S and Au providing adhesion of the molecule to the substrate, where the organisation and packing of the molecules in the monolayer is driven by van der Waal's forces.[64] The group in the molecule that facilitates adhesion of the molecule to the substrate is referred to as the head group. The group exposed at the surface of the SAM is referred to as the tail group, and is the group that defines the functionality of the SAM.

The different CSs that were prepared in this project are depicted in Figure 11, and individually are hereinafter referred to by their tail group:

1: CS-CH_3

2: CS-NH_2

3: CS-COOH

4: CS-OH

5: CS-NP

Further, the prepared CSs can be separated into two groups. CS-NH_2 and CS-NP are the constituent steps required in the proposed cantilever modification scheme, and CS-CH_3, CS-COOH, and CS-OH were added specifically for NP functionalised cantilevers to be tested against.

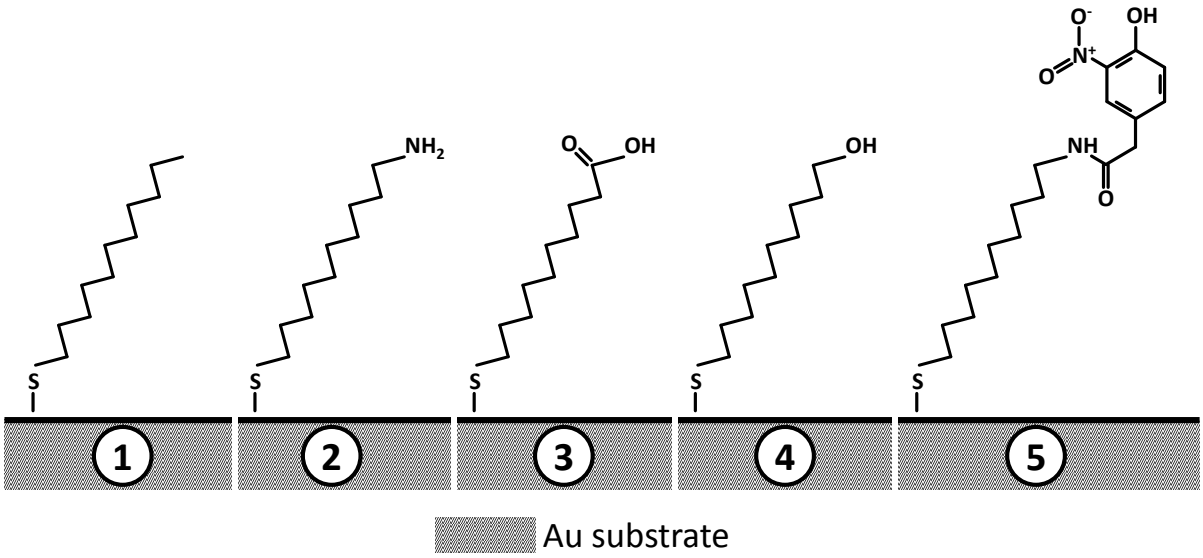

Figure 11 – Chemical Modifications of the Different CSs

All of the different chemical modifications of the CSs are based on the use of alkanethiols that due to the strong interaction between S and Au will form SAMs on the Au-coating of the silicon wafer substrates. CS-NH_2 (2) and CS-NP (5) are the constituent steps required in the proposed cantilever modification scheme, and CS-CH_3 (1), CS-COOH (3), and CS-OH (4) were added specifically for NP functionalised cantilevers to be tested against.

All AFM experiments are conducted in phosphate buffered saline (PBS), which is a buffer providing ionic strength and acidity similar to physiological conditions. While this is not required for the experiments in which NP functionalised cantilevers are tested against CSs, it is required for the maintenance of sensitive biological samples. Hence, in order to maintain comparability of different experiments, the same conditions were applied throughout.

The different compounds used for the preparation of the CSs were chosen on the basis that after successful SAM formation they are expected to produce surfaces with specific surface charges and wetting properties that yield distinct interactions when interrogated with NP functionalised cantilevers.

NP functionalised cantilevers are equipped with a nitro (O=N-O) and a hydroxyl (OH) moiety as part of the added NP. These moieties are both highly electronegative and hence NP functionalised cantilevers are expected to possess a negative electrostatic charge.

While CS-NH_2 was prepared primarily to investigate the first of the constituent steps of the cantilever modification scheme, NH_2 terminated SAMs are also routinely employed to model positively charged surfaces.[65] This means that with the inclusion of CS-NH_2, there are four different surfaces available for NP functionalised cantilevers to be tested against. The chosen surface modifications are used frequently, where CH_3 and OH terminated SAMs are used to model hydrophobic and hydrophilic neutral surfaces, and NH_2 and COOH terminated SAMs are used to model positively and negatively charged surfaces, respectively.[66] The bulk wetting properties for both NH_2 and COOH terminated SAMs are expected to be hydrophilic.[67]

Due to the different properties of the different CSs, the interactions that are expected to be produced in interrogation with NP functionalised cantilevers vary. The interactions produced in interrogation of the neutral CS-CH_3 and CS-OH are expected to be determined by their differing wetting properties, whereas interactions produced in interrogation of the hydrophilic CS-NH_2 and CS-COOH are expected to be determined by their electrostatic charge.

CS-NP was used only for interrogating the quality of the deposited surface modification and not for interrogation with NP functionalised cantilevers; as both are equipped with the same surface modifications. Literature describing the behaviour of NP terminated SAMs could not be found, however, based on the electronegativity of the contained nitro and hydroxyl moieties it is expected that the SAM will exhibit hydrophilic bulk properties.

To be able to infer characteristics from the collected data with confidence, the CSs themselves had to be assessed for their quality. The different techniques that were employed to assess the quality of the prepared CSs were ellipsometry, sessile drop contact angle, and X-ray photoelectron spectroscopy. The working principles of these techniques and the insights into the quality of the prepared surface modifications they provide are outlined in the subsequent sections (§4.1.1 - §4.1.3; pp.37-42)

In order to obtain different theoretical insights to the used molecules, that experimentally obtained results could be compared against, software package ChemBioDraw Ultra (v14.0.0.117, CambridgeSoft (Perkin Elmer)) was used to model the individual molecules, and software package ChemBio3D Ultra (v14.0.0.117, CambridgeSoft (Perkin Elmer)) was used to measure the molecules' lengths as they would be observed when unstrained in free space. The molecule structures as obtained from software are attached in Appendix 8.3 (p.215), and calculations for theoretical SAM thicknesses for the different molecules are attached in Appendix 8.4 (p.222). Predicted SAM thicknesses are determined using the theoretically

determined molecule length and a characteristic tilt angle of 30° of the molecule backbone from the surface normal for alkanethiols on Au(111).[68]

An overview of the different properties for the different molecules can be found in Table 1.

Table 1 – Collation of Property Information on CSs

The information collated in this table details properties for the molecules used in the preparation of the different CSs. For each CS the name of the compound used for SAM preparation and its chemical formula is given. The wettability of the prepared SAM and the corresponding contact angle are determined by the molecule tail group, and literature values for contact angles are given where available. The lengths of the different molecules were determined using computer software, the values of which were used to determine likely SAM thicknesses based on characteristic SAM molecule tilt angles.

Label	Compound	Chemical Formula	Water Wettability	Predicted Contact Angle [°] *	Molecule Length [nm] **	Predicted SAM Thickness [nm] ***
CS-CH_3	Dodecane-1-thiol	$HS(CH_2)_{11}CH_3$	hydrophobic	Θ_s 108.7 ± 0.6 [69] Θ_a 117.4 ± 0.2 [67]	1.609	1.393
CS-NH_2	11-Mercaptoundecan-1-aminium chloride	$HS(CH_2)_{11}NH_2HCl$	hydrophilic	Θ_s 42.0 ± 3.0 [70] Θ_s 43.0 ± 5.0 [66]	1.595	1.381
CS-COOH	11-Mercapto-undecanoic acid	$HS(CH_2)_{10}COOH$	hydrophilic	Θ_s <10.0 [66] Θ_a <10.0 [71]	1.581	1.369
CS-OH	11-Mercapto-1-undecanol	$HS(CH_2)_{11}OH$	hydrophilic	Θ_s 44.0 ± 2.0 [70] Θ_s 20.0 ± 2.0 [69]	1.583	1.371
CS-NP	2-(4-Hydroxy-3-nitrophenyl)-N-(11-mercaptoundecyl) acetamide	$HS(CH_2)_{11}NH$-$C_8H_6NO_4$	(hydrophilic)	n/a	1.511 + 0.631	1.309 - 1.855

* literature values ** according to ChemDraw software packages *** using theoretical molecule length and characteristic tilt angles.

Θ_s - sessile drop contact angle Θ_a - advancing contact angle

4.1.1 Ellipsometry

Ellipsometry assesses the thickness of thin surface modification layers deposited onto flat and smooth substrates. Quantifying the thickness of said layers, allows comparison to theoretical values of ideal monolayer thickness of each individual surface modification, and hence insight into whether a monolayer has indeed been achieved or if there is evidence of multiple molecule stacking.

4.1.1.1 Working Principle

Ellipsometry is a non-destructive optical technique that is typically conducted under ambient conditions. The basic set up for ellipsometry is depicted in Figure 12, and is comprised of a light source and polariser, and an analyser and detector. The light source steps through the light wavelength range of 250-800 nm, which is polarised before it hits the sample. The polarised light is reflected by the Au substrate, but its phase and amplitude is altered during interaction with the surface thin film. This change in amplitude and phase is quantified by the analyser-detector pairing, and subsequent fitting of mathematical models to the experimental data allows determining unknown sample parameters like the thickness of deposited thin films.[72] The ellipsometry technique and its underlying fundamental principles are discussed further in detail in Appendix 8.5.

Ellipsometry investigations were performed using a spectroscopic ellipsometer (Jobin-Yvon/Horiba, UK), operating with DeltaPsi v2.0.8 software, under ambient conditions. Measurements were taken in non-overlapping positions on the sample, where visibly damaged areas of the sample were avoided. Measurements where mathematical models could not be successfully fitted to the data were omitted from

the analysis. Considerations for the omission of measurements are discussed in more detail in §4.2.2.2 (p.63).

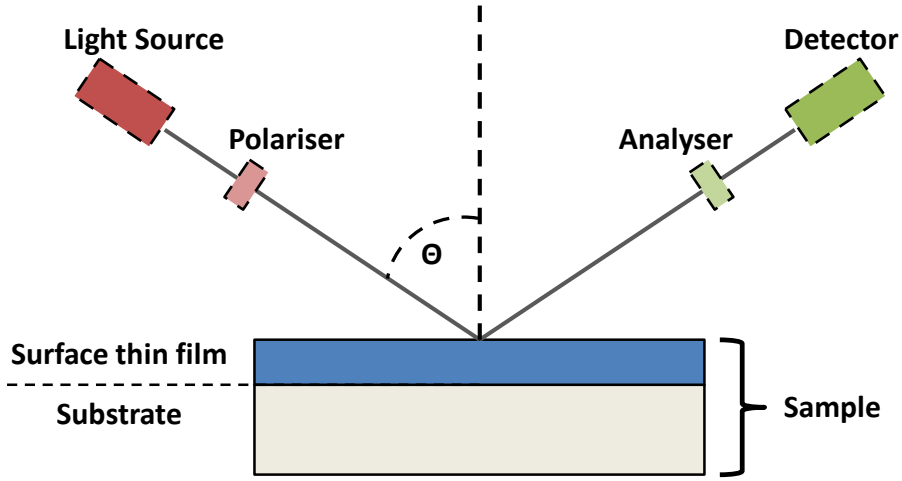

Figure 12 – Diagrammatic Depiction of Ellipsometry Setup

The typical ellipsometry set up is comprised of light source-polariser, and analyser-detector pairings. Light in the wavelength ranges of 250-800 nm is polarised before it is incident on the sample. The light is reflected by the Au substrate, but its amplitude and phase are altered by interaction with the surface thin film. The change in amplitude and phase is quantified by the analyser-detector pairing and subsequent mathematical modelling of the data provides values of the thin film thickness.

4.1.2 Sessile Drop Contact Angle

Sessile drop contact angle measurements are a quick characterisation tool assessing the surface chemistry of the investigated CSs, providing insights into the hydrophobic, or hydrophilic, qualities of the interrogated surface. With regards to the here investigated CSs it provides further information on the quality of the deposited SAMs by testing for the presence of the desired tail group moieties at the thin film surface, which due to their electrostatic potential produce distinct wetting properties.

More commonly used than sessile drop contact angle measurements are advancing and receding contact angle measurements. These are a more detailed interrogation of the quality of surface chemistries, but were not carried out in this project as

equipment that could facilitate such measurements was not available. Beyond the necessary equipment not being available, however, these measurements are also more time consuming and would have been beyond the time constraints of this project. It does however mean that available literature will more commonly quote values of advancing and receding contact angles for common surface chemistries, which is reflected in the information collated in Table 1 (p.36).

4.1.2.1 Working Principle

The setup for contact angle measurements is depicted in Figure 13. The sample is placed between a light source and a camera. A small droplet of water is then deposited on the sample using a syringe. The back-illumination makes the contours of the deposited droplet more easily distinguishable on the images that are taken with the camera. The sample rests on a height-adjustable stage which is used to ensure that in the field of view of the camera the sample is level. The volume of the water droplet dispensed from the syringe is kept to be small, but because the dispensing process is manual rather than automated, there are inevitably variations of the dispensed volume. It has however been shown for a range of droplet sizes that the measured contact angle is unaffected by the volume of the droplet, so long as the droplet is small enough that surface tension determines droplet shape rather than gravitational forces.[69]

The images acquired in contact angle measurements are later quantified using the image analysis software ImageJ (v1.49u, Wayne Rasband). Considerations for the image analysis process are shown in Figure 14. Using the ‘angle-tool’, a line is drawn between the two contact points of the free droplet arc with the sample, and the freely moveable line is then moved to draw a tangent with the droplet arc, where the

resulting angle between the two lines defines the contact angle of the droplet with the sample.

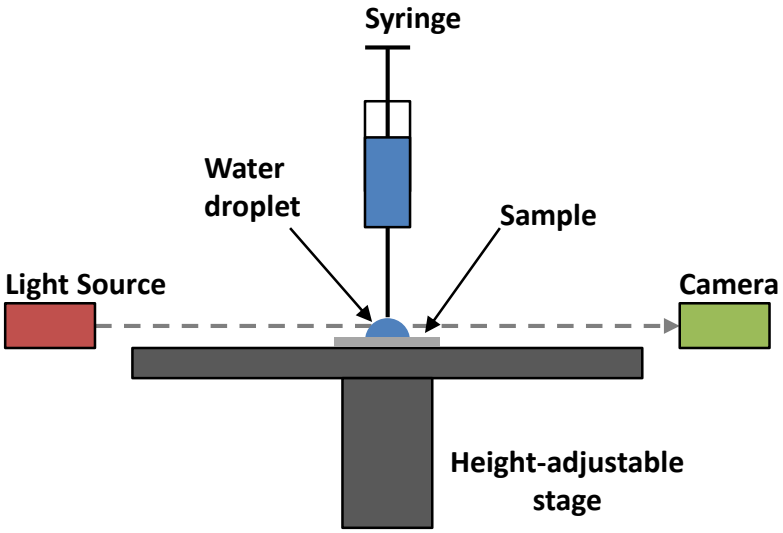

Figure 13 – Contact Angle Measurement Setup

The setup for contact angle measurements is comprised of a syringe with which to deposit a droplet onto the sample. The sample is placed between a light source and a camera, which ensures that the droplet contours are more easily distinguishable in the acquired images. The sample rests on a height-adjustable stage to ensure that the sample is level in the field of view of the camera.

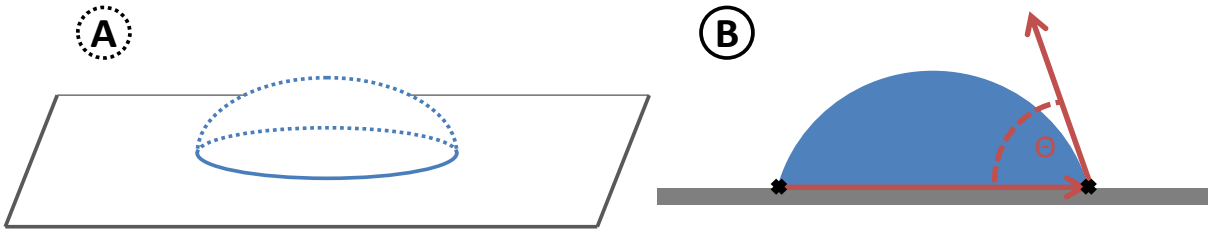

Figure 14 – Measuring Droplet Contact Angle in ImageJ

A small droplet of water is deposited on the sample (A). The height of the movable stage upon which the sample is placed is adjusted until in the field of view of the camera the droplet is seen in a quasi-2D view (B), in which the image is acquired. Using the 'angle tool' in ImageJ, a line is first drawn between the two contact points of the free droplet arc with the sample. The freely moveable line is then moved such that it draws a tangent with the droplet arc. The angle between the two lines defines the contact angle of the droplet with the sample.

4.1.3 X-Ray Photoelectron Spectroscopy

The technique of X-ray photoelectron spectroscopy (XPS), also known as Electron Spectroscopy for Chemical Analysis (ESCA), determines the elemental composition of surface layers of up to 10 nm deep. In the interrogation of the CSs such data determines the presence of the deposited molecules and their electronic states, but will also show the presence of (environmental) contaminants.

The XPS measurements carried out for this project were conducted at the Leeds EPSRC Nanoscience and Nanotechnology Research Equipment Facility (LENNF) on the 14th of October 2014, under LENNF application 118 (see Appendix 8.5 (p.223) for proposal acceptance)

All samples interrogated via XPS at LENNF were prepared at Birmingham University, transported to LENNF, and prepared for experiments at LENNF by myself. The experiments at LENNF and the subsequent processing of the data were conducted by Dr Kellye Curtis. Analysis and interpretation of the results was again conducted by myself.

4.1.3.1 Working Principle

In XPS measurements a focussed beam of X-rays, of approximately 500 μm in diameter, is used to irradiate the sample inside a high vacuum chamber. Highly energetic photons interacting with the sample cause electrons to be ejected from their orbitals into the vacuum. The energy of the electrons ejected into the vacuum is measured when they are detected and spectra of electron energies and their frequency of occurrence can be constructed. The electron energies are not only specific to the element from which they were ejected, but further specific to their chemical and electronic states. This means that XPS can not only give insight into

the elements present in the interrogated surface layers but also their bond structures and oxidation states.[73]

As the technique can only penetrate up to 10 nm of material, and the nominal thickness of the Au coating on the silicon wafers is 30 nm, everything other than Au that is detected in XPS interrogation can with confidence be assigned to the surface layers.

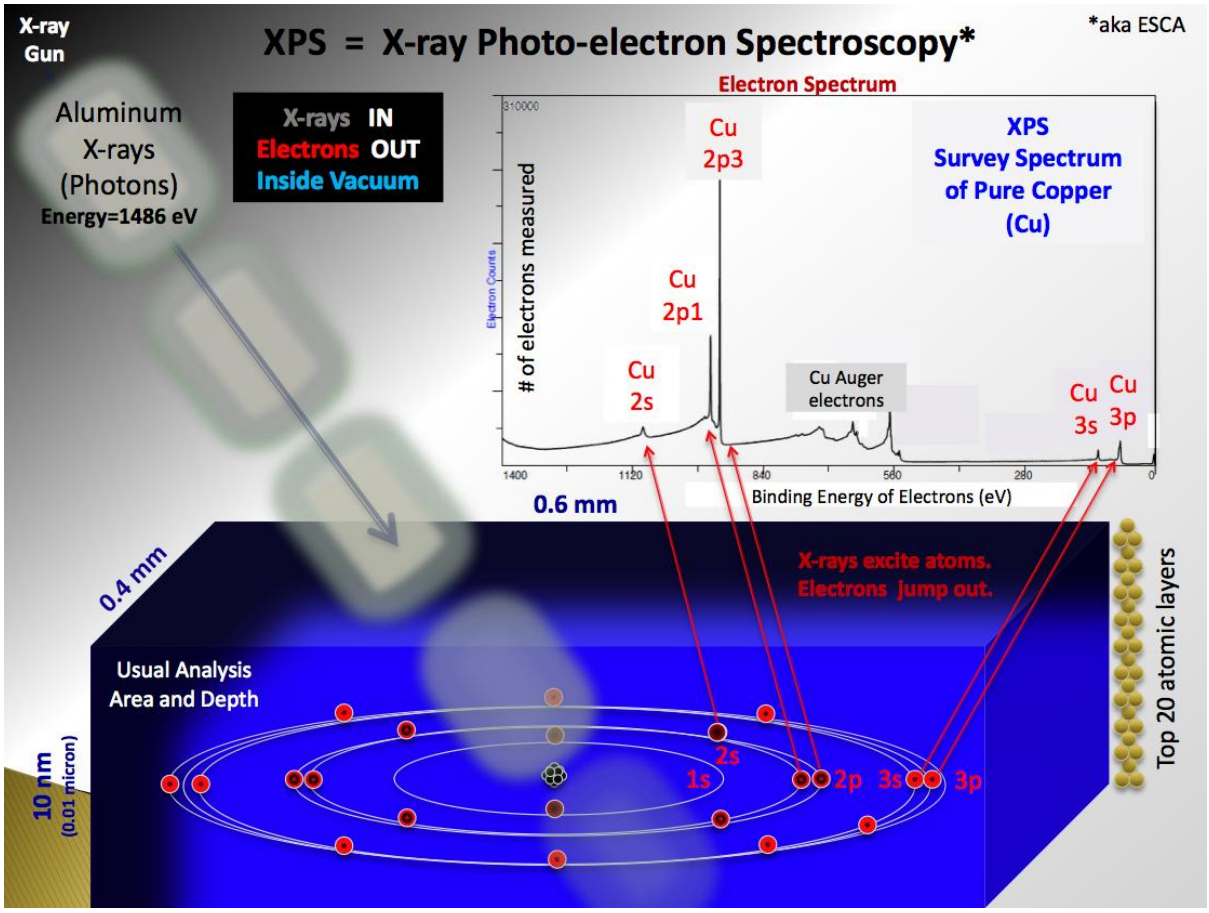

Figure 15 – X-Ray Photoelectron Spectroscopy

The diagram depicts the XPS measurement process, where the sample is irradiated inside a high vacuum chamber using a focussed X-ray beam. High energy photons cause electrons to be removed from their orbitals and be ejected into the vacuum. Measuring the energy of the ejected electrons allows building up energy spectra for the interrogated surface chemistry, where each peak distinctly corresponds to not only specific elements but also their chemical and electronic states.

Image source: https://commons.wikimedia.org/wiki/File:XPS_PHYSICS.png

4.2 Results

4.2.1 Consistency of Control Surface Preparation

Consistency in preparing the CSs is important with regards to both being able to reproducibly prepare good quality counter-surfaces to test NP functionalised cantilevers against, as well as demonstrating that successful cantilever modification itself can be achieved repeatedly with good consistency.

For this purpose, each of the five different CSs was independently prepared three times and interrogated using ellipsometry, sessile drop contact angle analysis, and X-ray photoelectron spectroscopy.

One NP functionalised cantilever was prepared alongside each CS-NP, and subsequent AFM measurements were conducted where the modified cantilevers were tested against one of each of the CSs.

4.2.1.1 Ellipsometry Results

The prepared CSs were first assessed via ellipsometry to determine the layer thicknesses of the deposited SAMs, where comparison against the predicted values shown in Table 1 (p.36) provides indication if the SAMs are in the correct conformation.

The results are shown in Figure 16, where each sample was measured in at least three non-overlapping positions; the values are attached in Appendix 8.7 (p.231). The data shows that CS-CH_3, CS-COOH, and CS-OH exhibit good consistency of SAM thicknesses close to the expected values as shown in Table 1 (p.36), with mean values of 1.85 ± 0.20 nm, 1.72 ± 0.17 nm, and 1.63 ± 0.21 nm, respectively. The determined values are above the predicted SAM thicknesses presented in

Table 1 (p.36), by 0.46 nm (33%), 0.35 nm (25%), and 0.26 nm (19%), respectively. While the percentage differences appear substantial, it must be considered that the absolute differences are in fact approaching the sensitivity limit of the instrument. Further, the determined values are in a range where even the very low surface roughness of the substrate of <1 nm becomes an influential factor. Considering, further, that the determined values are averages for areas of several mm², the consistency of the values indicate that good SAMs were achieved.

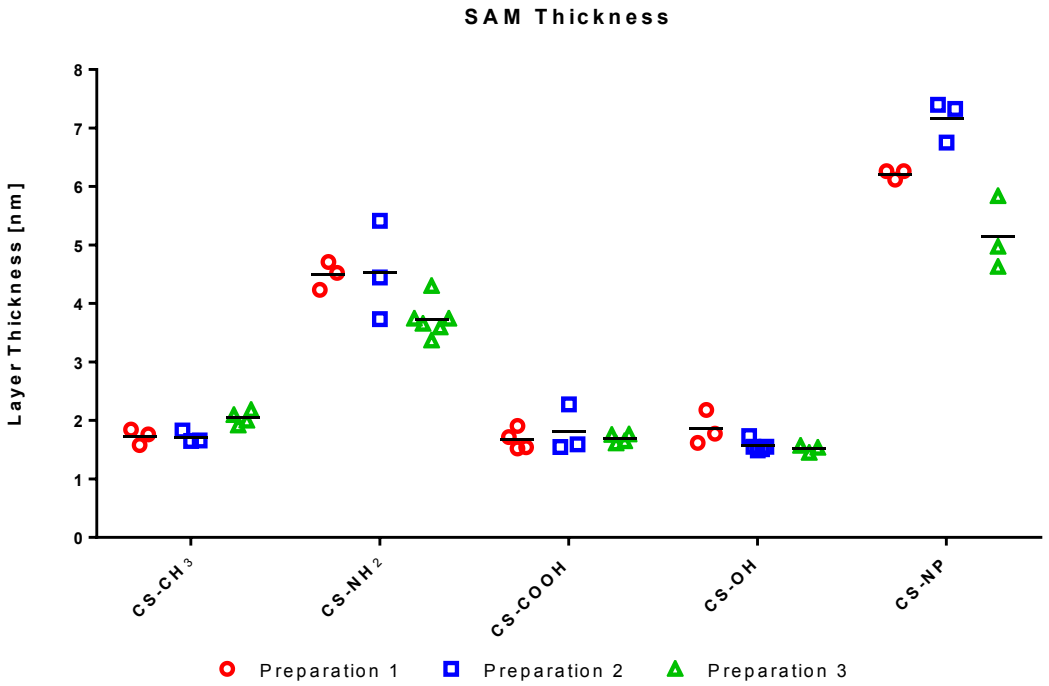

Figure 16 – Consistency of CS Preparation Assessed via Ellipsometry

The consistency of the CS preparation was assessed via ellipsometry, where each of the CSs was prepared three times, independently. Each CS was measured in at least three non-overlapping positions. Each measurement is represented by a marker on the graph, and black bars mark the mean for each group. CS-CH_3, CS-COOH, and CS-OH exhibit good consistency and are in the expected SAM thickness range, as compared to theoretical values. The SAM thickness of CS-NH_2 is above the expected value. A distinct further increase in layer thickness can be observed for CS-NP compared to CS-NH_2.

The obtained thickness values for CS-NH_2 are much more clearly above the expected values, with a mean value of 4.12 ± 0.59 nm. Compared to the predicted SAM layer thickness from Table 1 (p.36) of 1.38 nm, the obtained values are 2.74 nm (199%) above the expected values. For the SAM thickness to be multiple molecule lengths above the expected values is a strong indication that the SAM did not form correctly.

It follows that the thickness values obtained for CS-NP are also affected, as CS-NP builds on the same SAM that is deposited for CS-NH_2. The values obtained for CS-NP are above even those for CS-NH_2, and with a mean value of 6.17 ± 0.94 nm, is at least 4.30 nm (230%) above the predicted values shown in Table 1 (p.36). As previously for CS-NH_2, this calls into question the quality, and conformation of the surface modification. Assuming, however, that the underlying NH_2 SAM for CS-NP is comparable to that measured for CS-NH_2, a mean increase in layer thickness of 2.05 nm between CS-NH_2 and CS-NP would be observed, suggesting layer growth through NP addition.

4.2.1.2 Contact Angle Analysis Results

To test whether the correct water wetting properties were exhibited by the CSs, which indicates if the molecule tail group is correctly exposed at the sample surface, contact angle analysis was performed. The results are presented in Figure 17.

The contact angles determined for hydrophobic CS-CH_3 are 93 ± 2°, and for the hydrophilic CS-COOH and CS-OH, 26 ± 4° and 35 ± 7°, respectively. Contact angles determined for CS-NH_2 and CS-NP are very similar at 68 ± 4°, and 68 ± 3°, respectively. The images acquired for the contact angle assessment are shown in Appendix 8.8 (p.232).

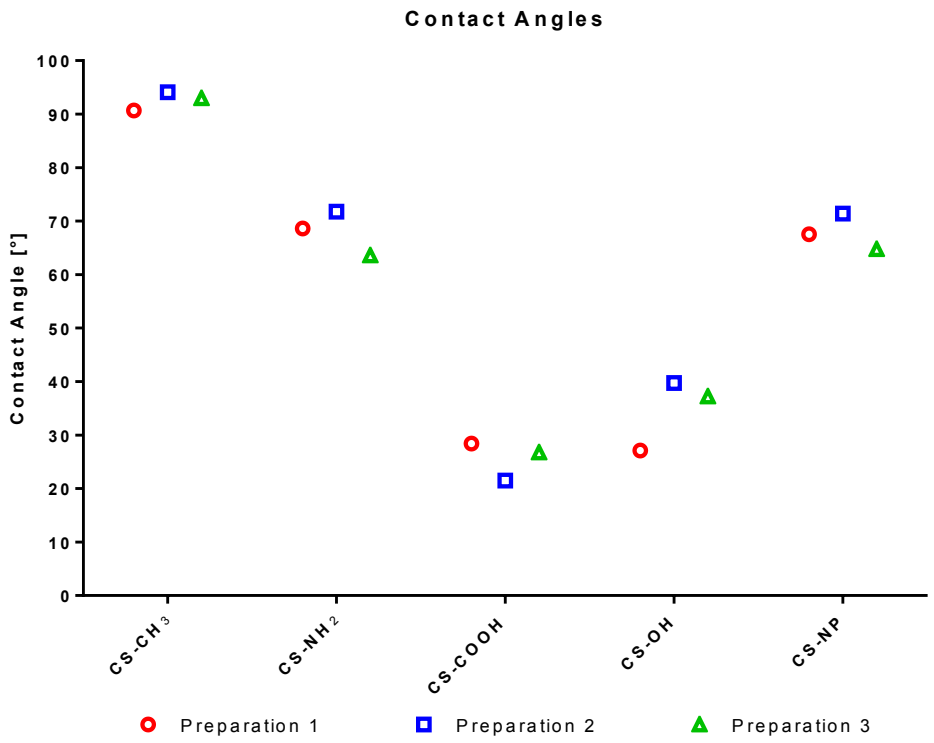

Figure 17 – CS Contact Angles

Contact angles were measured for three independently prepared samples of each of the five different CS preparations. Hydrophobic CS-CH_3 presents with contact angles of 93 ± 2°, and the hydrophilic CS-COOH, and CS-OH, present with contact angles of 26 ± 4° and 35 ± 7° respectively. Contact angles for CS-NH_2 and CS-NP are very similar at 68 ± 4°, and 68 ± 3°, respectively.

The results obtained for CS-CH_3 and CS-OH are in good agreement with the literature values presented in Table 1 (p.36), where small discrepancies are ascribed to the use of less sophisticated instrumentation. Thus wetting properties exhibited by CS-CH_3 and CS-OH are as expected, and thereby further consolidate the ellipsometry findings that these SAMs have formed correctly.

While the ellipsometry results for CS-COOH showed that the SAM layer thickness was within expected values, the contact angle results suggest that the surface chemistry of the SAM is not as expected, with contact angles above expected values.

Confidence in the correct assembly of the deposited SAMs is only established if both ellipsometry and contact angle interrogations produce the expected results.

The results obtained for CS-NH_2 differ from the expected values by a considerable margin, further consolidating the observation that the deposited SAM has not formed correctly. Ellipsometry results for CS-NH_2 showed the SAM thickness to be multiple molecule lengths above expected values, suggesting that multiple layers of the deposition molecule assembled on the surface. Here, the orientation of the deposited molecules will have an impact on the resulting contact angles, and both the amine tail group of the molecule, as well as the thiol (SH) head group of the molecule could be exposed at the SAM surface. A search of the literature determined possible contact angles for SH terminated SAMs to be 71 ± 3° (Θ_a)[74], which is much closer to the values produced by CS-NH_2. The contact angles produced by CS-NH_2 would suggest that a majority of the groups at the surface are SH, but in order to assess the orientation of the deposited molecules a much more detailed study with more sophisticated instrumentation would need to be conducted. A technique that could be employed for such a study would be angle-resolved XPS.

While there are no published or predicted contact angles for NP, the results obtained for CS-NP are not considered representative for only NP being exposed at the SAM surface. It is assumed that the attachment of NP is only achieved at exposed NH_2 groups, but as discussion of the CS-NH_2 results has highlighted, it is difficult to predict or confirm the correct orientation of the molecules of the underlying NH_2 SAM, and hence similarly difficult to predict the orientation of deposited NP groups, as well as the ratio of the SH, NH_2, and NP groups that could be exposed at the SAM surface. The produced contact angles are considered to be the result of a

combination of these groups being exposed at the SAM surface, but as for CS-NH_2, a more detailed study would need to be conducted to determine their ratios and distribution.

4.2.1.3 AFM Interrogation Results

Treated cantilevers, that were prepared alongside each of the independent CS-NP preparations, were used in the interrogation of one of each of the different CSs. However, the investigation of the consistency of the prepared surface modifications revealed that the NH_2 SAM cannot be considered to have formed correctly. Similarly, results for the subsequent NP addition, which builds on the NH_2 SAM, also indicated that correct conformation was not achieved (§4.2.1.1; p. 43 & §4.2.1.2; p. 45). Therefore, the interactions that were measured between treated cantilevers and CSs cannot be assumed to be characteristic of the intended surface modifications, and were subsequently omitted from the analysis. The results are included for completeness in Appendix 8.9 (p.235).

4.2.1.4 XPS Results

XPS analysis was employed to identify the elemental composition of the SAMs deposited on the CSs, and thereby determine if besides the deposited molecules any contaminants were present on the CSs.

The number of samples that was interrogated via XPS had to be limited due to the limited amount of time available at the LENNF. Hence, only one of each of the different CSs could be interrogated. The results are shown (pp. 56-60) and discussed on the following pages, where each figure shows a survey spectrum with subsequent, additional high resolution spectra for the elements of interest detected in the survey

scan. Reference values of binding energies that are stated below have been taken from the table[75] attached in Appendix 8.10 (p.238).

The XPS results for CS-CH_3 are shown in Figure 18 (p.56), where high resolution scans were taken for Au, S, C, and O. As mentioned previously in §4.1.3 (p.41), the presence of Au is expected to be dominant in these spectra. Electron binding energies for Au in the range of the survey spectrum between 0-1200 eV are stated as 57.2; 74.2; 107.2; 84.0; 87.6; **335.1**; **353.2**; **546.3**; **642.7**; and **762.1** eV; of which those shown in bold can be clearly attributed to peaks seen in the survey spectrum. The high resolution scan of Au is included with the interrogation of every sample to serve the purpose of quality control. Demonstrating that the distinct 84.0 eV and 87.6 eV peaks are at the correct values, as well as their characteristic distance apart, provides confidence that the instrument is set up correctly and that no undesired charging of the sample is occurring.

With regards to the analysis of the SAM deposited for CS-CH_3, the peaks observed for S are in the expected positions at 162.5 eV and 163.6 eV; which is evidence for successful SAM deposition. The peak for C is intense and narrow, and is only slightly shifted from its position, as stated in the literature, at 284.2 eV[76,77], with a small shoulder towards higher binding energy. This slight separation of the C peak can be attributed to the structure of the deposited molecule. The majority of the C in the molecule is linked to other C and gives rise to the intense peak. However, one C is linked to the S that attaches the molecule to the Au substrate, which gives rise to the small shoulder that can be observed on the main C peak. The electrons shared between S and C are drawn towards the S due to its electronegativity, making it more

difficult for electrons to be ejected from the C in this pairing, resulting in the small shoulder being at a higher binding energy.

The presence of O with CS-CH_3, however, is unexpected, as the deposited molecule does not contain any. It is unlikely that the presence of O is due to oxidation of the SAM, as the spectra for both S and C show no indication of such. The more likely source is defects in the substrate itself that can easily be caused through ordinary handling of the samples. Small defects expose the underlying Si layer that will readily oxidise, but it cannot be said with certainty without further testing, such as for example collecting a detailed spectrum for Si.

The results shown in Figure 19 (p.57) are of the interrogation of CS-NH_2, which forms the basis for subsequent functionalisation of AFM cantilevers with NP. While the high resolution scan for Au shows that the instrument is set up correctly, a distinct reduction in signal intensity can be observed in the survey spectrum, suggesting that fewer electrons are escaping from the Au layer. This implies that the thickness of the adsorbed SAM layer is increased compared to what was observed for CS-CH_3. A thicker SAM layer atop the Au layer increases the path length for electrons ejected from Au orbitals, decreasing the probability of said electrons to reach the vacuum in which they can be detected.

The S spectrum confirms that S is present and hence that SAM deposition has occurred, but the two discernible peaks that were seen for CS-CH_3 cannot be observed here. This suggests that not all the S that is present on the sample is in the correct conformation, and hence it cannot directly be inferred that the SAM has formed correctly. The quality of the SAM is further called into question by the

significant presence of O. The combination of the altered S spectrum and the presence of O with this SAM implies that some of the present S has oxidised, which, considering the increased SAM layer thickness, is plausible, as more of the deposition molecule is present than can be directly bound to the Au substrate. The O peak is shifted to lower binding energy as that quoted for elemental O at 543.1 eV, but it agrees with the value quoted in the literature for a (C-O) bond at 531.5 eV - 532.0 eV.[76] This value however also overlaps with that of SiO_2, which typically makes a deconvolution of the O peak into its constituents not possible. Similarly as for the O peak, the N peak is shifted towards lower binding energy than would be expected for elemental N, but is close to what would be expected for a (C-NH_2) bond at ~400eV.[76] The high resolution C spectrum shows a distinct narrow peak associated with the C in the C chain of the molecule, as has also previously been seen for CS-CH_3. In addition, however, two small shoulders towards higher binding energy can now be observed. As before, one C of the molecule is attached to an electronegative S, increasing the energy required to eject electrons from that C, but in addition now one C is attached to a N which has an even higher electronegativity; giving rise to the leftmost shoulder. Both the main C peak and the first shoulder have an increased intensity as compared to what was observed for CS-CH_3. This is however in keeping with an increased SAM layer thickness, composed of an increased amount of deposited molecule.

The results of the interrogation of CS-COOH are shown in Figure 20 (p.58). High signal intensity that is dominated by the characteristics of Au can again be observed in the survey spectrum, suggesting that the SAM layer thickness is low. The high

resolution Au spectrum confirms that the instrument is set up correctly, and the two peaks in the S spectrum confirm that SAM deposition has occurred correctly.

The C spectrum shows an intense peak associated with the C in the C chain of the molecule, with two small shoulders shifted to higher binding energies that can be associated with the (C-S) bonds and (C-O, C=O) bonds in the molecule respectively.

The spectrum for O shows an intense peak at the expected level, where characteristic values for (C-O) and (C=O) bonds are at 532.0 eV and 533 eV. While it is expected for both bond types to be present in this sample, their distance apart is too small to be deconvoluted sufficiently in the spectrum.

Interrogation of CS-COOH also revealed an unexpected presence of N with the sample. This may be due to cross-contamination occurring in the sample preparation, where CSs were prepared in sequence, as they are shown in Figure 11, 1 through 5. In spite of thorough rinses of the used forceps with both H_2O and EtOH in between each step, some amount of molecule used in the preparation of CS-NH_2 may have been retained on the forceps, and was carried across into the preparation of subsequent CSs such as CS-COOH.

The results of the interrogation of CS-OH are shown in Figure 21 (p.59), and, as for CS-COOH, high signal intensity of the survey spectrum suggests that the layer thickness of the formed SAM is low, and the high resolution spectra for Au and S suggest that the instrument is set up correctly and that the SAM has formed correctly. As before for CS-COOH, an unexpected presence of N is detected with this sample, but the intensity is reduced compared to what was observed for CS-COOH. This is in keeping with the hypothesis of cross-contamination in the sample preparation to

explain the presence of N with CS-COOH and CS-OH, as the intensity of N decreases the further along the sample is in the sample preparation sequence.

The spectrum for O confirms that O is present and at the expected level. The intensity of the peak is reduced as compared to CS-COOH, suggesting that a smaller amount is present, which is as expected from the structures of the deposition molecules.

The spectrum for C also presents as would be expected, with an intense peak that is associated with the majority of C present in the molecule C chain, and two small shoulders associated with the (C-S) and the (C-O) bonds respectively.

Figure 22 (p.60) shows the results for CS-NP, which is the preparation in which both steps of the proposed cantilever modification scheme have been applied. The first step is the same treatment as was investigated with CS-NH_2, and indeed the spectra for CS-NP show very similar characteristics. The survey spectrum shows a reduced signal intensity, suggesting that the SAM layer thickness is increased, and the S spectrum does not reveal two discernible peaks, which implies that the SAM has not formed correctly.

The spectrum for C again shows an intense peak with two smaller shoulders, where, as before, they could be attributed to the majority of the present C being in the C chain of the molecule deposited in the first step, and the smaller shoulders to the (C-S) and (C-N) bonds occurring in that molecule respectively. With the addition of NP in the second step of this preparation, additional C, in slightly different conformation, is added, but its presence cannot be confirmed from this spectrum.

The presence of O with this sample is expected, and while the level of the O peak agrees with (C-O) bonds that would characteristically occur at 533 eV, a deconvolution of the O spectrum to confirm the presence of (N-O, N=O) bonds, that would have been added with the addition of NP, is not possible.

The N spectrum confirms the expected presence of N, and is at an expected level, however, it does not allow for the differentiation of the N that is deposited with the first step of the preparation from the N that is deposited in the second step.

The interrogation of each of the different CSs via XPS has primarily confirmed the findings that had already been established via ellipsometry and contact angle analysis.

For CS-CH_3 and CS-OH the presence of the expected elemental species was confirmed, and their associated binding energies suggest that the deposited SAMs are in the correct conformation. Similarly, for CS-COOH, the XPS results suggest that the deposited SAM is in the right conformation; however, the correct contact angles were not achieved. Hence, in spite of ellipsometry and XPS results that suggest that good quality SAMs are achieved for CS-COOH, the presence of the correct surface chemistry is not proven.

The XPS results for CS-NH_2 and CS-NP are also in keeping with the ellipsometry and contact angle analysis findings, showing increased SAM layer thicknesses, and electron binding energies for the present elemental species that show the SAMs to not be in the right conformation.

The correct orientation of the deposited molecules, and by extension the presence of the correct surface chemistry, cannot be determined with the type of XPS that was

employed. An alternative type of XPS would be angle-resolved XPS, as was employed by Lee, *et al.*,[78], with which it is possible to collect spectra at different depths of SAMs. The use of such a technique would allow determining the presence of deposition molecule head and tail groups at the SAM surface or near the substrate.

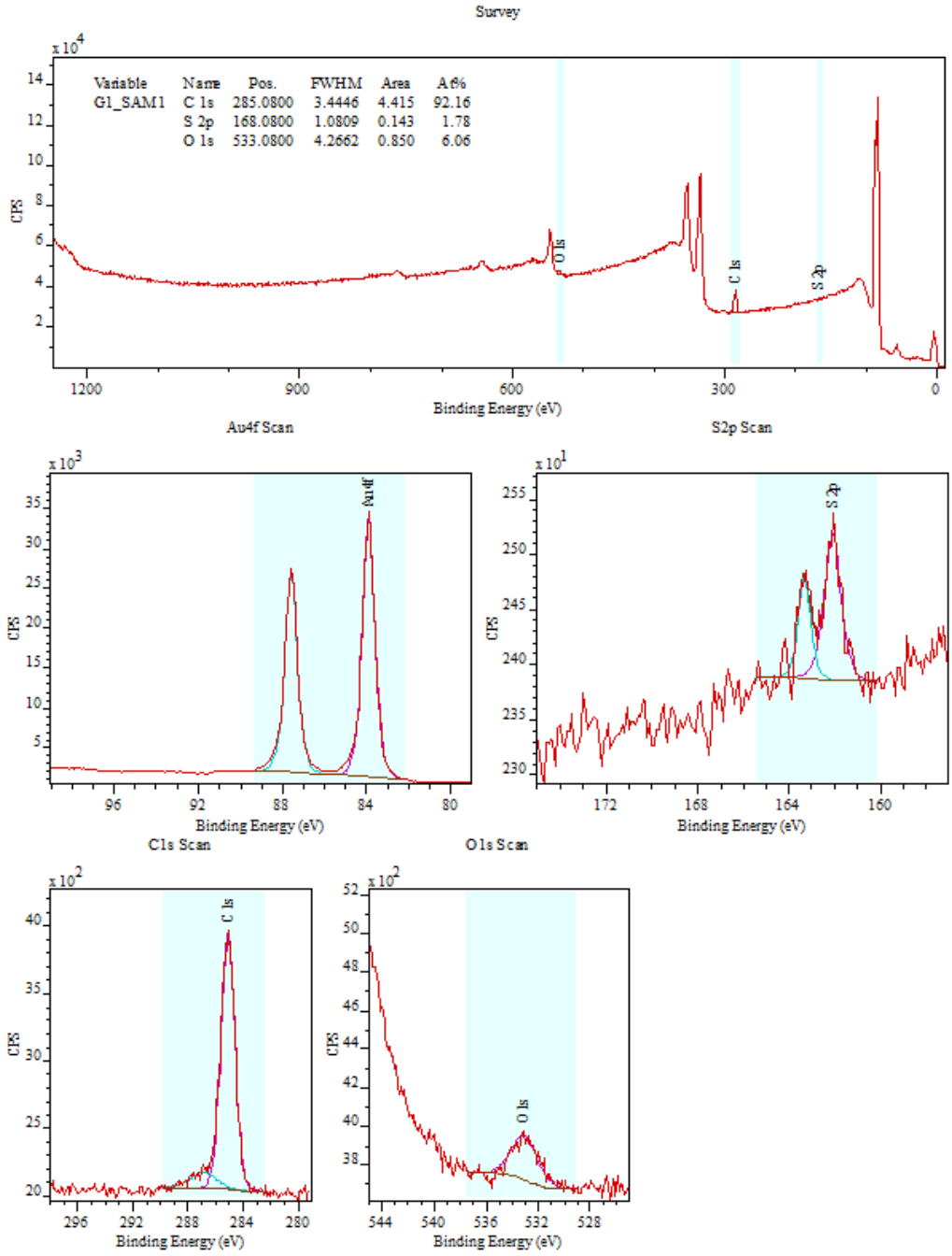

Figure 18 – XPS Spectra for CS-CH₃

XPS spectra for CS-CH_3, showing from top to bottom and left to right: one survey spectrum, and additionally high resolution spectra for Au, S, C, and O. The spectrum for Au shows the expected distinct peaks that are the characteristic distance apart. The two discernible peaks in the S spectrum suggest that the SAM formed correctly. The spectrum for C shows an intense narrow peak associated with the C in the C chain of the molecule, with a small shoulder attributed to the C linked to the S. The presence of O with this CS is unexpected, as the structure of the deposited molecule does not contain any.

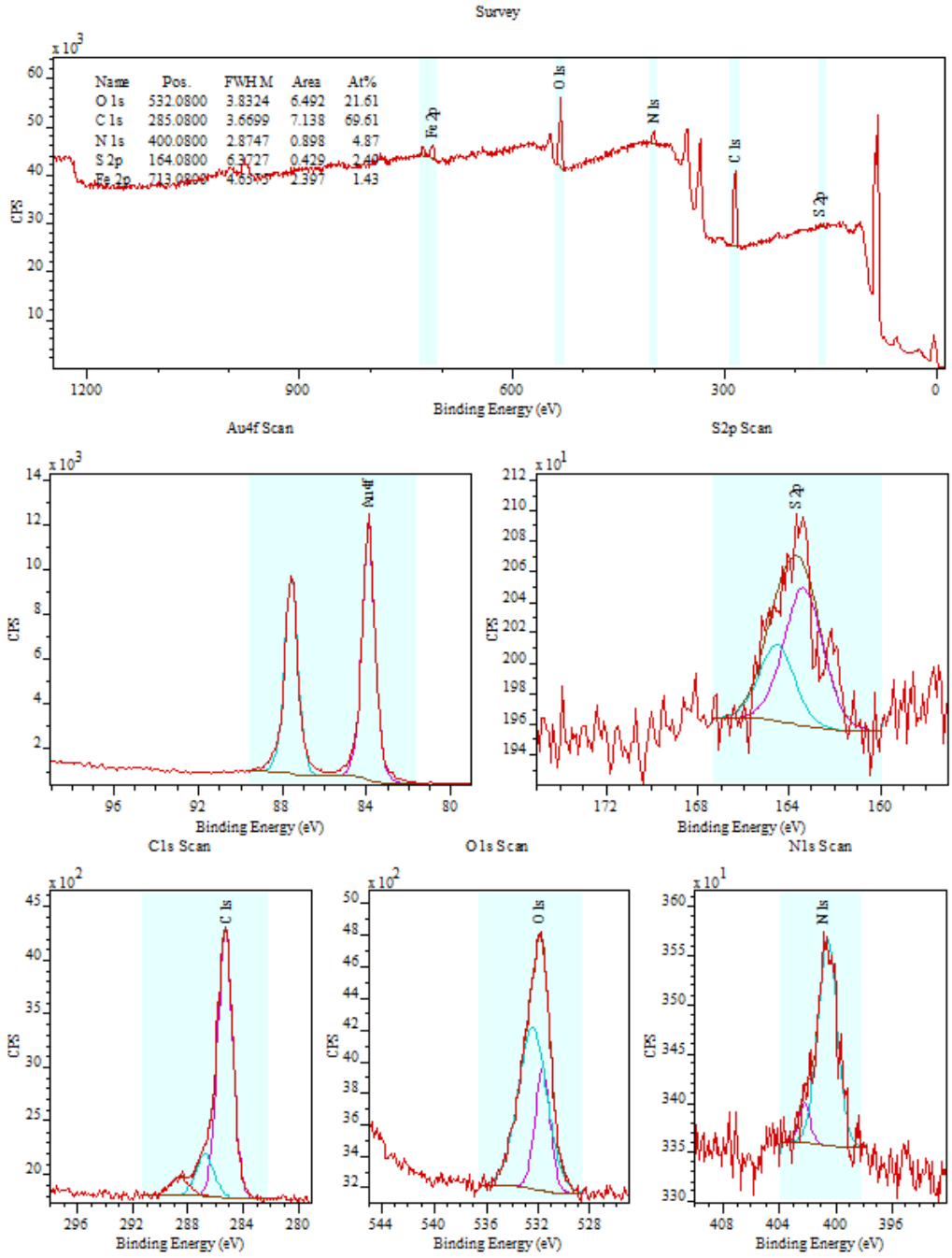

Figure 19 – XPS Spectra for CS-NH₂

XPS spectra for CS-NH_2 showing from top to bottom and left to right: one survey spectrum, and additionally high resolution spectra for Au, S, C, O, and N. A reduction in the signal intensity in the survey spectrum is evidence that a thicker layer has been deposited, allowing fewer electrons from Au orbitals to escape into the vacuum. The S spectrum confirms the presence of S and hence SAM deposition, but absence of two discernible peaks suggests that the SAM did not form correctly. The C spectrum shows an intense peak associated with the C in the C chain of the molecule, and small shoulders towards higher binding energies for (C-S) and (C-N) bonds respectively. The N spectrum is as expected for a (C-NH_2) bond. The presence of O is unexpected.

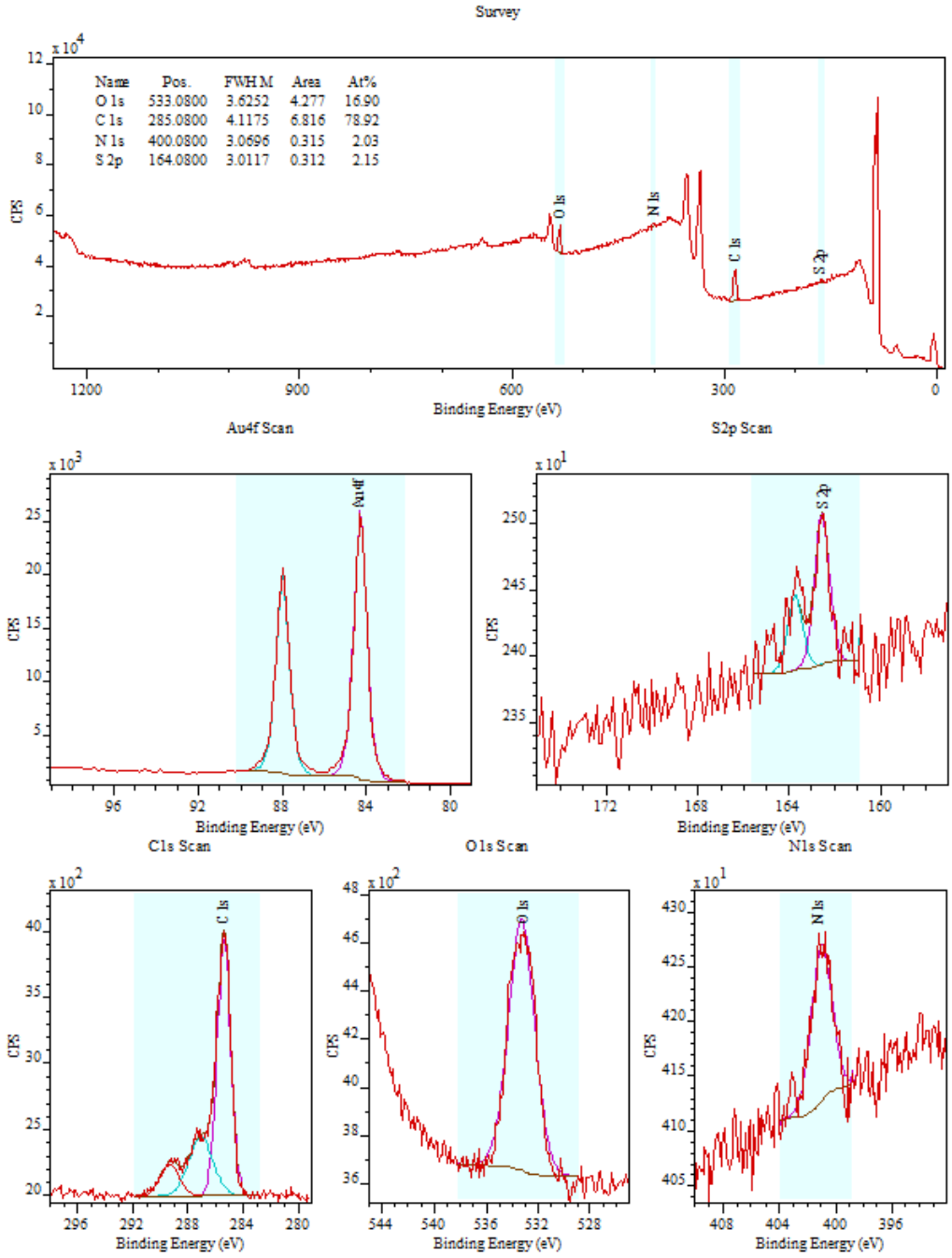

Figure 20 – XPS Spectra for CS-COOH

XPS spectra for CS-COOH showing from top to bottom and left to right: one survey spectrum, and additionally high resolution spectra for Au, S, C, O, and N. Strong signal in the survey spectrum suggests that a thin film has formed on the Au substrate, and the two discernible peaks in the S spectrum confirm the presence of the deposition molecule and that the SAM has formed correctly. The C spectrum presents characteristically for the deposited molecule, with an intense peak for the C in the C chain of the molecule, and two small shoulders towards higher binding energies for (C-S) and (C-O) bonds respectively. The O spectrum is as expected for (C-O) and (C=O) bonds. The presence of N is unexpected.

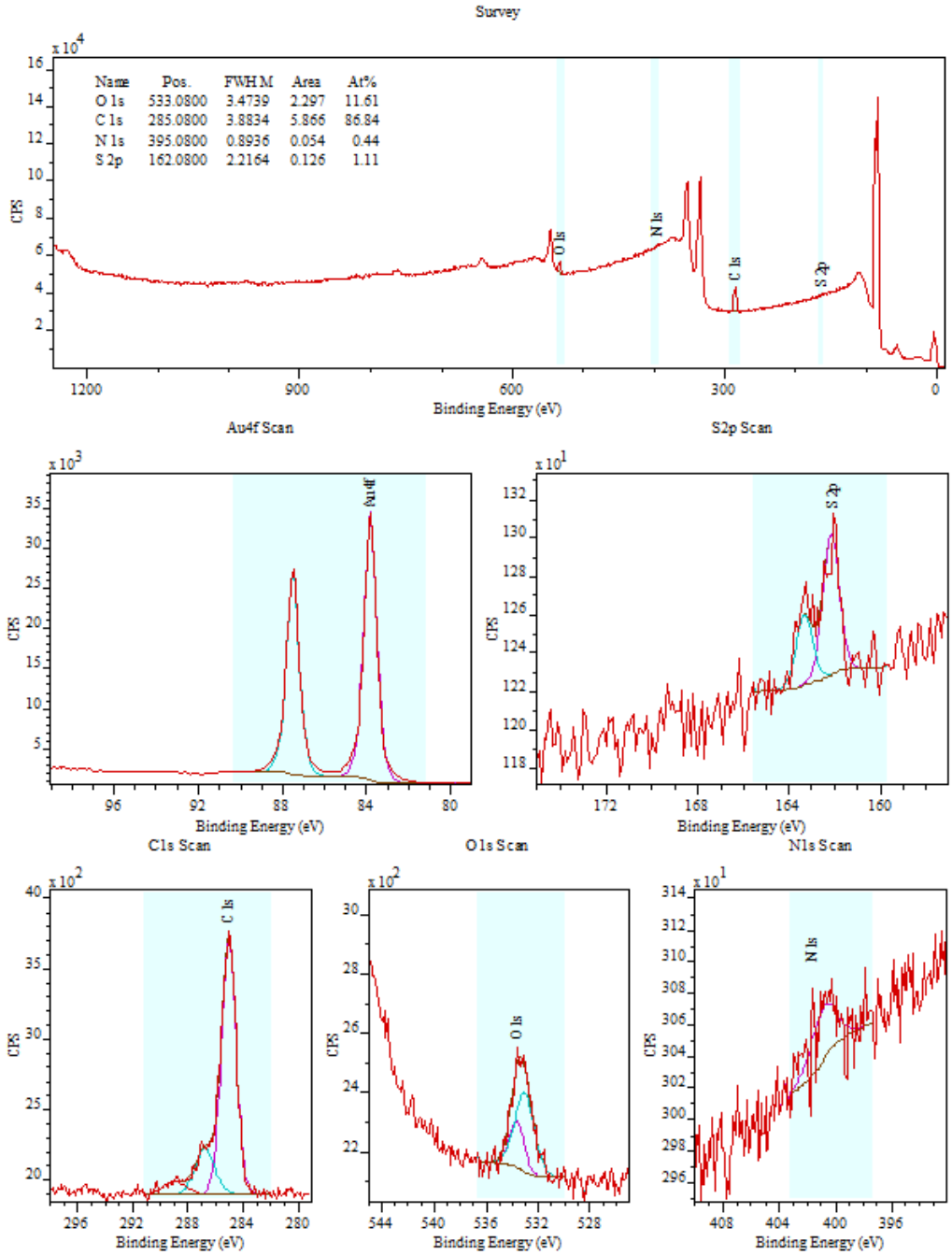

Figure 21 – XPS Spectra for CS-OH

XPS spectra for CS-OH showing from top to bottom and left to right: one survey spectrum, and additionally high resolution spectra for Au, S, C, O, and N. Strong signal in the survey spectrum suggests that a thin film has formed on the Au substrate, and two discernible peaks in the S spectrum confirm the presence of the deposition molecule, and that the SAM has formed correctly. The C spectrum presents with one intense peak, which is attributed to the C in the molecule's C chain, and two small shoulders towards higher binding energies for (C-S) and (C-O) bonds respectively. The spectrum for O is at the expected level, and a decreased intensity suggests that less O is present as compared to CS-COOH. The unexpected presence of N was also detected.

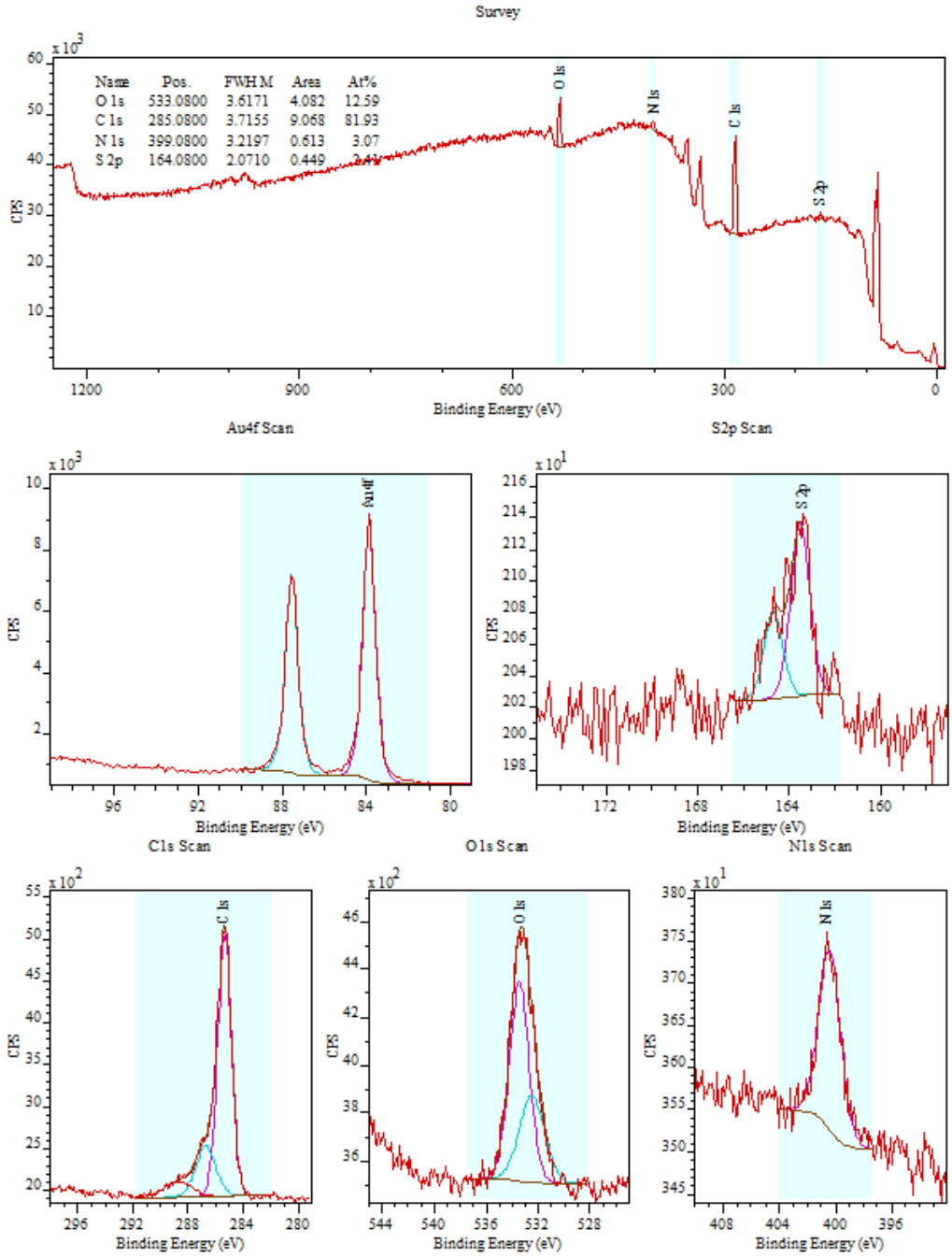

Figure 22 – XPS Spectra for CS-NP

XPS spectra for CS-NP showing from top to bottom and left to right: one survey spectrum, and additionally high resolution spectra for Au, S, C, O, and N. Reduced signal intensity in the survey spectrum suggests the presence of a SAM with increased layer thickness. The S spectrum confirms the presence of the deposition molecule, but the absence of two discernible peaks suggests that the SAM did not form correctly. The C spectrum presents an intense peak, attributed to the C in the molecule C chain, with two small shoulders at higher binding energies, attributed to (C-S) and (C-N) bonds respectively. The spectra for O and N confirm the presence of the species that would be expected from the deposition of a NH_2 SAM and the subsequent addition of NP.

4.2.2 Assessment of the Influence of Ellipsometry Modelling Parameters

The investigation of the consistency of the CS preparation has revealed that through ellipsometry alone a quick and easily accessible preliminary assessment can be made on whether the SAMs have formed correctly, by determining if the SAM layer thickness indeed corresponds to a monolayer.

Employing ellipsometry as the main experimental method for quality control for successful CS preparation warranted a brief investigation of the influence of the different parameters involved in the measurement process and subsequent mathematical modelling.

4.2.2.1 Effect of Modelling or Pre-Setting the Au Substrate Thickness

The mathematical models used to determine SAM layer thickness from ellipsometry data allow for the defining of different parameters. Both the SAM layer thickness as well as the Au substrate layer thickness can be determined through fitting of these mathematical models; as explained in more detail in Appendix 8.5. However, the Au substrate layer thickness can be pre-set to a reasonable value – such as the nominal value stated by the manufacturer – to reduce the number of modelled variables and thereby reduce the required computational time. Using the data shown previously in §4.2.1.1 (p.43), the influence of modelling or pre-setting the Au-substrate layer thickness on the obtained results was investigated. The results are shown in Figure 23.

Results shown in Figure 23 demonstrate that the obtained SAM thicknesses vary only minimally between when pre-setting the Au layer thickness, compared to when the Au layer thickness is modelled alongside the SAM layer thickness. The average difference across all 3 groups is 2.02 %, however, examining the absolute values

(shown in Appendix 8.11; p.244) reveals that this equates to differences on the order of 0.01 nm.

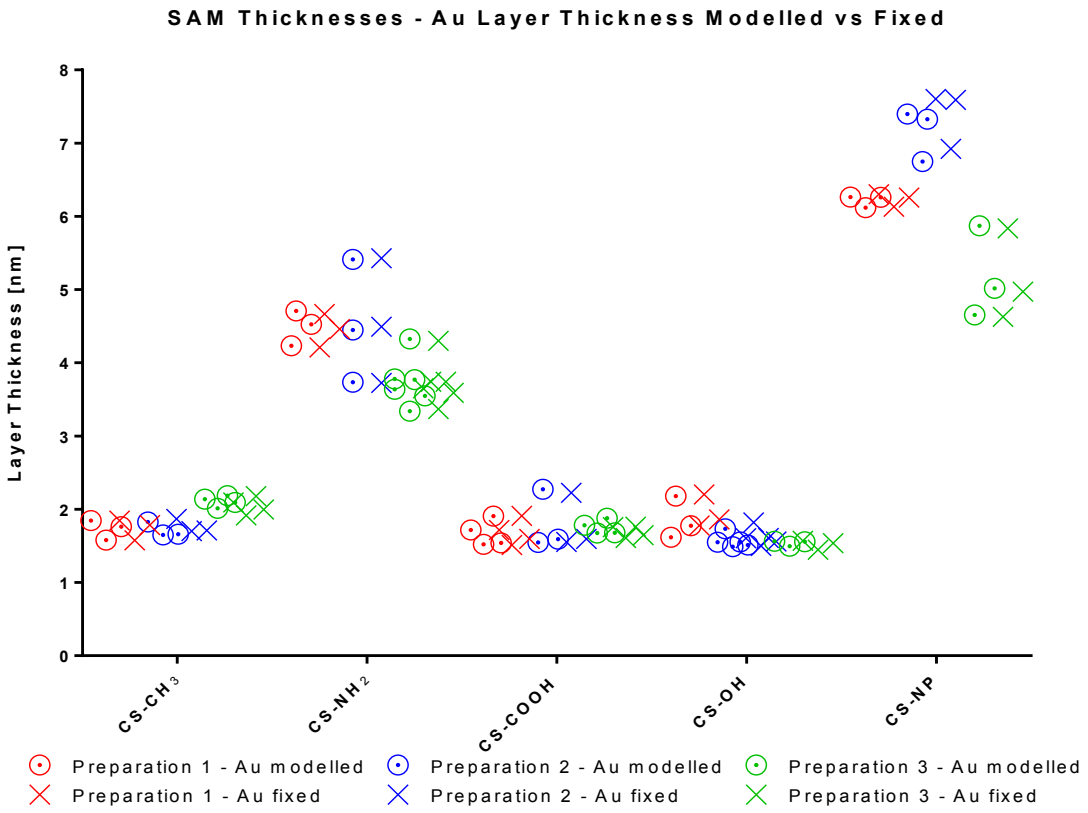

Figure 23 – Effect of Modelling or Pre-Setting Au Substrate Thickness

Shown are the SAM thicknesses as obtained when the Au substrate thickness was fixed (crosses), compared to when the Au substrate thickness was freely modelled (circles). For this comparison the data was used that was collected for assessing the consistency of the CS preparations.

Based on this assessment, subsequent modelling of SAM layer thicknesses was conducted with the Au layer thickness pre-set at the nominal 30 nm thickness provided by the manufacturer. To further consolidate this as a reasonable assumption, the Au layer thickness itself was assessed alongside the above experiments, with results shown in Figure 24 (values attached in Appendix 8.12; p.246). The Au substrate layer thickness was found to be adhering closely to the 30 nm quoted by the manufacturer. There appears to be a systematic underestimation of

the Au layer thickness for CS-OH, but this behaviour was not investigated further, because, albeit interesting, it has no tangible influence on the subsequent experiments.

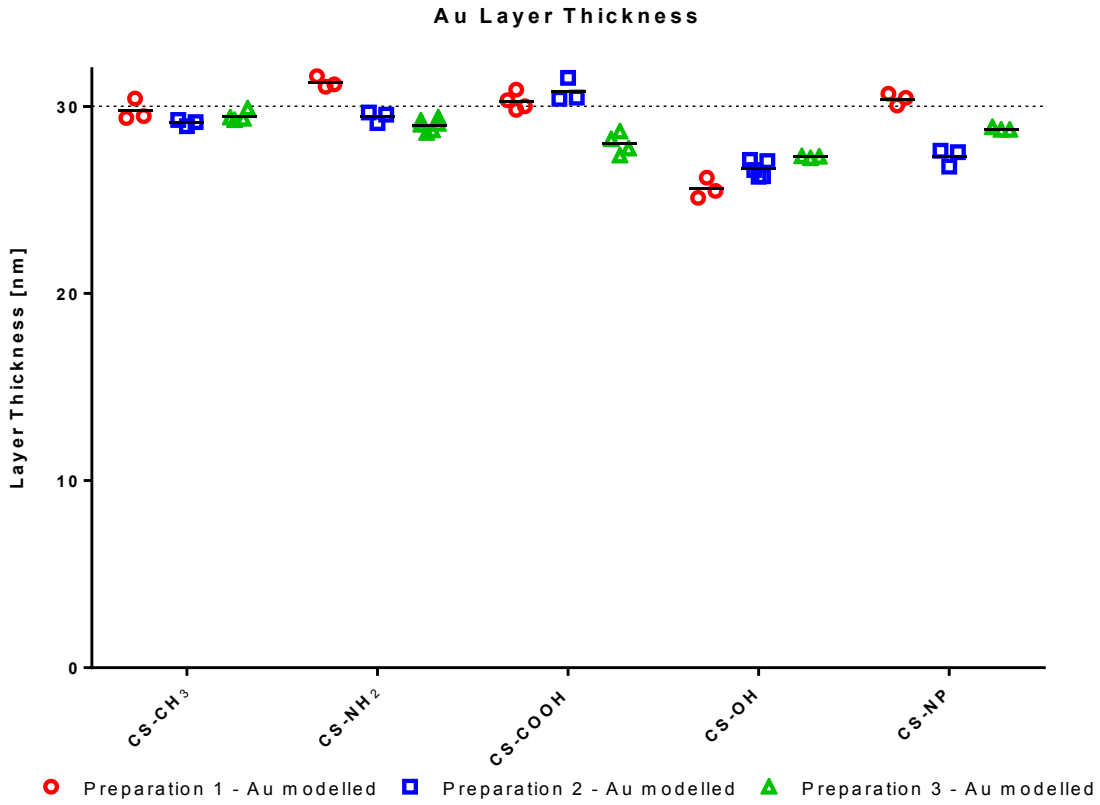

Figure 24 – Modelled Au Layer Thickness

Thickness of the Au layer as determined through fitting of mathematical models to ellipsometry data. The determined thicknesses of the Au layer are adhering closely to the 30 nm nominal Au layer thickness quoted by the manufacturer. A systematic underestimation of the Au layer thickness can be observed for CS-OH. Individual measurements are represented by a marker each, and black bars mark the mean for each group.

4.2.2.2 Effect of Spectroscopic Step Size

The ellipsometer can be set up to take a measurement every 2 nm, or every 5 nm, as it steps through the whole wavelength range. The influence of this parameter was investigated in a separate experiment where two CS-CH_3 samples were interrogated. CS-CH_3 samples were chosen for this investigation as previous results have shown

that the deposited SAM consistently forms with good quality. The results of the experiment are shown Figure 25.

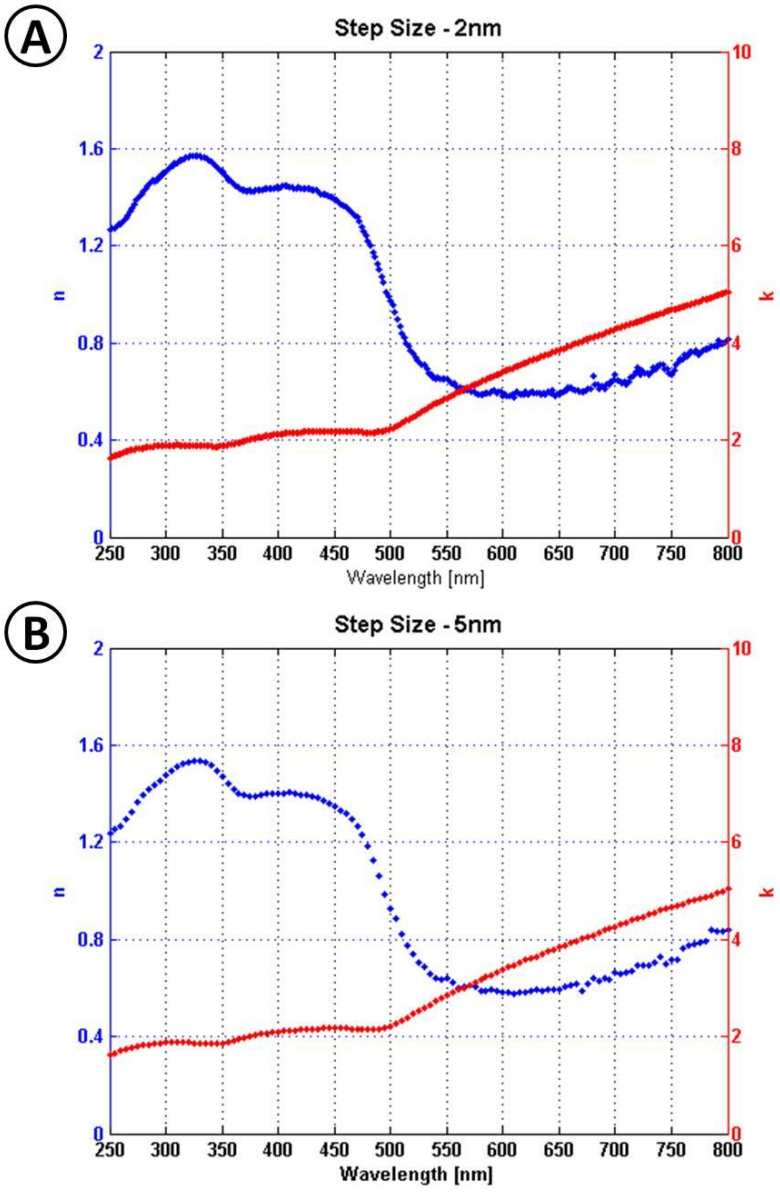

Figure 25 – Effect of Spectroscopic Step Size

Two CS-CH_3 samples were interrogated via ellipsometry using 2 nm (A), and 5 nm (B) step sizes. The reduced point density obtained using the larger 5 nm step size continues to describe the curve shape sufficiently.

Use of the smaller 2 nm step size produces a high point density (A), whereas use of the larger 5 nm step size produces data of a sparser point density (B). Despite the

reduced point density, however, the shape of both curves in (B) continues to be described with good detail.

As detailed in the description of the ellipsometry technique in Appendix 8.5, the stage critical to determining unknown sample parameters like the film thickness, is the fitting of appropriate models to the experimental data. These models are fitted to parameters I_s and I_c, and the goodness of fit (GOF) of the models to the experimental data is quantified in χ^2. Shown in Figure 26 are examples of well and poorly achieved fits to data acquired using the larger 5 nm step size.

The panels in Figure 26 show examples for the good (A) and bad (B) fitting of mathematical models (solid lines) to experimental ellipsometry data, where both data sets were obtained using the larger 5 nm step size. The quality of the obtained fit is expressed by χ^2, which assesses the distance of the points in the data set to the line of the obtained fit. Large values for χ^2 allow for the identification of measurements where models could not be fitted to experimental data sufficiently well, based on which they are subsequently omitted from analysis.

The time required for individual scans is 7 mins, and 3 mins, for scans using 2 nm, and 5 nm, step sizes, respectively. This is a considerable difference when taking into account the amount of samples that are being interrogated.

Based on the substantial time saving, the continued detailed description of the curves, and that measurements for which mathematical fits cannot be achieved sufficiently well can readily be identified using χ^2, subsequent interrogations were conducted using the 5 nm step size.

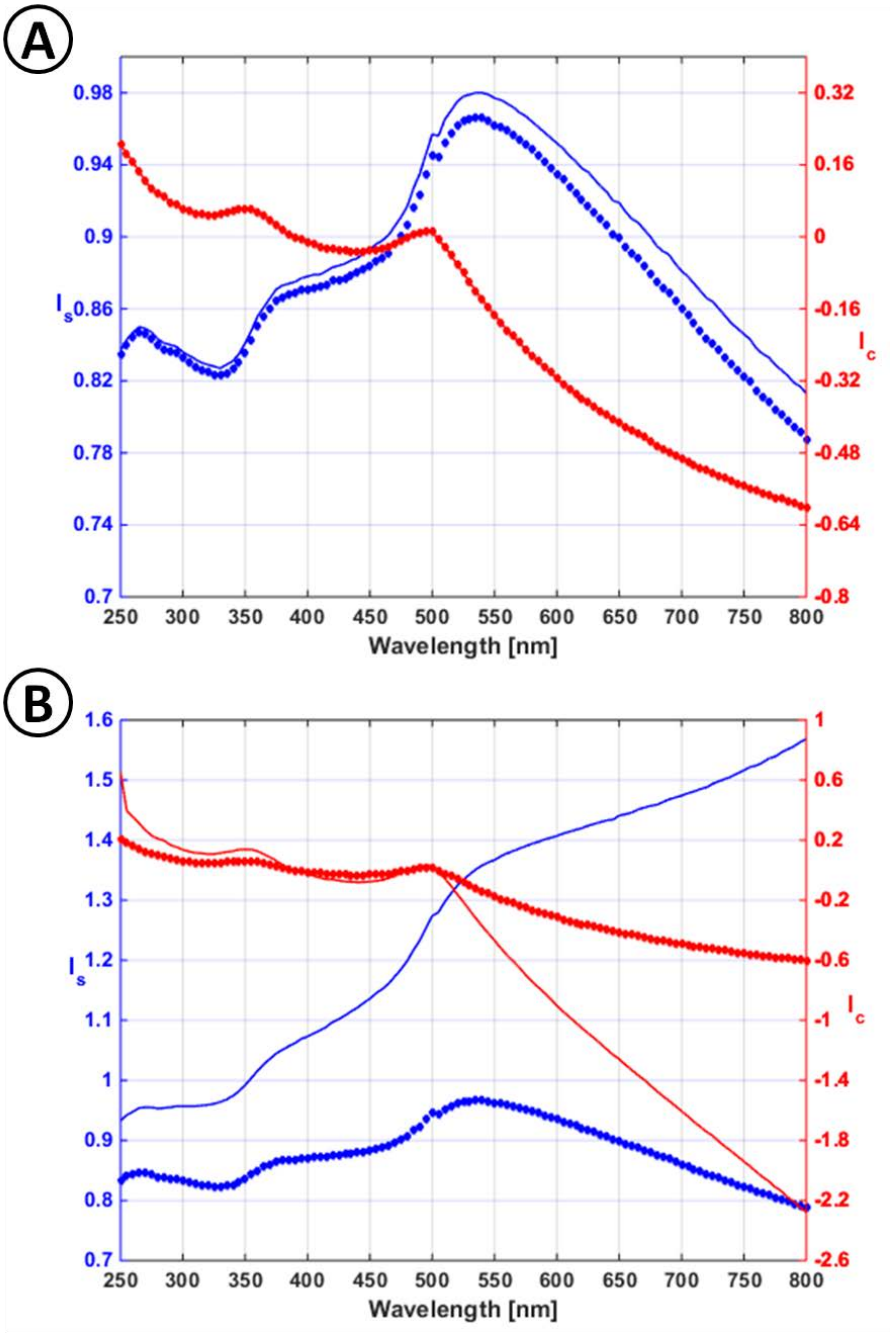

Figure 26 – Examples of Well and Poorly Achieved Fits to Experimental Ellipsometry Data

Examples of well, and poorly, achieved mathematical fits are shown in (A) and (B) respectively. The lines of fit are shown as solid lines, compared to the experimental data shown as markers. The quality of the fit is expressed in parameter χ^2 (A: $\chi^2 = 0.044$; B: $\chi^2 = 147.5$), which allows for the identification of measurements for which models could not be fitted sufficiently well without the need for visual inspection.

4.2.3 Effect of Sonication

In an effort to improve the SAM formation for CS-NH_2, and by extension for CS-NP, the literature was consulted to help identify improvements in the preparation protocols. In a study by Lee, *et al.*, [78], investigating the preparation of NH_2 terminated SAMs, a sonication step was included in the SAM preparation protocol. The sonication step was included as a rigorous washing step, to remove excess deposition solution and any non-specifically bound molecule. Prepared samples were sonicated for 3 minutes immediately after they were removed from the deposition solution.

This sonication step was added to the preparation protocols for CS-NH_2 and CS-NP, where samples were sonicated immediately after removal from NH_2 SAM deposition solution. The results are shown in Figure 27, which shows SAM thickness values as obtained via ellipsometry. For ease of comparison, previously obtained SAM thickness values for CS-NH_2 and CS-NP are shown alongside the results for the new, differently prepared samples.

As shown in Figure 27, only approximately half of the measurements, for samples subjected to sonication after removal from NH_2 SAM deposition solution, return reduced SAM layer thickness values. While XPS results for CS-NH_2 that was subjected to sonication (attached and discussed in Appendix 8.13; p.247) suggest that the formed SAM is in the correct conformation, as compared to the earlier discussed preparation without sonication (Figure 19), there is no consistent improvement of SAM layer thicknesses discernible from the ellipsometry results; with large variations even across individual samples. The addition of the sonication step therefore does not efficiently aid in the preparation of these CSs.

Furthermore, attempts to incorporate the sonication step into the cantilever modification scheme, where ultimately it would need to have been applied, resulted in a large proportion of cantilevers being sheared off from the chip. This, overall, makes the sonication step both inefficient and wasteful, and it was not considered further for the preparation protocols.

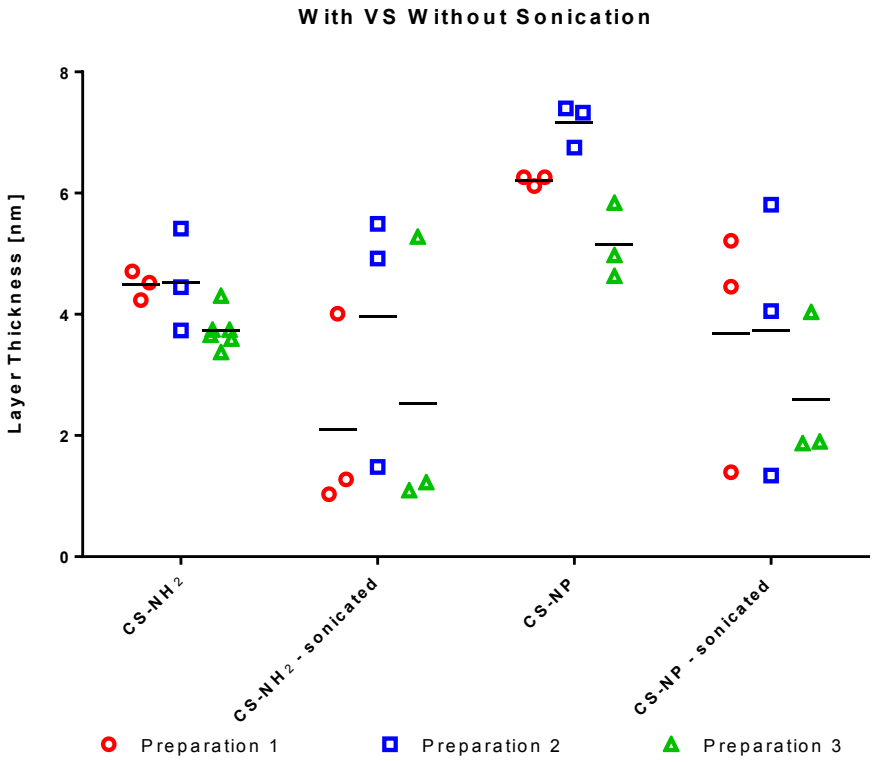

Figure 27 – Effect of Sonication on Layer Thickness

SAM layer thicknesses for CS-NH_2 and CS-NP are shown, for samples that were subjected to sonication after NH_2 SAM deposition, compared to previous samples that were not sonicated. For ease of comparison, previously obtained results for both CSs are shown alongside results for samples subjected to the newly included sonication step. For samples subjected to sonication after removal from NH_2 SAM deposition solution, only half of the measurements produced reduced SAM layer thicknesses. Individual measurements are represented by a marker each, and black bars mark the mean for each group.

4.2.4 Effect of HCl in Deposition Solution on NH_2 SAM Formation

As the intermediary step, that facilitates attachment of NP to AFM probes, the NH_2 SAM is of great importance in the proposed cantilever modification scheme, thus confirmation of its correct formation remained a primary concern. Continued search for improvements to the NH_2 SAM preparation protocol identified problems in the reproducible preparation of NH_2 SAMs to be prevalent in the literature. [65-67,79,80]

In general, the reason for incorrect formation of NH_2 SAMs is that in their amine form the molecule tail groups are able to enter interactions other than those intended. Specifically, the lone electron pair of the amine can donate electrons to form covalent Au-N bonds, distorting the alignment of the SAM molecules and enabling exposed S groups to oxidise[78], and additionally, that through interplane H-bonding between adsorbed molecules and free molecules in the bulk, additional layers of deposition molecule on top of the adsorbed SAM are created [66].

The study by Lee, *et al.*, [78], addressed the issue with the addition of hydrochloric acid (HCl) to the deposition solution. Through protonation of the amine groups to form ammonium ions, covalent Au-N interactions are prohibited. Further, amine group dimer formation through H-bonding is prohibited, where instead the positively charged ammonium groups repel each other; preventing multilayer formation.

To further investigate the NH_2 SAM formation, and determine whether the use of HCl produces SAMs of improved quality, a time series was conducted using deposition solution both with and without the addition of HCl. Separate samples were prepared for each time point in both series, which were each interrogated via ellipsometry in six non-overlapping positions. The results of the experiment are shown in Figure 28.

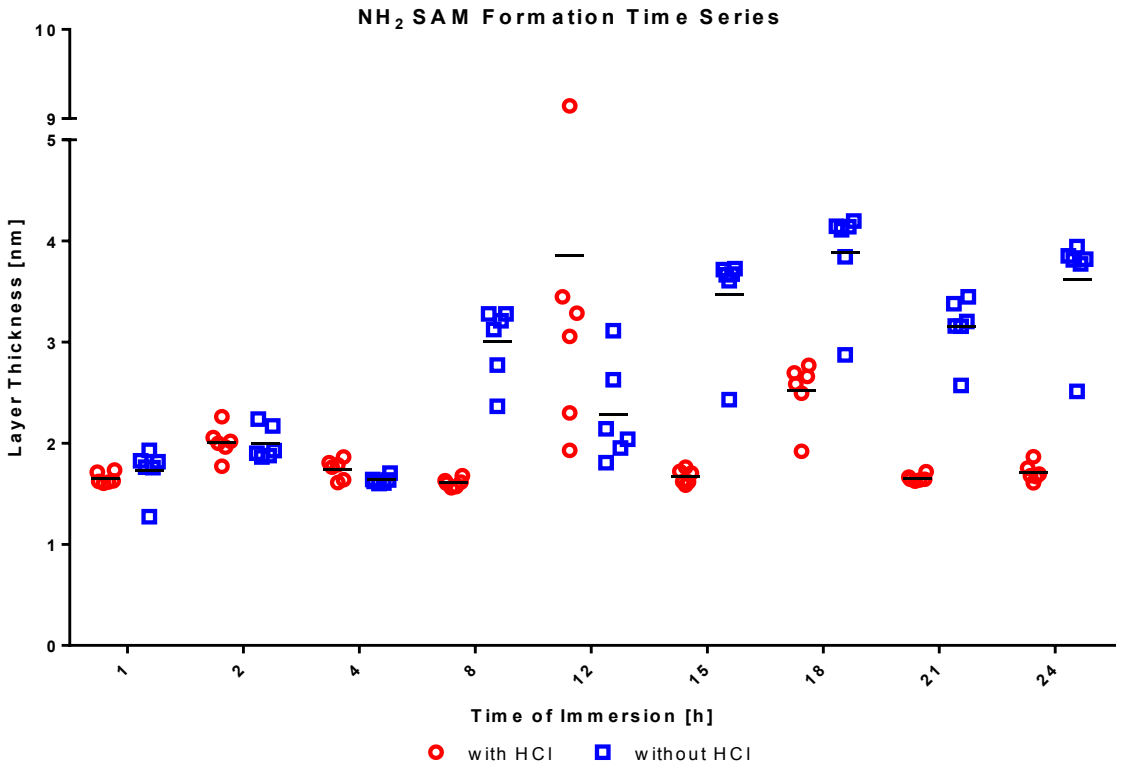

Figure 28 – The Effect of HCl in Deposition Solution on NH_2 SAM Formation

SAM thicknesses as determined via ellipsometry are shown, for samples prepared from deposition solution with added HCl (red circles), and deposition solution without added HCl (blue squares). One sample was prepared for each time point of each series, and each sample was measured six times in non-overlapping positions. Each measurement is represented by a marker on the graph, and black bars mark the mean for each group.

As seen in Figure 28, the SAM formation behaviour is the same for both the preparation with and without the addition of HCl for the first 4 h, where an initial increase in SAM layer thickness is followed by a subsequent reduction. The mean increase for the two series combined is 0.31 nm, followed by an equal reduction. This was thought to be comparable to what was reported by Yeung, *et al.*, [81], where a change in SAM thickness over time could also be observed. Conversely, the variation in SAM thickness was an initial decrease, followed by an increase, which ultimately plateaued at the expected thickness value. This gradual change in SAM thickness was attributed to SAM organisation and growth that plateaued once the SAM was

fully formed. It is probable that the change in SAM layer thickness observed in Figure 28 over the first 4 h is also due to progressions in SAM organisation, however, measurements of similar samples in subsequent experiments did not produce comparable behaviour.

After 4 h the series diverge in the obtained SAM thickness values. Results for samples prepared from deposition solution without added HCl consistently show increased SAM thicknesses with increased variability of values obtained for individual samples. This means that the formed SAMs are no longer in the desired conformation, where the formation of multiple layers of deposition molecule on top of the adsorbed SAM – due to the aforementioned interplane H-bonding between the amine groups – is the likely cause for the increased layer thicknesses.

Samples prepared from deposition solution with added HCl, for the most part, produce thickness values that are consistently in the range of expected values, where the results for samples removed from the deposition solution after 8, 15, 21, and 24 h of incubation were 1.61 ± 0.04 nm, 1.67 ± 0.07 nm, 1.66 ± 0.03 nm, and 1.71 ± 0.09 nm, respectively. These values are on average 0.28 nm (20%) above the predicted SAM layer thickness of 1.38 nm stated in Table 1 (p.36), but as previously discussed in §4.2.1.1 (p.43) this difference is within acceptable margins. Further, based on the consistency of the results, the SAMs that formed on these samples are considered to be in the correct conformation.

Samples that were removed from deposition solution with added HCl after 12 h and 18 h of incubation were distinctly above the expected values at 3.86 ± 2.65 nm, and 2.52 ± 0.31 nm, respectively, with increased variability of values obtained for individual samples. This was not reproducible, however, and repeated preparation of

samples at these time points (see Appendix 8.14; p.249) produced improved SAM layer thicknesses with good consistency.

From this it can be concluded that the use of HCl helps produce better quality NH_2 SAMs with more consistent layer thicknesses, although an inherent failure rate remains.

4.2.5 Repeatability of NH_2 SAM Preparation and Layer Growth Through Subsequent NP Addition

As the preceding results in §4.2.4 (p.69) have demonstrated, samples prepared from NH_2 SAM deposition solution with added HCl more consistently present with good quality SAMs, however, an inherent failure rate in the preparation remains. In an effort to quantify this failure rate, 10 samples were prepared independently under the same conditions, and were interrogated via ellipsometry. The chosen time of immersion in deposition solution for these samples was 4 h, because the results from the NH_2 SAM formation time series indicate that this provides sufficient time for the SAM to form fully, as well as preventing excessive deposition that occurs during longer times of immersion.

Additionally, those same samples were later also subjected to the addition of NP, in an effort to quantify the layer growth as a result of NP addition. The samples were again assessed via ellipsometry, where the first and second interrogations of the samples were in non-identical, but similar, positions. The results are shown in Figure 29.

From the results shown in Figure 29, the inherent failure rate to the preparation of NH_2 SAMs can be estimated at 30%, as samples 6, 8, and 10, present layer

thicknesses well above predicted values, as well as increased variability of results for individual samples. There is a strong connection between the consistency of the NH_2 SAM layer thicknesses and the consistency of layer thicknesses after subsequent addition of NP. The average increase in layer thicknesses due to NP addition is 0.174 ± 0.081 nm (p=0.035) for all samples, which decreases to 0.096 ± 0.041 nm (p=0.023) after the exclusion of samples 6, 8, and 10.

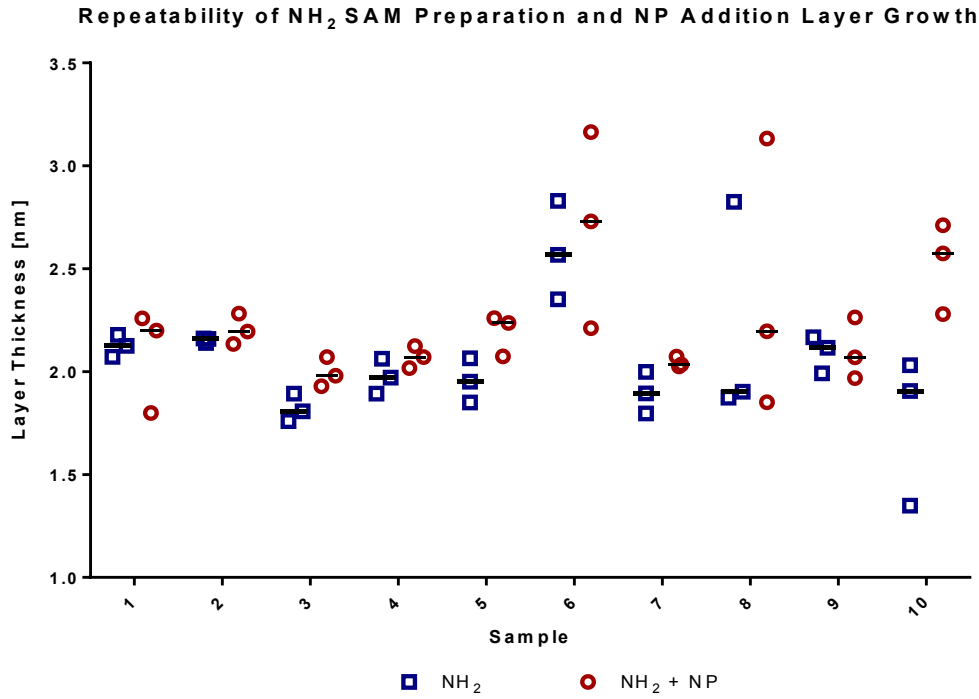

Figure 29 – Repeatability of NH_2 SAM Preparation, and Layer Growth Through NP Addition

Shown are the layer thicknesses as assessed via ellipsometry for 10 independently prepared samples. Samples were first measured after 4 h of immersion in NH_2 SAM deposition solution (blue squares), and again after addition of NP to the same samples (red circles). Individual measurements are represented by a marker each, and black bars mark the mean for each group.

The samples for which correct conformation of the NH_2 SAM was not achieved, still show a mean increase in layer thickness after NP addition of 0.357 ± 0.222 nm (n.s.). This indicates that incorrectly bound NH_2 SAM deposition molecules that are forming additional layers on top of the adsorbed SAMs, are later not displaced in the addition

of NP; further emphasising the importance of achieving correct NH_2 SAM formation prior to NP addition.

4.2.6 Effect of HCl Concentration

While the previous results have demonstrated that the use of NH_2 SAM deposition solution with added HCl produces samples of better quality, it does not manage to completely prevent occasional failures in the sample preparation.

To investigate whether using different concentrations of added HCl will improve its effect in producing better quality samples, deposition solutions with different concentrations of added HCl were prepared. Samples were immersed in the deposition solution for between 1 and 8 h, producing short time series for each of the different deposition solutions. As in the previous experiment in §4.2.5 (p.72), samples were first interrogated using ellipsometry after immersion in NH_2 SAM deposition solution, and were interrogated a second time after subsequent addition of NP; where each time every sample was measured in three non-overlapping positions.

For means of comparison, a short time series of SAM formation was also prepared for CS-CH_3, which is known to readily produce consistent layer thicknesses, and hence provides a reliable baseline against which other results can be compared. The results are shown in Figure 30.

The results in Figure 30 show the SAM thicknesses for CS-CH_3 increasing steadily during the first 4 h of incubation, by 0.105 ± 0.037 nm from 1 h to 2 h ($p=0.045$), and by 0.219 ± 0.056 nm from 2 h to 4 h ($p=0.017$). Beyond 4 h of incubation, the SAM thickness plateaus, at 1.84 ± 0.097 nm, which indicates completed assembly and

organisation of the SAM. A grey line across the graph was marked at this value to aid in comparison of the results.

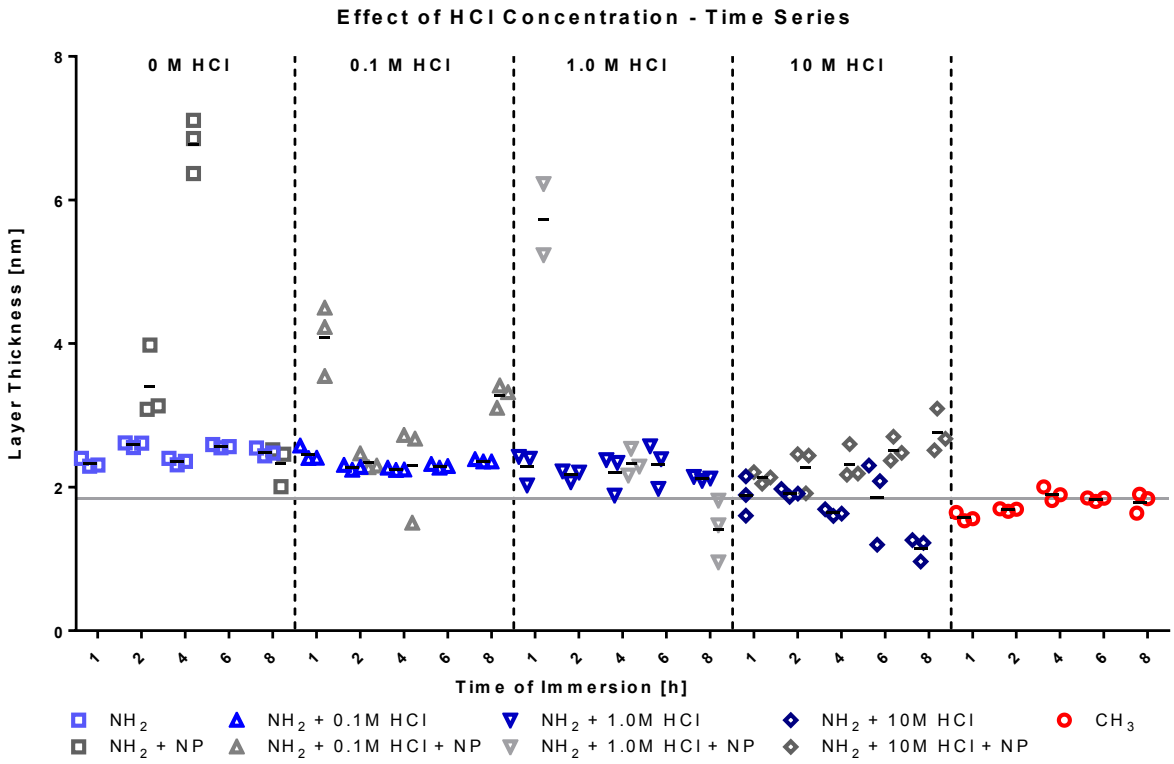

Figure 30 – Effect of HCl Concentration

SAM thicknesses assessed via ellipsometry are shown for samples prepared from NH_2 SAM deposition solution with different concentrations of added HCl, with times of immersion between 1 and 8 h (blue markers). The same samples were assessed again via ellipsometry after subsequent addition of NP (grey markers). CS-CH_3 samples were prepared for the same times of immersion (red circles) to provide a baseline SAM layer thickness for comparison of the data. This is marked by the grey line across the graph and is defined by the plateaued SAM thickness of CS-CH_3. Individual measurements are represented by a marker each, and black bars mark the mean for each group.

The results for the NH_2 SAMs demonstrate that with increasing concentration of HCl the obtained layer thicknesses decrease. The average decrease in SAM layer thickness between samples prepared from deposition solution with no added HCl compared to samples prepared from deposition solution with 0.1 M HCl added is 0.141 ± 0.038 nm (p=0.0009). Additional decreases in SAM layer thicknesses of

0.108 ± 0.055 nm ($p=0.063$), and 0.529 ± 0.112 nm ($p<0.0001$), are observed with each further 10-fold increase in concentration of added HCl.

For samples prepared from deposition solution with 10 M HCl added, however, the mean layer thickness is not an appropriate assessment, as for those samples a reduction in SAM layer thickness over time can be observed that is not apparent for the other groups. Within the first 2 h of incubation, the produced SAM layer thicknesses are comparable to the experiment baseline value determined from CS-CH_3 samples, but for incubation times beyond 2 h SAM layer thicknesses even below that are produced. Layer thickness values below the determined baseline suggest that instead of a densely packed SAM, a sparser distribution of the molecules is assembled on the surface.

The layer thicknesses that were determined after subsequent NP addition to the NH_2 SAM samples show great variability, and many measurements were excluded because mathematical models could not be fitted to the data sufficiently well. The most consistent results were obtained for NP addition to samples prepared from NH_2 SAM deposition solution with 10 M HCl added. However, layer thicknesses after NP addition are increasingly greater for samples for which lower NH_2 SAM thicknesses were previously determined. This suggests that more NP binds to more sparsely assembled NH_2 SAMs. One scenario in which this behaviour is plausible, is that for densely packed SAMs, the density of amines exposed at the surface is too great, and steric effects are impeding the attachment of NP. With increasing sparsity of the exposed amine groups, the proportion of amine groups to which NP can bind increases also, enabling an overall greater amount of NP to be retained.

From these results it can be concluded that an increase in the concentration of the HCl added to the NH_2 SAM deposition solution aids in producing better quality SAMs that are presenting with layer thicknesses that more closely adhere to predicted values. This also positively influences the subsequent addition of NP, where layer thicknesses in the range of predicted values are obtained with increased consistency. Based on these findings, the best preparations are achieved using NH_2 SAM deposition solution with 10 M HCl added, combined with increased incubation times.

4.3 Discussion of Tip Modification Verification and Quality Control

The surface area of AFM cantilevers is very limited, and hence not accessible for common interrogation techniques. Therefore, in order to inspect the chemical modifications applied to cantilevers, and confirm their correct conformation, an alternative medium was required. Au-coated silicon wafers were chosen as substitute substrates, as their Au coating provides the same chemical properties that are expected from the cantilever Au coating. Furthermore, they provide a substantial planar surface on which surface modifications can be interrogated with commonly available techniques.

The five different CSs that were prepared in this manner could be divided into two groups: **1**—CS-NH_2 and CS-NP were prepared to investigate the constituent steps of the proposed cantilever modification scheme outlined in §3.2.1. (p.27), and **2**—CS-CH_3, CS-COOH, and CS-OH were prepared as robust counter surfaces with consistent surface chemistries against which modified cantilevers could be tested, in order to establish characteristic interaction profiles that would allow identifying successfully NP functionalised cantilevers. As previously discussed in §4.1 (p.31), CS-NH_2 was to be used in both groups, such that four different CSs would be available against which NP functionalised cantilevers could be tested.

CS-CH_3 and CS-OH are routinely used to model hydrophobic and hydrophilic surfaces, respectively, that carry a neutral charge.[65] Hence, interactions with NP functionalised cantilevers are expected to be determined by the different wetting properties. Similarly, CS-NH_2 and CS-COOH are used to model positively and negatively charged surfaces, respectively, that are both hydrophilic.[65] Hence,

differences in interactions with NP functionalised cantilevers are expected to be determined by the different surface charges.

To be able to use CSs as reliable quality control measures, their preparation needs to be reproducibly of good quality. Hence, the first conducted investigation was of CSs, to demonstrate that the SAMs for each of the different surface modifications formed well, and with good consistency.

The results for CS-CH_3 and CS-OH showed that under the used preparation parameters the SAMs formed well reproducibly. Ellipsometry results showed that thin films were adsorbed onto the Au substrates, with layer thicknesses within the range of theoretically predicted values, and the results of the contact angle analysis confirmed that the assembled surface chemistries were exhibiting the expected wetting properties. Together, confirming that the SAM is in the correct conformation.

Prepared CSs were primarily interrogated using ellipsometry and contact angle measurements, because the readily obtainable insights allow for the identification of good quality samples. However, samples were only considered to be in the correct conformation when tests from both techniques produced the expected results. This is exemplified by the results for CS-COOH. Ellipsometry results determined SAM layer thicknesses for CS-COOH to be well within the range of predicted values, but contact angle analysis did not produce the expected results. Hence, the correct conformation of the deposited SAM could not be inferred.

A selection of samples could also be interrogated via XPS, the insights from which largely confirmed the findings from ellipsometry and contact angle measurements. The XPS results for CS-CH_3, CS-COOH, and CS-OH all presented with high signal

intensities in their survey spectra, confirming thin layer thicknesses for the SAMs adsorbed onto the Au substrates. Further, the XPS results confirmed the presence of the elemental components of the different deposition molecules, and the two discernible peaks in each of their S spectra suggested that the SAMs had formed correctly. The XPS results for CS-COOH could not confirm incorrect conformation of the SAM, not showing peaks in the S spectrum characteristic for unbound or oxidised S.[65,82] However, the XPS results can also not be used to infer correct conformation of the SAM as it does not provide information on the orientation of the molecules. Therefore, despite XPS and ellipsometry results suggesting that the SAM on CS-COOH had formed correctly, it is not considered to be in the correct conformation, and in this instance the contact angle results remain deterministic in calling the quality of the SAM into question. Further, while XPS results may be more detailed, the technique is also not available to provide continuous assessment of samples for quality control throughout the project.

XPS results for CS-COOH and CS-OH did determine the presence of N on the interrogated samples, which was unexpected as neither of the deposition molecules contains any. The most plausible cause for the presence of N on these samples was through cross-contamination in the sample preparation. In the preparation, samples were handled in sequence, 1 through 5, as shown in Figure 11 (p.114).

Although the forceps that were used to handle the samples were washed in both H_2O and EtOH in between samples, some traces of the N containing molecule used in the preparation of CS-NH_2 likely remained. The absence of N on CS-CH_3, and the

intensity of the detected N peak decreasing from CS-COOH to CS-OH, supports this hypothesis.

To prevent cross-contamination in future sample preparations, a small amount of piranha solution, used to clean the Au substrates, was retained for rinsing of the forceps in between handling samples, in addition to the rinses in H_2O and EtOH. Additionally, when different CSs needed to be prepared, they were no longer prepared in sequence. The required amount of replicate samples for each of the different chemical modifications was prepared together, and all rinsing solutions were replaced, and handling tools cleaned, before preparing samples of the next chemical modification.

The investigation of the consistency of CS preparations revealed that SAMs on CS-NH_2, and by extension those on CS-NP, did not form correctly. Ellipsometry results for both showed that the thicknesses of the adsorbed layers were distinctly above the predicted values. While distinct increases in layer thickness could be observed for CS-NP compared to CS-NH_2, suggesting that addition of NP was occurring, it could not be assumed that the surface modifications were in the designed conformation. Results from contact angle analysis confirmed that CS-NH_2 did not possess the correct surface chemistries, where both CS-NH_2 and CS-NP produced contact angles that were more characteristic for SH groups being exposed at the SAM surface.[74]

XPS results for CS-NH_2 and CS-NP support the ellipsometry findings, where reduced signal intensities in the survey spectra suggest that films with increased layer

thicknesses have been adsorbed. The S spectra for both CSs further confirm that the SAMs did not form correctly, lacking two discernible peaks, and are characteristic of unbound SH groups rather than oxidised S.[66,78,82]

The S spectra confirming that no oxidised S is present on the sample, however, leaves the presence of O on CS-NH_2 unexplained. A study by Baio, *et al.*,[65], addressed this issue specifically, investigating the source of significant amounts of O commonly found on NH_2 SAMs. Detailed multi-technique analysis of NH_2 SAMs found that only fractional amounts of O, below the detection limit of XPS, are present due to oxidation of species in the deposition molecule, and determined that the majority of detected O is due to O containing coadsorbates at the SAM surface, such as tightly bound water.

With the addition of NP on CS-NP, the presence of O is expected, but a deconvolution of the O spectrum into the different conformations of O is not possible, and the applied type of XPS does not provide information on the location of O in the SAM. Hence, while the XPS results confirm the presence of the elemental components of the deposition molecules, they do not allow for a distinction between the parts that are deposited in the individual steps of the surface modifications.

To improve on the quality of prepared CS-NH_2, and by extension CS-NP, modifications to the preparation protocols were considered.

In the preparation of NH_2 SAMs described by Lee, *et al.*, [78], samples were sonicated for 3 min after SAM deposition in order to remove any excess of solution and loosely bound molecule. While the XPS results from interrogation of a CS-NH_2 sample subjected to sonication after removal from NH_2 SAM deposition solution suggest that

thinner layer thicknesses are achieved, the ellipsometry results for a group of samples prepared in that fashion reveal that this is not the case for all samples. Variability is observed for individual samples, and across samples, where only approximately half of the measurements yield layer thickness values that are within range of predicted values. The remainder of the measurements determine layer thicknesses to be above the expected values, much like the values that are obtained for samples that were prepared without sonication. In addition to variability in the produced results, attempts to apply the sonication step to AFM cantilevers resulted in approximately half of the cantilevers being sheared off from the chip in the process. Hence the inclusion of the sonication step was determined to be ineffective and not considered further.

Another modification of the CS-NH_2 preparation protocols that was considered was the addition of HCl to the SAM deposition solution. In its amine form the N can donate a lone pair of electrons to Au to form covalent Au-N bonds, which compromises the correct alignment of the molecules and disrupts the structure of the SAM on the Au substrate. Added HCl protonates the amine to form ammonium ions, which does not bond covalently to Au.[78] Further, the formation of amine dimers is disrupted, which previously easily formed through H-bonding between the H and the N's lone pair of electrons. Instead the positively charged ammonium groups repel each other, which prevents multilayers from forming.[66,78]

A comparative time series between deposition solutions with and without added HCl first highlighted the beneficial effects of added HCl. The results for the different

preparations were comparable for shorter incubation times, but the effects became increasingly pronounced for extended incubation times. The preparation with added HCl continued to produce samples that, for the most part, presented with SAM layer thicknesses in the range of predicted values, whereas samples prepared from deposition solution without added HCl produced layer thicknesses increasingly variable and distinctly above predicted values.

While the preparation with added HCl provided better quality samples more consistently, an inherent failure rate remained. A subsequent assessment of the repeatability of preparations approximated this failure rate at 30 %.

A subsequent investigation of the effects of concentration of HCl added to NH_2 SAM deposition solution revealed that improved results are obtained by increasing the concentration of added HCl. Best results were obtained for samples prepared from NH_2 SAM deposition solution with 10 M HCl added. Increased times of immersion produced SAMs with increasing sparsity of deposited molecules. Beneficial effects of increased sparsity were observed for the subsequent addition of NP, allowing an increased amount of NP to be retained on the samples.

Evidence of successful addition of NP can be seen for all CS-NP samples compared to CS-NH_2, but correct conformation of the complete modification cannot be assumed for preparations where there is evidence that the NH_2 SAM did not form correctly. While improved results were obtained through altering and adapting different parameters of the preparation, the possibility of preparations failing cannot be eliminated; emphasising the need for means whereby which successfully modified cantilevers can be identified.

Out of the four different CSs that were initially to be used for this purpose, results showed that CS-CH_3 and CS-OH can reproducibly be prepared with good quality. Freshly prepared surfaces for testing modified cantilevers against will be tested using ellipsometry and contact angle analysis, as these techniques are readily available and provide sufficient information to assess the quality of the preparation. Correct SAM layer thicknesses confirm that the SAM has formed correctly and the correct water wetting properties confirm that the correct tail group moieties are present at the sample surface. Results from both techniques are required to match expected values for samples to be considered in the correct conformation.

5 Preparation and Interrogation of Biological Samples via AFM

This chapter discusses the preparation of biological samples for atomic force microscopy (AFM) adhesion measurements, and what sample preparation techniques are most favourable for those purposes. The computational means developed for the analysis of large amounts of AFM data are presented, and their functionalities are introduced.

5.1 Hybridoma Cell Lines

During the development and testing of the technique, a control target was required that would remain consistent across different experiments to ensure that results are comparable. For this purpose the use of hybridoma cell lines was chosen. The hybridoma technique was developed in 1975 by Milstein and Köhler [83], and is briefly described in Appendix 8.15 (p.250). The hybridoma technique yields monoclonal, immortal cell lines that produce monospecific antibodies, and is since its inception employed routinely in research and diagnostics applications.

The hybridoma cell lines that were used in this project are described in Table 2, and were provided to the Toellner lab in 2008, by Claudia Uthoff-Hachenberg, of Cologne University. The cell lines were chosen to all be of the same isotype (IgG1), in order to limit the number of variables being introduced. The IgG1 isotype is the monomeric form of antibody, and was chosen because it is associated with higher affinity antibodies that emerge at progressed stages of an immune response and hence is expected to produce more distinct interactions, but also because it is the lowest valence form of antibody with only two antigen binding sites, which reduces the

number of combinations of possible binding interactions compared to other isotypes such as IgM, which is pentavalent and as such has 10 potential antigen binding sites. Prior to use of the cell lines in experiments, flow cytometry was employed to confirm their isotype as well as their specificity towards (4-hydroxy-3-nitrophenyl)acetyl (NP) (data shown in Appendix 8.16; p.252). The results in Table 2 show the percentages of the assessed populations positive for each. Further, the relative affinity of the different cell lines was assessed via surface plasmon resonance (SPR), using purified antibody secreted by the respective cell lines (the data, which were kindly provided by Dr Jennifer Marshall, and a brief introduction to SPR can be found in Appendix 8.17; p.254).

Table 2 – Hybridoma Cell Lines

The table details properties of the different hybridoma cell lines that were used in experiments. All cell lines were of the IgG1 isotype, and specific towards the antigen NP. Both cell line isotype and NP-specificity were confirmed via flow cytometry, showing the percentage of the assessed populations positive for each. Relative affinity of the cell lines was assessed via SPR, using purified antibody secreted by the respective clones.

Cell Line	S24.1.47	N1.G9	B1.48	18.1.16
% $IgG1^+$	99.9	96.6	99.8	98.5
% NP^+	97.4	95.5	97.0	95.5
Relative affinity	High	Medium-High	Medium-Low	Low

5.2 Sample Preparation

For the preparation of samples suited to interrogation via AFM, a number of different requirements needed to be considered.

One of the main characteristics of AFM is that the probe is in physical contact with the sample. That means that for every tip-sample interaction, at every point interrogation, a force is exerted on the sample. While the applied compressive force is chosen such that no plastic deformations are incurred in the sample, the possibility remains that the force is sufficient to cause displacement. For cells specifically, this means that while the force exerted on a cell will not be sufficient to damage the cell, it can be sufficient to move the cell from its location, prohibiting repeated interrogations. Therefore, sample preparation techniques were required that provided sufficient immobilisation; prohibiting lateral displacement of cells upon (repeated) interrogation, as well as prohibiting cells from detaching from the sample holder during the loading of adhesion events.

The next consideration was the location of facilities. The culturing of cells, preparation of samples, and interrogation of prepared samples on the AFM, needed to each be conducted in separate departments. Cells would remain in cell culture medium after harvesting, which made the transport between departments unproblematic. However, sample preparation techniques were required that produced samples robust enough for short term storage and transport prior to interrogation.

Lastly, the practical application of the method being developed was considered. While during initial testing cultured cells were interrogated, the ultimate goal is to employ the developed technique in the interrogation of tissue sections. Therefore, aspects of sample preparation technique similar to those used for tissue sections need to be used for the samples used in initial testing and characterisation of the technique. Preparation of tissue sections typically involves fixation in order to preserve tissue structure and antigens that may be detected by immunohistological

staining techniques. Therefore, a range of fixation methods was tested to determine which was best suited for samples interrogated via AFM.

5.2.1 Cell Monolayer Preparation

There are two main techniques for the preparation of samples using (cultured) cells, 1—cytospins, where cells in tissue culture medium are gently accelerated towards the sample holder through centrifugal force, forcing adhesion upon contact with microscope slides, and 2—sedimentation, where cells are allowed to sediment onto the sample holder from a cell suspension and adhesion is aided through a coating of the sample holder surface.

For the preparation of samples used in this project, 1 G sedimentation was chosen over centrifugal force assisted sedimentation. The used hybridoma cells contain copious amounts of NP-specific antibody. The strain that is put on the cells during cytospins may rupture their plasma membranes, making the internal antibody accessible to the NP-equipped AFM probe. As internal antibody is not anchored in the cell membrane, unlike the cell surface receptors studied here, it may, after binding to the NP on the probe, remain attached to the probe when the probe is retracted. This would lead to the NP-equipped probe becoming saturated with NP-specific antibody; causing the probe to lose its specificity.

The protocol for the preparation of cell monolayers through sedimentation can be found in Appendix 8.18 (p.258), where, in an adaption of the techniques employed by Shaw, *et al.*, [84,85], Ø13 mm glass coverslips were coated in polylysine to aid in the adhesion of the cells to0 the coverslips.

5.3 Measurement Process

The AFM is operated in contact mode. With the aid of low magnification top-down optics, the cantilever is positioned near the cell (or cluster of cells) that is to be interrogated, before it is approached to the surface. Target cells are subsequently identified using the AFM in force mapping mode.

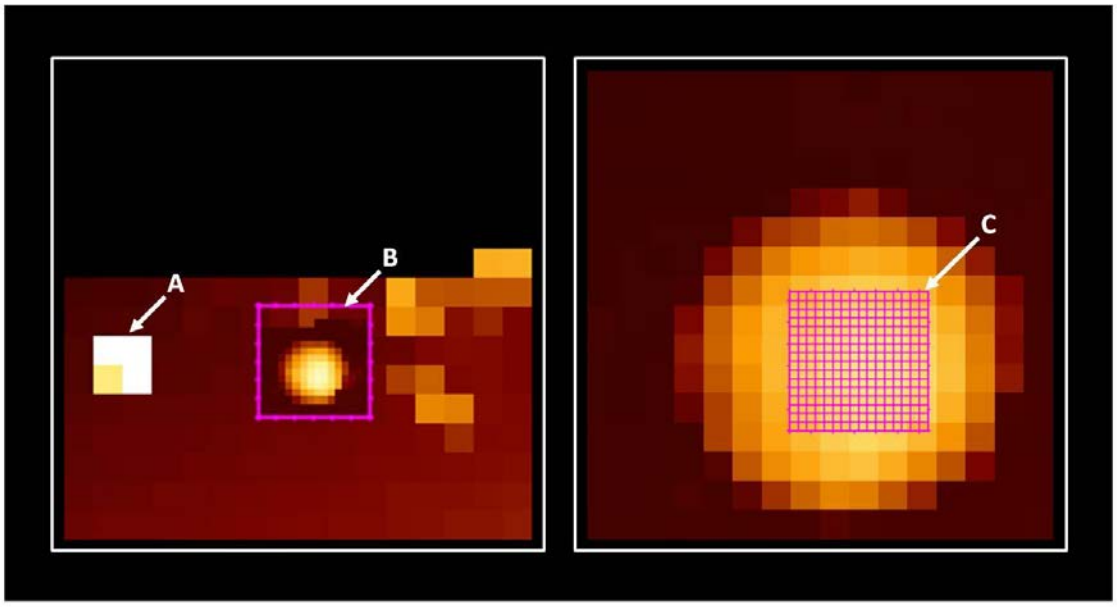

Figure 31 – Localising Target Cells.

Topographical maps are built up of the sample surface to identify target cells. Using the force mapping mode, a coarse scan reveals the approximate location of cells (A), which is subsequently determined more accurately with a finer scan of a smaller region, providing a description of the shape of the cell (B). The finer scan is used to select a 3.2 µm x 3.2 µm surface area, centrally, on the cell (C), in which, in the force spectroscopy mode, the cell is interrogated with 16 x 16 evenly spaced point interrogations.

As illustrated in Figure 31, a coarse topographical map of the sample surface is built up to identify target cells (A). Subsequently, a finer scan of smaller regions covering individual identified cells provides a more accurate description of the cell's shape and location (B). The finer scan of the identified cell is used to select the desired scan

region. A 3.2 μm x 3.2 μm area is selected on the surface of the cell; centrally, in an effort to minimise the effects of the curvature of the cell (C).

Switching to the force spectroscopy mode, the selected surface area is interrogated with an evenly spaced grid of 16 x 16 point interrogations. At each location, force-distance curves are acquired at 1 μm/s moving speed. The probe is in contact with the sample only during the indentation and retraction phase, with no additional in-contact pauses. The used cantilevers were CSC17/Cr-Au (MikroMasch, USA), and OMCL-RC800PB (Olympus, USA), for which the typical radii of curvature of the tip are <35 nm [86], and 30 nm [87], respectively; as stated by the manufacturer.

5.4 Data Processing

For every point interrogation a force curve, as was shown diagrammatically in Figure 8, is produced, from which the desired information needs to be extracted. As has been detailed in the description of the measurement process in §5.3 (p.90), hundreds of force curves are recorded for every interrogated cell, producing many thousands of force curves in every experiment. This volume of data cannot be analysed manually within realistic timeframes, and even larger volumes of data are expected to be collected in the interrogation of tissue sections. It was therefore necessary to develop robust, automated analysis routines that are able to process the acquired data.

Using the example of a data set from a real interrogation point, the developed algorithms are described below. Shown in Figure 32(A) is an example of data collected for one point interrogation, which for the purpose of analysis is divided into its constituent components: the approach curve (B) and the retraction curve (C).

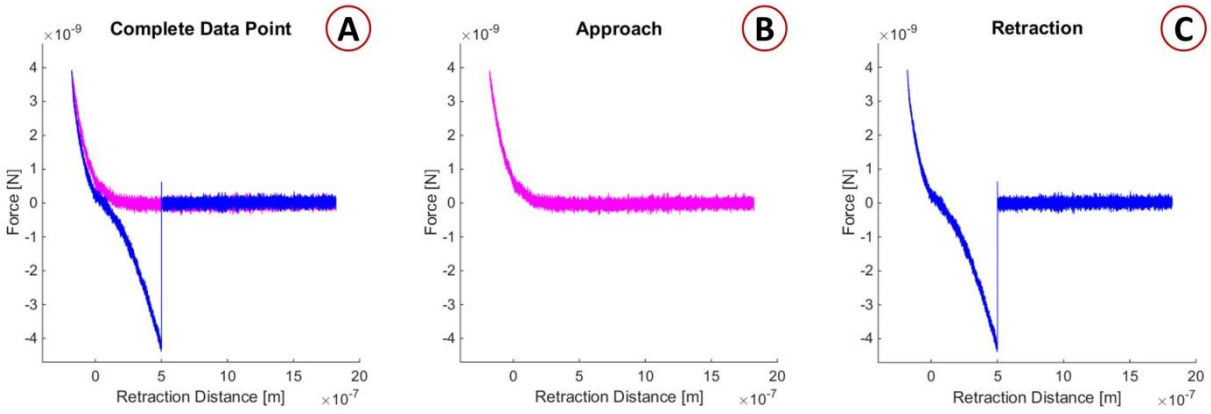

Figure 32 – Example Data Point

Example of a real data point (A) that has been divided into its constituent components; showing the approach curve (B) and the retraction curve (C) individually.

The analysis focuses almost exclusively on the retraction curve, shown in more detail in Figure 33, as the majority of the parameters describing the tip-sample interaction are extracted from here.

Baseline Determination – To be able to determine differences, references need to first be established. The main reference against which calculations are made is the value of the baseline of the un-deflected cantilever in its unstrained state. The baseline value is determined by first calculating the mean of an initial cluster of 100 data points starting at (A). Progressively, the size of this initial baseline cluster is increased. Sequentially, the mean of additional clusters of 10 data points is determined. If the mean of the additional cluster is within 3 standard deviations (SDs) of the mean of the baseline cluster, the two clusters are merged and the overall mean is re-determined. This allows the baseline cluster to grow, increasing the accuracy of the determined baseline value, and advancing the amount of points considered in its determination towards (B). Once the mean of the next considered 10 point cluster lies outside 3 SDs of the baseline cluster, the baseline cut-off point (B) has been found. No further additions to the baseline cluster are made, and the final baseline value is

calculated using only the previously considered points. Graphically, as shown in Figure 33, the baseline value is shown by the black line, and the green lines either side mark 3 SDs from the baseline.

Force of Interaction – The force of interaction is determined using the difference between the peak cantilever deflection and the baseline. The peak cantilever deflection is taken as the lowest point in y of the retraction curve data set (C) that is to the left hand side of the previously determined baseline cut off (B). The absolute difference in y between the peak cantilever deflection and the baseline, multiplied by the known cantilever spring constant, subsequently yields the force of adhesion associated with the tip-sample interaction.

Event 'Significance' – The 'significance' of adhesion events is assessed by expressing the distance between the peak cantilever deflection and the baseline in multiples of SD of the baseline (Equation 4).

$$E_S = \frac{\Delta x_{max}}{\sigma_R}$$

Where:

E_S	=	event 'significance'	
Δx_{max}	=	maximum cantilever deflection	[N]
σ_R	=	SD of the retraction curve baseline	[N]

Equation 4 – Event 'Significance'

The 'significance' of adhesion events is assessed by expressing the maximum cantilever deflection in multiples of SD of the retraction curve baseline.

The event 'significance' is determined to aid in the interpretation of results. Large adhesion forces detected for a sample being accompanied by values of low event 'significance' are a good indication that large variations exist in the retraction curve baselines, and hence call into question the reliability of the obtained results.

Conversely, if the adhesion forces that are detected are low, but are accompanied by high values of event 'significance', it can be assumed with confidence that there are only small variations in the retraction curve baselines, and hence that results are reliable.

Event Selection – Point interrogations are classed based on their event 'significance'. If the value is found to be less than 3 (SDs), the interrogation is classed as a 'zero'-interaction event, because the value that is found as the peak cantilever deflection is within the noise level of the baseline. When this occurs, all values that would otherwise be calculated are automatically set to zero.

Conversely, point interrogations for which the event 'significance' is above 3, are classed as positive adhesion events.

Energy of Interaction – The energy associated with a tip-sample interaction is defined by the area between the retraction curve and the baseline (D), multiplied by the known cantilever spring constant. This area is calculated as the sum of the distances between points and the baseline, each multiplied by the spacing between points. Points considered in the determination of the area (D), must be to the left hand side of the baseline cut-off (B), and below the determined baseline value.

Apparent Loading Rate – The point at which the baseline crosses the retraction curve at (E) marks the start of negative cantilever deflection in adhesion events. The line (F) between points (C) and (E) is used to determine a loading gradient for the tip sample interaction, which takes into account the speed at which the cantilever is retracted. Determination of this parameter is inspired by, but not directly comparable to, the loading-rate parameter that is used to describe the energy-landscape of agonistic interactions.

Overview Maps – To allow for the quick inspection of data collected for individual samples, a selection of parameters, such as force, energy, and event 'significance', are displayed on results maps, as for the example shown in Figure 34. Determined parameters are shown on the same grid on which interrogation occurred, which, as is discernible from the point ID map, occurs in a snake-like fashion.

The maps for force and energy show that, for this particular measured cell, only the results for a small number of point interrogations stand out. These are the points which were classed as positive adhesion events. The values for the remaining point interrogations in the force and energy maps were set to zero, as the event 'significance' associated with these point interrogations was less than 3.

The point ID map, accompanying each overview map, aids in the identification of points of interest. Upon selection of the position of a point of interest in the point ID map, the index for that point is shown. This index is also included in the image file produced for every analysed force curve, which allows for the detailed inspection of specific points of interest. In the example overview map shown in Figure 34, the indices for the points of interest are 56, 35, and 19; and the images for their analysed force curves are shown in Figure 35, and Figure 36(A) and (B) respectively.

Points of Interest – The images in Figure 35, and Figure 36(A) and (B), show the analysed data for only the point interrogations that were identified as points of interest in Figure 34, but an image is produced for every single point interrogation. Graphically marked in the images are landmark values determined in the analysis, such as: 1—the baseline value (red line) ± 3 SDs (green lines), 2—the baseline cut-off point (black dotted vertical line), 3—the baseline cross-over point (bold black

cross), 4—point of maximum cantilever deflection (bold black cross), 5—gradient line of loading (solid black line); where 1 through 3 are determined for both the approach and the retraction curves, and 4 and 5 are determined on the retraction curve only. Further, the values of calculated parameters are printed into the graph legend. As detailed in Figure 35, showing the point of interest with index number 56, the graph legend in each image states: 1—the point interrogation index, 2—the force [N] and 3—the energy [J] associated with the point interrogation, 4—the approach and the 5—the retraction curve baseline SDs [N], and 6—the loading gradient [N/s]. The title of each graph shows the file name of the corresponding data point to ensure that data files associated with each point interrogation can easily be located.

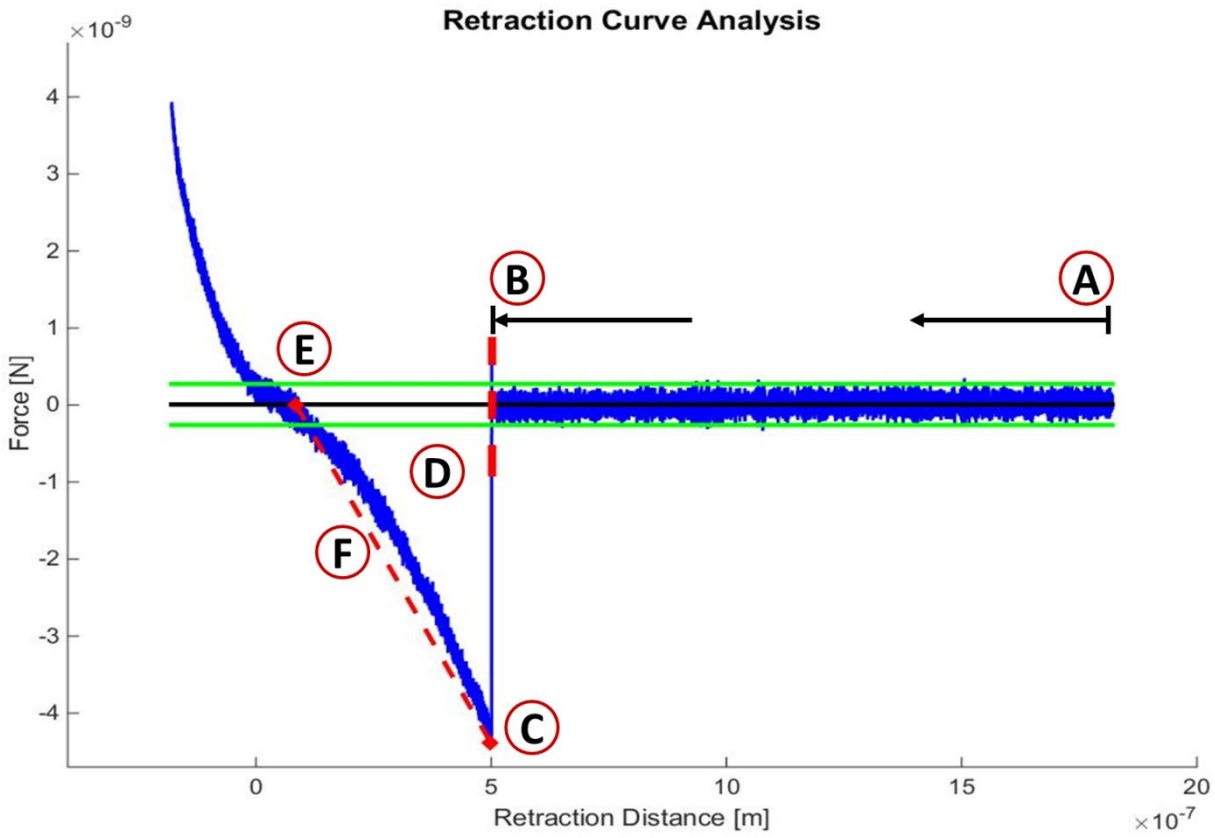

Figure 33 – Retraction Curve Analysis

The majority of parameters describing the tip-sample interaction at each interrogation point are extracted from the retraction curve. The baseline of the retraction curve is determined by incrementally increasing the number of points considered, in the direction of the arrow starting at (A). An initial baseline cluster is sequentially expanded with additional 10 point clusters, if the mean of the additional cluster is within 3 SDs of the baseline cluster. Once the mean of the additional cluster is outside 3 SDs of the baseline cluster, the baseline cut-off point (B) has been found, and no further additions to the baseline cluster are made. The peak cantilever deflection at (C) is defined as the lowest point in y on the retraction curve, to the left hand side of the baseline cut off (B). The distance between the peak cantilever deflection and the baseline, multiplied by the cantilever spring constant, yields the force associated with the tip-sample interaction. The energy associated with the tip sample interaction is given by the area between the retraction curve and the baseline (D). The area is calculated as the sum of the distances between points and the baseline, each multiplied by the spacing between points, for every point that is below the baseline and to the left hand side of the baseline cut off. The retraction curve crosses the baseline at point (E), marking the position where in adhesion events negative cantilever deflection starts. The line (F) between points (C) and (E) is used to determine a loading gradient for the tip-sample interaction.

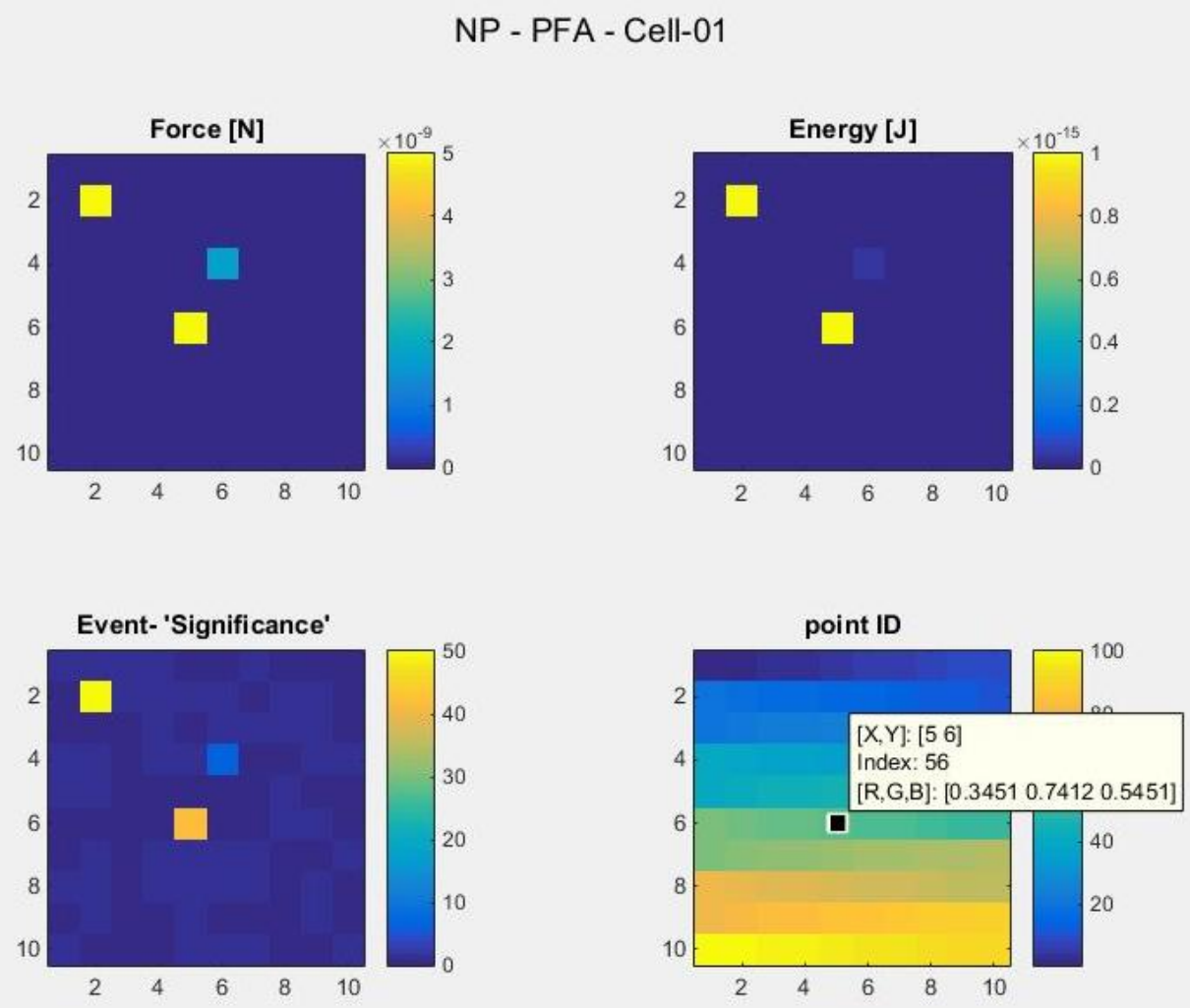

Figure 34 – Sample Overview Map

For quick inspection of results for a sample, overview maps are automatically produced by the analysis algorithms. A choice of parameters is displayed on the same grid that the data was acquired. This example overview map displays force [N], energy [J], and event 'significance', alongside a point ID grid. As can be seen in the maps for force and energy, only a small number of points stand out, which are the points that were classed as positive adhesion events. The remaining interrogation points were classed as 'zero'-interactions, and their values were set to zero. The point ID grid is included to allow for the quick identification of points of interest. Upon selection, the interrogation point index is displayed, which is also printed into the image files produced for every analysed force curve; as is depicted further in Figure 35.

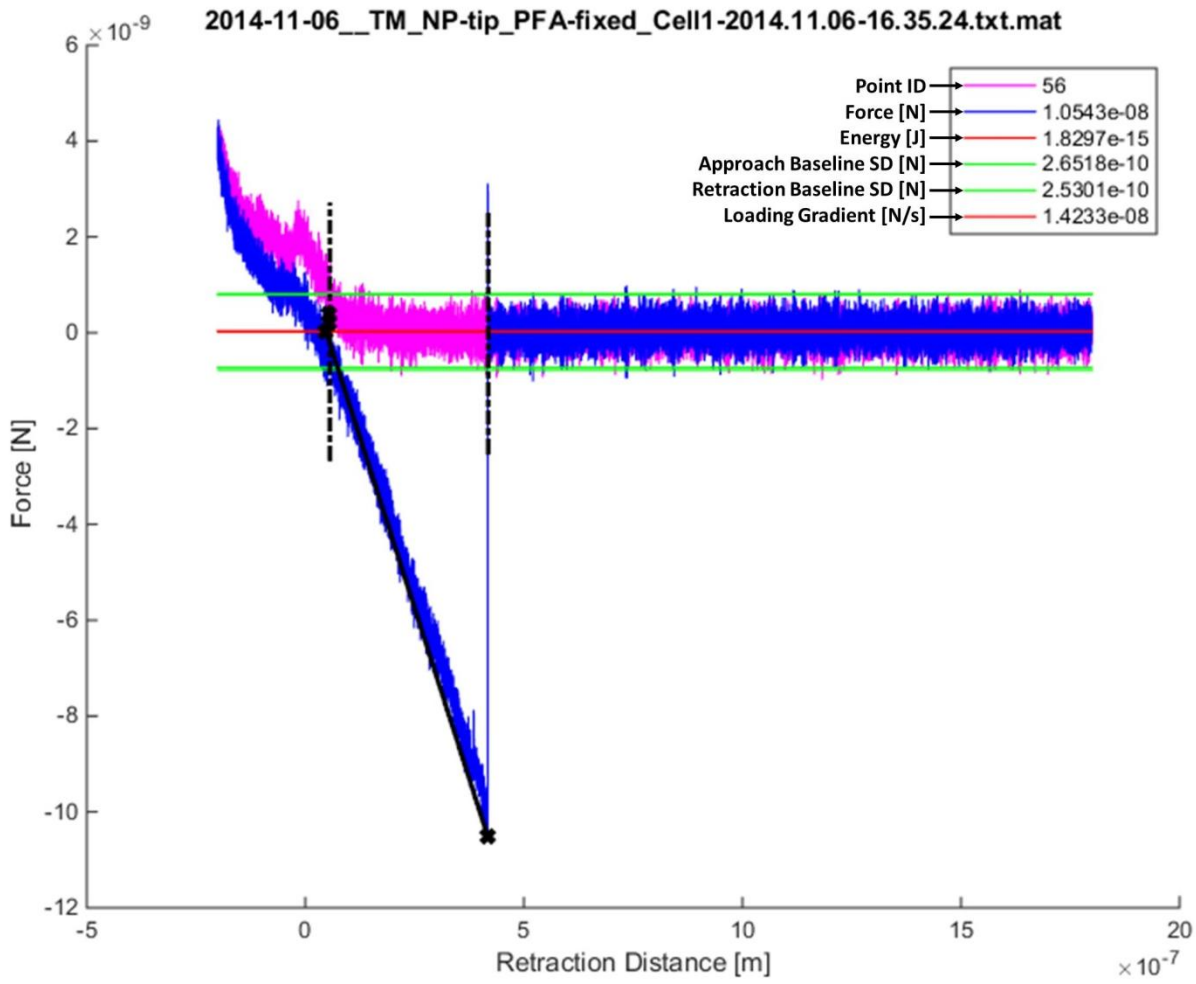

Figure 35 – Point of Interest – Index 56

From sample overview maps, points of interest can easily be identified using their index as determined from the point ID map. Here, the point of interest identified in the example overview map with index number 56 is shown. Images like this are generated to allow for the quick visual inspection of specific data points, and confirmation that landmark values were determined correctly. Shown for both the approach and retraction curves are the baseline value (red line) ± 3 SDs (green lines), the baseline cut-off point (black dotted vertical line), and the baseline cross-over point (bold black cross). When only one baseline (red line) is apparent, the approach and retraction curve baselines overlap. Shown for the retraction curve only are the point of maximum cantilever deflection (bold black cross), and the gradient line of loading (solid black line). The values of calculated parameters are printed in the legend of each graph, stating the values for: point ID, force [N], energy [J], SD of both the approach and retraction curves [N], and the loading gradient [N/s]. The title of each graph states the file name of the corresponding data point.

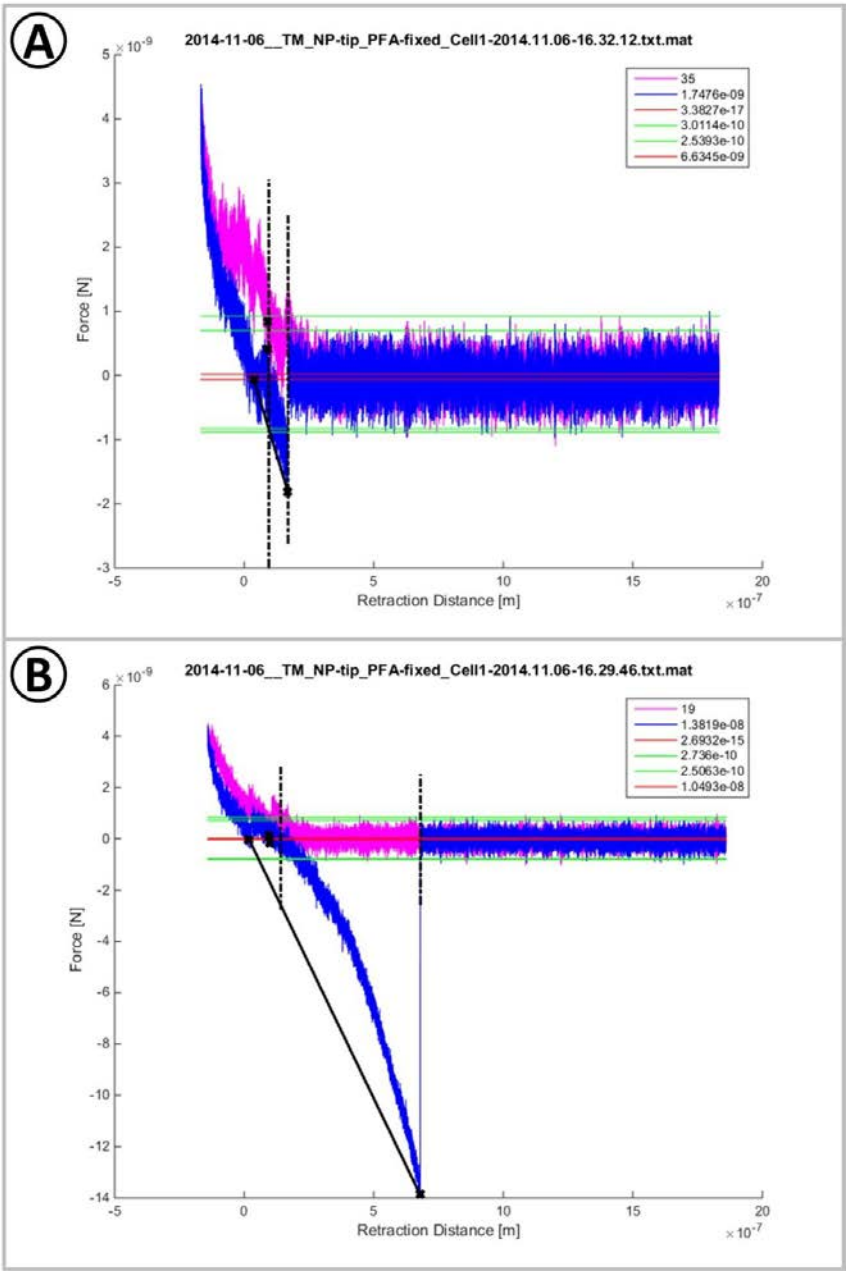

Figure 36 – Points of Interest – Indeces 35 and 19

Shown are the points of interest with indeces 35, and 19, in (A), and (B), respectively; as identified in the example overview map shown in Figure 34. As detailed in Figure 35, images show the baseline value (red line) ± 3 SDs (green lines), the baseline cut-off point (black dotted vertical line), and the baseline cross-over point (bold black cross), for both the approach and retraction curves, and the point of maximum cantilever deflection (bold black cross), and the gradient line of loading (solid black line), for the retraction curve only. The values of calculated parameters are printed in the legend of each graph, from top to bottom stating the values for: point ID, force [N], energy [J], SD of both the approach and retraction curves [N], and the loading gradient [N/s]. The title of each graph states the file name of the corresponding data point.

5.5 Effects of Fixation

Fixation was used in the preparation of cell samples for interrogation via AFM. As previously discussed, the final application of the technique is in the interrogation of tissue sections. Therefore, the cell samples used in the testing and characterisation of the AFM technique needed to be prepared using sample preparation techniques that could also be applied to tissue sections.

Fixatives that are routinely used in the preparation of biological samples are acetone and formaldehyde (FA), where acetone is commonly used for fixation of tissue sections, and FA is used for fixation of cells in solution.

Under standard ambient temperature and pressure FA (HCHO) is a gas, but it readily dissolves in water, and is typically kept as a 40 % (by weight) aqueous solution; which is called formalin. In aqueous solution, FA reacts with water to form methylene hydrate ($HO\text{-}CH_2\text{-}OH$), which over time can react together to form precipitates of paraformaldehyde ($OH(CH_2O)_nH$). This process of polymerisation is inhibited in commercially available solutions through the addition of methanol. Due to the slow degradation of formalin, freshly prepared solutions should be used for optimal results.

When applied to biological samples, the aldehyde groups form a $\text{-}CH_2\text{-}$ cross link between the nitrogen, and other constituent atoms, of proteins. The formation of this so called methylene bridge constitutes the fixative action of formaldehyde, which creates an insoluble matrix of cross-linked proteins that traps other substances such as carbohydrates, and lipids that remain chemically unchanged unless exposed to formaldehyde for weeks.[88,89]

Due to the water based nature of the FA fixative, the sample does not experience any dehydration, or shrinkage due to dehydration.

Acetone (CH_3COCH_3 or $H_3CC(=O)CH_3$) is an organic solvent, whose mode of action lies in the physical chemistry, and is comparable to that of alcohols. In solution, acetone interferes with the hydration cloud of charged proteins that keeps them soluble, causing them to precipitate, and it is furthermore a good solvent for lipids; removing exposed lipid components that are not tightly bound.[90] Acetone must be used cold (0-4°C)[91], as acetone that is used at room temperature can unravel the tertiary structure of proteins that depends on hydrogen bonding. Much like alcohols, acetone is a dehydrating agent, and as such can cause shrinkage of samples.[90,91]

The following experiments were conducted to determine the effects of the different fixatives on samples prepared from cultured cells, and what the effect of the introduced conformational changes are on subsequent AFM adhesion measurements.

In the following experiments, cell samples were prepared as previously described in §5.2.1 (p.89), and subsequently either: fixed using acetone, fixed using 10 % formalin, or left unfixed.

Cells from each of the different sample preparations were then interrogated via AFM, using three different cantilever modifications. The chemical modifications of the used cantilevers were equivalent to those of CS-NH_2, CS-COOH, and CS-NP.

5.5.1 Cell Elasticity

Computationally, the extraction of elasticity values from AFM force-displacement data is not as trivial as the extraction of force and energy values that has been described in §5.4 (p.91), but it is equally readily accessible. Commercial AFM systems are provided with analysis software containing a range of built-in deformation models that can be applied to experimental data. The process for quantifying cell elasticity that has been employed, and its underlying principles, is discussed in detail in Appendix 8.19. In short, measurements of the applied load and the resulting depth of penetration of the indenter into the specimen are used to inform a Hertzian contact mechanics model; shown in Equation 5 below.

$$F = \frac{E}{1-\nu^2}\frac{4\sqrt{R_c}}{3}{h_t}^{3/2}$$

Where:

F	=	applied load	[N]
E	=	Young's modulus	[Pa]
ν	=	Poisson's ratio	
R_C	=	radius of curvature of the indenter tip	[m]
h_t		depth of penetration	[m]

Equation 5 – Hertzian Model of Deformation for Determination of Specimen Elasticity

The employed Hertzian model of deformation shows the relationship of the applied load F, the depth of penetration of the indenter into the specimen h, the Poisson's ratio ν and the Young's modulus E of the specimen, and the radius of curvature of the tip of the indenter R_C. F and h are experimentally determined values, ν and R_C are assumed to be prior knowledge and appropriate values are specified for use in the model. A value of E that produces the least discrepancy between the model and experimental data is subsequently determined through computational means

As is shown on the example curve in Figure 37, the model of deformation is fitted to the approach curve. Shortly after initial contact the model fit starts to deviate from the experimental data. The indentation and deformation associated with the tip-sample

contact only adheres to the assumption of purely elastic deformations during the application of very small forces, and is primarily governed by visco-elastic behaviour. Another indication that the deformation of the specimen is not purely elastic is the difference between the approach and retraction curves. If only purely elastic deformations were occurring, and in the absence of adhesion hyteresis, the approach and retraction curves should be identical. Rarely desirable plastic deformations can occur during the application of larger forces.

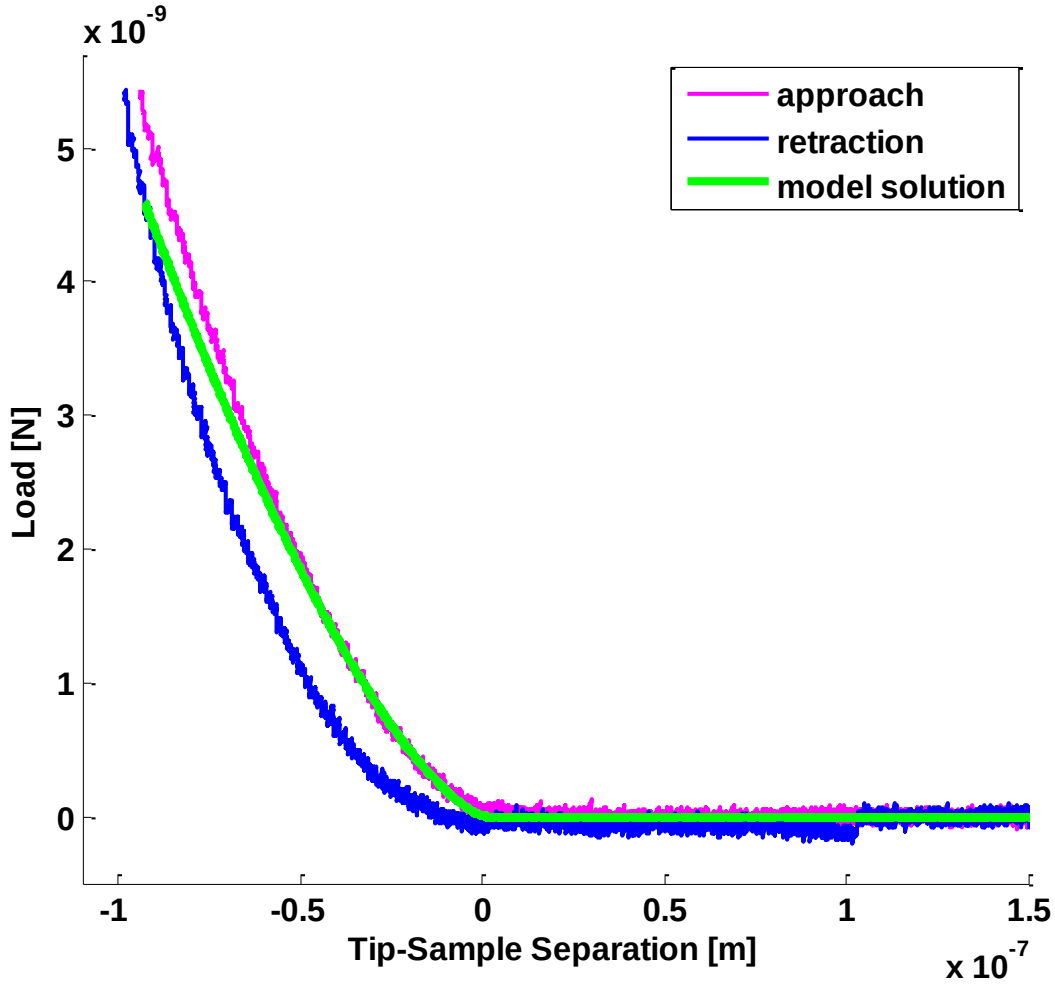

Figure 37 – Determination of Cell Elasticities

Example of force-displacement data, showing the approach curve in magenta, and the retraction curve in blue. The green curve shows the fitting of the deformation model (presented in Equation 5) that is fitted to the approach curve. The model fit starts to deviate from the experimental data shortly after initial contact. The RMS value (assessing the goodness of the model fit to the experimental data) for this representative data point is 35.69 pN.

While it is acknowledged that research into determining optimal experimental parameters for measurements of cell elasticities [92-94], as well as furthering the accuracy of accompanying mathematical models [92-96], is active and ongoing, the already available means were deemed sufficient. Given that the experimental conditions are the same throughout the investigation, a comparative assessment of the effect of the different fixatives on the samples can be made.

The cell elasticities were determined using the Hertzian deformation model shown in Equation 5, using the assumption of a paraboloid tip shape with a radius of curvature of the tip of 35 nm (R_C = 35 nm), and a specimen Poisson's ratio of 0.5 (ν = 0.5). The obtained elasticity values are given as Young's modulus, which describes the relationship between the linearly elastic deformations of a material proportional to the force per unit area that is applied to it.

5.5.1.1 Cell Elasticity Results

The results shown in Figure 38 were collected by interrogating hybridoma cells from all of the different sample preparations with each of the different cantilever modifications. Cells that were left unfixed, or were fixed using acetone or formalin, are shown in blue, red, and green respectively, with different shadings of the colours marking the different cantilever modifications.

Figure 38 shows that clear differences are discernible between the cells' Young's moduli as a result of acetone or formalin fixation, where the Young's moduli determined for samples prepared using acetone fixation are an order of magnitude greater than what is observed for samples prepared using formalin fixation.

The results that were obtained for cells left unfixed varied widely, with differences in Young's moduli for individual cells of up to three orders of magnitude.

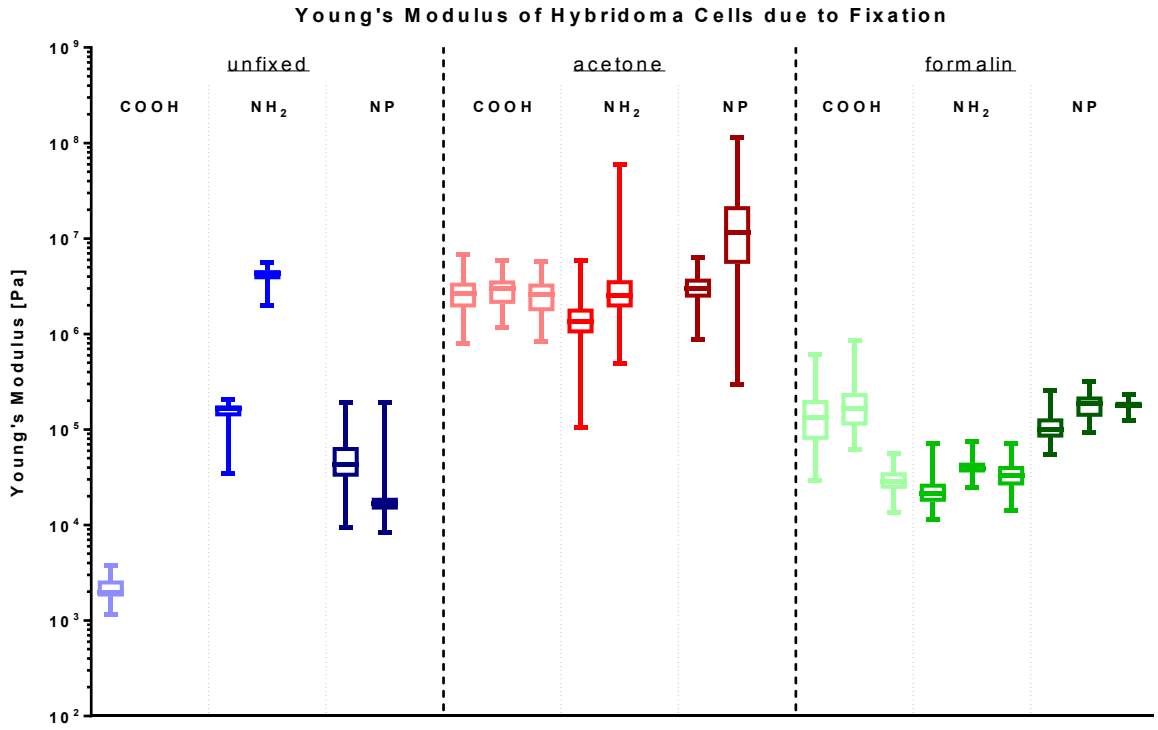

Figure 38 – Young's Modulus of Hybridoma Cells due to Fixation

Cells from each of the different sample preparations were interrogated using each of the different cantilever modifications; showing unfixed cells, and cells that were fixed using acetone or formalin, in blue, red, and green respectively. Different shadings of the colours mark the different cantilever modifications, showing COOH, NH_2, and NP functionalised cantilevers with light, intermediate, and dark shades respectively. Boxes show 25th percentile, median, and 75th percentile, and whiskers show the minimum and maximum values. Each box and whiskers plot represents one cell, and comprises data from 100 indentations.

To assess the differences between the different sample preparations, data were grouped for cells that were prepared under the same conditions. Although differences within the groups can be observed, the different cantilever modifications are considered to have no impact on the determined Young's moduli, as the indentation behaviour of the cantilevers should not be altered. The results are shown in Figure 39.

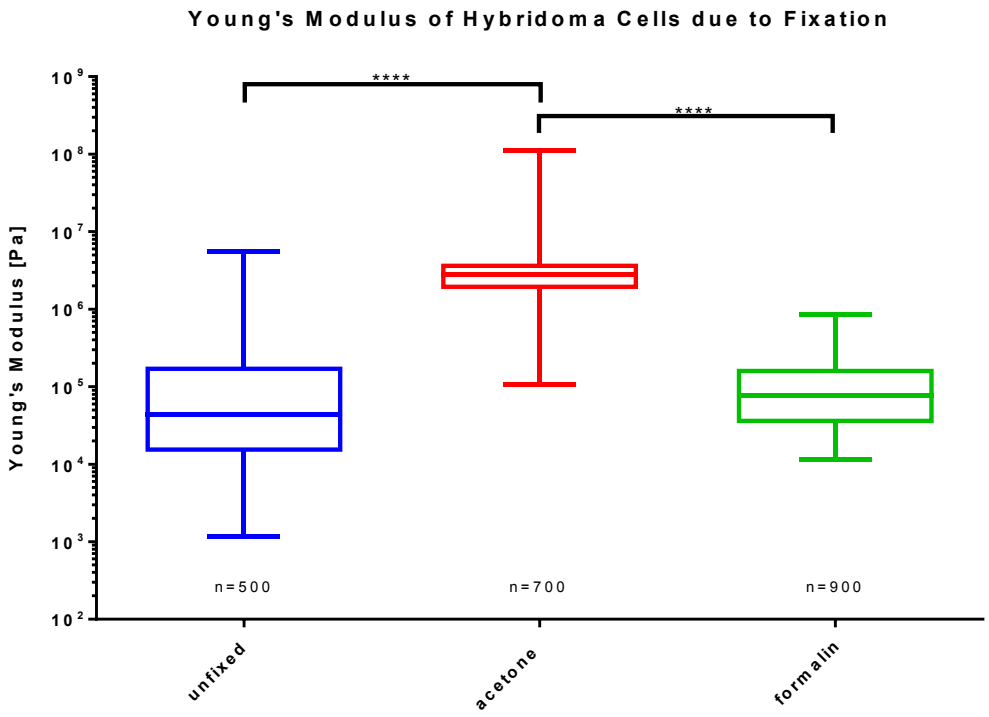

Figure 39 – Young's Modulus of Hybridoma Cells Grouped by Sample Preparation

Based on the assumption that the different cantilever modifications do not impact the indentation behaviour of the cantilevers, the data from Figure 38 were grouped for cells prepared under the same conditions. Boxes show 25th percentile, median, and 75th percentile, and whiskers show the minimum and maximum values. Results show that the differences in Young's modulus, due to different sample preparation, are highly significant ($p<0.0001$).

The results in Figure 39 show the previously identified difference in Young's moduli for cells prepared using acetone fixation and cells prepared using formalin fixation to be highly significant ($p<0.0001$), with the mean values for cells fixed in acetone ($4.96 * 10^6$ Pa) being approximately 50 times larger than those for cells fixed in formalin ($1.07 * 10^5$ Pa).

A likely source for the differences in Young's modulus is the different mode of action of the two used fixatives that has previously been highlighted in §5.5 (p.101). Acetone is a dehydrating agent, where the dehydration effects, and the thereby incurred shrinkage of the sample, are likely the cause for the observed increase in

Young's modulus. Samples fixed using formalin do not experience dehydration due to the water based nature of the fixative, and the shape of cells is to a greater extent preserved through the matrix of cross-linked membrane proteins that traps the constituent components of the cell.

Statistical assessment of the grouped data in Figure 39 further revealed the difference in Young's modulus between cells left unfixed and cells subjected to fixation to also be highly significant ($p<0.0001$). However, the results that were obtained for cells left unfixed were highly variable (Figure 38, p.106), ranging from values comparable to cells subjected to acetone fixation, to several orders of magnitude below what was determined for cells subjected to formalin fixation. Consequently, due to the great variability of the results obtained for unfixed cells, the significance of the difference between unfixed cells and fixed cells is acknowledged with reservations. Because, while it is expected that fixed cells produce significantly different behaviour due to conformational changes as a results of fixation, the here obtained results for unfixed cells are not seen as representative.

The great variability in the results obtained for unfixed cells is likely due to the cells remaining more susceptible to environmental conditions. As previously discussed in §5.2 (p.87), sample preparation, and interrogation of samples, needed to be conducted in separate facilities. This exposed sample cells to deterioration and death during short term storage as well as transport between facilities.

Further, the continued ability of live cells to respond to environmental stimuli means that cells may be adversely affected by interrogation itself, where the repeated application of compressive forces may cause apoptosis.[97]

In a similar experiment, isolated primary murine B cells were used instead of hybridoma cells, which were again either left unfixed, fixed using acetone, or fixed using formalin. In this experiment samples were interrogated using only a NP functionalised cantilever. The data is presented in Figure 40, and again shows the determined Young's moduli for cells that were left unfixed, and cells that were fixed in acetone, or fixed in formalin, in blue, red, and green respectively.

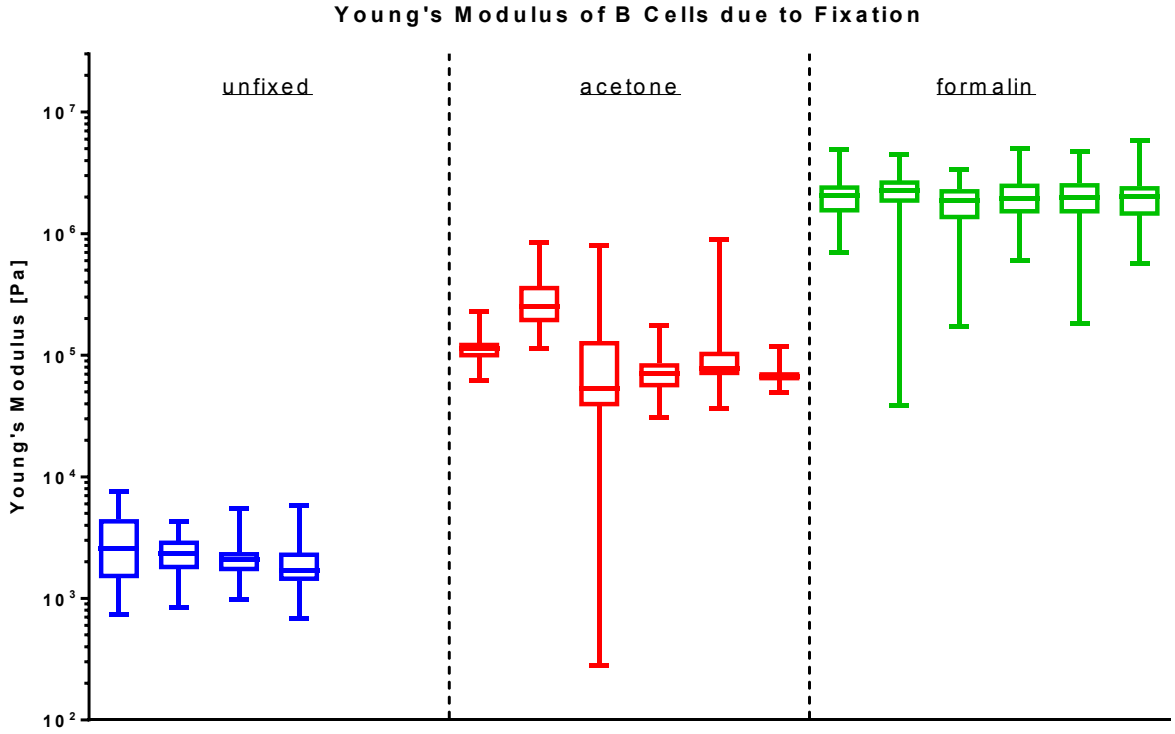

Figure 40 – Young's Modulus of B Cells due to Fixation

Samples from isolated primary murine B cells were prepared using the different preparation methods, showing unfixed cells, and cells that were fixed in acetone, or fixed in formalin, in blue, red, and green respectively. Boxes show 25th percentile, median, and 75th percentile, and whiskers show the minimum and maximum values. Each box and whiskers plot represents one cell, and comprises data from 100 indentations.

The results presented in Figure 40 show clear differences between the Young's moduli in response to the different preparation methods, where the results obtained for each of the different preparation methods show good consistency.

The Young's moduli determined for cells prepared using formalin fixation are an order of magnitude greater than what is observed for cells prepared using acetone fixation; which is the converse behaviour of what was previously observed for hybridoma cells.

The results obtained for cells left unfixed are much less variable than what was previously observed for hybridoma cells, with Young's moduli distinctly below what is observed for cells subjected to acetone fixation.

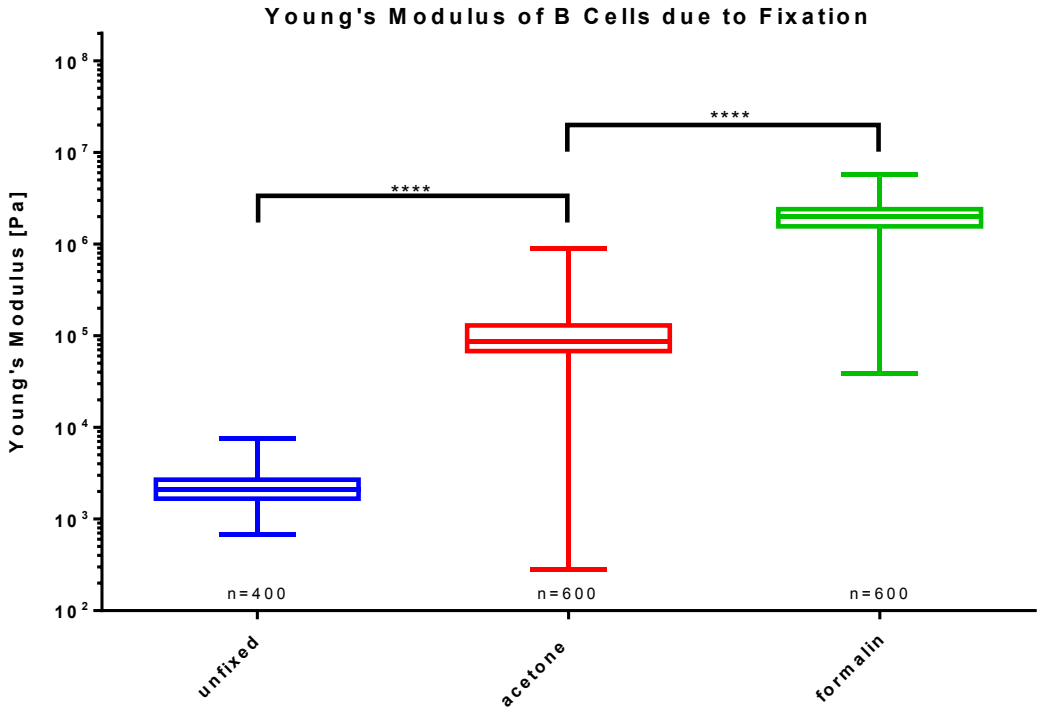

Figure 41 – Young's Modulus of B Cells Grouped by Sample Preparation

The data from Figure 40 were grouped for cells prepared under the same conditions, showing unfixed cells, and cells fixed using acetone, or fixed using formalin, in blue, red, and green respectively. Boxes show 25th percentile, median, and 75th percentile, and whiskers show the minimum and maximum values. Results show that the differences in Young's modulus due to different preparation methods are highly significant ($p<0.0001$).

To again assess the differences between the different preparations, data were grouped for cells prepared under the same conditions, and the results are shown in Figure 41.

The results in Figure 41 show the differences between the different sample preparations to be highly significant ($p<0.0001$). The mean Young's modulus for unfixed cells ($2.42 * 10^3$ Pa) is two orders of magnitude smaller than what was determined for cells subjected to acetone fixation ($1.30 * 10^5$ Pa); and the highest Young's moduli were determined for cells subjected to formalin fixation ($2.06 * 10^6$ Pa), which were an order of magnitude greater even than what was observed for cells subjected to acetone fixation.

In this experiment, the results obtained for unfixed cells showed less variability than what was previously observed for hybridoma cells, and can with increased confidence be viewed as representative of unfixed cells. Unfixed cells were determined to have a distinctly lower Young's modulus than cells subjected to fixation, where conformational changes due to fixation are the likely cause of the increased Young's modulus of fixed cells.

The difference in Young's modulus of cells fixed in acetone compared to cells fixed in formalin is comparable in magnitude to the difference that was observed for hybridoma cells, but is the converse in behaviour. Compared to cells fixed in acetone, the Young's moduli for B cells fixed in formalin is an order of magnitude greater, whereas it is an order of magnitude lower for hybridoma cells fixed in formalin. In both experiments only little variability was observed in the results for fixed cells, therefore the observed difference in behaviour of the two different cell types is not

likely due to measurement artefacts, but rather because the two different cell types react differently to the different sample preparation methods.

While for both cell types the observed differences in Young's modulus are up to two orders of magnitude, the obtained values are in keeping with results reported in the literature. Isolated unfixed cells under compression in AFM experiments exhibited Young's moduli of 3.2 ± 0.5 kPa [98], 3.3 ± 0.2 kPa [99], 1.14 ± 0.32 kPa [100], and 1.2 ± 1.25 kPa [101], which compare well to the 2.42 ± 1.31 kPa obtained for unfixed isolated B cells presented in Figure 41 (p.110) above.

Cell elasticity values for cells subjected to fixation are a lot more sparse in the literature, but formalin fixation has been reported to substantially increase the Young's modulus of cells. Lulevich, *et al.*, [102], reports Young's modulus values of 10 – 35 MPa for cells subjected to formalin fixation, which is an order of magnitude greater than the results for formalin fixed hybridomas (107 ± 95.7 kPa) presented in Figure 39 (p.107), but is in good agreement with the results for formalin fixed B cells (2.06 ± 0.825 MPa) presented in Figure 41 (p.110). The stated reason for the substantial increase in Young's modulus is the formation of covalent imine bonds through the reaction of aldehyde groups with primary amines in membrane and cytoskeletal proteins [88,89]; as was postulated with the description of the mode of action of the formalin fixative in §5.5 (p.101).

The mode of action is also the principal determinant for the elasticities displayed by cells fixed in acetone. Besides the removal of loosely bound lipids to expose protein targets, and its dehydrating effects, acetone also permeabilises the cell membrane [103]. That means that the inner fluid in cells can no longer transduce the compression

pressure homogeneously, which means that the compression mechanics of permeabilised cells are dictated by the compression of the cell interior rather than that of the cell membrane.[102] Young's modulus values for permeabilised cells are reported at 150-230 kPa [102], which are an order of magnitude lower than the results for acetone fixed hybridomas (4.96 ± 10.1 MPa) presented in Figure 39 (p.107), but in good agreement with the results for acetone fixed B cells (130 ± 127 kPa) presented in Figure 41 (p.110).

The differences in response of the two cell types to the different fixatives are likely due to their structural differences, which is discussed in more detail in §5.6 (p.125).

5.5.2 Frequency of Interactions

The results presented next were produced from further analysis of the data obtained in the aforementioned interrogation of the hybridoma cells using three differently functionalised AFM cantilevers.

Each cell that was measured, was first interrogated using a relative set point (RS) of 1 nN, and subsequently, on the same grid of point interrogations, using a RS of 10 nN. As described with Figure 8 in §3.1.1 (p. 18), the RS is the pre-specified compressive force with which the cantilever is pushed into the sample before contact with the sample is considered to have been achieved, and cantilever retraction is begun.

First, the effects of fixation on event selection were assessed. Shown in Figure 42 is the percentage of point interrogations that were classed as positive adhesion events,

out of all point interrogations made; showing, separately, values for interrogations made using RSs of 1 nN (RS-1), and 10 nN (RS-10). Cells that were left unfixed, fixed using acetone, or fixed using formalin, are shown in blue, red, and green respectively, with different shadings of the colours marking the different cantilever modifications.

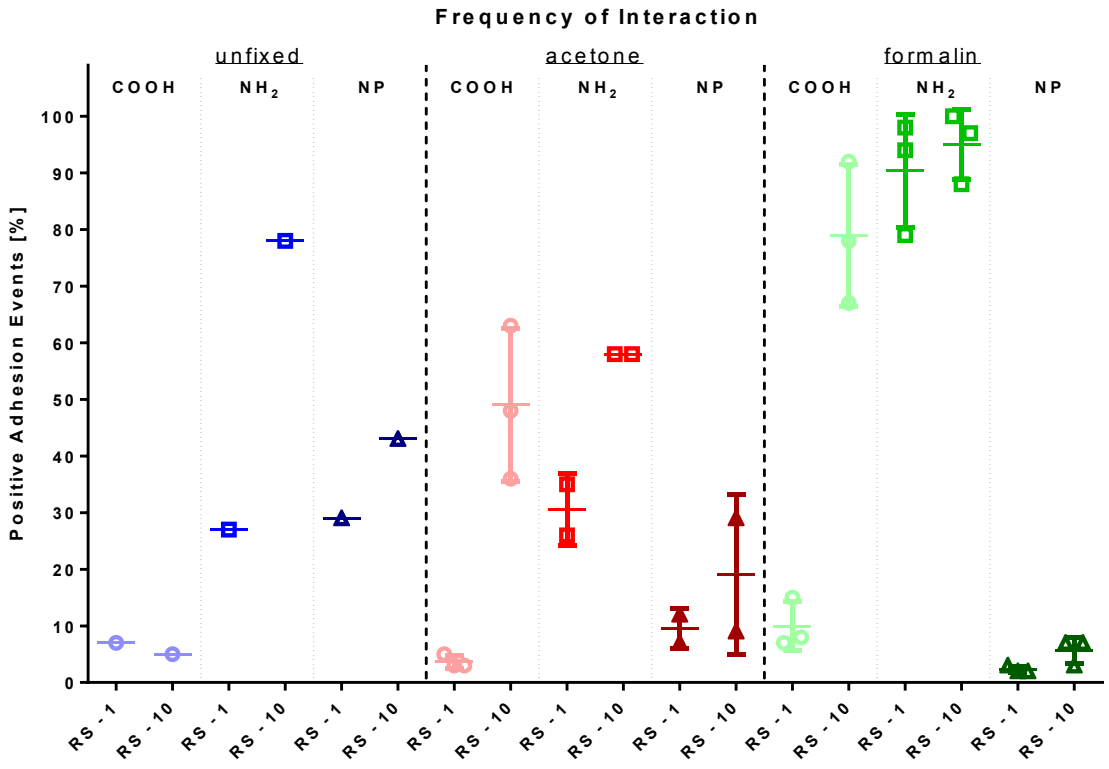

Figure 42 – Frequency of Interaction

Cells from each of the different sample preparations were interrogated using each of the different cantilever modifications; showing unfixed cells, cells fixed using acetone, and cells fixed in formalin, in blue, red, and green, respectively. Different shadings of the colours mark the different cantilever modifications; showing COOH, NH_2, and NP functionalised cantilevers with light, intermediate, and dark shades, respectively. Cells were interrogated using RSs of 1 nN (RS-1) and 10 nN (RS-10). Results for all different experimental conditions show the percentage of point interrogations classed as positive adhesion events from all point interrogations made; where every marker represents the results for one cell.

The results presented in Figure 42 show that the highest rates of positive adhesion events are produced for interrogations made using the NH_2 equipped cantilever.

Using this cantilever, similar results are produced for unfixed cells (RS-1: 27 %, RS-10: 78 %) and cells fixed in acetone (RS-1: 30.5 %, RS-10: 58 %), however, a much higher frequency of positive adhesion events is produced in interrogation of cells fixed in formalin (RS-1: 90.3 %, RS-10: 95 %).

The results obtained from interrogations using the COOH equipped cantilever are similar for the different sample preparations at low indentation forces, with 7 %, 3.7 %, and 10 % at RS-1 for unfixed cells, cells fixed in acetone, and cells fixed in formalin, respectively. At higher indentation forces, however, for the same samples, the results differ distinctly, with 5 %, 49 %, and 79 % at RS-10, respectively.

For samples interrogated with the NP equipped cantilever, the differences between interrogations with smaller (RS-1) and greater (RS-10) forces of indentation are not as pronounced, where the highest rates of positive adhesion events are observed for unfixed cells (RS-1: 29 %, RS-10: 43 %), followed by cells fixed in acetone (RS-1: 9.5 %, RS-10: 19 %), and the lowest rates are observed for cells fixed in formalin (RS-1: 2.3 %, RS-10: 5.7 %)

A trend that is observed for all pairings of sample preparation and cantilever modification (except only unfixed cells interrogated with the COOH equipped cantilever) is that higher rates of positive adhesion events are produced for interrogations using higher forces of indentation (RS-1<RS-10). This behaviour can be expected, as with higher forces of indentation the surface area of contact between the cantilever tip and the sample is increased, thus increasing the probability of molecular interactions occurring.

When using the specific NP equipped cantilever, the number of interactions occurring is greater for unfixed cells compared to cells subjected to fixation. A likely cause for that behaviour is the freedom of movement of the targeted B cell receptors (BCRs). Conformational changes of the cells, introduced through fixation, could reduce the freedom of movement of the BCR, hence reducing the probability that the BCR can successfully bind the NP antigen. The results presented in Figure 42 suggest that this effect is more pronounced for cells fixed in formalin, as compared to cells fixed in acetone. The conformational changes introduced through fixation are, however, not limited to altering cell elasticity. As discussed in the introduction of the modes of action of the different fixatives in §5.5 (p.101), formalin covalently cross-links cell surface proteins and may interfere with the targeted receptors, and acetone can unravel the tertiary structure of proteins, which would leave the targeted receptors non-functional. These possible hindrances to successfully measuring receptor binding are discussed in more detail in §5.6 (p.125).

Conformational changes introduced through fixation are likely also the reason for the differing behaviours in response to interrogation with the COOH and NH_2 equipped cantilevers. Based on the results in Figure 42, the effects of acetone fixation are less influential, causing only a small increase in the number of unspecific interactions when probed with the COOH equipped cantilever, whereas formalin fixation yields distinct increases in the number of unspecific interactions for interrogations with both the COOH and NH_2 cantilevers.

5.5.3 Magnitude of Interactions

The following section examines in more detail the point interrogations that were identified as positive adhesion events. Specifically, the magnitudes of the forces and energies associated with these events were inspected.

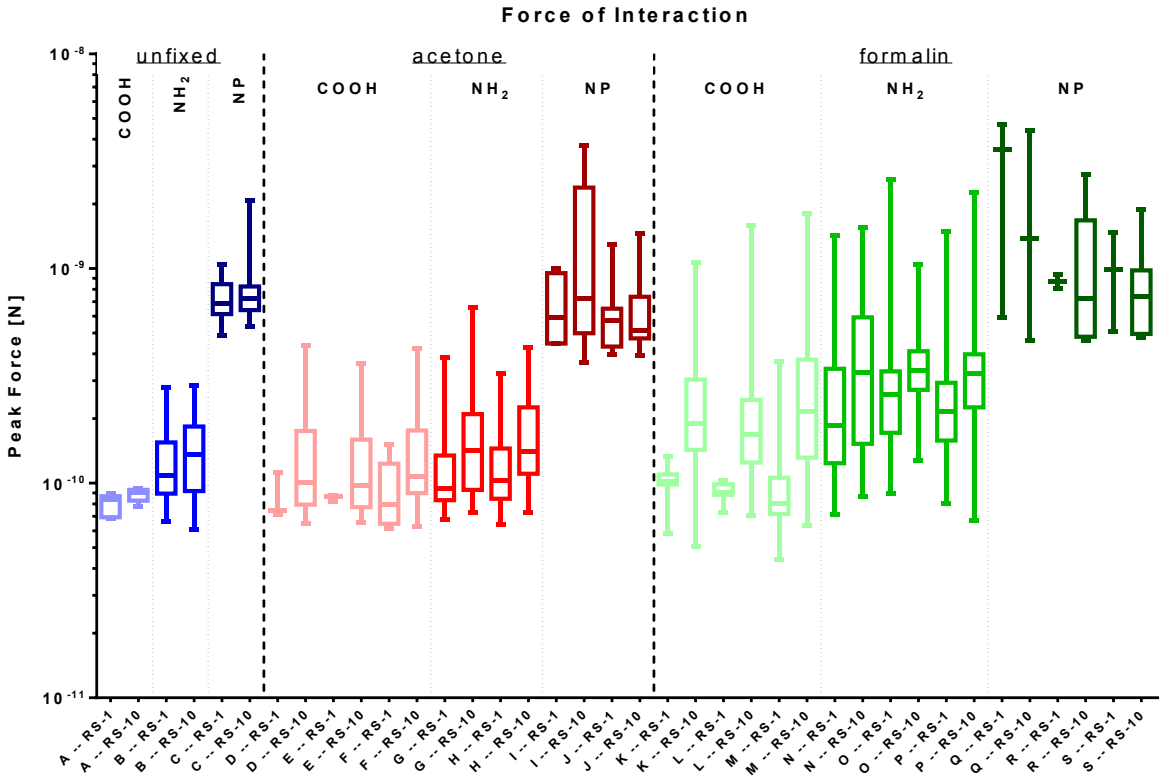

Figure 43 – Force of Interaction

Individual cells (denoted by letters) from each of the different sample preparations were interrogated using RSs of 1 nN (RS-1) and 10 nN (RS-10). Unfixed cells, cells fixed in acetone, and cells fixed in formalin are shown in blue, red, and green, respectively. Different shadings of the colours mark the different cantilever modifications; showing COOH, NH_2, and NP functionalised cantilevers with light, intermediate, and dark shades, respectively. Boxes show 25th percentile, median, and 75th percentile, and whiskers show the minimum and maximum values. Results show the peak forces associated with positive adhesion events only.

Shown in Figure 43 are the peak forces that were measured for individual cells from the different sample preparations, showing separately results for interrogations with low (RS-1), and greater (RS-10), forces of indentation. Cells from the different

sample preparations are shown in different colours, where different shadings within mark the different cantilever modifications with which they were interrogated.

The results shown in Figure 43 reveal there to be an order of magnitude difference between adhesion events detected when using the non-specific cantilevers equipped with COOH, or NH_2, functional groups, compared to cantilevers equipped with the BCR specific NP. For unfixed cells, and cells fixed in acetone, the separation between specific and non-specific adhesion events is distinct, whereas for cells fixed in formalin the separation is not as clear, as a greater variation in the obtained results is observed.

Differences in forces for interrogations conducted with different forces of indentation were determined to be mostly non-significant. Significant differences were determined to be no greater than $1.01 * 10^{-10}$ N, and as low as $5.07 * 10^{-11}$ N, and were found only for cells G*, H**, K*, M**, N*, P**; which are all interrogations conducted with non-specific cantilever modifications.

While the differences between interrogations conducted with different forces of indentation were significant for some cells, the absolute differences were deemed small enough for the data to be considered similar. In order to assess the differences between the different sample preparations, similar data were grouped. This is shown in Figure 44.

The results in Figure 44 show the differences between the different sample preparations to be significant. The peak forces associated with non-specific adhesion events measured on unfixed cells (COOH: $8.36 * 10^{-11}$ N; NH_2: $1.39 * 10^{-10}$ N) and

cells fixed in acetone (COOH: $1.34 * 10^{-10}$ N; NH_2: $1.56 * 10^{-10}$ N) are comparable. The differences between the two non-specific cantilever modifications are significant (unfixed: p=0.0019; acetone: p=0.0174), where the greater peak forces are produced when using the NH_2 equipped cantilever.

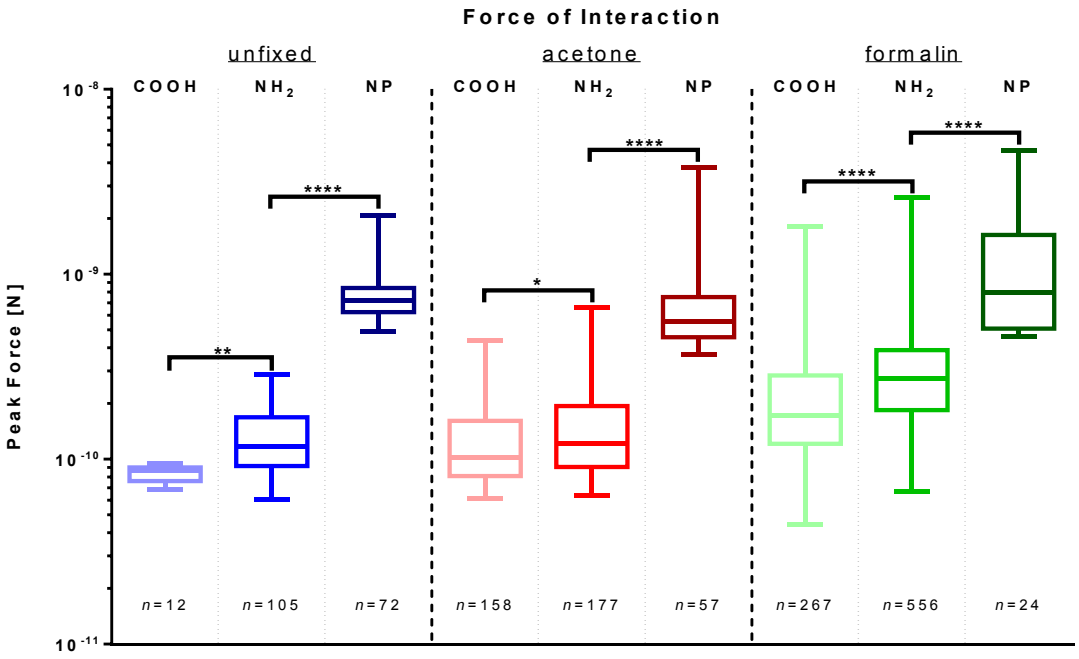

Figure 44 – Statistical Differences in Forces of Interaction

The data from Figure 43 were grouped for similar samples, showing peak forces associated with positive adhesion events only. The number of positive adhesion events contained in each box and whiskers plot is given by *n*. Cells left unfixed, fixed in acetone, and fixed in formalin, are shown in blue, red, and green, respectively. Different shadings of the colours mark the different cantilever modifications; showing COOH, NH_2, and NP functionalised cantilevers with light, intermediate, and dark shades, respectively. Boxes show 25th percentile, median, and 75th percentile, and whiskers show the minimum and maximum values. Differences between non-specific (COOH, NH_2) and specific (NP) adhesion events are highly significant (p<0.0001).

The peak forces associated with non-specific adhesion events measured on cells fixed in formalin (COOH: $2.40 * 10^{-10}$ N; NH_2: $3.35 * 10^{-10}$ N) are greater compared to the other two sample preparations, where the difference between the two

cantilever modifications is determined to be highly significant ($p<0.0001$), and the greater peak forces are again produced when using the NH_2 equipped cantilever.

The peak forces associated with specific adhesion events (unfixed: $7.54 * 10^{-10}$ N; acetone: $7.41 * 10^{-10}$ N; formalin: $1.35 * 10^{-9}$ N) are distinctly greater than what is observed for the non-specific adhesion events. The forces produced using the NP equipped cantilever are 5.4, 4.7, and 4.0 times greater than forces produced using the NH_2 equipped cantilever for unfixed cells, cells fixed in acetone, and cells fixed in formalin, respectively, and these differences were determined to be highly significant ($p<0.0001$).

Shown in Figure 45 are the energies associated with the positive adhesion events for which the forces were inspected in Figure 43. As before, the graph shows data for individual cells from the different sample preparations, showing separately results for interrogations with low (RS-1), and greater (RS-10), forces of indentation. Cells from different sample preparations are shown in separate colours, where different shadings within mark the different cantilever modifications with which they were interrogated.

The results in Figure 45 show that the differences between the different cantilever modifications and different sample preparations are not as distinct as previously seen in Figure 43.

For unfixed cells, and cells fixed in acetone, there is still a discernible difference between energies measured using the non-specific cantilevers equipped with COOH, or NH_2, functional groups, compared to when using the BCR specific cantilever

equipped with NP. For cells fixed in formalin, however, greater variability of the results is observed, which prevents such distinctions.

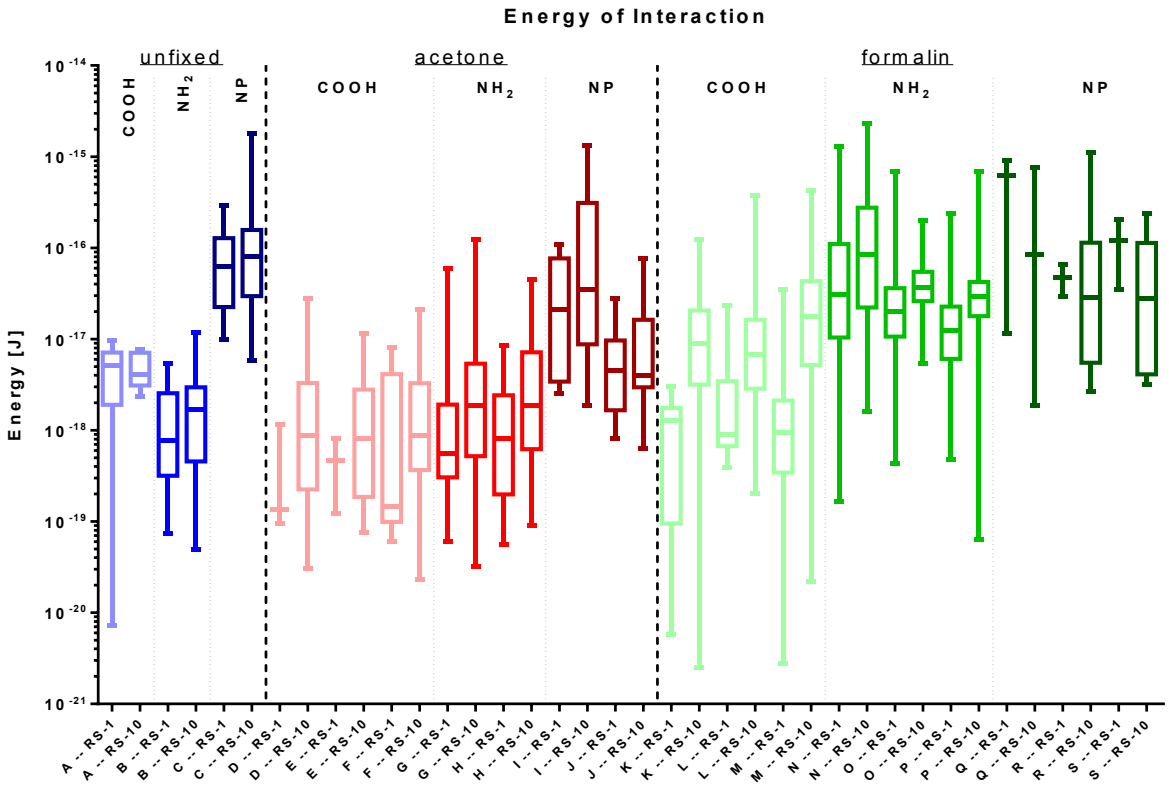

Figure 45 – Energy of Interaction

Individual cells (denoted by letters) from each of the different sample preparations were interrogated using RSs of 1 nN (RS-1) and 10 nN (RS-10). Unfixed cells, cells fixed in acetone, and cells fixed in formalin are shown in blue, red, and green, respectively; where light, intermediate, and dark shades represent COOH, NH_2, and NP equipped cantilevers, respectively. Boxes show 25th percentile, median, and 75th percentile, and whiskers show the minimum and maximum values. Results show the energies associated with positive adhesion events only.

Differences in the magnitudes of the energies produced in interrogations conducted with different forces of indentation were again determined to be mostly non-significant; where significant differences were determined only for cells H*, M*, P**. As before, data for these cells represent interrogations conducted with non-specific cantilever modifications, and their absolute differences are considered small enough for the data to be considered similar.

To assess the differences between the different sample preparations, similar data were again grouped, despite significant differences having been determined for the three aforementioned samples; the results are presented in Figure 46.

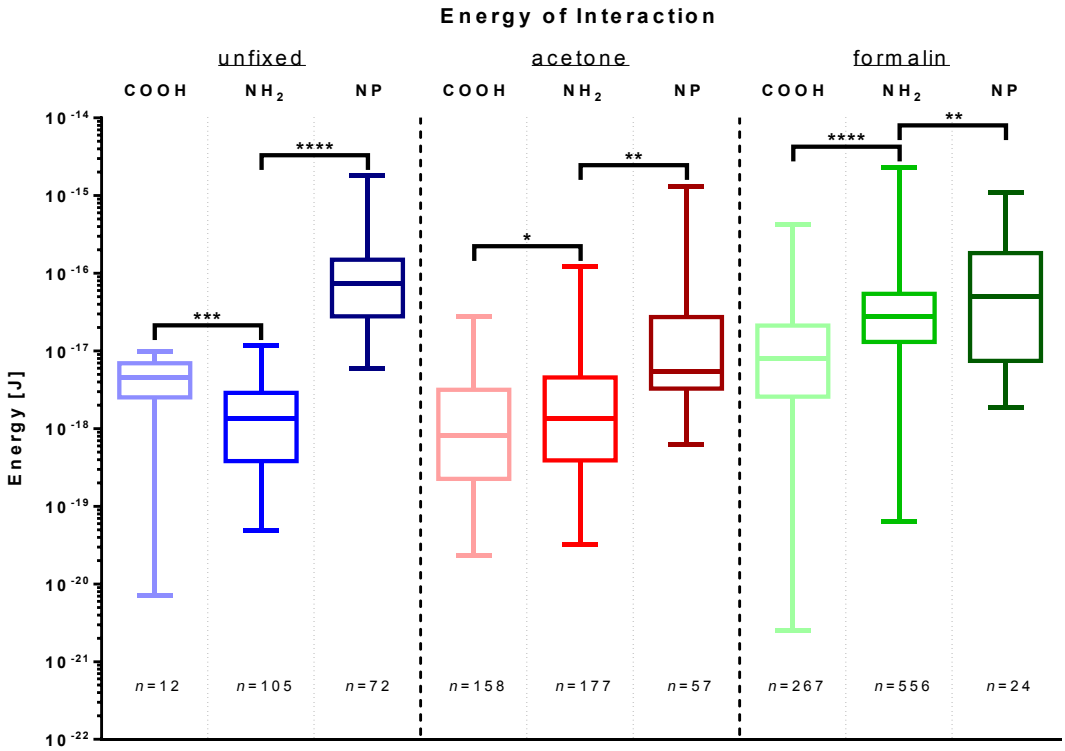

Figure 46 – Statistical Differences in Energies of Interaction

The data from Figure 45 were grouped for similar samples, showing energies associated with positive adhesion events only. The number of positive adhesion events contained in each box and whiskers plot is given by *n*. Unfixed cells, cells fixed in acetone, and cells fixed in formalin are shown in blue, red, and green, respectively. Different shadings of the colours mark the different cantilever modifications; showing COOH, NH_2, and NP equipped cantilevers with light, intermediate, and dark shades, respectively. Boxes show 25th percentile, median, and 75th percentile, and whiskers show the minimum and maximum values.

The results presented in Figure 46 show the differences between the different sample preparations to be significant. The most distinct differences are observed for unfixed cells, where the energies associated with specific adhesion events (NP: $1.21 * 10^{-16}$ J) are up to two orders of magnitude greater than non-specific adhesion events

(COOH: $4.75 * 10^{-18}$ J; NH_2: $2.04 * 10^{-18}$ J); a difference that was determined to be highly significant ($p<0.0001$).

While it remains significant (acetone: $p=0.0014$; formalin: $p=0.0011$), the difference between specific and non-specific adhesion events for fixed cells diminishes as the variability of the obtained results increases.

The differences between the two non-specific cantilever modifications are again determined to be significant for all sample preparations (unfixed: $p=0.0001$ acetone: $p=0.0014$; formalin: $p=0.0011$), where the greater energy values are produced when using the NH_2 equipped cantilever in interrogation of fixed samples, and when using the COOH equipped cantilever in interrogation of unfixed samples.

Overall, the results obtained for cells fixed in formalin suggest that formalin fixation promotes the occurrence of non-specific adhesion events; producing the highest number of events when interrogated with the non-specific COOH, or NH_2, cantilever modifications out of all tested sample preparations, and the corresponding magnitudes of these events exhibit the greatest variability. A likely cause for the increased variability may be that multiple molecular interactions are occurring during individual tip-sample contacts, which increases the range of detectable values, and would be concurrent with an overall increased probability of events occurring for cells fixed in formalin. This hypothesis is further supported by both force and energy values associated with non-specific adhesion events being consistently greater for measurements conducted with greater forces of indentation, even though these differences were determined to be significant only in isolated instances.

More importantly, interrogations of samples fixed in formalin produce the lowest number of specific adhesion events out of all tested sample preparations. A likely cause for this behaviour is the mode of action of the formalin fixative that, as described in §5.5. (p.101), cross-links proteins by forming methylene bridges between constituent atoms of said proteins. This interaction with surface proteins is likely to also introduce conformational changes in the targeted BCRs, preventing successful binding to NP on the probe.

Conversely, the results obtained for cells fixed in acetone suggest that acetone fixation is preferable for preparation of samples for interrogation in AFM adhesion experiments. The interaction behaviour that is produced more closely resembles that of unfixed cells, with a smaller increase in the number of unspecific adhesion events, and a smaller reduction in the number of specific adhesion events. A distinct separation between specific and non-specific adhesion events is maintained, and results for both exhibit greater consistency.

As for formalin, acetone causes conformational changes on the sample as part of its fixative action. As described previously in §5.5. (p.101), this can include unravelling of the tertiary structure of proteins through disruption of constituent H-bonds, and may be a likely cause for the reduction in specific adhesion events that is observed for samples fixed in acetone. However, acetone also aids in exposing protein targets by dissolving lipids [90], which may be the reason for the reduction in the number of specific events being smaller for samples fixed in acetone as compared to formalin fixation.

5.6 Discussion of Preparation and Interrogation of Biological Samples

The ultimate goal of this project is to adapt the AFM technique for the interrogation of BCRs in tissue sections. This requires tissue fixation, which is essential in preserving tissue structure and immunohistological staining applied for the identification of regions of interest.

While the preparation of tissue sections for examination via light microscopy is well established, it could not be assumed that samples prepared under the available protocols exhibit characteristics that allow for accurate AFM adhesion measurements. Hence, different sample preparation techniques were tested, and their effects on AFM adhesion measurements investigated, to determine which sample preparation technique produces the most favourable results.

For testing and establishing adaptations to the AFM technique, a consistent biological target was required to ensure that results were comparable across experiments. For this purpose hybridoma cells were chosen. These can be maintained in cell culture indefinitely, and are hence available for experiments as needed. Further, their monoclonal nature implies that all cells in culture are genetically identical, and hence are expressing NP-specific receptors that are all of the same affinity. Several different hybridoma cell lines were available to this project, which were tested for their affinity via SPR (Table 2; p.87). In the investigation of the effects of sample preparation on AFM adhesion measurements only the cell line with the highest affinity (S24.1.47) was used.

Alongside development of the AFM technique, bespoke algorithms for computerised analysis of the collected data were developed. These were shown to not only be able to process the large amounts of data being produced, but furthermore, to automatically identify points of interest. Further, overview maps produced from whole data sets for individual cells allow for the quick identification of points of interest for more detailed inspection where required.

The experiments in the investigation of the effects of different sample preparation techniques were conducted using three different AFM cantilever functionalisations. Cantilevers were equipped with COOH, NH_2, and NP functional groups; where the NP functionalisation is designed for detecting NP-specific BCRs, and measure the strength with which they bind to the probe.

The NH_2 functionalisation was included to quantify the interactions that should be expected from incomplete or unsuccessful NP functionalisation. As described in §3.2.1 (p.27), the functionalisation of AFM cantilevers with NP is a two-step process, in which cantilevers are first equipped with NH_2, onto which NP is attached in the second step. Measuring the interaction profile for both constituent steps of the modification scheme was aimed at producing reference data that will aid in the identification of successfully and unsuccessfully functionalised cantilevers.

Additionally, the NH_2 functionalisation was also included as a non-specific control alongside the COOH functionalisation. The NH_2 and COOH functionalisations carry a positive and negative charge respectively [65,66], expected to produce distinct interactions with the negative surface charge of cells [104]; where detecting changes in

these interactions would allow assessing conformational changes on cells introduced by fixation.

The fixation methods that were tested were acetone and formalin fixation. These were compared against samples that were left unfixed, to better assess the effects of the different fixation methods. The use of unfixed tissue sections, however, is not feasible, as lack of mechanical stability makes the tissue sections susceptible to degradation during lengthy scans as well as spatial drift; which would hinder subsequent spatial registration of the AFM data to optical images of the tissue sections.

The first characteristic that was examined was how the Young's modulus of cells is altered as a result of being subjected to the different fixation methods. This information was extracted from data collected in adhesion measurements, not from separately conducted experiments. Thus, the experimental conditions would not be considered tailored to measurements of cell elasticity, where, for example, micro spheres attached to cantilevers would be used for compression of cells to more closely emulate the Hertz model of deformation.[102,105,106] A setup which would have been more conducive to cell elasticity measurements was not employed because of the designed end application of the developed AFM method, where specific interactions are to be detected in tissue sections. In this application it is required to chemically modify AFM probes to achieve specificity, and while through the diverse methods of probe functionalisation available [54] even the chemical modification of colloidal microsphere probes could be achieved, cantilevers pre-coated in Au were

chosen, as here functionalisation can more readily be achieved. Much more importantly, however, it is an application in which the size of the probe is a determining factor for the resolution that can be achieved by the imaging system. The diameter of the microspheres attached to colloidal probes is on the order of 1-10 μm [102,105,106], which compared to the tip radius of ~30 nm of the cantilevers employed in this project is several orders of magnitude larger. The inevitably greater area of contact between the probe and the sample would be accompanied by an inherent loss in spatial resolution in the detection of specific binding events.

However, as discussed in Appendix 8.19, the employed model parameters reflected the experimental conditions and the produced results allowed for a comparative assessment of the effect of the different fixatives on both B cells and hybridomas.

Cell elasticity data both for hybridoma cells, which were used for the majority of the conducted experiments, as well as for isolated primary murine B cells, showed that the Young's modulus for fixed cells is increased compared to unfixed cells. However, it was found that the two different cell types are affected differently by the two investigated fixatives. For hybridoma cells it was found that the increase in Young's modulus caused by acetone fixation is more than an order of magnitude (46x) greater than for formalin fixation (Figure 39; p.107); whereas for B cells the increase in Young's modulus due to acetone fixation is more than an order of magnitude (16x) lower than for formalin fixation (Figure 41; p. 110). Considering the properties of the two cells types it becomes apparent that, beyond their specificity towards the antigen NP, hybridomas and B cells do not share many similarities, and that their structural differences are likely responsible for the difference in the obtained results.

As is described in Appendix 8.15 (p.250), the used hybridoma cell lines are fusions comprised of antibody producing splenocytes and non-producing plasma cytoma cells (NS0), both of which have the ability to impart structural properties. Considering the myelomal portion of the cell fusion, it has been shown that the bulk properties of cancerous tissues demonstrate a significant increase in Young's modulus compared to the non-invaded surrounding tissue [107,108], however, studies investigating changes in Young's modulus of cancerous material compared to benign material on a cellular level, consistently find that cancerous cells are of lower Young's modulus compared to their non-malignant counterparts.[109-111] The lower Young's modulus of cancerous cells is attributed to significant reductions in well-defined actin filaments, resulting in a weaker cytoskeletal structure; which is hypothesised to give these cells the ability to more easily migrate through surrounding tissue matrices and capillaries.[109] These properties are, however, not beneficial to cells maintained in culture, where high levels of stress experienced by the cell, amongst others induced by agitation, have been shown to lead to cell necrosis and apoptosis.[112] The NS0 cell line has now been maintained in cell culture for several decades, where through steady genomic drift a selection towards more resilient cells will have occurred. This will have direct implications on the structural properties that the myelomal portion of the fusion imparts on the hybridoma. Conversely, the structural properties of B cells are adapted solely to the environment they were extracted from, where no such pressure for selection towards increased resilience existed.

One easily observed difference is in the size of the two cell types, which has been approximately measured in Appendix 8.19 (p.260) using representative force scan maps from each cell type. This shows that hybridoma cells are larger than B cells,

with approximate diameters of ~14 µm and ~8 µm respectively. The difference in size implies that hybridoma cells are comprised of more material, including a larger amount of water internally. The increased Young's moduli of hybridoma cells as a result of acetone fixation are possibly due to the dehydrating effects, where, analogous to grapes and raisins, the remainder of the cell after water extraction is a denser, stiffer mass.[102] While it was possible to show that there is a size difference between hybridoma cells, and B cells, post fixation with acetone, the change in size of the two cell types as a result of acetone fixation was not assessed. This should be quantified in future experiments. Further, the varying progress in differentiation and maturation of the two cell types should be considered. In the evolution of a naïve B cell into an antibody producing plasma cell, the BCR – the surface bound form of the later produced antibody – is expressed at progressively lower levels, as it is thought that BCR signalling does not play any further role for the survival of the finally differentiated plasma cell.[113] This means that, in similar fashion, fewer different receptors need to be expressed on the cell surface with increasing commitment towards a maturation fate. The plasma cell fused into the hybridoma has progressed through several stages of differentiation, which means that many different receptors are no longer expressed on the surface.

Conversely, primary B cells are comprised of cells over a range of differentiation stages, which have not yet lost the expression of many of their surface receptors.

It is that difference in the amount of membrane bound protein that may cause the differing Young's moduli obtained for the two cell types in response to formalin fixation. As detailed in §5.5 (p.101), the fixative action of formalin comprises the cross-linking of proteins, of which for B cells a larger amount is expected to be

present on the surface. This creates a denser matrix of cross-linked proteins, likely responsible for the increased Young's moduli observed for B cells in comparison to hybridoma cells.

The next parameter that was examined was the frequency with which positive adhesion events were detected between the different pairings of cantilever functionalisations and sample preparations. The results revealed that the number of events that was detected using the BCR specific NP functionalisation, in general, was considerably lower than the number of events detected using the non-specific COOH, or NH_2, functionalisations; where the only exception was observed for unfixed cells (Figure 42; p.114).

The reduction in the frequency of specific events for fixed cells, compared to unfixed cells, is ascribed to the conformational changes on the samples caused by fixation, where the cross-linking of surface proteins that occurs as part of formalin fixation interferes with the BCRs to a greater extent than the disruption of H-bonds caused by acetone fixation (9.0x and 2.5x reductions, respectively).

The conformational changes on the samples introduced by fixation also affected the frequency with which non-specific events were detected. This was particularly pronounced for cells fixed in formalin, where, when using the positively charged NH_2 cantilever functionalisation, twice as many events were produced as compared to unfixed cells and cells fixed in acetone; suggesting that formalin fixation produces an increased negative surface charge on the cells.

Self-selectivity - Particularly interesting, however, is the distinct difference in the frequency of events (Figure 42; p.114) between the non-specific NH_2 functionalisation and the specific NP functionalisation (unfixed: 1.5x; acetone: 3.1x formalin: 23.2x). It implies that through the addition of NP in the second step of the cantilever modification, specificity towards only the targeted BCR is imposed, and that as such the modified cantilevers are inherently self-selective towards only specific interactions. This fulfils objective 1 as stated in §2 (p.14).

Inspection of the magnitudes of the detected binding events further supports the observation of modified cantilevers being inherently self-selective; where the high number of binding events detected with the non-specific COOH, or NH_2, functionalisations correspond to low force interactions, and, conversely, the low number of binding events detected with the specific NP functionalisation correspond to high force interactions (Figure 43; p.117).

The separation of specific and non-specific binding events by magnitude of force is most clearly observed for unfixed samples, where the force values obtained for specific events (NP: $7.54 * 10^{-10}$ N) are an order of magnitude greater than for non-specific events (COOH: $8.36 * 10^{-11}$ N; NH_2: $1.39 * 10^{-10}$ N). While this difference remains clearly discernible for fixed samples, the separation of specific and non-specific events is, especially for samples fixed in formalin, less pronounced.

The energies that correspond to the detected binding events do not show as clear a difference between the specific and non-specific events as was observed for the associated force values. The determination of interaction energies, does not only depend on maximum cantilever deflection, but also takes into account the distance

over which the cantilever had to be retracted to produce the force that ultimately causes rupture. As was seen in §5.5.1.1 (p.105), the cell elasticity changes in response to the different sample preparations, which means that the distance that the cell membrane upon which is pulled can move varies. Therefore comparison between different samples based on the determined interaction energies should only be made cautiously.

Consistently seen across all sample preparations is the effect of using increased forces of indentation (RS-10) in experiments. The number of events, as well as their associated force and energy values, is increased for interrogations conducted with higher force of indentation (RS-10). The increased force of indentation means that the probe is pushed into the sample further, increasing the depth of indentation and concurrently the surface area of contact between the probe and the sample; where the increase in contact area increases the probability of molecular interactions occurring. Upon retraction, a greater force is required to rupture the increased number of molecular interactions made. This is illustrated diagrammatically in Figure 47. Initially, in (1), there is no applied force, and no area of contact exists between probe and specimen. In (2), a compressive force is exerted on the specimen by the probe, where in Scenario A the application of a small compressive force $F_{A\text{-}C}$ is depicted, and in Scenario B the application of a large compressive force $F_{B\text{-}C}$ ($F_{A\text{-}C} < F_{B\text{-}C}$). Due to the application of a larger force, a greater depth of indentation is achieved in Scenario B, producing a greater area of contact between probe and sample ($A_A < A_B$). As, in (3), the applied force is removed, the different produced areas of contact are maintained. Upon retraction of the probe, in (4), an adhesive

force is experienced, where the adhesive force $F_{A\text{-}A}$ in Scenario A is smaller than the adhesive force $F_{B\text{-}A}$ experienced in scenario B ($F_{A\text{-}A} < F_{B\text{-}A}$).

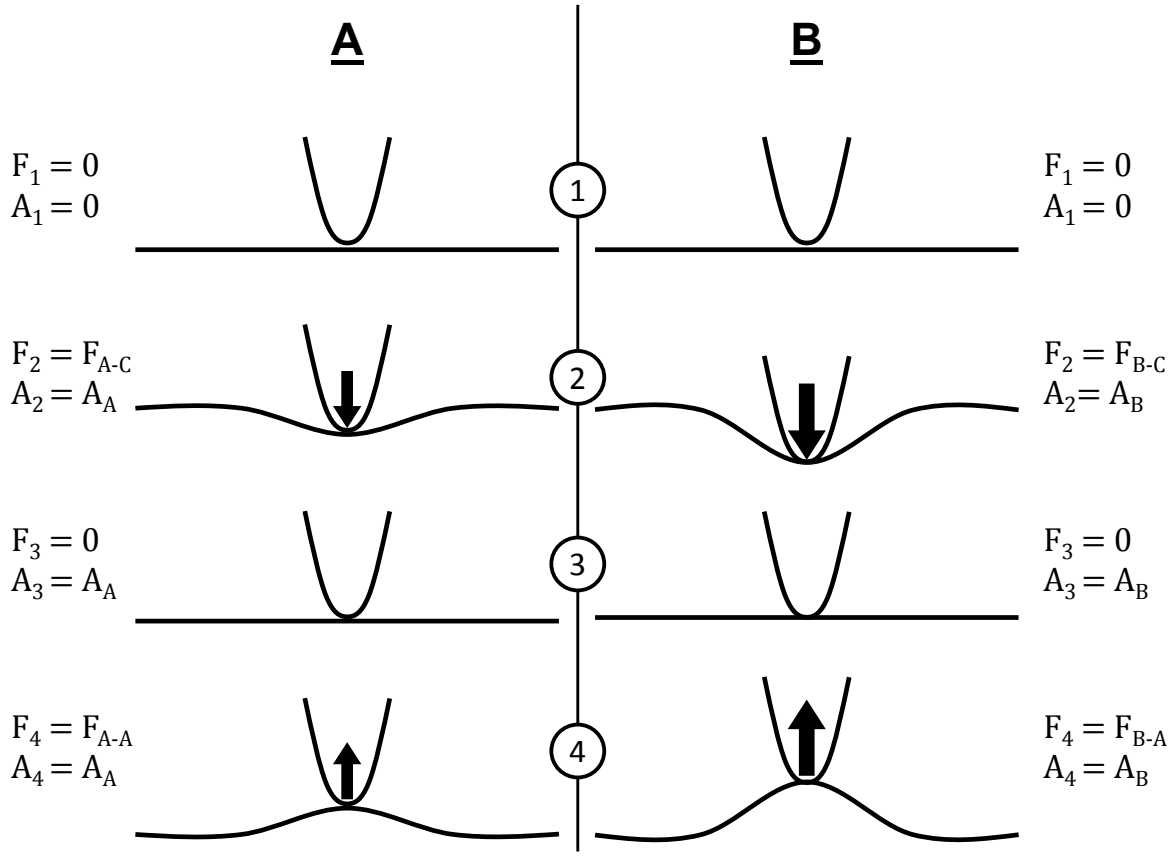

Figure 47 – Effects of Small and Large Compressive Forces on Produced Adhesive Forces

Illustrated are the effects that different forces of indentation have on the subsequently produced force of adhesion experienced by the probe. (1) In both scenarios, no initial compressive force is applied, and no initial area of contact exists. (2) In scenario A, a small compressive force $F_{A\text{-}C}$ is applied, that produces a small area of contact A_A. In scenario B, a large compressive force $F_{B\text{-}C}$ is applied ($F_{A\text{-}C} < F_{B\text{-}C}$), producing a larger area of contact A_B ($A_A < A_B$). (3) Upon the removal of the applied compressive force, the produced areas of contact are maintained. (4) During retraction, the probe experiences a small adhesive force $F_{A\text{-}A}$ in Scenario A, and a large adhesive force $F_{B\text{-}A}$ in Scenario B ($F_{A\text{-}A} < F_{B\text{-}A}$).

While these results are contrary to what the Hertzian contact mechanics model would predict, in which the contact area should return to zero as the load is reduced to zero, the Hertzian model omits the consideration of adhesive forces (including ubiquitous van der Waal's forces).

Experimental contradictions to the Hertz theory adequately describing the unloading and separation of the contact between two bodies were reported as early as 1968 by Kendall [114], and Roberts [115], where contact areas between two bodies were considerably larger than those predicted by Hertz and tended towards a finite value as the load was reduced to zero. Jointly with Johnson, Kendall and Roberts formulated a revised model of elastic contact (the JKR model) that was inclusive of adhesive forces, and Johnson, *et al.,* were able to corroborate their newly formulated analytical solution experimentally.[116]

A simple analogy would be to imagine pressing one's finger onto the sticky side of a piece of Sellotape. With increasing applied pressure, the surface area of contact is increased, increasing the number of adhesive connections. At the removal of the initially applied pressure the contact area does not return to zero, and ultimately a larger force is required to separate the connection.

Overall, the conclusion from this work was that acetone fixation provides preferable results in AFM adhesion measurements, showing a clearer separation between specific and non-specific interactions, as well as a higher number of specific events, as compared to formalin fixation. Thus, acetone fixation was used for sample preparations in subsequent experiments.

Most confidence in the technique was drawn from the self-selecting characteristics of the cantilever modification, where substantial reductions in the number of adhesion events were seen between NH_2, and NP, functionalised cantilevers.

The finding that fully functionalised cantilevers exhibit specificity towards the targeted receptors as well as prohibit non-specific binding, gave sufficient confidence to progress with the developed technique, and investigate its sensitivity in the application to a greater range of biological systems. The experiments and results are discussed in the subsequent Chapter 6.

6 Testing of NP Functionalised Cantilevers and Their Application to Biological Samples.

Results from experiments presented in the previous Chapter 5 indicated that the proposed cantilever modification scheme (§3.2.1; p.27) produces atomic force microscopy (AFM) probes that are inherently self-selecting towards specific interactions. Presented here in Chapter 6 are experiments aimed at matching successfully functionalised cantilevers to distinct interaction profiles in interrogation of control surfaces (CSs), testing the sensitivity of the AFM technique in differentiating between high and low affinity interactions with biological samples, as well as testing of the AFM technique in the interrogation of tissue sections.

6.1 Testing of NP Functionalised Cantilevers

Based on the self-selecting qualities of the adapted AFM technique towards only specific interactions – as described in the previous Chapter 5 – it was decided that adhesion measurements on cells expressing B cell receptors (BCRs) specific towards (4-hydroxy-3-nitrophenyl)acetyl (NP) are a good identifier of successfully functionalised cantilevers. The preparation and interrogation of biological samples, however, remains laborious when compared to that of the CSs that were introduced in Chapter 4. Therefore, it was not deemed feasible to prepare and interrogate biological samples as a means to confirm successful cantilever modification ahead of experiments reliant on receptor specific probes. Thus, the experiments in the current section were conducted in an effort to match successful adhesion measurements on cells with a characteristic interaction profile against CSs, in order to be able to utilise

CSs as readily available quality control measures through which successful cantilever functionalisation can be demonstrated.

For this purpose, AFM cantilevers were prepared under slightly varied preparation parameters, and were subsequently used in the interrogation of cells of the already previously described high affinity hybridoma cell line (S24.1.47), and a selection of CSs (CS-CH_3, and CS-OH).

Cell samples were prepared as before, with fixation in acetone, according to the protocol shown in Appendix 8.18 (p.258).

In the preparation of the CSs, three identical samples were prepared for each of the surface modifications, in order to mitigate against variations, due to self-assembled monolayers (SAMs) not forming correctly, or samples becoming unusable, e.g. through accidental contamination. The prepared CSs were interrogated via ellipsometry to ensure that good quality SAMs were achieved.

The results of the ellipsometry interrogation of the CSs prepared for the current experiment are shown in Figure 48. The results indicate that good quality SAMs were achieved, as the SAM thicknesses (CS-CH_3: 1.44 ± 0.17 nm; CS-OH: 1.32 ± 0.29 nm) are very close to the predicted values (Table 1; 36); and are in fact adhering closer to the predicted values than previous results (Figure 16; p.44).

The samples chosen for use in experiments were sample 1 from the CS-CH_3 preparation, and sample 2 from the CS-OH preparation, as SAM thickness across these samples showed the lowest variability (SD of 0.048 nm, and 0.086nm, respectively).

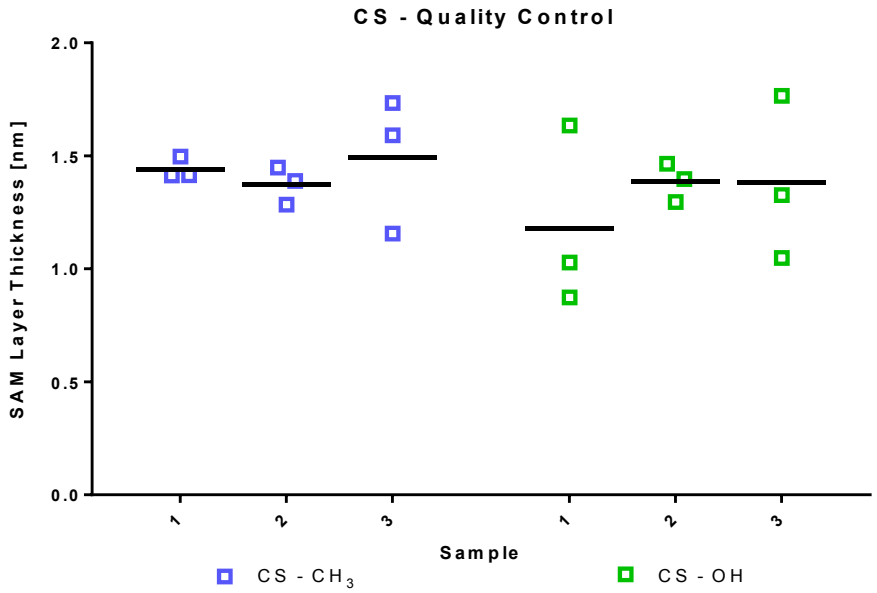

Figure 48 – Ellipsometry Results for CSs

Results show SAM layer thicknesses for CS preparations CS-CH_3 (blue), and CS-OH (green). Three samples were prepared for each of the surface modification (1-3). Each sample was interrogated in three non-overlapping positions (each interrogation represented by a marker), and black bars shows the mean layer thickness for each sample.

The different cantilevers and the conditions under which they were prepared are detailed in Table 3, where the parameters in the preparation protocol that were varied are: the length of time that cantilevers were immersed in NH_2 SAM deposition solution, and the concentration of HCl that was added to the deposition solution.

Previous investigation of the NH_2 SAM (§4.2.4; p. 69 & §4.2.6; p.74) revealed that both the length of time of immersion, as well as the concentration of HCl added to the deposition solution, affect the formation of the SAM. The aim of varying these parameters in the preparation of these cantilevers was to quantify their effect on AFM adhesion measurements in interrogation of biological samples.

Table 3 – Cantilever Preparations - I.

Detailed below are the different NP functionalised cantilevers, and the conditions under which they were prepared. The parameters that were varied were length of time of immersion in NH_2 SAM deposition solution, and the concentration of HCl added to the deposition solution.

Cantilever	Concentration of added HCl [M]	Time of Immersion [h]
NP 1	1	2
NP 2	1	4
NP 3	10	2
NP 4	10	4

The results presented in the previous chapter (Figure 43 in §5.5.3; p. 117) showed that good distinctions between specific and non-specific interactions could be made based on the measured force of adhesion. Therefore, the force of adhesion (determined as detailed in §5.4; p. 91), produced by the different NP functionalised cantilevers in interrogation of the CSs ($CS\text{-}CH_3$, CS-OH), and hybridoma cells (S24.1.47), was inspected, and the results are shown in Figure 49.

Figure 49 shows that the previously seen self-selecting qualities of the cantilever functionalisation are not apparent in this experiment. The interrogation of hybridoma cells (S24.1.47) produces a higher frequency of positively classed adhesion events, which has increased at least 2-fold, to ~40 % of point interrogations producing adhesion events, from ~10-20 % previously seen for samples fixed in acetone (Figure 42; p.114).

As described in §5.4 (p.91) – 'Event Selection', point interrogations are classed as positive adhesion events when the peak cantilever deflection is greater than at least three times the SD of the baseline. The mean value of this selection threshold was

determined for all cantilevers (0.167 nN) and is marked by the red line across the graph to aid in the interpretation of the results.

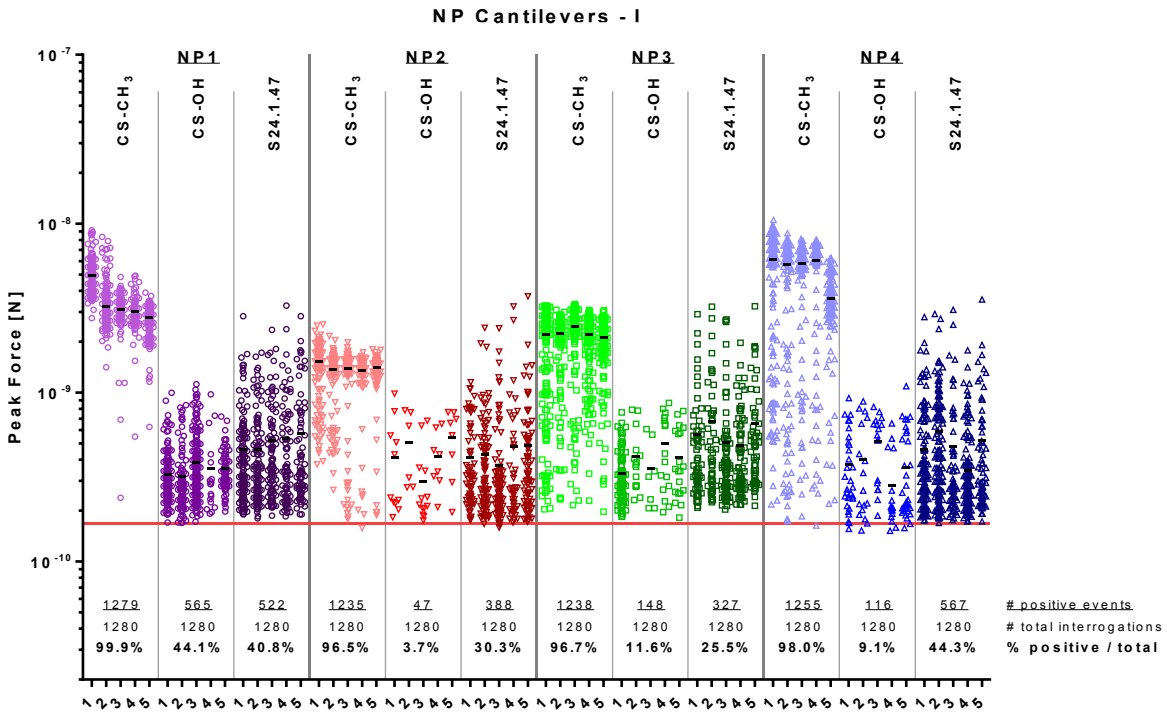

Figure 49 – NP cantilevers – I

AFM cantilevers were functionalised with NP (shown in different colours) under varied preparation parameters. Each cantilever was tested against CS-CH_3, CS-OH, and hybridoma cells (S24.1.47), marked by light, intermediate, and dark shading, respectively. Five hybridoma cells, and five non-overlapping positions on CSs (1-5), were measured with each cantilever, using a grid of 16 x 16 evenly spaced point interrogations. Black bars show the mean for each sample. The number of positively classed adhesion events, the total number of point interrogations, and the corresponding percentage ratio, is given for each cantilever-sample pairing; where each positive event is represented by a marker on the graph. The average limit for positive classification for all cantilevers is shown by the red line across the graph.

Many of the peak forces produced in the interrogation of cells are found around the nN range, where previously (Figure 43; p.117) specific interactions with S24.1.47 hybridoma cells were located. This suggests that specific interactions are occurring. However, the majority of peak forces lie just above the threshold for positive classification, indicating that primarily non-specific interactions are occurring.

In the interrogations of CS-CH_3 high frequencies of events are observed, with almost every point interrogation producing an adhesion event. The peak forces associated with these events are clustered primarily at high magnitudes (NP1: 3.43 ± 1.06 nN; NP2: 1.41 ± 0.30 nN; NP3: 2.52 ± 0.67 nN; NP4: 5.47 ± 2.11 nN), however, a considerable proportion of determined interaction forces do not fall within those clusters; where the cantilever for which least deviation was observed is NP1.

In the interrogation of CS-OH, overall, the lowest frequencies of events are observed (NP1: 44.1 %; NP2: 3.7 %; NP3: 11.6 %; NP4: 9.1 %). The peak forces associated with these events are at low magnitudes, just above the threshold for positive classification (NP1: 0.35 ± 0.16 nN; NP2: 0.42 ± 0.22 nN; NP3: 0.37 ± 0.17 nN; NP4: 0.38 ± 0.22 nN); distinctly below the main cluster of peak forces produced in the interrogation of CS-CH_3.

As outlined in §4.1 (p.31), CS-CH_3, and CS-OH, are model hydrophobic and hydrophilic neutral surfaces, respectively, thus interactions with the expected hydrophilic NP functionalisation of the AFM cantilevers are expected to be determined by their wetting properties.

In the approach of functionalised cantilevers against CS-CH_3, the effects of the hydrophobic surface chemistry of the CS are ‘felt’ as the separation between cantilever tip and CS is reduced to only a few water molecules. In order for the tip to be fully approached against CS-CH_3, H-bonded water molecules surrounding the tip have to be shed, creating an initially repulsive contact. The adhesive force experienced during cantilever retraction is due to the surface area of contact between

tip and surface 'resisting' rehydration, where the force of adhesion increases with increasing hydrophobicity of the surface.[117]

Conversely, for interrogations of CS-OH low forces are expected, as both the hydrophilic tip and hydrophilic CS allow H-bonded water molecules on their surface. It has been shown that in water, the adhesive forces between two hydrophilic surfaces are very small [118], not dissimilar to what was measured here, and this characteristic interaction has in fact been used to demonstrate successful deposition of SAMs.[117]

Ultimately, in the absence of the self-selecting qualities of the modified cantilevers in interrogation of cells, successfully modified cantilevers could not be identified, and thus could not be matched to a distinct interaction profile in interrogation against CSs. Based on the data available, the behaviour of NP1 was considered most preferable. While it did produce the highest frequency of events in interrogation of CS-OH, the magnitudes of these events did not exceed what was produced by any of the other cantilevers, and lie just above the threshold for positive classification. Further, many of the events produced in interrogation of cells are in the range of what has previously been seen for specific interactions with S24.1.47 hybridoma cells. Lastly, interrogations of CS-CH_3 produced the most consistent cluster of events out of all tested cantilevers.

In the continued effort to match successfully modified cantilevers to a distinct interaction profile in interrogation against CSs, and to provide an independent reproduction, the experiment was repeated with cantilevers prepared under the previously employed conditions and, additionally, with cantilevers prepared from

deposition solution with no added HCl. While previous investigations (Figure 30; p.75) had shown that high concentrations of HCl added to the NH_2 SAM deposition solution had preferable effects on SAM formation, the results presented in Figure 49 indicate that cantilevers prepared from deposition solution with lower concentrations of HCl demonstrate preferable behaviour in AFM adhesion experiments, concurrencies that, while unexpected, are not mutually exclusive as different parameters are being assessed. Hence, the second group of cantilevers that was prepared included a condition where no HCl was added to the NH_2 SAM deposition solution. The different cantilevers and their preparation parameters for this experiment are detailed in Table 4.

Table 4 – Cantilever Preparations - II

Detailed below are the second group of different NP functionalised cantilevers and the conditions under which they were prepared; where the parameters that were varied are, as before, the length of time of immersion in NH_2 SAM deposition solution, and the concentration of HCl added to the deposition solution. Cantilevers NP5, and NP8, got damaged in preparation of experiments, and hence are crossed out, as complete data sets could not be collected.

Cantilever	Concentration of added HCl [M]	Time of Immersion [h]
~~NP 5~~	~~0~~	~~2~~
NP 6	0	4
NP 7	1	2
~~NP 8~~	~~1~~	~~4~~
NP 9	10	2
NP 10	10	4

Cantilevers NP5 and NP8 are crossed out from the list as these cantilevers got damaged in preparation of the experiment, specifically during attempts of mounting the cantilevers in the AFM cantilever holder. The spring-loaded mechanism has to be operated with tweezers, and small inaccuracies can lead to cantilevers being ejected and becoming damaged. This prevented data sets from being collected for these cantilevers; an eventuality that was unfortunately not mitigated against.

The available cantilevers were, as before, used for the interrogation of CSs (CS-CH_3, CS-OH), and hybridoma cells (S24.1.47). The results of the experiment are presented in Figure 50.

The results presented in Figure 50, closely resemble those of the previous experiment presented in Figure 49, where again the self-selecting qualities of functionalised cantilevers in the interrogation of cells was not observed, for which in fact the frequency of events has increased further (NP6: 76.1 %; NP7: 78.6 %; NP9: 94.5 %; NP10: 88.9 %). The peak forces associated with these events are again found over a wide range. Many of the interrogations have produced peak forces in the nN range, where previously (Figure 43) specific interactions with S24.1.47 hybridoma cells were seen, but the majority of the peak forces are an order of magnitude smaller, located just above the threshold for positive classification. This indicates that some specific interactions, but primarily non-specific interactions, are occurring.

The mean threshold for positive classification for the second group of cantilevers was 0.0496 nN, and is marked by the red line across the graph to aid in comparison of the results.

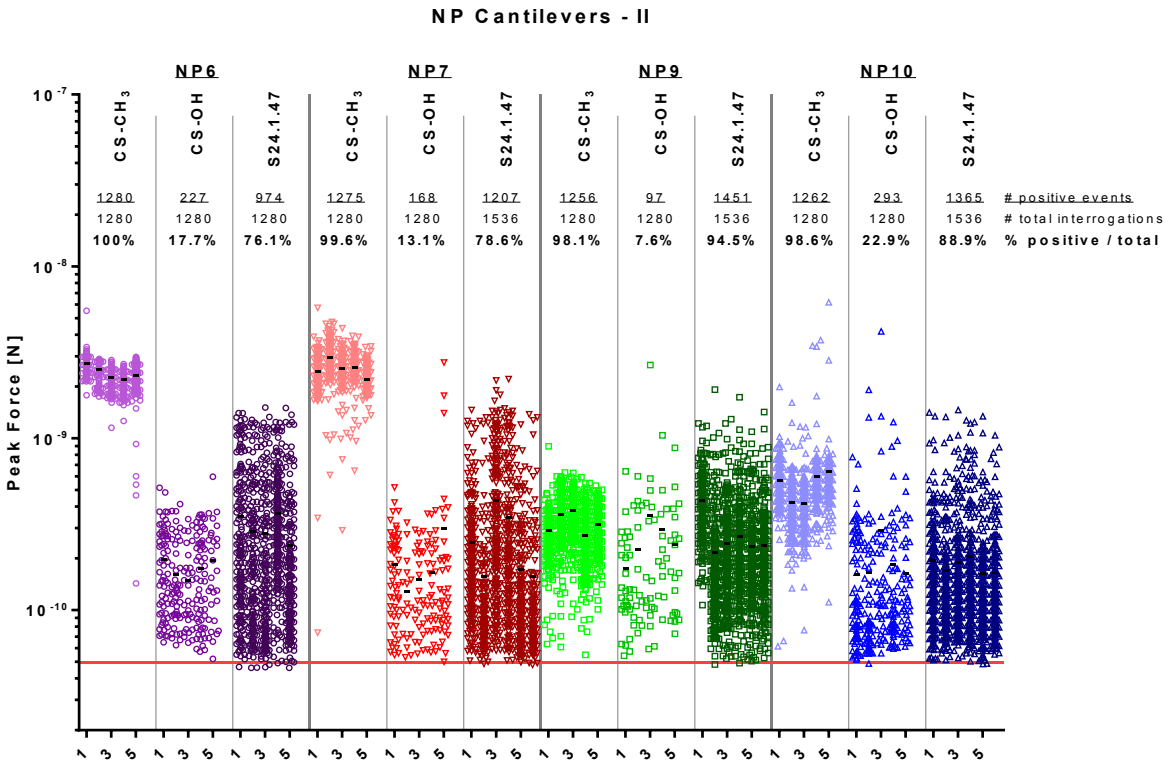

Figure 50 – NP cantilevers – II

Multiple AFM cantilevers (shown in separate colours) were functionalised with NP with varied preparation parameters. Each cantilever was tested against CS-CH_3, CS-OH, and hybridoma cells (S24.1.47), denoted by light, intermediate, and dark shadings respectively. A minimum of five hybridoma cells, and five non-overlapping positions on CSs, were measured with each cantilever, using a grid of 16 x 16 evenly spaced point interrogations; black bars show the mean for each sample. The number of positively classed adhesion events, the total number of point interrogations, and the corresponding percentage ratio, is given for each cantilever-sample pairing; where each positive event is represented by a marker on the graph. The average limit for positive classification for all cantilevers is shown by the red line across the graph.

As before, the highest frequency of events is observed in the interrogation of CS-CH_3, with almost every point interrogation producing an adhesion event. The peak forces associated with these events (NP6: 2.40 ± 0.36 nN; NP7: 2.54 ± 0.52 nN; NP9: 0.32 ± 0.10 nN; NP10: 0.53 ± 0.28 nN), are clustered at high magnitudes for NP6 and NP7, with very few values outside of those clusters. For NP9, and NP10,

however, the peak forces are reduced, and show greater variability, and thus the correct conformation of their surface chemistries is called into question.

The lowest frequency of events, again, is observed in the interrogation of CS-OH (NP6: 17.7 %; NP7: 13.1 %; NP9: 7.6 %; NP10: 22.9 %), for which the associated peak forces are of low magnitude, just above the threshold for positive classification (NP6: 0.18 ± 0.10 nN; NP7: 0.20 ± 0.27 nN; NP9: 0.25 ± 0.31 nN; NP10 0.19 ± 0.31 nN).

While the interaction profiles of NP6, and NP7, suggest that hydrophilic surface chemistries were assembled on these cantilevers, indicating that functionalisation was successful, neither of these cantilevers demonstrated self-selecting qualities in the interrogation of cells. Hence, successfully functionalised cantilevers could again not be identified, and therefore could not be matched to distinct interaction profiles in interrogation of CSs.

From the available data, however, the interaction profile of cantilever NP7 was considered most preferable. Interrogations of CS-CH_3 produced densely clustered interaction forces that are distinctly above what is produced in interrogation of CS-OH, for which the lowest frequency of events was produced out of all tested cantilevers. Furthermore, many of the peak forces produced in interrogation of cells are in the range of what has previously been identified as specific interactions with S24.1.47 hybridoma cells.

6.2 Investigation of Cell Samples

The data presented here were acquired during the same two experimental sessions in which the two different groups of NP functionalised cantilevers were investigated. In spite of the investigation of the functionalised cantilevers in §6.1 (p.137) not allowing for the identification of unequivocally successfully functionalised cantilevers, the subsequent experiments were conducted in an effort to make best use of the very limited time available on the AFM instrument.

The experiments were designed to demonstrate the sensitivity of the adapted AFM technique, by interrogating a range of hybridoma cell lines with defined affinities towards the antigen NP, as well as different isolated primary murine B cells with NP-specific BCRs. The experiments tested whether it is possible to distinguish antibody affinities displayed by different cell lines based on the data collected in AFM adhesion measurements.

6.2.1 AFM Adhesion Measurements on Different Cell Strains - I

The cell lines that were investigated are the different hybridoma cell lines that were previously introduced in Table 2 in §5.1. (p.87). These are all of the IgG1 isotype with specificity towards NP with varying affinity. Further, two different strains of isolated murine B cells specific towards NP (B1.8, and B1.8hi), with a 10-fold difference in affinity[119], were included, as well as a non-specific hybridoma cell line (BU59r31) acting as a negative control.

In this experiment, cell samples were prepared as before, with fixation in acetone, according to the protocol in Appendix 8.18 (p.258). From each of the different cell

strains, 10 cells were measured. Each cell was interrogated using a 16 x 16 grid of evenly spaced point interrogations; except for S24.1.47 cells, which were interrogated using a 10 x 10 grid of evenly spaced point interrogations. Experiments were conducted using NP1, from the first group of functionalised cantilevers discussed in §6.1. (p.137).

Firstly, to assess the conformation of the interrogated cell samples, the data collected in the AFM adhesion measurements were subjected to mathematical modelling for the extraction of cell elasticity values, as introduced in §5.5.1 (p.103), and discussed in detail in Appendix 8.19 (p.260). The results are shown in Figure 51.

The results in Figure 51 show distinct differences in Young's modulus between hybridoma cells and B cells. While statistically, accentuated by the high number of data points, the differences between all cell lines are highly significant ($p<0.0001$), primarily the difference between the two different cell types is considered relevant. The mean Young's moduli for the different hybridoma cell lines (S24.1.47: 0.84 ± 0.79 MPa; N1G9: 0.53 ± 0.18 MPa; B1.48: 0.66 ± 0.19 MPa; 18.1.16: 0.62 ± 0.19 MPa; BU59r31: 0.68 ± 0.25 MPa) are comparable to each other, and are approximately two orders of magnitude greater than what was determined for the two B cell strains (B1.8: 8.75 ± 4.65 kPa; B1.8hi: 16.49 ± 8.15 kPa).

These results are comparable to previous data, which show the Young's moduli of hybridoma cells following acetone fixation (Figure 39; p.107) to be at least an order of magnitude greater than for B cells fixed in acetone (Figure 41; p.110), and further

support the hypothesis, discussed in §5.6 (p.125), that structural differences between the two cell types cause the different behaviours in response to fixation.

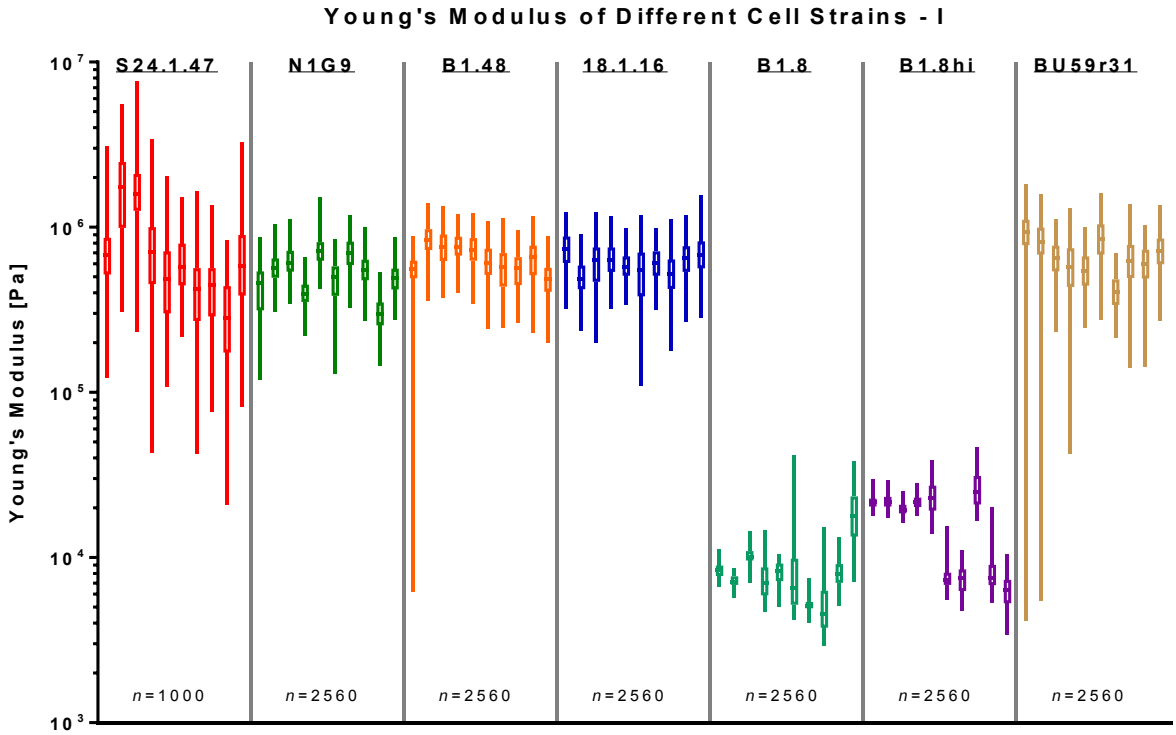

Figure 51 – Young's Modulus of Different Cell Strains - I

Young's moduli for different cell strains are shown. Each cell line is shown in a different colour, and each box and whiskers plot represents one cell. 10 cells were measured for each of the different cell strains. Cells were interrogated using grids of 16 x 16 evenly spaced point interrogations; 10 x 10 for S24.1.47. Boxes show 25th percentile, median, and 75th percentile, and whiskers show the minimum and maximum values. Differences between all cell strains are highly significant ($p<0.0001$), accentuated by the high number of data points.

As previously discussed (§5.5.3; p.117), results from the initial interrogation of cells (Figure 43; p.117) showed that distinctions between interactions produced by different samples are most clearly seen in the force of adhesion. Hence, this parameter was inspected first to determine whether the adapted AFM technique could distinguish between the different receptor affinities of the interrogated cell lines. The results are shown in Figure 52.

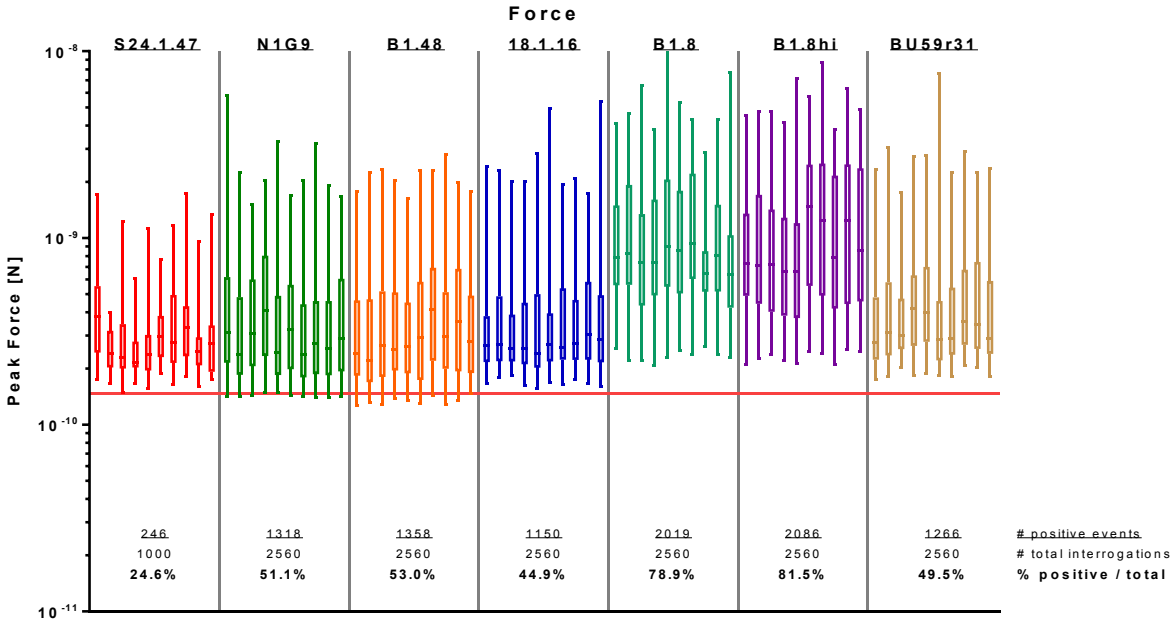

Figure 52 – Forces of Interaction - I

Data shows peak forces associated with positive adhesion events produced in interrogation of different cell lines. Each cell line is shown in a different colour, and each box and whiskers plot represents one cell. Boxes show 25th percentile, median, and 75th percentile, and whiskers show the minimum and maximum values. 10 cells were measured for each of the different cell lines. The number of positively classed adhesion events, the total number of point interrogations, and the corresponding percentage ratio, is given for each cell line. The average limit for positive classification is shown by the red line across the graph.

The peak forces of the positively classed adhesion events, produced in the interrogation of the different cell strains, presented in Figure 52, show that the peak forces for the different hybridoma strains (S24.1.47: 0.34 ± 0.19 nN; N1G9: 0.47 ± 0.20 nN; B1.48: 0.44 ± 0.20 nN; 18.1.16: 0.44 ± 0.20 nN; BU59r31: 0.51 ± 0.25 nN) are comparable to each other, and statistically significant differences ($p<0.0001$) are found only for S24.1.47, and BU59r31, compared to the very similar results for N1G9, B1.48, and 18.1.16.

The peak forces produced in the interrogation of the two B cell strains are in a similar range, with B1.8hi cells producing slightly higher interaction forces (B1.8: 1.15 ± 0.34 nN; B1.8hi: 1.26 ± 0.43 nN; p=0.0023)

The interaction forces produced in the interrogation of B cells are approximately three times higher than forces determined for hybridoma cells; this difference is highly significant (p<0.0001).

Overall the results are similar to what was produced in the interrogation of cells in §6.1 (p.137), in that a minority of the peak forces are in the nN range, where previously specific interactions with cells were observed (Figure 43). However, the majority of interactions is found to be just above the limit for positive classification and is considered to have been produced in non-specific interactions. Further, the results do not show differences between the different cell lines that are concurrent with their respective affinities.

The differences that exist between the hybridoma cells, and the B cells, can be attributed to the difference in elasticity of the two different cell types. The relative set point (RS) – the force with which the probe is pressed into the sample – was kept constant throughout the experiment. However, at a constant compressive force, the depth of indentation, and subsequently the surface area of contact between tip and cell, is greater for samples with a lower Young's modulus.[120] As previously discussed in §5.6 (p.125), in reference to Figure 42 (p.114), greater depth of indentation produces an increased frequency of events – which is in keeping with the event frequency observed for B cell samples compared to hybridomas – and is concurrent

with greater peak forces through multiple molecular interactions occurring during individual tip-sample contacts.

Because the parameter force of adhesion did not reveal differences between the cell lines that match with their affinities, the remaining parameters that are calculated in the analysis (as outlined in §5.4; p.91) were inspected also.

The parameter directly related to the determined peak forces is the event 'significance'. This parameter is used for the classification of data points, and is calculated as given in Equation 4 (p.93). The values of event 'significance' of all positively classed adhesion events are shown in Figure 53.

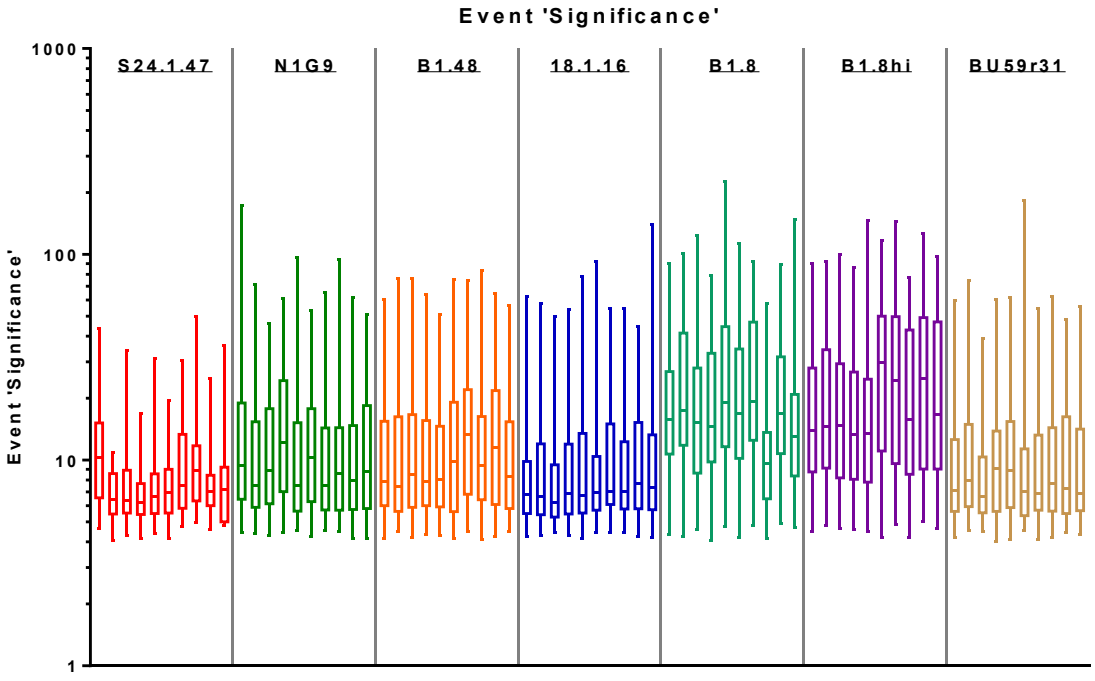

Figure 53 – Event 'Significance' of Positively Classed Adhesion Events - I

The event 'significance' of all positively classed adhesion events is shown. Boxes show 25th percentile, median, and 75th percentile, and whiskers show the minimum and maximum values, where each box and whiskers plot represents one cell. The different cell lines are shown in separate colours. 10 cells were measured for each cell line.

The results in Figure 53 show the same trend as was observed for the forces of interaction; with no distinct differences between the different hybridoma cell lines, or the two different B cell strains. On average the event 'significance' for B cells (B1.8: 23.58 ± 7.14; B1.8hi: 25.35 ± 8.66) is twice of what is observed for hybridoma cells (S24.1.47: 9.33 ± 5.46; N1G9: 14.41 ± 6.31; B1.48: 14.32 ± 6.37; 18.1.16: 11.48 ± 5.20; BU59r31: 12.04 ± 5.87); which was determined to be highly statistically significant ($p<0.0001$).

The fact that the graphs for forces of interaction, and for the corresponding event 'significance', are very similar is positive, as it indicates that the retraction curve baselines are consistent throughout the experiment. While consistency in the retraction curve baselines can be expected, as the same cantilever was used throughout the experiment, it is furthermore also indicative of stable experimental conditions throughout the experiment.

The next parameter that was inspected was the separation distance, which describes the distance over which the cantilever needed to be retracted to cause rupture of the adhesion event. Shown in Figure 54 are the separation distances for all positively classed adhesion events.

The results in Figure 54 show that the values for the hybridoma cell lines (S24.1.47: 36.98 ± 35.10 nm; N1G9: 127.50 ± 66.79 nm; B1.48: 93.54 ± 50.92 nm; 18.1.16: 96.90 ± 68.56 nm; BU59r31: 101.40 ± 66.18 nm) are again comparable to each other; with the exception of S24.1.47, for which reduced values were obtained. Similarly, the results for the B cells (B1.8: 0.94 ± 0.25 µm; B1.8hi: 0.86 ± 0.26 µm) are again

similar. However, the difference between the two cell types is more pronounced, with values for B cells an order of magnitude greater (10x) than for hybridomas.

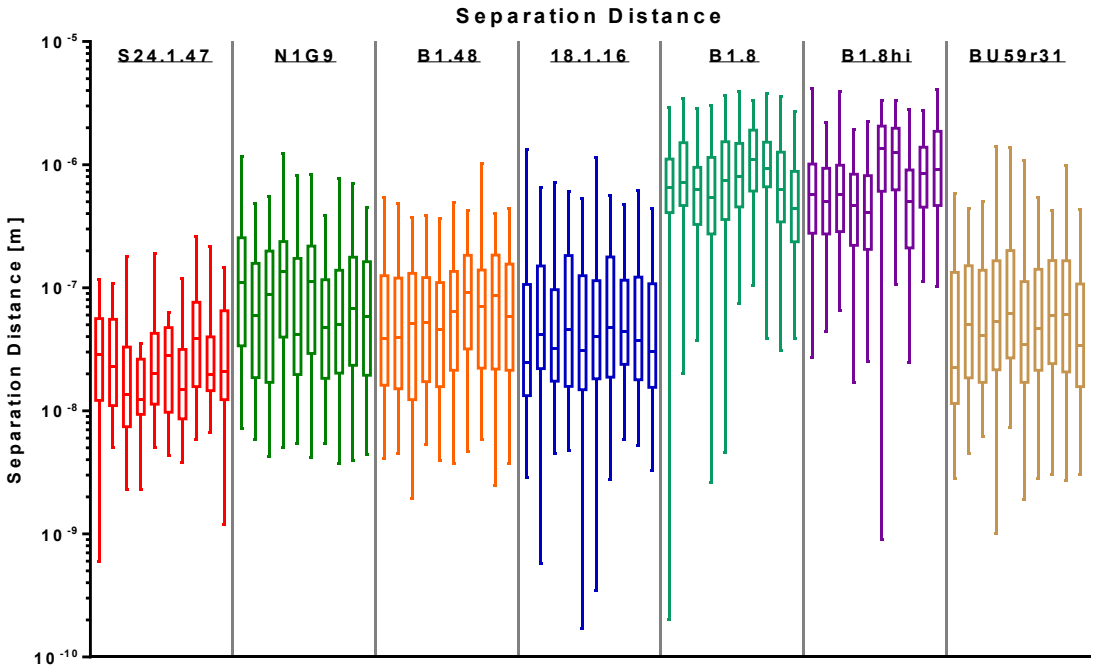

Figure 54 – Separation Distance - I

The separation distance for all positively classed adhesion events is shown, which describes the distance over which the cantilever needed to be retracted to cause rupture of the probe-sample contact. Boxes show 25th percentile, median, and 75th percentile, and whiskers show the minimum and maximum values. Each box and whiskers plot represents the data acquired for one cell. 10 cells were measured for each cell line. Different cell lines are shown in separate colours.

The differences that are seen between the different cell lines, and cell types, can be explained by their varying Young's moduli (Figure 51; p.150), which affect the separation distance considerably. Samples with a lower Young's modulus are more easily deformable, allowing for a greater range of motion when pulled upon, which means that a greater distance is required to produce the force required to rupture the tip-sample contact; as seen for the B cells. Conversely, samples with a higher Young's modulus cannot provide great range of motion, and hence only a shorter distance is required to produce sufficient force to rupture the tip-sample contact. This

effect however is compounded. As previously discussed, samples with a lower Young's modulus allow greater depth of indentation at constant compressive forces, creating greater surface areas of contact between tip and sample, and a subsequently increased frequency of molecular interactions occurring. This means that for samples with a lower Young's modulus greater forces are required to rupture tip-sample contacts, further increasing the separation distance; and vice versa.

This is illustrated further in Figure 55, which is similar to Figure 47 (p.134), but instead of illustrating how greater compressive forces can subsequently produce greater forces of adhesion, the applied compressive force is the same and the specimen elasticity is varied.

For illustrative purposes, the contacted cell surface is considered a film suspended between two springs, each with a spring stiffness k. In scenario A the spring stiffness k_A is large, representing a specimen with a higher Young's modulus; i.e. hybridomas. Scenario B represents specimen with a lower Young's modulus, i.e. B cells, where the spring stiffness k_B is low ($k_A > k_B$). As previously in Figure 47 (p.134), in (1), there is no initial applied force and no area of contact exists. In (2), the same compressive force is applied in both scenarios ($F_{A\text{-}C} = F_{B\text{-}C}$), however, in Scenario A the compressive force produces a small depth of indentation and a small area of contact A_A, whereas in Scenario B a greater depth of indentation is achieved that produces a larger area of contact A_B ($A_A < A_B$). As, in (3), the applied compressive force is removed, the different areas of contact are maintained. Upon retraction of the probe, in (4), an adhesive force is experienced, where the adhesive force $F_{A\text{-}A}$ in Scenario A is smaller than the adhesive force $F_{B\text{-}A}$ experienced in scenario B ($F_{A\text{-}A} < F_{B\text{-}A}$). As a result of the greater force pulling on the specimen in Scenario B, the specimen

deformation τ_B is substantially larger than the deformation τ_A in Scenario A ($\tau_A < \tau_B$). Already at equal sample elasticity, the greater experienced adhesive force would suffice to produce a greater specimen deformation, but the lower specimen Young's modulus in scenario B compounds the effect.

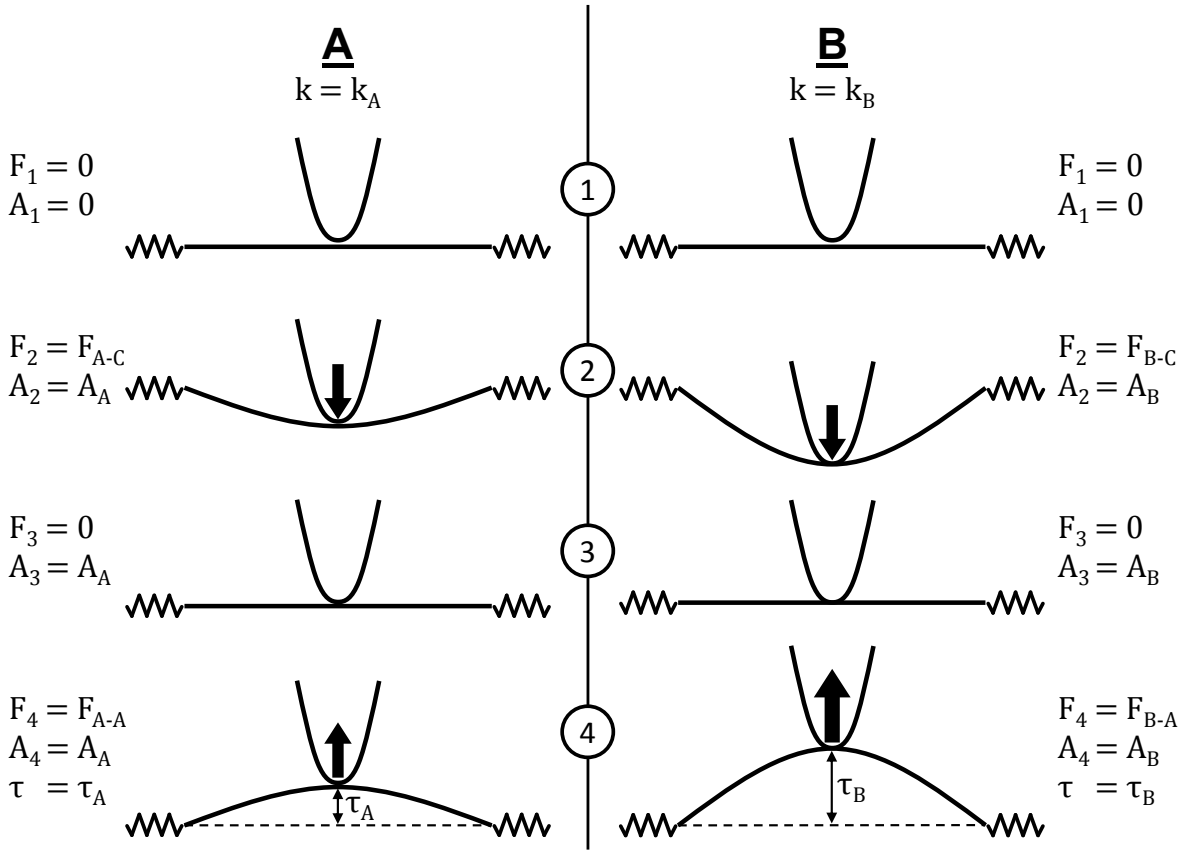

Figure 55 – Effects of Sample Elasticity on Produced Adhesive Force and Separation Distance

Illustrated are the effects of sample elasticity on the experienced adhesive force and specimen deformation. The contacted sample surface is considered a film suspended between two springs with spring stiffness k, where the spring stiffness k_A in Scenario A, representing specimen with a greater Young's modulus, is greater than the spring stiffness k_B in Scenario B, representing specimen with a lower Young's modulus ($k_A > k_B$). (1) Initially, no force is applied, and no area of contact exists. (2) At equal compressive force greater depth of indentation is achieved for samples with a lower Young's modulus, and concurrently a greater area of contact ($A_A < A_B$). (3) At the removal of the applied compressive force, the different areas of contact are maintained. (4) Due to the greater area of contact in scenario B, a greater adhesive force is experienced ($F_{A\text{-}A} < F_{B\text{-}A}$), which, compounded by the lower specimen Young's modulus, produces a substantially larger specimen deformation in scenario B ($\tau_A < \tau_B$).

The next inspected parameter was the energy of interaction, which, as described with Figure 33 in §5.4 (p.91), is defined as the area between the retraction curve and its baseline, and is thus affected by both the separation distance and the force of interaction. The results are shown in Figure 56.

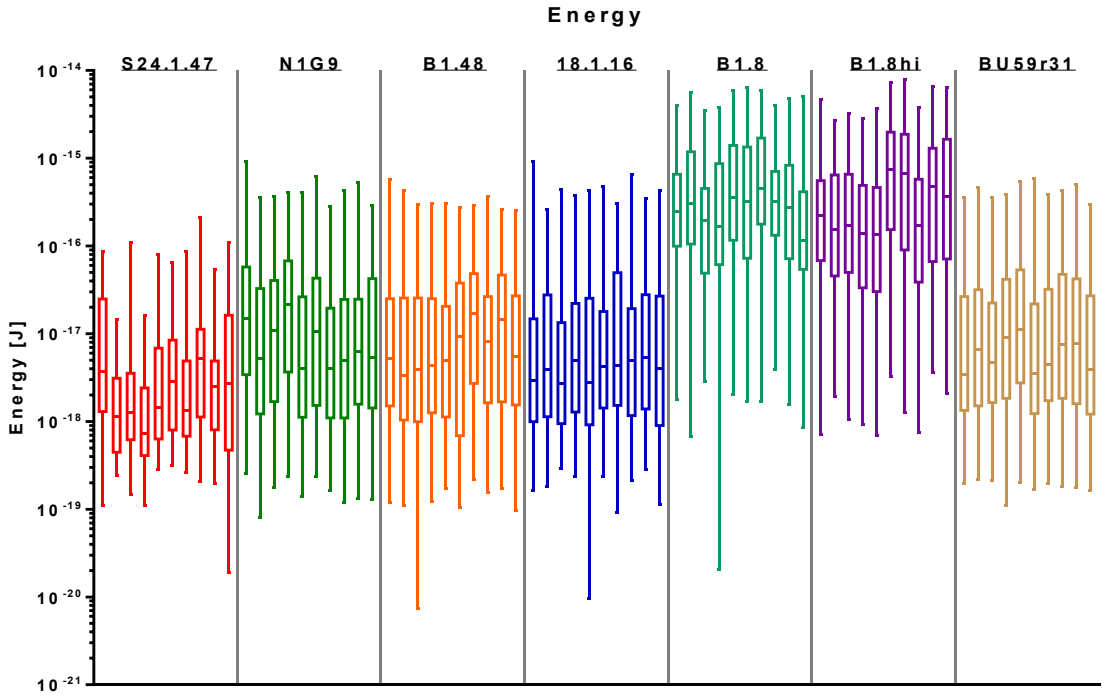

Figure 56 – Energies of Interaction - I

Energies associated with positive adhesion events are shown. Boxes show 25th percentile, median, and 75th percentile, and whiskers show the minimum and maximum values, where each box and whiskers plot represents one cell, 10 cells were measured for each cell line. Different cell lines are shown in separate colours.

The results in Figure 56 show the same trend that was observed for the separation distance. The values for the hybridoma cell lines (S24.1.47: 10.23 ± 23.57 aJ; N1G9: 40.47 ± 38.65 aJ; B1.48: 29.92 ± 27.64 aJ; 18.1.16: 31.59 ± 36.77 aJ; BU59r31: 34.92 ± 34.78 aJ) are comparable to each other, as are the values for the two different B cell strains (B1.8: 0.70 ± 0.33 fJ; B1.8hi: 0.67 ± 0.37 fJ); and the values for the B cells are more than an order of magnitude (23x) greater than for hybridomas.

The differences that are seen between the different groups can again be explained by their respective Young's moduli. As mentioned above, the energy of interaction is affected by both the separation distance, as well as the force of interaction, two parameters that have already been found to be elevated for B cells compared to hybridoma cells, which has a compounding effect on the energy of interaction.

Lastly, the apparent loading rate for all adhesion events was inspected; which is determined as described in §5.4 (p.91), and estimates the rate at which tip-sample contacts are loaded by taking into account the force of interaction, separation distance, and the speed of the tip. The apparent loading rates determined for positive adhesion events are shown in Figure 57.

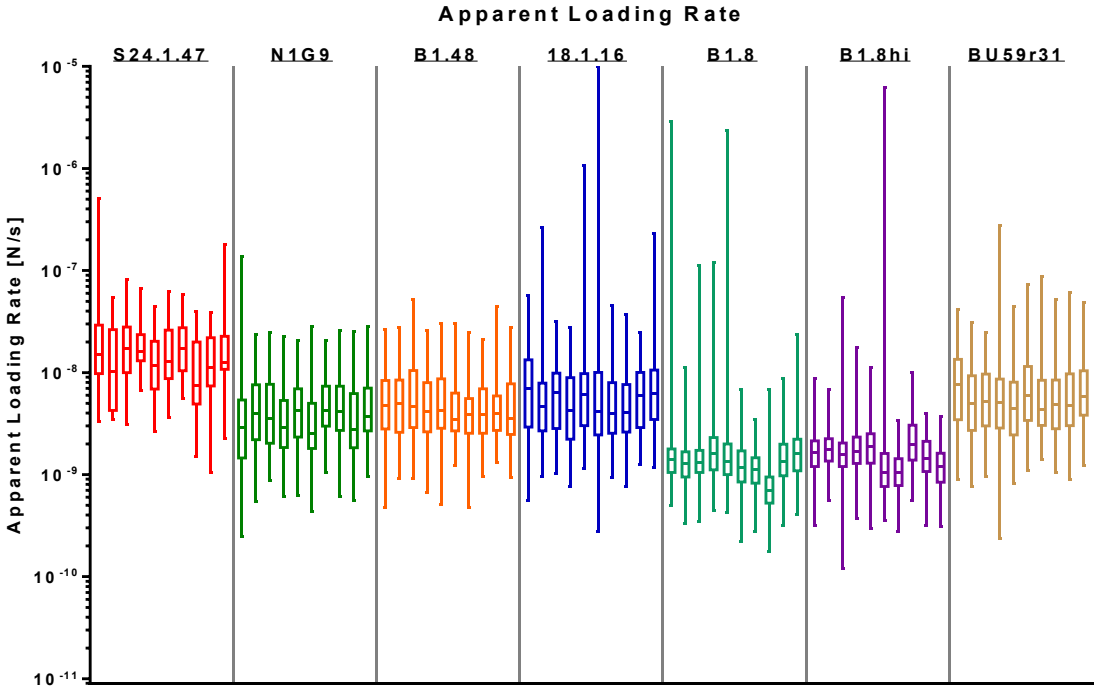

Figure 57 – Apparent Loading Rate - I

The values of apparent loading rate for positive adhesion events are shown; which is determined as the gradient between the point at which cantilever loading due to adhesion starts and the maximum cantilever deflection, taking into account tip speed. Boxes show 25th percentile, median, and 75th percentile, and whiskers show the minimum and maximum values. Each box and whiskers plot represents one cell, 10 cells were measured for each cell line. Different cell lines are shown in separate colours.

The results presented in Figure 57 show that the apparent loading rates are greater for the hybridoma cells with a greater Young's modulus (S24.1.47: 19.10 ± 16.61 nN/s; N1G9: 5.09 ± 2.33 nN/s; B1.48: 6.10 ± 2.71 nN/s; 18.1.16: 15.80 ± 105.60 nN/s; BU59r31: 7.62 ± 4.80 nN/s), and reduced for the B cell samples with a lower Young's modulus (B1.8: 4.07 ± 27.61 nN/s; B1.8hi: 4.78 ± 48.25 nN/s).

The apparent loading rate is affected by both force of interaction, and the separation distance, which have been shown to both be increased for samples with a lower Young's modulus, and the influence of their effects compounded has been seen in the energy of interaction (Figure 56). Their relationship in the determination of apparent loading rates, however, is altered, with apparent loading rates now inversely proportional to separation distance (Equation 6).

For the apparent loading rates to be reduced for samples with a lower Young's modulus, means that separation distance is affected to a greater extent than the force of interaction, which means that a lower Young's modulus in itself has greater effect on the results than the increased number of molecular interactions that it promotes.

$$L \propto F \propto \frac{1}{D}$$

Where:

L	=	apparent loading rate	[N/s]
F	=	force of interaction	[N]
D	=	separation distance	[m]

Equation 6 – Influences on Apparent Loading Rate

The apparent loading rate is affected by both maximum cantilever deflection, and separation distance, to which it is directly, and inversely, proportional, respectively.

Ultimately, the inspection of the remaining parameters that are determined in the data analysis did not reveal differences that are concurrent with the affinities of the interrogated cell lines either. The differences that have been observed between the different cell lines, and the different cell types, were all explained by the varying Young's moduli of the cells. Samples with a lower Young's modulus allow greater depth of indentation at constant compressive forces. The increased surface area of contact between tip and sample increases the frequency of molecular interactions, causing increases in the force of interaction, separation distance, and energy of interaction, required to rupture tip-sample contacts. Conversely, the increased range of motion allowed by samples with a lower Young's modulus causes a decrease in the apparent loading rate, which showed that the effects of a reduced Young's modulus on the obtained results outweigh the effects of higher frequencies of events that occur through a reduced Young's modulus.

The results are considered to have been produced primarily in non-specific interaction. The initial results for the characterisation of the used cantilever (Figure 49: NP1; p.141) already showed a large proportion of the events produced in the interrogation of cells to be in the range of what was considered non-specific interactions, thus somewhat expectedly, the subsequent results (Figure 52; p.151) presented with the same trend. Some of the events are in the range of what was previously seen for specific interactions with cells (Figure 43; p.117), but differentiation of specific from non-specific events is not possible with the available data analysis algorithms.

6.2.2 AFM Adhesion Measurements on Different Cell Strains - II

The second group of samples that was investigated was similar to the samples discussed in the previous experiment. The same hybridoma cell lines of different affinity towards NP (Table 2; p.87) were again used, in addition to the non-specific cell line BU59r31 acting as negative control, and one B cell strain (B1.8hi). The aim of the experiment remained to demonstrate that the different interrogated cell lines could be differentiated based on their affinity from data collected in AFM adhesion measurements.

Because the previous experiments had shown that the values obtained in interrogation of the negative control cell line were very similar to the antigen-specific hybridoma cell lines, an additional negative control was included to test whether the interactions obtained in interrogation of the non-specific cell line (BU59r31) were non-specific crossreactivity. The newly included NS0 cell line used in this experiment is the unfused fusion partner used in the preparation of hybridoma cells, and as such does not express B cell receptors on its surface that could possess crossreactivity for NP.

The cantilever that was used in this experiment was NP7 from the second group of NP functionalised cantilevers, for which data is shown in Figure 50 in §6.1 (p146). At the end of the experiment the cantilever was again tested against CSs to demonstrate that interrogation of biological samples does not cause any changes to the cantilever functionalisation.

In this experiment, a minimum of 7 cells from each of the different cell lines, and a minimum of 5 non-overlapping positions on CSs, were interrogated using a 16 x 16 grid of evenly spaced point interrogations.

As has been detailed in the previous section, results in interrogation of cell samples are primarily influenced by the Young's modulus of the sample. Therefore, the data collected in the AFM adhesion measurements was again subjected to mathematical modelling for the extraction of Young's modulus values for the different cell lines; as introduced in §5.5.1 (p.103), and discussed in detail in Appendix 8.19 (p.260). The results are presented in Figure 58.

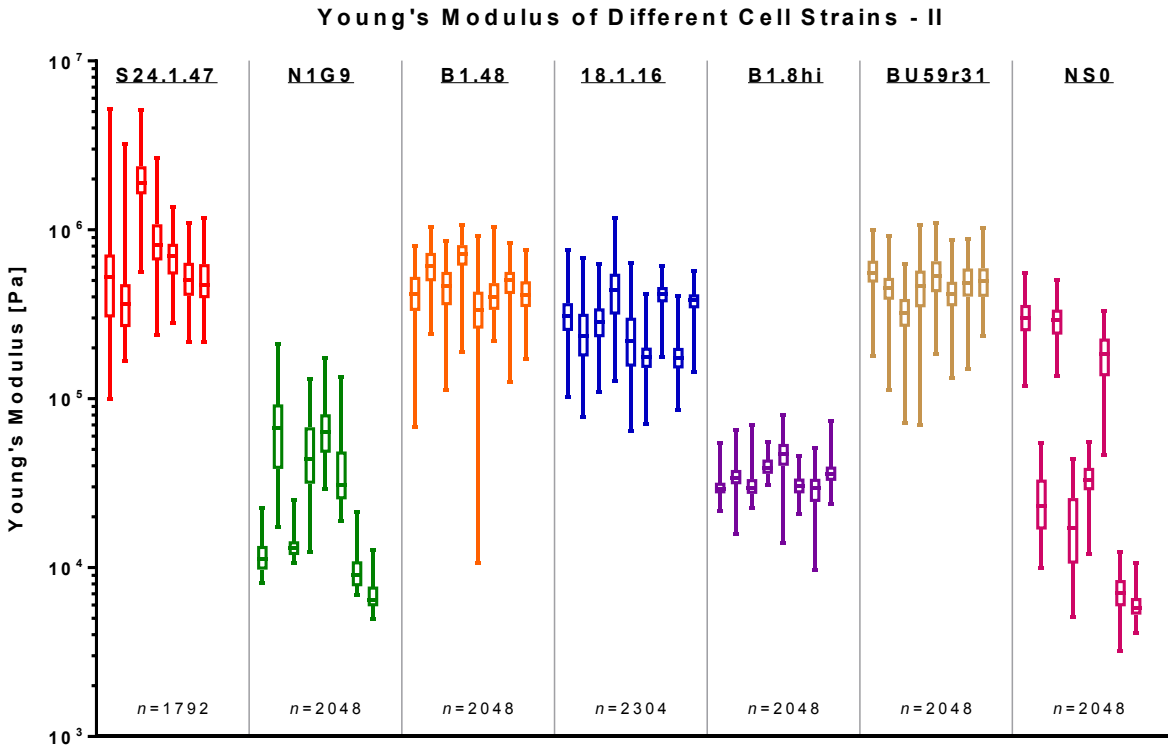

Figure 58 – Young's Modulus of Different Cell Strains - II.

Data from AFM adhesion measurements were subjected to mathematical modelling for the extraction of Young's modulus values for the different interrogated cell strains. Each cell line is shown in a separate colour. Boxes show 25th percentile, median, and 75th percentile, and whiskers show the minimum and maximum values, and each box and whiskers plot represents one cell. Each cell was interrogated using a grid of 16 x 16 evenly spaced point interrogations. Differences between all cell lines are highly significant ($p<0.0001$), accentuated by the high number of data points.

The results in Figure 58 show trends similar to the previous experiment (Figure 51). The Young's moduli for the majority of the hybridoma strains (S24.1.47: 0.82 ± 0.67

MPa; B1.48: 0.49 ± 0.18 MPa; 18.1.16: 0.30 ± 0.14 MPa; BU59r31: 0.47 ± 0.15 MPa) are at least one order of magnitude (13x) greater than for the B cell strain (B1.8hi: 35.21 ± 9.06 kPa), with the exception of the N1-G9 cell line (N1G9: 33.43 ± 31.39 kPa) for which the Young's modulus is greatly reduced compared to results from the previous experiment. Cells from the NS0 cell line (NS0: 0.11 ± 0.13 MPa) exhibit varied behaviour, where Young's moduli range from values lower than what is observed for B cells, to values as great as those recorded for hybridoma cells.

The reduced Young's moduli observed for N1G9 call into question the conformation of these samples, as these results deviate from what was previously seen for this cell line and from what is observed for similar samples.

Similarly, the variable results observed for NS0 are unexpected. It was expected that interrogation of NS0 cells would produce Young's moduli comparable to hybridoma cells. As previously discussed (§5.6; p.125), hybridomas are fusions of B cells and NS0 cells, where B cells have been shown to have substantially lower Young's moduli (Figure 51; p.150), hence it was expected that the greater Young's moduli of hybridomas was an attribute imparted by the NS0 portion.

Variable results for cell elasticities have previously been seen for unfixed cells (Figure 38; p.106), the cause for which were assumed to be degradation over time and exposure to environmental stimuli. The here interrogated cells, however, were fixed, and fixed samples are expected to be more resilient towards environmental conditions. Therefore, the N1G9, and NS0, cells will likely have experienced degradation prior to fixation, which is supported by the remaining cell samples producing results comparable to the previous experiment.

To determine whether the results of the experiment show differences between the different cell lines that are concurrent with their affinities, the different parameters that are calculated in the data analysis were inspected individually.

The first parameter that was inspected was again the force of interaction, shown in Figure 59.

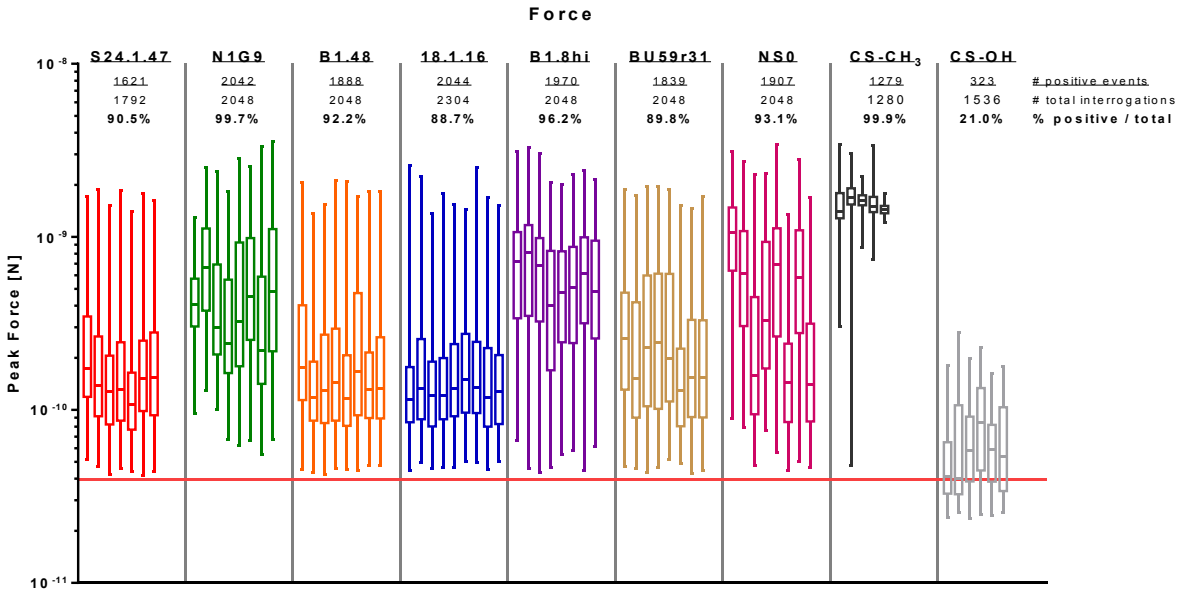

Figure 59 – Forces of Interaction - II

Shown are peak forces associated with positive adhesion events produced in interrogation of cells from different cell lines, and CSs. Each of the different samples is shown in a different colour. A minimum of 7 cells from each cell line, and a minimum of 5 non-overlapping position for CSs, were interrogated; each represented by a box and whiskers plot. Boxes show 25th percentile, median, and 75th percentile, and whiskers show the minimum and maximum values. The number of positively classed adhesion events, the total number of point interrogations, and the corresponding percentage ratio, is given for each sample group. The average limit for positive classification is shown by the red line across the graph. Differences between dissimilar samples are highly significant ($p<0.0001$).

The results in Figure 59 show the same trend that was observed in the previous experiment (Figure 52). The interaction forces produced in interrogation of the hybridomas with generally greater Young's moduli (S24.1.47: 0.25 ± 0.11 nN; B1.48:

0.27 ± 0.12 nN; 18.1.16: 0.24 ± 0.11 nN; BU59r31: 0.33 ± 0.12 nN) are lower compared to samples with lower Young's moduli (N1G9: 0.56 ± 0.16 nN; B1.8hi: 0.67 ± 0.17 nN; NS0: 0.62 ± 0.20 nN). Statistically, the differences between dissimilar data are highly significant ($p<0.0001$). The implications are again that a greater indentation depth in samples with lower Young's moduli produces an increased surface area of contact between probe and sample, allowing a greater number of molecular interactions to occur, subsequently requiring a greater force to rupture the tip-sample contact.

The values obtained in interrogation of the CSs compare well with the data acquired in the initial testing of the cantilever that was presented in Figure 50 in §6.1 (p.146); where results for interrogation of CS-CH_3 (1.58 ± 0.17 nN) are densely clustered, and the low number of positive adhesion events produced in interrogation of CS-OH (75.30 ± 40.48 pN) are low in magnitude. The interaction behaviour of the cantilever against the CSs remaining the same is indicative of no conformational changes occurring on the probe.

Data for the next inspected parameter – event 'significance' – are shown in Figure 60, which is calculated as in Equation 4 (p.93), and is used in the classification of point interrogations.

The results shown in Figure 60 are concurrent with the trends that have been observed for the determined forces of interaction. As in the previous experiment (Figure 53; p.153), the event 'significance' determined for samples with a lower Young's modulus (N1G9: 47.09 ± 13.77; B1.8hi: 70.10 ± 18.82; NS0: 56.09 ± 18.22), is on average, two-fold of what is observed for samples with a greater Young's

modulus (S24.1.47: 23.24 ± 10.52; B1.48: 25.84 ± 11.37; 18.1.16: 22.52 ± 10.20; BU59r31: 31.74 ± 11.72). The most extreme values are observed for the CSs (CS-CH_3: 158.50 ± 16.50; CS-OH: 12.79 ± 7.09).

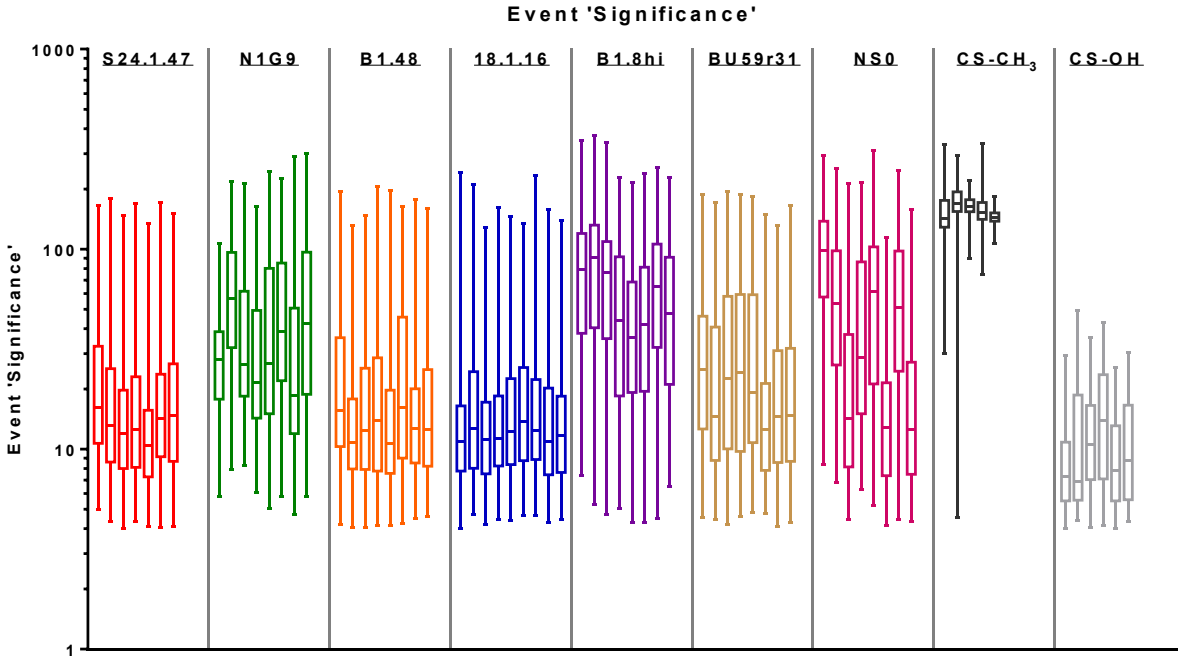

Figure 60 – Event 'Significance' of Positively Classed Adhesion Events - II.

The event 'significance' of all positively classed adhesion events is shown. Different sample groups are shown in separate colours. Results for individual cells, and individual areas on CSs, are represented by separate box and whiskers plots. Boxes show 25th percentile, median, and 75th percentile, and whiskers show the minimum and maximum values.

It can be expected that results for event 'significance' and force of interaction follow the same trend, as both take into account the maximum cantilever deflection. In addition, the event 'significance' takes into account the SD of the retraction curve baseline, where the similarity of the trends seen for both force of interaction and event 'significance' indicate that the variation of the retraction curve baseline is low, and consistent throughout the experiment.

The next inspected parameter, the separation distance, describes the distance over which the cantilever needed to be retracted to cause rupture of the probe-sample interaction; for which the data is shown in Figure 61.

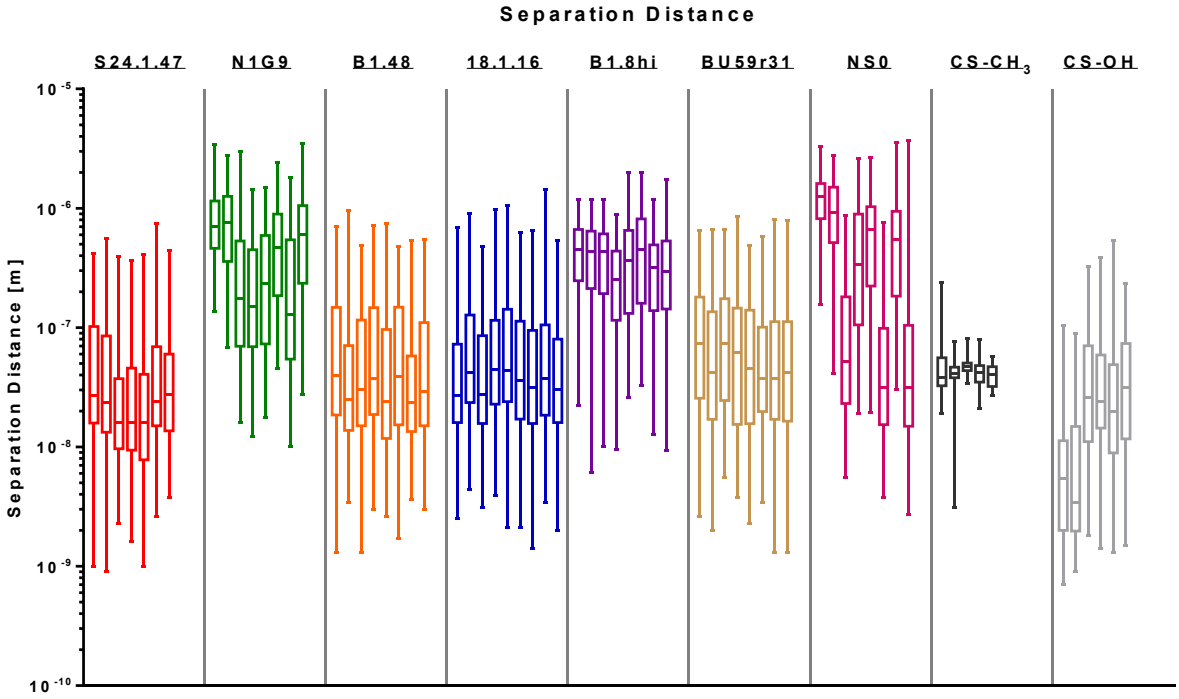

Figure 61 – Separation Distance - II

The separation distance for all positively classed adhesion events is shown, which describes the distance over which the cantilever needed to be retracted to cause rupture of the probe-sample contact. Different sample groups are shown in separate colours. Results for individual cells, and individual areas on CSs, are represented by separate box and whiskers plots. Boxes show 25th percentile, median, and 75th percentile, and whiskers show the minimum and maximum values.

The results in Figure 61 again show the separation distances for samples with lower Young's moduli (N1G9: 0.54 ± 0.17 µm; B1.8hi: 0.42 ± 0.10 µm; NS0: 0.59 ± 0.19 µm) to be greater than for samples with greater Young's moduli (S24.1.47: 54.91 ± 30.94 nm; B1.48: 88.04 ± 43.26 nm; 18.1.16: 92.84 ± 51.03 nm; BU59r31: 93.99 ± 43.36 nm).

As in the previous experiment (Figure 54; p.155), the observed differences between the different cell lines are amplified through the compounding effects of greater numbers of molecular interactions occurring for samples with a lower Young's modulus through greater indentation depths, as well as samples with a lower Young's modulus being more easily deformable and allowing for greater ranges of movement.

The results obtained for the CSs (CS-CH_3: 44.27 ± 7.25 nm; CS-OH: 45.75 ± 59.13 nm), are very similar to each other, and indeed this similarity between the two samples can be expected, despite their very different surface chemistries, as the Au substrates onto which the SAMs are deposited are rigid and hence do not offer any range of motion when pulled upon.

The results in Figure 62 show the energies of interaction, which are calculated as the area between the retraction curve and its baseline, as described with Figure 33 in §5.4 (p.91).

As in the previous experiment (Figure 56; p.158), the results in Figure 62 show the interaction energies for samples with a lower Young's modulus (N1G9: 0.24 ± 0.10 fJ; B1.8hi: 0.20 ± 0.08 fJ; NS0: 0.35 ± 0.17 fJ) to be an order of magnitude (11x) greater than what was observed for samples with a greater Young's modulus (S24.1.47: 14.47 ± 14.47 aJ; B1.48: 24.75 ± 21.25 aJ; 18.1.16: 24.87 ± 23.30 aJ; BU59r31: 28.36 ± 20.23 aJ).

The differences between dissimilar data are again accentuated by the energy of interaction being affected by both separation distance, and force of interaction, which have both been shown to be increased for samples with lower Young's moduli.

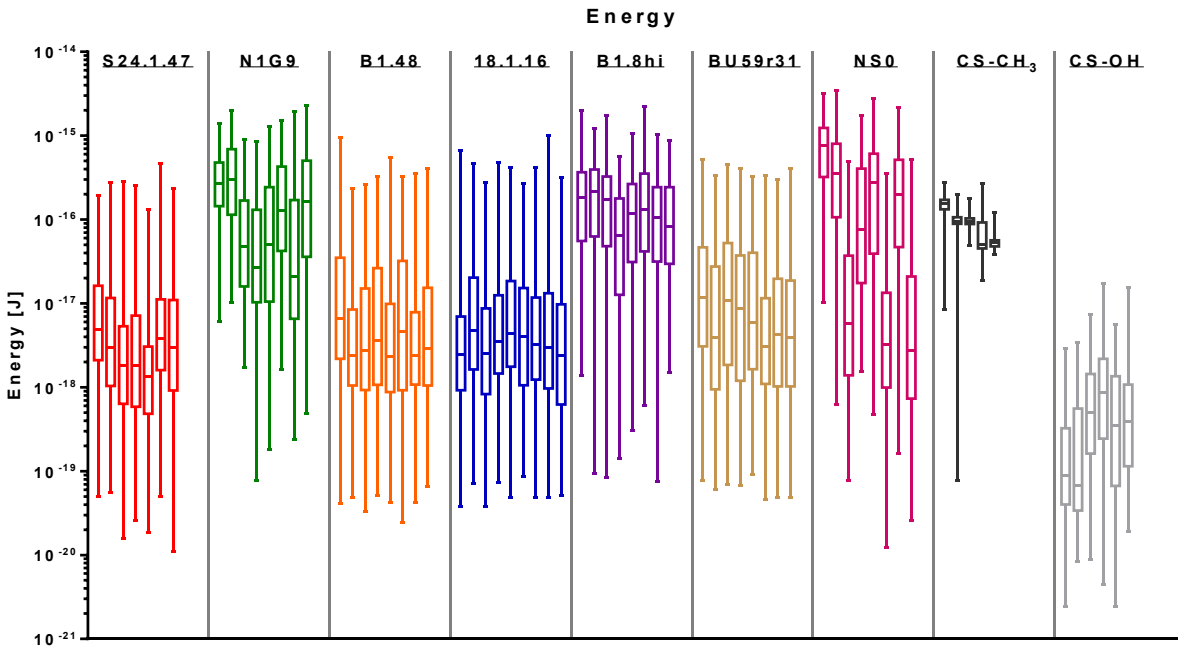

Figure 62 – Energies of Interaction - II

The energies associated with positive adhesion events are shown, where each box and whiskers plot represents the values determined for one cell, and the different colours denote the separate cell lines. Boxes show 25th percentile, median, and 75th percentile, and whiskers show the minimum and maximum values. The main difference in the data is found to be between samples of lower or greater Young's modulus, where the energies determined for samples with a lower Young's modulus are up to two orders of magnitude greater than for samples with a greater Young's modulus.

The values for CS-CH_3 (93.41 ± 15.88 aJ) are slightly lower than what is observed for the samples with lower Young's moduli, but the energies produced in interrogation of CS-CH_3 will, almost exclusively, be associated with the tip-sample interaction. Contributions from sample elasticity are expected to be negligible due to the high rigidity of the Au substrate onto which the SAMs are deposited. This is supported by the separation distance (Figure 61) for both CSs being the same. The energies produced in interrogation of CS-OH (1.14 ± 1.73 aJ) are more than an additional order of magnitude (20x) smaller than what was observed for cell samples with

greater Young's moduli, further demonstrating that very few interactions are occurring at tip-sample contacts.

Finally, the apparent loading rate was again inspected; showing results in Figure 63. This parameter is determined as described in §5.4 (p.91), and estimates the rate at which tip-sample contacts are loaded.

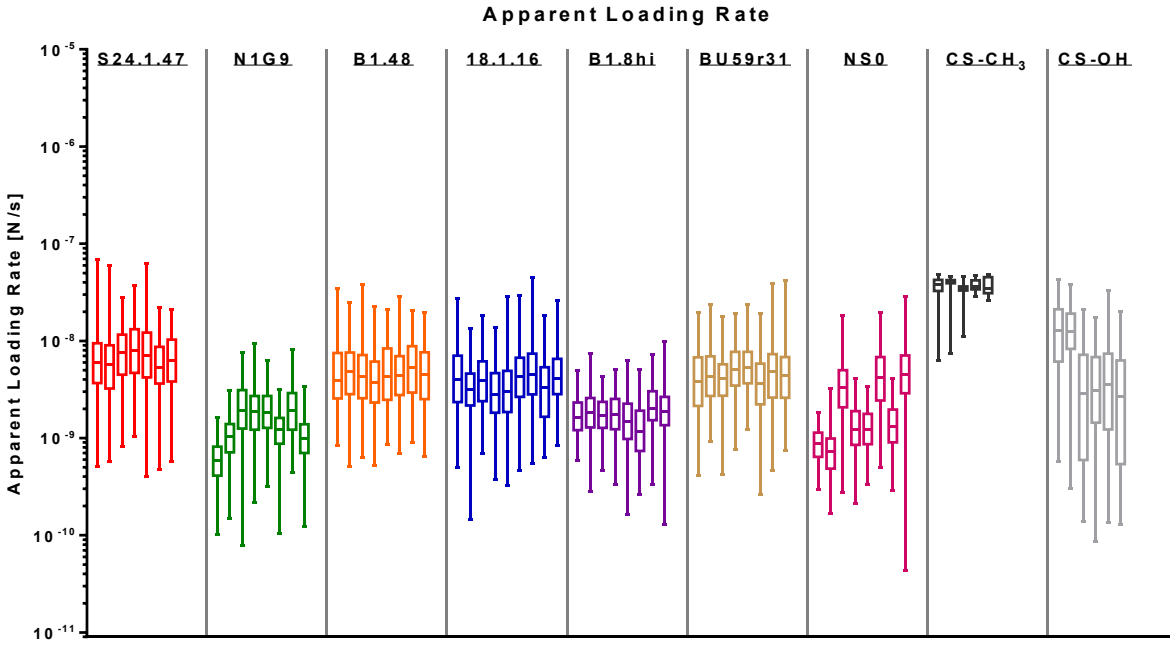

Figure 63 – Apparent Loading Rate - II

Showing the values of apparent loading rate for positively classed adhesion events. Boxes show 25th percentile, median, and 75th percentile, and whiskers show the minimum and maximum values, where each box and whiskers plot represents one cell, and the different cell lines are shown in separate colours. The main difference in results is determined by the Young's modulus of the different samples, where values for samples with lower Young's moduli are up to an order of magnitude lower than for samples with greater Young's moduli.

Figure 63 shows that similar results were obtained for samples with a greater Young's modulus (S24.1.47: 7.86 ± 2.28 nN/s; B1.48: 5.49 ± 1.48 nN/s; 18.1.16: 4.52 ± 1.22 nN/s; BU59r31: 5.37 ± 1.43 nN/s), which are increased compared to

samples with lower Young's moduli (N1G9: 1.63 ± 0.37 nN/s; B1.8hi: 1.92 ± 0.36 nN/s; NS0: 2.39 ± 0.79 nN/s).

The apparent loading rate is affected by both the force of interaction, and the separation distance; as previously described in Equation 6 (p.160). Hence, as in the previous experiment (Figure 57; p.159), the reduced loading rates that are observed for samples with lower Young's moduli show that the effects of a reduced Young's modulus outweigh the effects of increased numbers of molecular interactions that occur for samples with lower Young's moduli.

The results for CS-OH (7.15 ± 6.10 nN/s) are comparable to what is observed for cell samples with a greater Young's modulus. This is due to the small forces of interaction produced in interrogation of CS-OH (Figure 59; p. 165) being ruptured after very short distances (Figure 61; p. 168); due to the high rigidity of the Au substrate onto which the SAMs are deposited.

The Au substrate rigidity is the same for CS-CH_3 as for CS-OH, hence tip-sample interactions are ruptured after equally short distances. However, the interaction forces produced in interrogation of CS-CH_3 are high, therefore the resultant apparent loading rates (37.11 ± 2.74 nN/s) are the highest observed in this experiment.

Much like the previous experiment, the repeated interrogation of cells did not produce differences in any of the inspected parameters that are concurrent with the affinities of the interrogated cell lines. The differences that were observed between different cell lines, and cell types, are considered the results of the varying Young's moduli, where samples with lower Young's moduli allow for a greater depth of indentation at

constant compressive forces. The subsequently increased surface area of contact between tip and sample increases the frequency of molecular interactions, which increases the force, separation distance, and energy, required to rupture the tip-sample contact. Apparent loading rates, however, are reduced for samples with lower Young's moduli, demonstrating that a reduced Young's modulus affects results more than the increased frequency of molecular interactions that occur for samples with lower Young's moduli.

As in the previous experiment, results are considered to have been produced in non-specific interaction, as interrogations of cell lines specific for NP have produced results comparable to the non-specific cell line BU59r31, and the additionally included negative control cell line NS0.

The interaction profile produced in interrogation of the CSs is unchanged compared to initial testing of the used cantilever (Figure 50: NP7), which demonstrates that extensive interrogation of biological samples does not change the conformation of the tip modification, and that no contamination of the tip is occurring through parts of the interrogated samples becoming dislodged and adhering to the tip.

6.3 Investigation of Tissue Sections

In the same manner as for the investigation of cell samples, presented in the previous section, two germinal centres (GCs) in two separate tissue sections were investigated in the two separate experimental sessions. Despite the investigation of prepared cantilevers not revealing unequivocally successfully functionalised cantilevers, the interrogations were conducted to test the behaviour of tissue sections in AFM adhesion measurements, and determine whether the behaviour of cells in tissue sections shares similarities with isolated immobilised cells. As for the investigation of cell samples, the treated cantilevers that were used for the interrogation of the two GCs were NP1 and NP7 from the first and second experimental session respectively.

At the time of the experiments, it was not possible to integrate the AFM with an inverted optical microscope, and hence brightfield and fluorescence images of the interrogated tissue sections were taken after interrogation via AFM on separate microscopes. For the purpose of later registration of the different data, images were taken of the cantilever in the corner positions of the scan field, to act as reference points.

In preparation for AFM interrogations, tissue sections were stained immunohistologically to allow identification of GCs by labelling the surrounding structures. The GCs themselves were at first not stained, in order to not saturate the targeted receptors, however, after AFM interrogation, fluorescent staining was applied to the GCs to demonstrate NP-specificity of the interrogated areas. The protocol for the preparation of the tissue sections can be found in Appendix 8.21 (p.276).

6.3.1 Germinal Centre I

The tissue section that was interrogated first can be seen in Figure 64, which shows a brightfield image of the immunohistology staining in which the structures surrounding the GCs have been labelled. The T-zone (T) – labelled in blue – is adjacent to the GC (GC), and the B follicle (B) – labelled in brown – surrounds the GC. The GC itself was not labelled so as to not occupy the NP specific receptors targeted in the AFM interrogation. The red square is the to-scale 100 µm x 100 µm area in which the tissue section can be interrogated via AFM without physically adjusting the position of the sample. In order to acquire the most possible information, the instrument was set up to interrogate the whole of the maximum possible area marked by the red square. The position of the red square is a close approximation of the area actually interrogated via AFM, where an exact registration of the data acquired on different instruments could not be made.

With the software setup available at the time, the interrogation area could be probed with a maximum of 128 x 128 evenly spaced point interrogations. The area was scanned consecutively, four times completely, with a final fifth scan that was terminated prematurely; acquiring a total of 80528 data points over the course of 63 h. The data shown in Figure 65 is the summation of the 5 individual scans, where the values of individual parameters for the same locations were summed up. Individual parameters are shown in separate maps, alongside a point ID map; akin to the overview maps initially introduced in Figure 34. The results for the individual scans are shown in Appendix 8.22 (p.281).

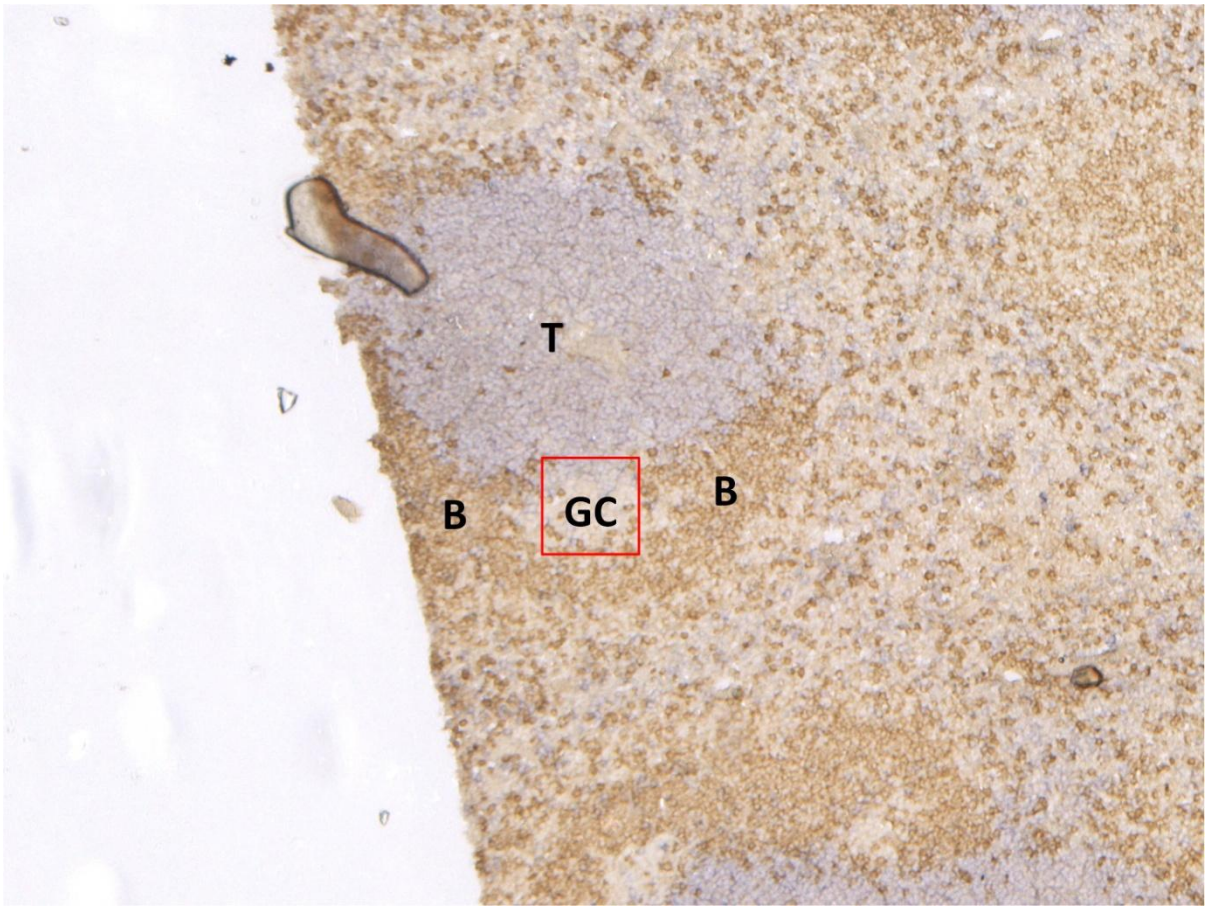

Figure 64 – Brightfield Image of GC-I

Brightfield image of a mouse spleen section containing the first scanned GC (GC). The T-zone (T) was labelled in blue by staining for CD3. The non-stained GC (GC), is adjacent to the T-zone, and is surrounded by the B follicle (B), which was labelled in brown by staining for IgD. The red square is the to-scale 100 µm x 100 µm area that can be interrogated on the AFM instrument without physically adjusting the position of the sample, where the position of the red square is a close approximation of the area actually interrogated via AFM. The image was acquired on a Leica DM6000 with a 10x lens.

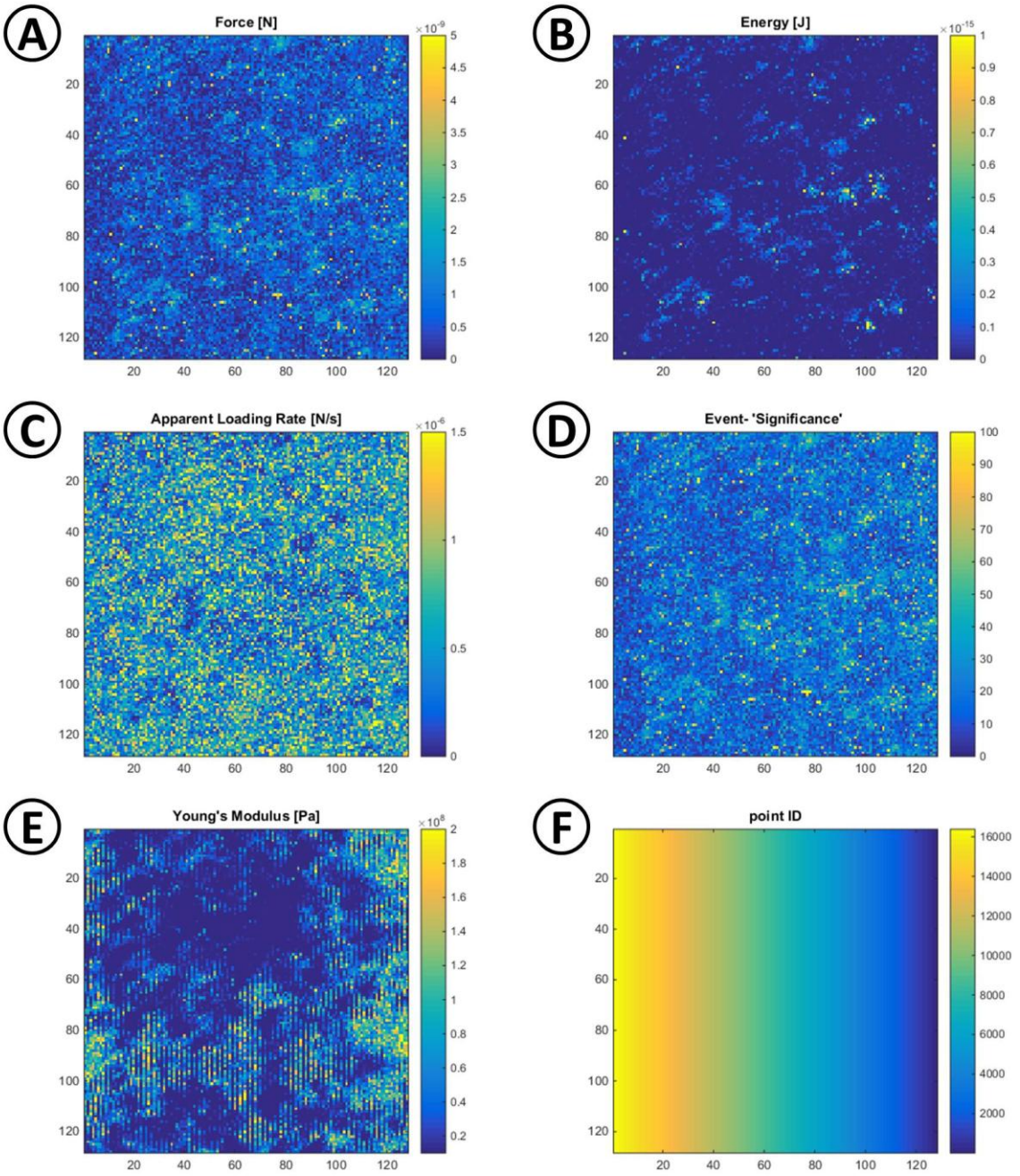

Figure 65 – AFM Results for GC-I

Shown is the combination of the 5 scans of the same tissue section area, where values of individual parameters at the same location were summed up. Individual maps show values of force of interaction (A), energy of interaction (B), apparent loading rate (C), event 'significance' (D), Young's modulus (E), and point ID (F). The point ID map shows that the orientation of the AFM data was adapted, to match the orientation of the microscope images. The x and y axes are divided into 128 segments, denoting the number of points; rather than distance.

The results in Figure 65 show that noticeable areas of increased energies can be observed in (B), which correspond to, less accentuated, high forces and event 'significance' in (A) and (D) respectively. Conversely, these same areas correspond to low magnitudes of apparent loading rates in (C). Inspection of the results for the individual scans (Appendix 8.22; p.281) reveals that the identified areas can be observed in each of the scans. As the individual scans are reproducible, their summation leads to better representation of high/low magnitude areas and to a reduction in background noise.

The concurrence of high forces/energies with low apparent loading rates stands out. Similar concurrencies were seen previously in the interrogation of cells (§6.2; p.148), where, primarily influenced by the Young's modulus of the sample, high forces/energies, paired with low apparent loading rates, were seen for samples with a lower Young's modulus, and vice versa. The different parameter maps in Figure 65 show this relationship to be varied across the interrogated area, suggesting that the elasticity of the tissue section changes locally.

While the map in (E) confirms that the Young's modulus of the tissue section varies across the interrogated area, it does not reveal a direct concurrence of high forces/energies with a reduced Young's modulus of the sample.

In order to assess whether the stand-out areas identified from the AFM data match up with specific structures in the tissue, the tissue section was stained fluorescently after AFM interrogation. The images are shown in the panel in Figure 66; showing brightfield illumination in (A), cell nuclear staining in (B), staining for NP-specificity in

(C), and, to aid in comparison, in (D) the previously shown brightfield image of the immunohistology staining that was applied before interrogation via AFM.

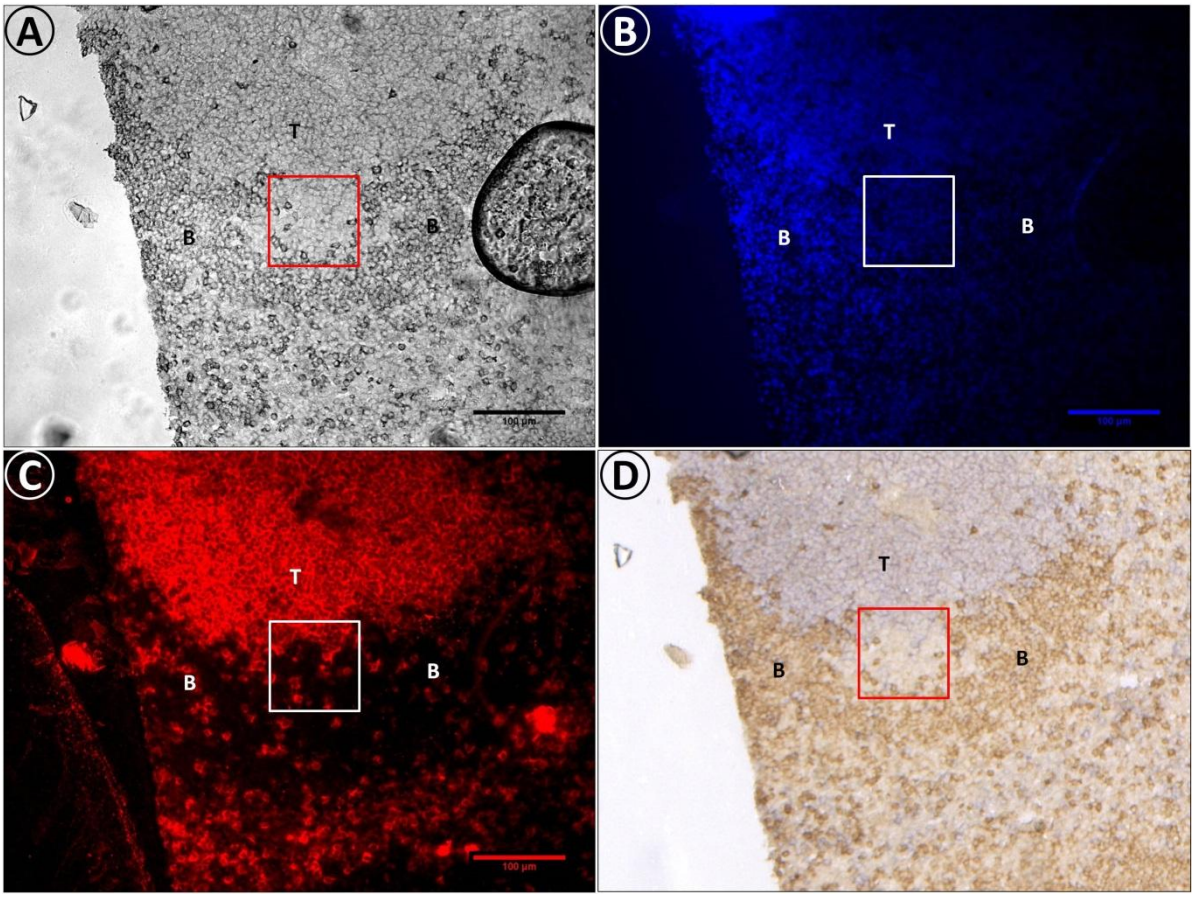

Figure 66 – Fluorescent Staining of GC-I

The tissue section was stained fluorescently after interrogation via AFM. Images show brightfield illumination (A), cell nuclear stain (B), stain for NP-specificity (C), and, to aid in comparison, the immunohistology staining prepared before interrogation via AFM (D). The red/white square in each image is 100 µm x 100 µm, to-scale, and closely approximates the area actually interrogated via AFM. The position of the T-zone (T), and the B-follicle (B), are marked in each image to aid in orientation. Images were acquired on a Leica DM6000 with a 10x lens.

The images shown in (A) and (D) of Figure 66 demonstrate that good spatial registration can be achieved between images acquired on different instrument setups, and the detected fluorescence shown in (B) has identified the individual cells present in the interrogated tissue section.

The detected fluorescence shown in (C) does not appear to have successfully identified NP specific regions that are expected to be found in the GC, and instead very closely mimics the $CD3^+$ staining seen in blue in (D). Taking into consideration that, at the stage at which the fluorescent staining was applied, the tissue section had already gone through several cycles of rehydration and drying, and that, as previously mentioned, proteins are susceptible to damage upon dehydration [63], it is plausible that the targeted NP-specific receptors could not be successfully labelled due to their degradation.

Inspection of the separate staining panels, as depicted in Figure 67, reveals that, in the absence of NP-specific labelling, the fluorescent marker applied for the identification of NP-specific cells, reacted only with a portion of the much earlier applied staining for T cells. Considering the different staining panels as independent experiments, allowed for this mislabelling to occur. However, even if NP-specific cells could have been successfully identified, it would not have created images that demonstrated NP specificity in the interrogated regions. This is because in the applied staining strategy both the desired NP-specific cells would have been labelled, as well as simultaneously the $CD3^+$ T-zone due to the aforementioned cross-reactivity of the used reagents.

Comparison of the AFM results with the different microscope images of the interrogated tissue section does not reveal any clear concurrencies. The high energies in Figure 65(B) are seen primarily centrally, and towards the bottom half of the map, which does correspond to the GC, where NP specificity would be expected,

and lies below the T-zone, where NP specificity would not be expected, but even though the individual scans of the GC via AFM have repeatedly produced the same areas of high/low magnitudes, these areas cannot clearly be assigned to visible structures within the tissue.

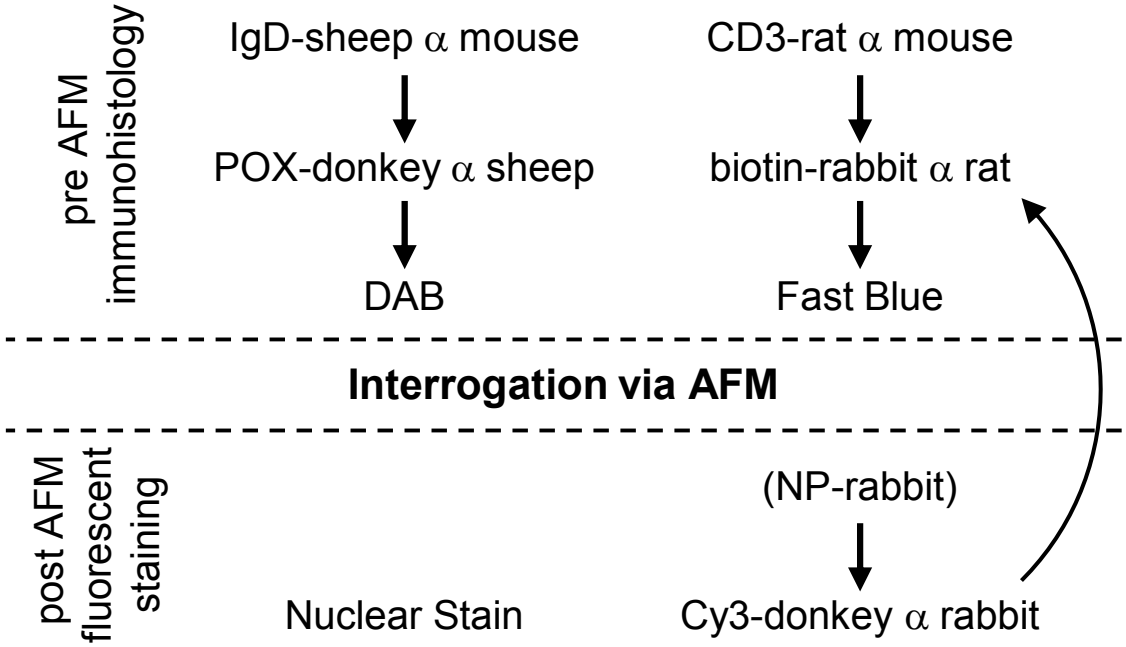

Figure 67 – Tissue Section Staining Panels

Schematic for the different staining panels that were applied to the investigated tissue sections. The immunohistology staining applied prior to AFM interrogation stained non-activated naïve B cells that are IgD^+ in brown, and T cells that are $CD3^+$ in blue. Post AFM interrogation, a cell nuclear stain was added to identify individual cells, and NP-specific receptors were to be labelled with Cy3. The Cy3-donkey antibody is specific towards rabbit antibody, and, in the absence of NP-specific labelling, reacted only with the earlier applied staining for T cells.

6.3.2 Germinal Centre II

The second interrogated GC (GC-II) is shown in Figure 68, showing a brightfield image of the immunohistology staining that was applied prior to interrogation via AFM, in which the structures surrounding the GC have been labelled. The T-zone (T) – labelled in blue – has three GCs (GC) adjacent, which are surrounded by the B follicle (B) – labelled in brown. The GC that was interrogated is contained within the red square, which marks the to-scale 100 µm x 100 µm area in which the tissue section can be interrogated via AFM without physically adjusting the sample position.

The AFM instrument software was updated for the second experimental session, and now allowed for the scannable area to be probed with up to 512 x 512 evenly spaced point interrogations. The 100 µm x 100 µm field was, however, not interrogated with the maximum number of points possible, as this put too much demand on the PC linked to the AFM instrument, which would lead to (parts of) individual data points not being recorded. The scannable area was instead interrogated once with a grid of 256 x 256 evenly spaced point interrogations; acquiring 65536 data points over the course of just less than 23 h.

The results of the AFM interrogation of GC-II are presented in Figure 69, showing separate maps for the determined parameters of force (A), energy (B), apparent loading rate (C), event ‘significance’ (D), Young’s modulus (E), and point ID (F); where the orientation of the data was again matched to the orientation of the tissue section images.

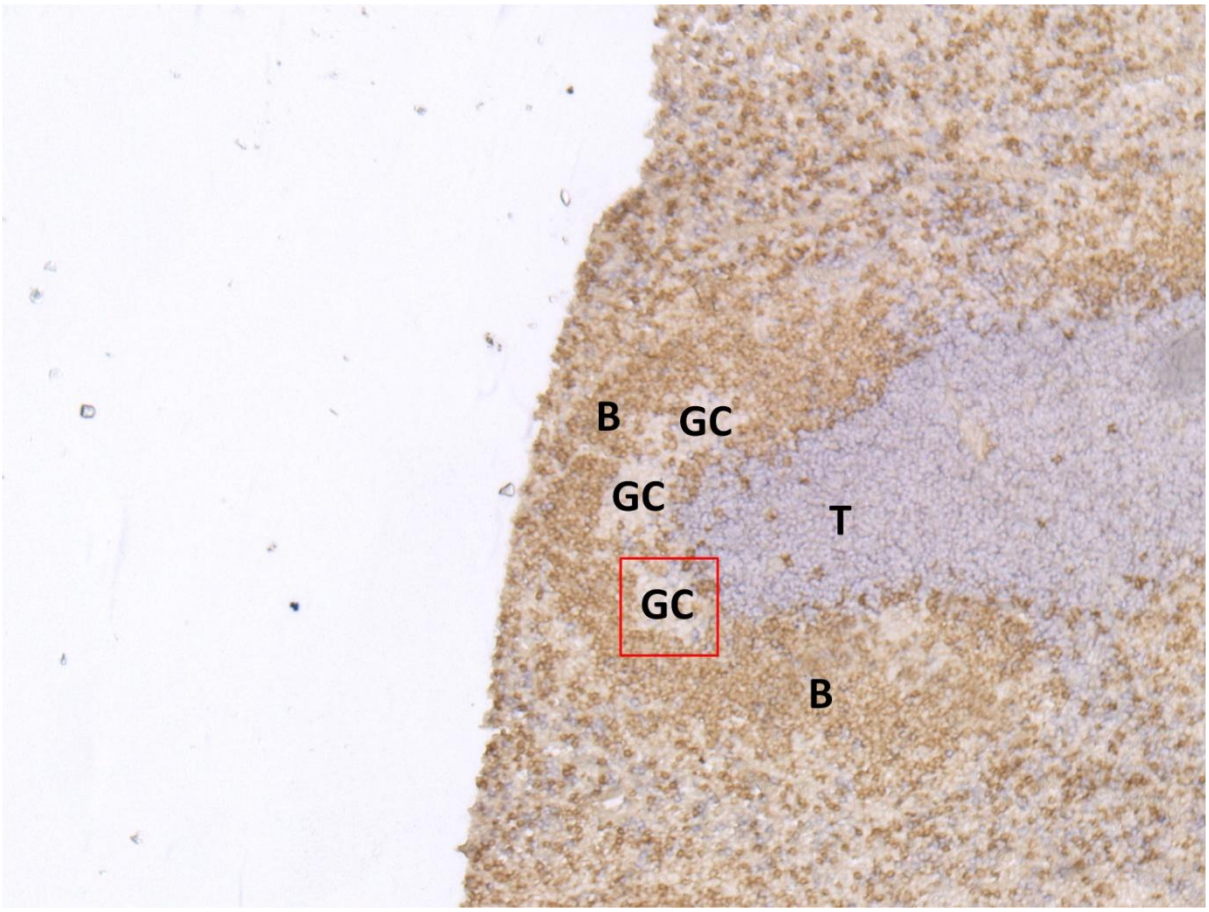

Figure 68 – Brightfield Image of GC-II

Brightfield image of the immunohistology staining that was applied to a section of a mouse spleen to identify GCs by labelling surrounding structures. Three non-stained GCs (GC) are visible in the tissue section. These are adjacent to the T-zone (T), which was labelled in blue by staining for CD3, and are surrounded by the B follicle (B), which was labelled in brown by staining for IgD. The GC interrogated via AFM is contained in the red square, which marks the to-scale 100 µm x 100 µm area that can be interrogated via AFM without physically adjusting the sample position. The position of the red square is a close approximation of the area actually interrogated via AFM. The image was acquired on a Leica DM6000 with a 10x lens.

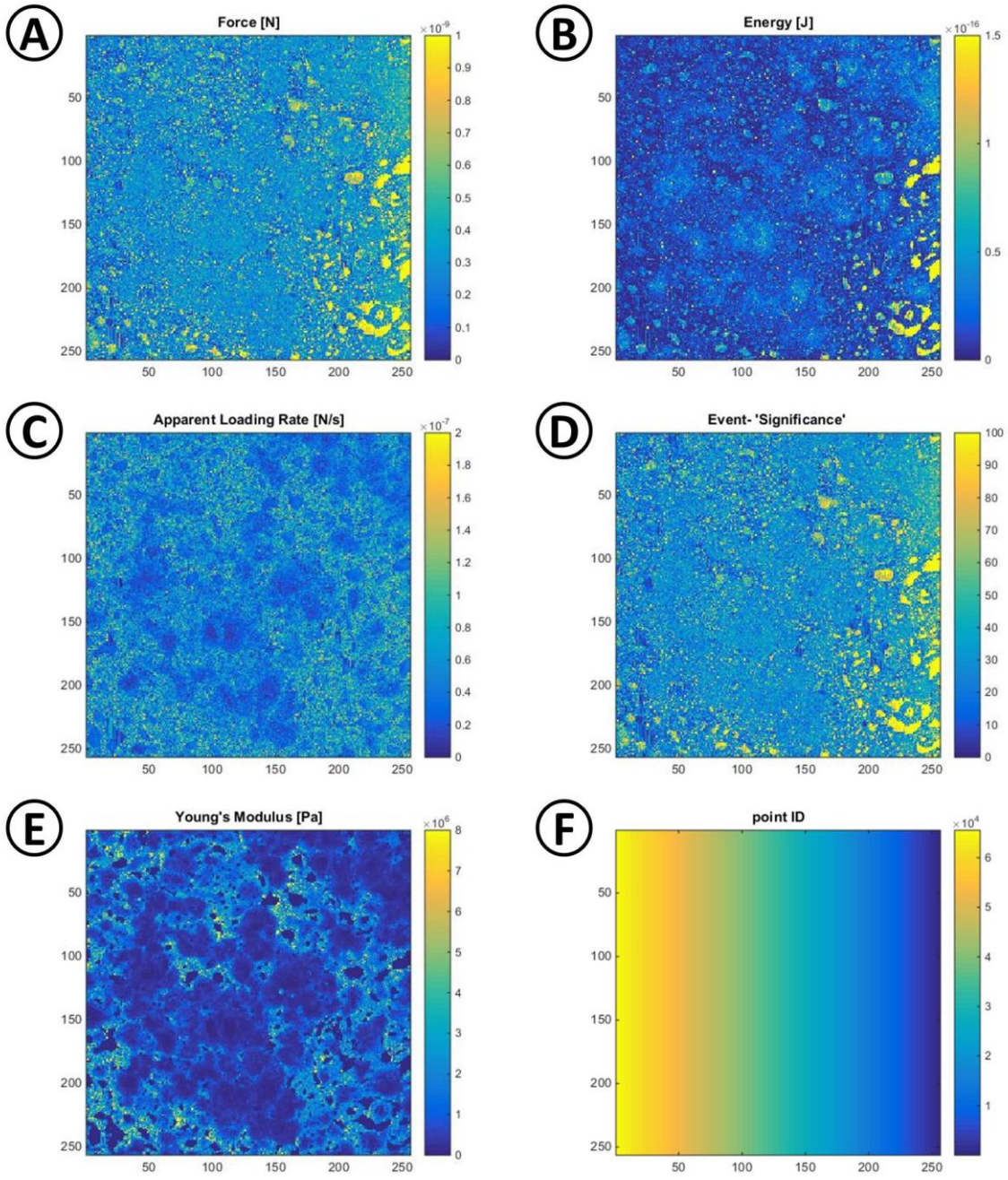

Figure 69 – AFM Results for GC-II

Shown are the results from the AFM interrogation of GC-II, with individual maps showing force of interaction (A), energy of interaction (B), apparent loading rate (C), event 'significance' (D), Young's Modulus (E), and point ID (F); where the orientation of the data was matched to the orientation of the microscope images. The division of the x and y axes into 256 segments denotes the number of points; rather than distance.

The data in Figure 69 shows that, as previously for GC-I (Figure 65), there is a concurrence between high forces, energies, and event 'significance', which, conversely, correspond to low apparent loading rates. However, the AFM results for GC-II appear to be more coherent. Instead of the detection of seemingly isolated points of high/low magnitude, that only through their repeated occurrence over multiple scans highlighted general areas of interest, a single scan has produced parameter maps in which general areas of high/low magnitude can more easily be identified, and which, furthermore, contain smaller regions with identifiable boundaries.

The concurrence of high energies with low apparent loading rates, again, suggests that the Young's modulus of the sample changes across the interrogated area. Unlike for GC-I, the Young's modulus map in (E) shows a clear concurrence of decreased Young's modulus with increased forces/energies. These same concurrencies were observed initially in the interrogation of cells in §6.2 (p.148). There the conclusion was that for samples with a lower Young's modulus greater depths of indentation occur at constant compressive forces. The subsequently increased surface area of contact between tip and sample increases the frequency of molecular interactions, which subsequently require greater forces/energies to be ruptured.

In order to assess whether the stand-out areas identified in the AFM interrogation correspond to specific structures within the tissue, the tissue section was stained fluorescently after AFM interrogation. The images are shown in the panel in Figure 70, showing brightfield illumination in (A), cell nuclear staining in (B), staining for NP-specificity in (C), and, for ease of comparison, the previously shown brightfield

image of the immunohistology staining that was applied prior to interrogation via AFM in (D).

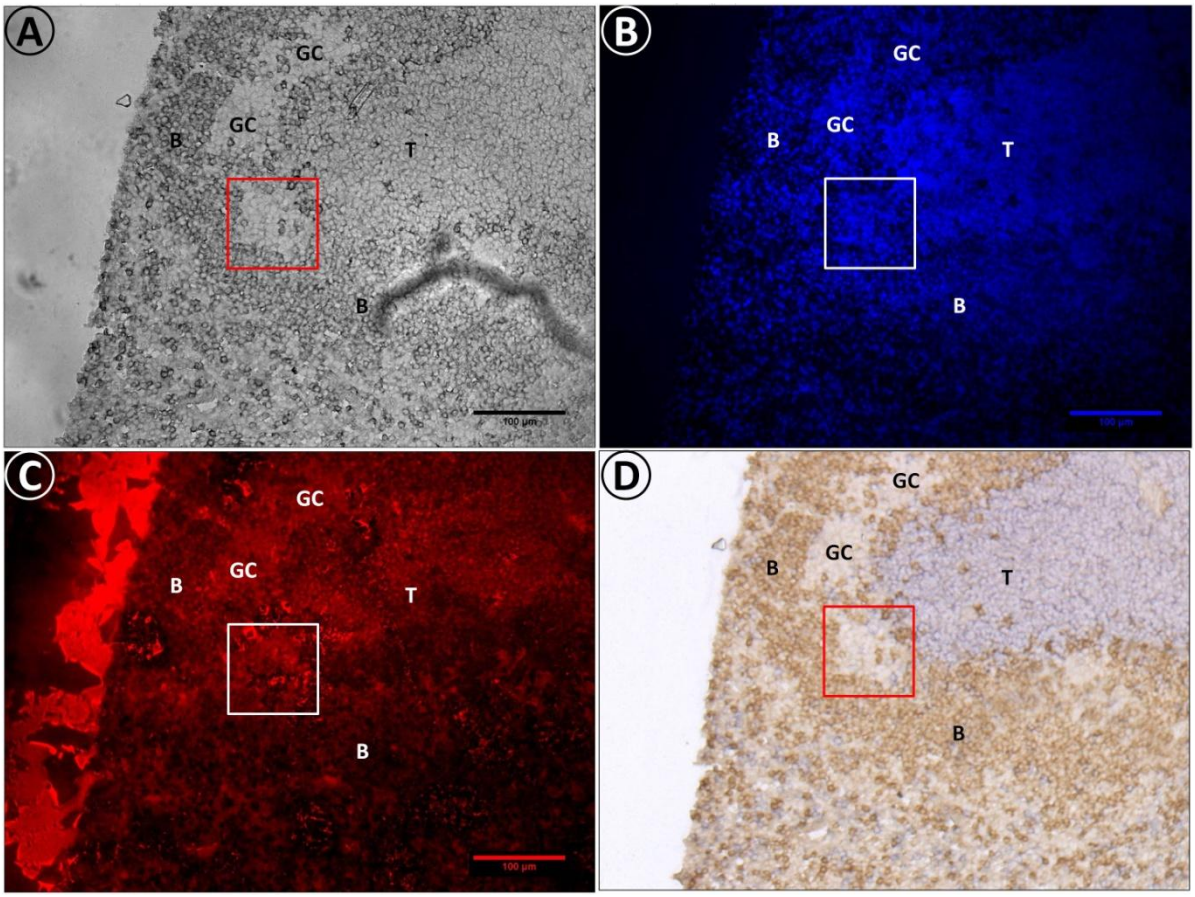

Figure 70 – Fluorescent Staining of GC-II

The tissue section was stained fluorescently after interrogation via AFM to demonstrate NP-specificity of the interrogated GC. Images show brightfield illumination in (A), cell nuclear stain for identification of individual cells in (B), stain for NP-specificity in (C), and, to aid in comparison, the previously shown brightfield image of the immunohistology staining prepared before the interrogation via AFM in (D). The red/white square in each image is 100 µm x 100 µm, to-scale, and closely approximates the area actually interrogated via AFM. The position of the T-zone (T), and the B-follicle (B), and additional, un-interrogated GCs (GC) are marked in each image to aid in orientation. Images were acquired on a Leica DM6000 with a 10x lens.

The images (A) and (D) in Figure 70 show that a good spatial registration can be achieved between images acquired on different instrument setups, and (B) shows how the individual cells in the interrogated tissue section have been identified.

The staining in (C), with which the NP-specificity of the interrogated GC was to be demonstrated, did not identify the expected areas. As discussed with the results for GC-I, the tissue sections are exposed to environmental conditions during transport and storage prior to interrogation via AFM, and undergo multiple cycles of freezing, drying, and rehydration before the application of fluorescent staining. During exposure to these conditions degradation of the targeted receptors can occur, which prohibits the detection of NP specificity both via AFM and fluorescent staining. Furthermore, both the GC-I, and GC-II, tissue sections were treated together with the staining strategy described in Figure 67, hence even if NP specific receptors were available, they would not have been labelled exclusively due to the cross-reactivity of the used reagents.

Due to the increased coherence of the AFM results, however, comparison to the microscope images of the stained tissue sections is more intriguing. In Figure 71 the different images of the stained tissue sections have been reduced to the areas of interest, and have been lined up alongside the different parameter maps. A free drawn line has been added to all the images to further aid in comparison. As can be seen most clearly in images (E) and (H), the added line mimics the border between the GC and the surrounding B follicle. When added to the different parameter maps of the AFM results, this line follows the outside of a large central region of low signal intensity in (A) and (D), and follows the outside of multiple smaller regions of high magnitude in (B) and low magnitude in (C). As is apparent from the images, the added line is not in the same position in relation to the borders of the areas of interest and the borders of the different parameter maps. As previously mentioned, the AFM results and the images of the stained tissue sections were acquired on different,

independent instruments, and hence an exact positional registration was not possible.

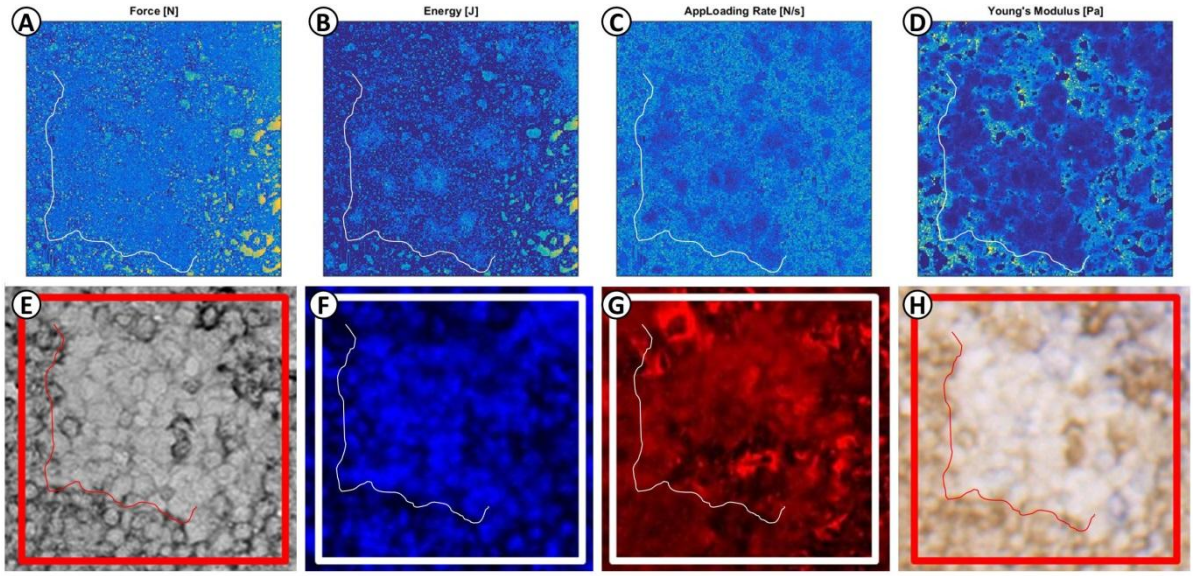

Figure 71 – Comparison of AFM to Optical Data

Images of the stained tissue sections were reduced to the areas of interest, and placed alongside the different parameter maps produced from the AFM interrogation of the tissue section; where an additional line in all the images was drawn to further aid in comparison. The position of the added line in relation to borders of the parameter maps, and the borders of the images, is not the same, where exact spatial registration between data acquired on different, independent instruments could not be made. Parameter maps from the AFM interrogation show: force (A), energy (B), apparent loading rate (C), and Young's modulus (D). Microscope images show: brightfield illumination of fluorescently stained tissue section (A), cell nuclear stain (B), stain for NP specificity (C), and immunohistology staining applied prior to AFM interrogation (H).

While it has to be accepted that the results of the AFM interrogation cannot be considered to have been produced in specific interaction of the probe with the sample, there is a strong concurrence of reduced Young's modulus (D) with the unstained GC (H). The implication of this concurrence is that the Young's modulus of the tissue section was increased locally through the immunohistology staining applied prior to AFM interrogation, forming chemical complexes to visualise the T-zone and B-follicle.

Attempts to match individual cells, as for example visible in (E), to low Young's modulus sub-regions of the GC in (D), are tempting, but may lead to an over-interpretation of the data. Due to the optical translucency of the tissue sections, individual cells can be identified in microscope images, as optical information is collected from throughout the tissue section. To AFM, however, only the surface of a sample is accessible. As illustrated in Figure 72, this means that indentation of the sample occurs in positions where not always the membranes of cells in the tissue are exposed. While undoubtedly this has implications on the availability of targeted receptors, the amount of cell membrane in the tissue section in the direction of compression will also influence the local elasticity of the sample.

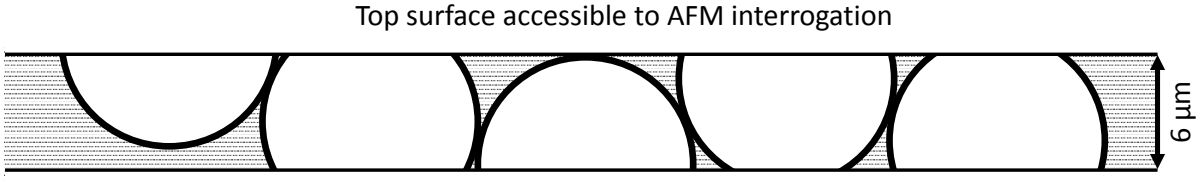

Figure 72 – Cells in a Tissue Section

Tissue sections do not necessarily contain whole cells, and both the interior of a cell, and cell membrane, may be exposed at the tissue section surface. Due to optical translucency of the tissue section, optical information in microscope images is collected from throughout the tissue section, whereas to AFM only the surface of the sample is accessible.

Due to the lack of information on the distribution of cell membrane in the tissue section, however, an assessment of how it affects the relative elasticity of the sample could not be made.

6.4 Discussion of the Testing of NP Functionalised Cantilevers and their Application to Biological Samples.

Based on the results presented in Chapter 5, a self-selecting quality of the developed technique was identified, in which successfully NP functionalised cantilevers would be selective towards only specific interactions. The implication of that behaviour was that even low magnitude adhesion events, which were expected to be produced in the interrogation of lower affinity samples, would be distinguishable; even if the magnitudes were in the region of what was previously identified as non-specific interactions. Based on those findings it was deemed reasonable to conduct experiments in which the technique was employed in the investigation of different biological samples.

Firstly, the observed self-selecting nature of NP functionalised cantilevers, in interrogation against biological samples, was to be used in the identification, and subsequent characterisation, of successfully modified cantilevers. In addition to the interrogation of high affinity hybridoma cells (S24.1.47), as was previously conducted in Chapter 5, functionalised cantilevers were also tested against a selection of CSs. Successfully functionalised cantilevers were to distinguish themselves through the produced adhesion events in interrogation of cell samples – in both their frequency of occurrence as well as their magnitude – and the interaction profile produced in interrogation of CSs would subsequently serve as a characteristic identifier of such cantilevers prior to future investigations of biological samples. The use of CSs for this purpose is preferable, as their preparation is less laborious than the preparation of

cell samples, more readily available, decidedly more consistent, and CSs are less susceptible to degradation during storage.

Experiments were conducted with two separate groups of cantilevers functionalised with NP under slightly varied preparation parameters, and each cantilever was then used in the interrogation of cells and the separate CSs.

The results obtained from both experimental sessions (§6.1; p.137) were similar, where the interrogation of cell samples failed to replicate the results that were previously obtained in Chapter 5. Instead of producing high forces at a low frequency, the obtained forces ranged from values comparable to what was previously seen for specific interaction (Figure 44; p119), to just above the detection limit, at a frequency at least 2-fold of what was previously observed (Figure 42; p.114).

Failure to replicate previous results on cells may be due to a variety of reasons. In the absence of measures whereby which unequivocally successfully functionalised cantilevers can be identified, the possibility of failed cantilever functionalisation cannot be excluded. This is in spite of the results of the interrogation of the CSs, which exhibit the trend that interrogations of CS-CH_3 produce high frequencies of adhesion events with high forces, and that the few adhesion events produced in interrogations of CS-OH are with low forces that lie just above the detection limit. As discussed in §6.1 (p.137), these trends are indicative of hydrophilic surface chemistries having assembled on the tip; which the NP functionalisations are expected to be.

Further, despite differences in the preparation parameters of the functionalised cantilevers, the interaction profiles that are produced in the interrogation of cells and CSs are similar, suggesting that similar chemistries assemble on the modified cantilevers, and, thus, giving confidence in the validity of the proposed modification scheme.

Failure to replicate previous results on cells may, further, be due to the conformation of the interrogated samples. As has previously been discussed, proteins such as the targeted receptors are susceptible to damage upon dehydration.[63] Due to the location of the employed facilities and equipment, samples could not be interrogated immediately after preparation, and degradation may have occurred during necessary short-term storage or transport.

The investigation of the different available hybridoma cell lines was conducted on the premise that successfully functionalised cantilevers would produce only specific interactions. Consequently, low magnitude adhesion events that were expected to be produced in the interrogation of low affinity samples, would be distinguishable, even if their magnitudes were in the region of what was previously classed as non-specific interactions. Because the preceding investigations did not identify a successfully functionalised cantilever in either experimental session (§6.1; p.137), it was consequently not unexpected that the produced results were not indicative of specific interactions occurring. In fact, the interactions produced in the interrogation of the NP specific hybridoma cell lines were the same as for the non-specific cell lines. This suggests that no specific binding has occurred, based on the assumption that in the interrogation of non-specific cell lines no specific binding can occur.

A portion of the interaction forces produced in the interrogation of cells in §6.1 (p.137) and §6.2 (p.148) where in the region of what was previously identified as specific interactions in interrogation of S24.1.47 cells (Figure 43; p.117), which means that these data sets may have been produced in a combination of specific and non-specific interactions. Differentiation of these different interactions may be achievable through more extensive analysis of collected data. As discussed by Noy, *et al.*, [121], distinction between single and multiple, simultaneous bonds is achievable through further analysis of retraction curves. As shown in Figure 73, fitting of models to the portion of the retraction curve that describes bond loading allows characterising the tip-sample interaction according to the number of bonds involved (N.B. presentation of the force curves in Figure 73 is inverted compared to the standards adopted in this thesis). Such analysis sub-routines could be incorporated into the currently available analysis algorithms, however, a training data set, containing a known combination of (multiples of) specific and non-specific interactions, would be required to extend functionality to the differentiation of specific and non-specific interactions.

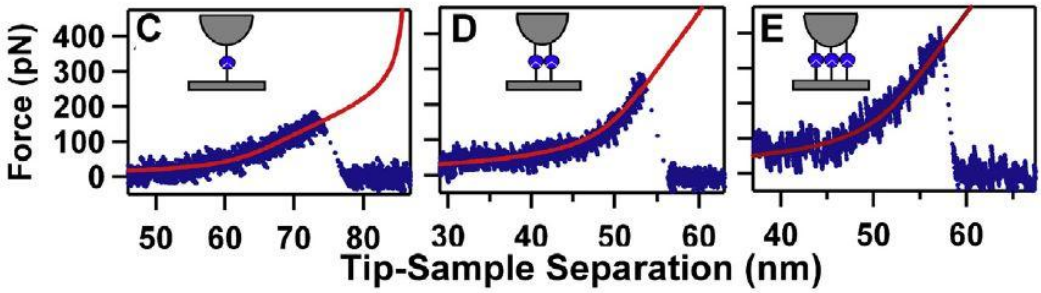

Figure 73 – Distinguishing Between Single and Multiple Bond Interactions

Fitting of models to the portion of the retraction curve that describes bond loading allows characterising the tip-sample interaction by the number of bonds involved. The loading regimes differ distinctly for the involvement of single (C), two (D), or three (E) bonds. Image taken from [121].

The main finding from the interrogation of the different cell lines was that the elasticity of the sample was the principal influence on the parameters describing the probe-sample interaction. At constant compressive forces, a greater depth of indentation is produced for samples with a lower Young's modulus, creating a greater surface area of contact between the probe and the sample. The consequently increased frequency of molecular interactions required greater forces for the rupture of tip-sample contacts.

The differences in the results for the different cell lines, and cell types, could all be attributed to their differences in Young's modulus. Generally, the results for the structurally similar hybridomas were comparable, as were results for the different B cell samples; with the greatest differences observed between the different cell types.

Because of the shown impact of the elasticity of the sample on obtained results, future experiments should routinely determine the elasticity of the interrogated sample. Additionally, methods may need to be explored that will allow compensating for the elasticity of the sample. Such compensatory measures would need to consider the local sample elasticity for each point interrogation, seeing that the interrogation of tissue sections has already shown that elasticity can vary substantially across individual samples.

At the end of each experimental session, a GC (GC-I and GC-II) was also interrogated using the developed AFM technique; each contained in a separate tissue section. These interrogations were conducted in an effort to identify NP

specific binding in a GC, as well as measure the strength of binding; one of the ultimate aims of the project.

GC-I was scanned multiple times consecutively, where seemingly isolated points of high/low magnitude were identified in each individual scan. Through the summation of the individual scans, however, it was made apparent that points of high/low magnitude were identified consistently in the same locations; highlighting general areas of interest.

These general areas of interest did, however, not have identifiable boundaries, preventing a matching to structures in the tissue that were visible in the microscope images. As previously mentioned (initially in Figure 64; p.176), the squares in the microscope images that mark the area of interrogation are to-scale, but spatially are an approximation of the area actually interrogated via AFM. To make this approximation, images were taken of the cantilever in the corner positions of the scan field, to act as reference points for the later registration of the different data. Thus, despite being an approximation, the spatial discrepancies are expected to only be minimal. This means that the AFM data could not be matched to structures in the tissue, because the AFM interrogation did not reveal any, rather than such attempts being made of unrelated data.

In comparison, the interrogation of GC-II produced more coherent results. A single scan of GC-II produced parameter maps in which general areas of interest were more easily identifiable, and also contained smaller regions with distinct boundaries. Close comparison of the AFM data with the microscope images (Figure 71; p.188) revealed that locally the Young's modulus was reduced substantially in the area of

the unstained GC. The variations of the different parameters across the interrogated area vary in accordance with the sample's Young's modulus, which is the same behaviour that was previously observed for cell samples (§6.2; p.148).
The comparison in Figure 71 (p.188) also further illustrates how the spatial registration of the different data is not exact, but that a close approximation was achieved.

Many of the issues encountered in the interrogation of tissue sections could be addressed with the integration of the AFM instrument with a fluorescence microscope. Instead of the immunohistological staining, required for the identification of GCs, fluorescent labels could be used. Further, efforts to minimise spatial discrepancies between data acquired on separate instruments would no longer be required.

In the interrogation of the GCs specific interaction was not detected, for which multiple possible reasons exist. The used cantilevers could not be identified as unequivocally successfully functionalised in §6.1 (p.137), hence the specificity of the probes remained unproven. Furthermore, the conformation of the tissue sections has been a concern. The fluorescent staining of the tissue sections did not show NP specific binding in the GC as would be expected, which calls into question the availability of the NP specific receptors. As discussed previously, the tissue sections go through multiple cycles of freezing, drying, and rehydration, prior to fluorescent staining. Instead of attempting to apply all the desired stains on the same tissue section, adjacent tissue sections could be used in future, where one section could be

used in the AFM interrogation, and fluorescent stains could be applied to the pristine adjacent section.

Degradation of the targeted receptors during exposure to these conditions may be one of the reasons that the fluorescent staining failed. However, degradation may have also occurred prior to interrogation via AFM. Figure 71D and H (p.188) show how the sample's Young's modulus is increased substantially where immunohistological staining was applied, and the formation of the chemical complexes of the immunohistological staining may interfere with the targeted receptors.

Lastly, as alluded to in Figure 72 (p.189), the method of preparation of the tissue sections themselves may be inherently ill-suited for interrogations via AFM. Unlike immunohistological, or fluorescent, staining that can label targeted structures by diffusing into the tissue, AFM can access only the exposed surface of a tissue section. The frequency with which the cell membrane of individual cells will be exposed at the surface is unknown, but assuming a stochastic distribution of cells within tissue, that frequency is likely very low. An alternative tissue section preparation method would be the use of a vibratome, which as reported by Christ, *et al.*, [122], can be used to produce tissue sections with viable cells exposed at the surface. A quantification of the frequency of exposed viable cells at the surface was not provided, and the substantially increased section thickness (225 μm) poses new challenges with regards to sample immobilisation, but the technique may aid in producing tissue section that are better suited for interrogations via AFM.

While the interrogation of different biological samples yielded some unintended, yet interesting, results, it has highlighted primarily the continued need for measures through which the identification of successfully functionalised cantilevers can be achieved prior to the investigation of samples in which probe specificity is required. Given the knowledge that interrogations were conducted with a specific probe, more detailed assessments of sample quality would be possible, and future efforts could be concentrated on eliminating factors that adversely affect sample quality. Such efforts could include assessing the extent to which denaturation of BCRs may occur prior to interrogation via AFM, e.g. during sample preparation, and how sample preparation techniques can be improved to minimise their effects on the targeted receptors.

7 Conclusions and Outlook

This project was sponsored through a studentship in the Centre for Doctoral Training (CDT) in the Physical Sciences of Imaging in Biomedical Sciences (PSIBS). The centre recruits researchers from the engineering and physical sciences to bring new skills and perspectives to tackle problems in the biomedical sciences. Ideologically, the centre is located at the interface of the physical sciences, biomedical sciences, and computer science, aiming to equip researchers with solid foundations in each discipline, supported by a co-supervisor in each, to tackle multidisciplinary projects. While this format requires researchers to embrace steep learning curves, in order to familiarise themselves with the fundamental principles of multiple, initially alien, disciplines, it also grants researchers access to knowledge, expertise, and equipment beyond any one discipline. The downside to this progressive approach, however, is that the facilities that could cater to the full scope of such an inclusive project do not yet exist; an issue that certainly affected this project throughout:

The data presented in this thesis was acquired almost exclusively using instruments housed in the Chemical Engineering (CE) department; i.e. contact angle analysis, ellipsometry, and atomic force microscopy (AFM). However, supplementary facilities that were required for sample preparation are not available. The CE department does not have a fume hood, which is an unconditional prerequisite for the safe use of Piranha solution that is required in the preparation of control surfaces (CSs). Consequently, CSs could not be assessed directly after preparation, and methods for the safe storage and transport of CSs needed to be considered. Subsequently, this called into question the effects of such storage and transport methods on the samples themselves.

Similarly, the CE department does not have cell culture facilities, such as incubators or cell culture hoods. This again meant that samples could not be interrogated directly after preparation, and methods for storage and transport were an issue; the investigation of the effects of different sample preparation techniques was partially inspired by this.

Use of the instruments in the CE department is shared between many researchers, which, particularly for the AFM, meant that access was limited and needed to be booked sometimes months in advance. This increased the importance of individual experimental sessions, granting reduced opportunity for adjustments throughout, and limiting the number of parameters in sample preparation technique and AFM cantilever functionalisation that could be investigated in isolation. Extended access to instruments was possible primarily through the help of co-supervisor to this project, Dr. James Bowen, who was managing the facilities during the time of the project.

In my opinion, future projects that are seeking to operate in, and across, multiple disciplines will benefit greatly from more centralised facilities.

With regards to what the project set out to achieve, progress towards establishing a technique that enables measuring B cell receptor affinity maturation in germinal centres (GCs) *in situ* was made.

The proposed modification scheme of AFM cantilevers to achieve specificity towards the targeted receptors is still considered suitable for the intended application. The attachment of the intermediary linker molecule, as well as the subsequent addition of

(4-hydroxy-3-nitrophenyl)acetyl (NP), occurs through covalent bonds. These are irreversible under physiological conditions [123] and the forces required to break them are an order of magnitude greater than what is expected to be observed for the targeted interaction.[38,46,60,61] That means that once assembled, the cantilever functionalisation will not be compromised by the conditions encountered in application.

Furthermore, the modification scheme avoids the use of proteins, unlike the modification scheme used by Natkanski, *et al.*, [55]; the only other study that could be identified in which AFM cantilevers were equipped with NP. Because the modification scheme employed by Natkanski included the use of proteins, freshly prepared cantilevers needed to be used in experiment directly after preparation. Such an approach was not feasible for replication in this project due to the aforementioned location of the available facilities, but, furthermore, it limits flexibility in planning and conducting experiments.

The results for the CSs that were investigated for their feasibility as readily available control measures for the identification of successfully functionalised cantilevers are somewhat inconclusive. While the results of the investigation of the CSs themselves have shown that these can be prepared with good consistency, interaction profiles characteristic for functionalised cantilevers could not be established, due to the lack of unequivocally successfully functionalised cantilevers. Thus, the premise of testing functionalised cantilevers against well-defined chemistries, and using their interaction profiles to demonstrate successful functionalisation, continues to bear many

advantages. However, it first requires the establishment of trustworthy baseline values against which a comparison can be made.

Concurrently, problems were encountered with the preparation of CS-NH_2, and CS-COOH, which were to be used as model positively and negatively charged surfaces, respectively. Because these surfaces could not be prepared in the correct conformation reproducibly, they were not used in the interrogation of functionalised cantilevers against CSs. This meant that the charge of functionalised cantilevers could not be assessed, and primarily only their wetting properties were assessed in interrogation against neutral hydrophobic and hydrophilic surfaces CS-CH_3, and CS-OH, respectively.

One of the possible reasons for CS-NH_2 and CS-COOH not exhibiting the expected properties was identified as incorrect alignment of the self-assembled monolayer (SAM) molecules on the substrate. This could however not be confirmed. Using angle-resolved X-ray photoelectron spectroscopy (XPS), the conformation of the CSs could in the future be assessed in more detail, determining the orientation of deposited molecules and quantifying the ratio of correctly and incorrectly orientated molecules.

Further use of the CS approach could be made in the continued investigation of the assembly of the tip functionalisation chemistry. The assembly of the NH_2 SAM on freshly cleaned substrates could be imaged with (high-resolution) AFM imaging, as could the subsequent addition of NP. This interrogation could provide valuable insight into the optimal concentration of NH_2 SAM deposition solution for the subsequent NP addition to be unaffected by steric effects.

Furthermore, functionalised cantilevers could be periodically tested against freshly prepared CSs to quantify any potential degradation of the cantilever functionalisation over time; an approach that has already shown that no conformational changes on functionalised cantilevers occur during extensive interrogation of biological samples (§6.2.2; p.162).

Supplementations to the current experimental setup will be required for future experiments aimed at the interrogation of tissue sections with increased throughput. Such a supplementation would be the integration of a fluorescence microscope with the AFM. This was already considered throughout the project, and while physically this integration is possible, the acquisition of a compatible system was far beyond the financial constraints of this project.

With the aid of an integrated system, spatial registration of AFM data to optical images could be performed directly, eliminating the current discrepancies between the two data. Further, the current immunohistological approach for the identification of regions of interest in tissue sections could be replaced with fluorescent staining. While fluorescent staining, like any staining, will add mass to the tissue section, which will impact the interrogation of the sample to some degree, it avoids the formation of chemical complexes on the surface of the sample, which has already been seen to greatly impact the local elasticity of tissue sections.

Ultimately, the project achieved to address all the aims set out in §2 (p.14); albeit with varying degrees of success. While the chemistry employed in the proposed cantilever

modification scheme is considered to be suitable for the intended application, with results in Chapter 5 showing clear differentiation between specific and non-specific binding events, and the developed data analysis methods having facilitated the detailed analysis of large amounts of varied AFM data, the interrogation of the different biological samples in Chapter 6 highlighted the need for control measures whereby which successfully functionalised cantilevers can be identified prior to the interrogation of precious samples in which specificity of the probe is required. In the absence of such control measures, it cannot be said if the interactions measured in the interrogations in Chapter 6 are non-specific due to the lack of specificity of the probe, or due to the absence of NP specific receptors on the samples.

Once control techniques have been established to demonstrate successful tip functionalisation, future progressions of this project can more intensively focus on further improving sample preparation techniques, after which the developed AFM technique can be used more extensively in elucidating the role of affinity in regulating the fundamental processes occurring in GCs.

8 Appendices

8.1 Cantilever and Control Surface Preparations

8.1.1 Cantilever Functionalisation Protocol

1. The proposed cantilever modification scheme is based on the use of cantilevers that are pre-coated in Au. The cantilevers used in this project were:

    1. CSC17/Cr-Au, MikroMasch, USA
    2. OMCL-RC800PB, Olympus, USA

    where (2) was used only when the preferred (1) had become unavailable.

2. To eradicate all possible biological contaminants on the cantilevers prior to functionalisation, they are treated in piranha solution, consisting of:

- 7 parts sulphuric acid (H_2SO_4) – Sigma-Aldrich, USA
- 3 parts hydrogen peroxide (30% (w/w) H_2O_2) – Sigma-Aldrich, USA

3. Piranha solution is highly toxic and corrosive; therefore:

- appropriate personal protective equipment must be worn at all times
- work should only be conducted in clean fume hoods
- volumes no greater than 100 mL should be prepared
- the solution should be prepared fresh every time prior to use
- the solution should not be stored

4. To prepare the Piranha solution:

- place a clean beaker into an ice water bath
    - inspect the beaker for damages prior to use
- pour the sulphuric acid into the beaker
- pour the hydrogen peroxide into the beaker

- Upon mixing of the two chemicals the solution boils instantaneously; therefore, allow the solution to cool (~30 mins) before use

- Once work with Piranha solution is completed, turn the beaker onto its side in the ice water bath, allowing the solution to be diluted at least 10-fold
- Flushing with copious amounts of water, pour the solution down the sink

5. Use the Piranha solution to clean all glassware:
    - Pipette required amounts into glassware
    - Leave for ~20 mins
    - Decant Piranha solution back into the beaker
    - Rinse with 18 MΩ deionised water
    - Rinse with HPLC ethanol
    - Allow to dry in the fume hood
6. Clean cantilevers using Piranha solution
    - Place cantilevers into a cleaned glass dish, with the tips pointing upwards
    - Spot a droplet of Piranha solution onto the tip
        - Larger volumes of Piranha solution can be used, but oxidation bubbles will cause the cantilever chip to float, making extraction of the cantilevers from solution without damage more difficult
    - Leave for ~20 mins
    - Wash the cantilever in 18 MΩ deionised water, by moving it gently below the water surface
    - Wash the cantilever in HPLC ethanol, as previously in water

7. Prepare the amine-terminated alkanethiol (ATAT), and NP-O-Succinimide, deposition solutions as detailed in Appendix 8.1.3 (p.211).

8.1. Step 1 of modification scheme

- Place the cleaned cantilevers in 1 mM ATAT deposition solution, resting them on the bottom of the dish
- Cover the dish with a lid to prevent contamination, and reduce evaporation of the solution

➢ The time of immersion of the cantilevers in deposition solution was a parameter in the preparation protocol that was investigated, and varied between 1 and 24 h

- After desired immersion time, wash the cantilever in HPLC ethanol
- Wash the cantilever in 18 MΩ deionised water

8.2. Step 2 of modification scheme

- Place the cantilevers in NP-O-Succinimide solution, resting them on the bottom of the dish
- Leave for 24 h
- Cover the dish with a lid to prevent contamination, and reduce evaporation of the solution

9. Dry and store

- Remove the cantilevers from the solution and wash in 18 MΩ deionised water

- Dip the cantilevers in HPLC ethanol and subsequently place on a dry glass surface repeatedly to dry them
- Place cantilevers in an adhesive gel box for safe transport, and storage in the dark under ambient conditions

8.1.2 Control Surface Preparation

The preparation of CSs is for the most part the same as for the functionalisation of the cantilevers detailed previously in 8.1.1.

1. The substrate that was used for the preparation of the CSs was:
    - polycrystalline Au with 30 nm thickness on a 4 inch diameter silicon (100) wafer, pre-coated with titanium for better adhesion; nominal RMS surface-roughness < 1 nm; Georg Albert PVD – Beschichtungen, Silz, Germany
2. Cutting of silicon wafers
    - Place the silicon wafer onto a clean soft surface, with the Au-coated side facing down
    - Using a ruler and a diamond tipped scribe, weaken the back of the silicon wafers, marking the lines over which to first break them into stripes, and subsequently into 0.5-1.0 cm^2 chips
3. Follow steps 2. through 5. in 8.1.1 for the preparation of Piranha solution and cleaning of all glassware
4. Clean silicon wafer segments
    - Immerse segments in Piranha solution for ~20 mins, and periodically move them around gently to free them of oxidation bubbles and re-submerge them in solution

- Wash segments in 18 MΩ deionised water
- Wash segments in HPLC ethanol

5. Molecule deposition

- Place the cleaned segments in 1 mM deposition solution, resting them on the bottom of the dish
    - Deposition solutions are prepared as detailed in the subsequent Appendix 8.1.3 (p.211).
- Cover the dish with a lid to prevent contamination, and reduce evaporation of the solution

➢ The time of immersion in deposition solution for the CSs was 24 h, varying only for CSs on which the NH_2 SAM formation was investigated

6. Dry and store

- After desired immersion time, wash the cantilever in HPLC ethanol
- Blow dry with a stream of nitrogen
- Store prepared CSs individually in a bijoux filled with 18 MΩ deionised water, and keep in a light sealed box
- Blow dry with a stream of nitrogen again before use

8.1.3 Solution Preparations

The preparation of some of the used solutions includes the use of DMSO, which is known to dissolve some plastics, and therefore the use of plastic consumables has been avoided in the preparation of all solutions; instead using only glass containers, pipettes, and weighing boats that had all first been cleaned with Piranha solution.

8.1.3.1 Preparation of SAM Deposition Solutions for Control Surfaces

The SAM deposition solutions for the preparation of the different CSs were prepared at 1mM concentrations, and 10mL of solution were required to fill the used dishes. The table below details the amounts of each compound required in the preparation; which were dissolved in HPLC ethanol.

Amounts of Compound Required

The table details the amounts of compound required for the preparation of 10 mL of deposition solution, at 1 mM concentration, for the preparation of the different CSs.

Label	Compound	Chemical Formula	Molecular Weight	Required Amount [mg]
CS-CH_3	Dodecane-1-thiol	$HS(CH_2)_{11}CH_3$	202.40	2.02
CS-NH_2	11-Mercaptoundecan-1-aminium chloride	$HS(CH_2)_{11}NH_2HCl$	239.85	2.40
CS-COOH	11-Mercapto-undecanoic acid	$HS(CH_2)_{10}COOH$	218.36	2.18
CS-OH	11-Mercapto-1-undecanol	$HS(CH_2)_{11}OH$	204.37	2.04

The different compounds were purchased from:

- CS-CH_3: Sigma-Aldrich, USA. Cat.# 471364
- CS-NH_2: ProChimia, Gdansk, Poland. Cat.# FT004-m11-0.2
- CS-COOH: Sigma-Aldrich, USA. Cat.# 674427
- CS-OH: Sigma-Aldrich, USA. Cat.# 674249

Solution Preparation:

- Weigh out the amounts specified in the table into a glass vial
- Add 10 mL of HPLC ethanol into the vial. With the aid of intermittent stirring the compounds should dissolve within 10 mins

8.1.3.2 Preparation of NP-OSuc Solution

The preparation of the NP-OSuc solution consists of:

- 1 part 20 mg/mL NP-OSuc (Biosearch Technologies, Inc., USA. Cat.# N-1010) in DMSO (Sigma-Aldrich, USA)
- 5 parts 3% $NaHCO_3$ (Fisher Scientific International Company, Loughborough, UK) in water

1. Preparation of $NaHCO_3$ buffer

- Weigh out 0.3 g of $NaHCO_3$ into a glass vial, and add 10 mL of 18 MΩ deionised water to dissolve the compound
- The solution should be clear within 30 mins with the aid of intermittent stirring

2. Preparation of NP-OSuc constituent

- Weigh out 20 mg of NP-OSuc into a glass vial
- Add 1 mL of DMSO to dissolve the compound, aiding with intermittent stirring

3. Combining solutions

- Add 5 mL of the $NaHCO_3$ buffer to the vial containing the NP-OSuc constituent
- Place the vial into a warm water bath or incubator overnight at 37°C for all NP-OSuc fragments to dissolve completely

8.2 Formation of Self-Assembled Monolayers

The process of SAM formation is depicted diagrammatically below.

a) Deposition molecules in solution arrive at the substrate, and the molecule head group physisorbs onto the substrate.

b) The molecule head group chemisorbs to the substrate. For the alkanethiol molecules used in this project, specifically, that means formation of covalent bonds between the S head group of deposition molecule and Au substrate.

c) Increasing numbers of molecules attach to the substrate, attempting to occupy all available binding sites. Van der Waal's interactions between adsorbed molecules are affecting molecule orientations.

d) All available binding sites are occupied, and the fully formed SAM has equilibrated.

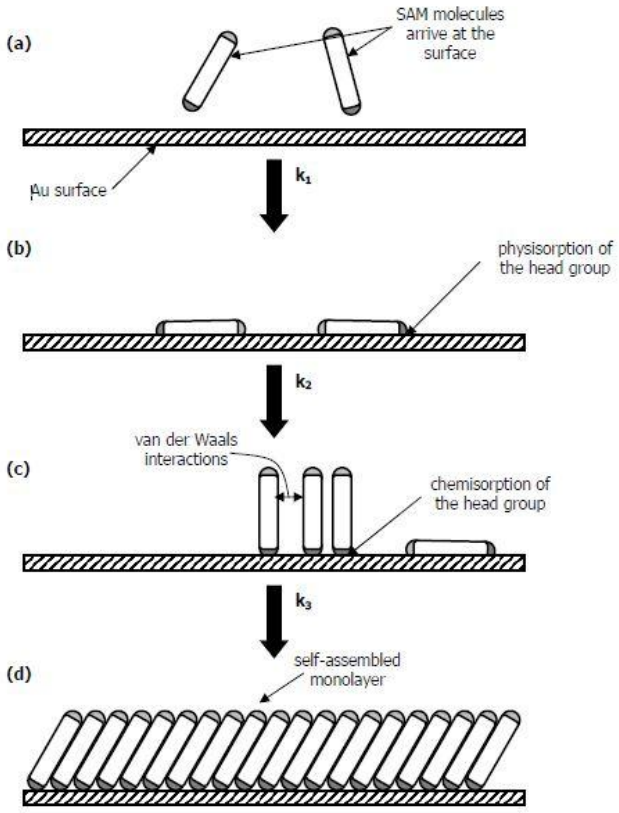

Image taken from [124]

8.3 Control Surface Compounds in ChemBioDrawUltra

The compounds used in the preparation of the CSs were created in the software package ChemBioDrawUltra, and the length of the molecules, as unstrained in free space, measured using the software package ChemBio3D.

The following pages show images of the modelled compounds as displayed by ChemBio3D, and their lengths measured in Ångstrom from the S element to the final element in the chain. The lengths are given to a precision of fractions of Ångstrom, which is a precision that is typically generated by computer software that is not realistic. Rounded to the nearest Ångstrom, however, the molecules used for the preparation of CS-CH_3, CS-NH_2, CS-COOH, and CS-OH, would all be of the same length. Therefore, the values are shown in the aforementioned fashion (to 2 decimal places), to show that, if only theoretically, the deposition molecules are of different lengths.

8.3.1 CS-CH_3

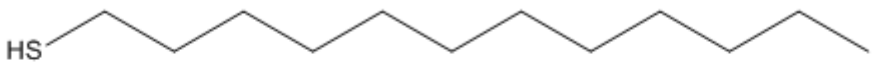

dodecane-1-thiol
Chemical Formula: $C_{12}H_{26}S$
Exact Mass: 202.18
Molecular Weight: 202.40
m/z: 202.18 (100.0%), 203.18 (13.3%), 204.17 (4.5%)
Elemental Analysis: C, 71.21; H, 12.95; S, 15.84

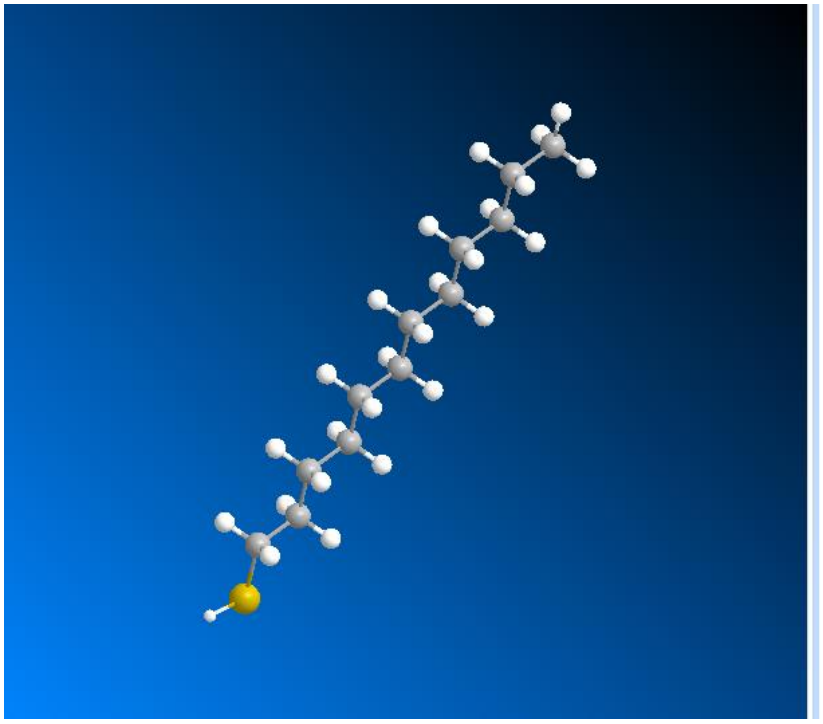

Molecule Length – S to final element: 16.09 Å

8.3.2 CS-NH_2

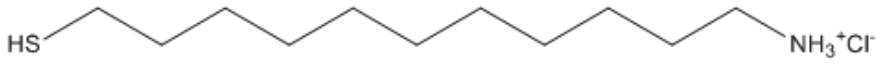

11-mercaptoundecan-1-aminium chloride
Chemical Formula: $C_{11}H_{26}ClNS$
Exact Mass: 239.15
Molecular Weight: 239.85
m/z: 239.15 (100.0%), 241.14 (36.5%), 240.15 (13.0%), 242.15 (4.5%), 243.14 (1.5%)
Elemental Analysis: C, 55.09; H, 10.93; Cl, 14.78; N, 5.84; S, 13.37

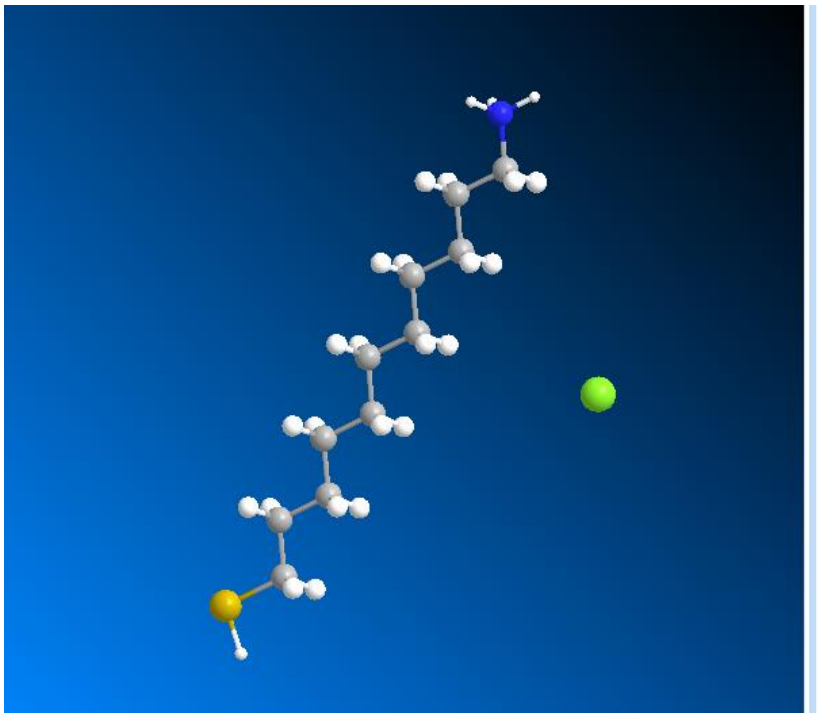

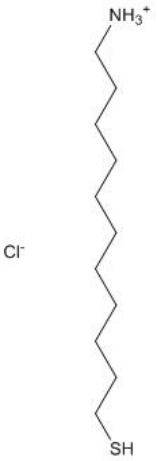

Molecule Length – S to final element: 15.95 Å

8.3.3 CS-COOH

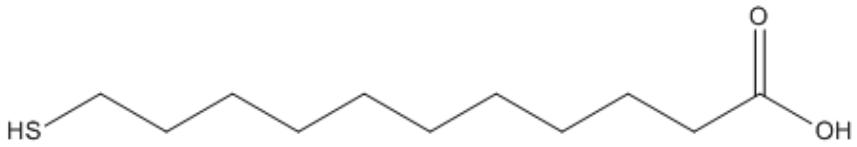

11-mercaptoundecanoic acid
Chemical Formula: $C_{11}H_{22}O_2S$
Exact Mass: 218.13
Molecular Weight: 218.35
m/z: 218.13 (100.0%), 219.14 (12.2%), 220.13 (4.5%), 220.14 (1.2%)
Elemental Analysis: C, 60.51; H, 10.16; O, 14.65; S, 14.68

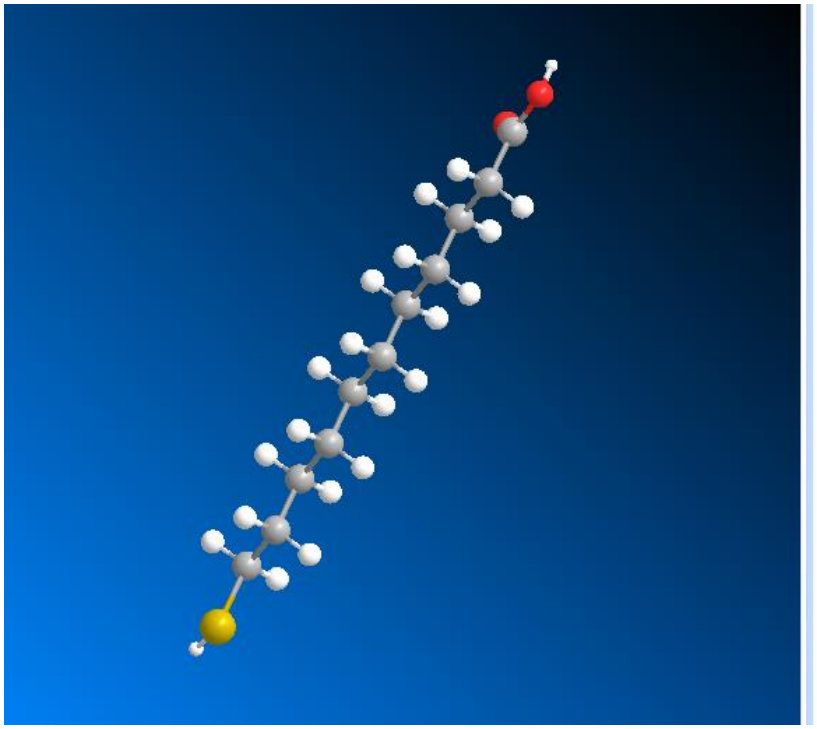

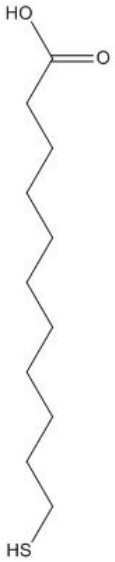

Molecule Length – S to final element: 15.81 Å

8.3.4 CS-OH

11-mercaptoundecan-1-ol
Chemical Formula: $C_{11}H_{24}OS$
Exact Mass: 204.15
Molecular Weight: 204.37
m/z: 204.15 (100.0%), 205.16 (12.2%), 206.15 (4.5%)
Elemental Analysis: C, 64.65; H, 11.84; O, 7.83; S, 15.69

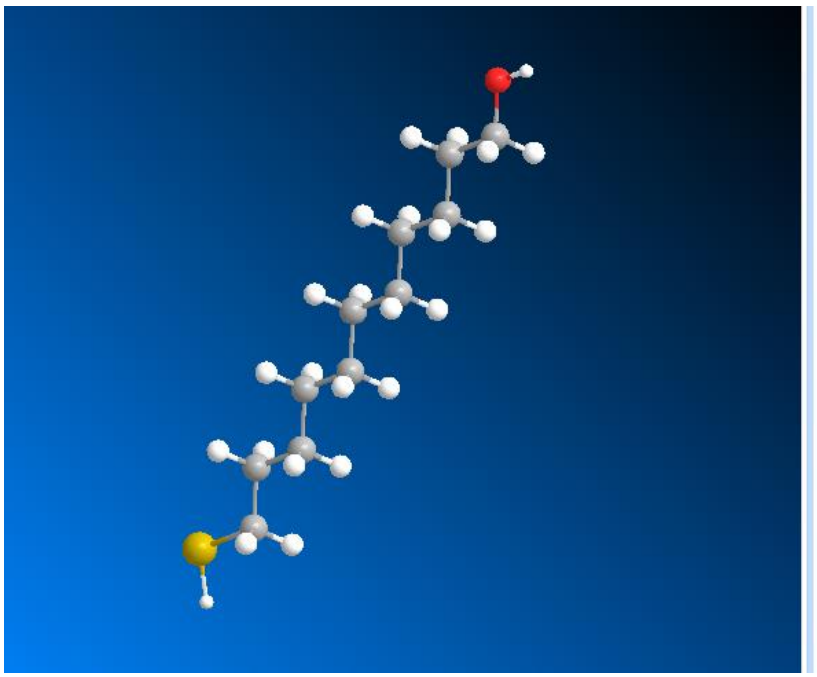

Molecule Length – S to final element: 15.83 Å

8.3.5 CS-NP

CS-NP is a combination of the compound used in the preparation of CS-NH_2, with the later addition of NP-OSuc; where the attachment of the latter is via the exposed amine group of the former. The molecule on its own in free space will arrange such that the later added NP will be at a right angle with the amine terminated linker molecule. Due to steric effects, however, the conformation of the joined compound may be altered when assembled on the Au substrate where the NP will need to attach to an already formed SAM.

Based on the assumption that the amine group onto which the NP will attach can act as a hinge for the joined compound, lengths for the joined compound were determined for maximum and minimum hinge angles.

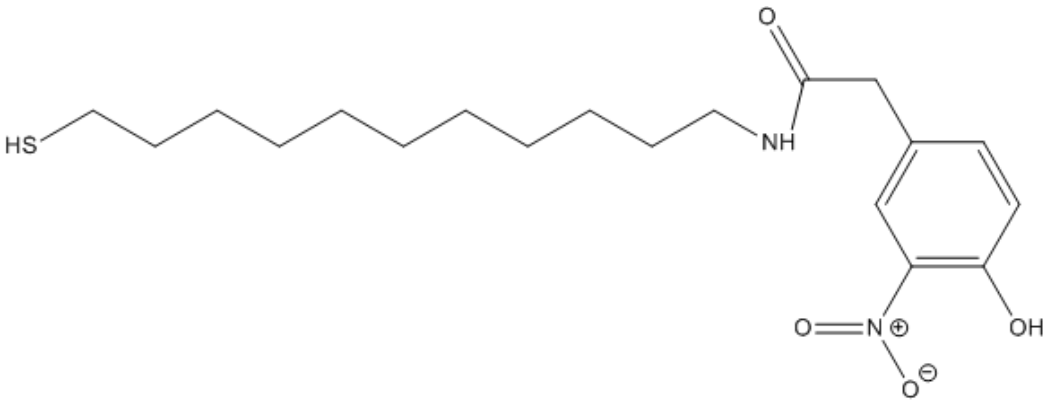

2-(4-hydroxy-3-nitrophenyl)-*N*-(11-mercaptoundecyl)acetamide
Chemical Formula: $C_{19}H_{30}N_2O_4S$
Exact Mass: 382.19
Molecular Weight: 382.52
m/z: 382.19 (100.0%), 383.20 (21.0%), 384.19 (4.7%), 384.20 (3.1%), 383.19 (1.5%)
Elemental Analysis: C, 59.66; H, 7.91; N, 7.32; O, 16.73; S, 8.38 .

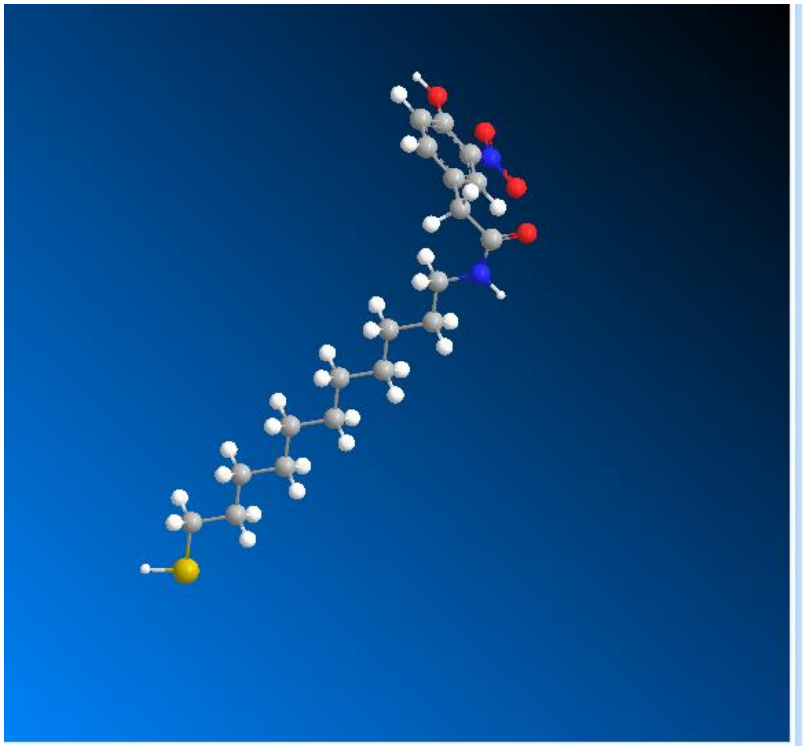

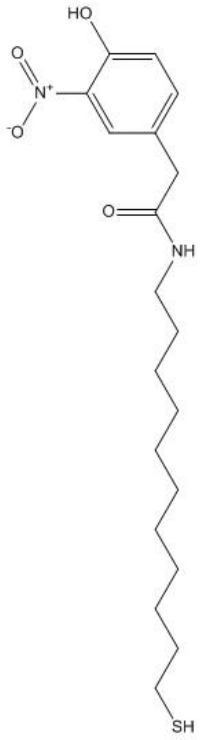

Molecule Length – amine terminated linker molecule: 15.11Å

Molecule Length – added NP portion: 6.31Å

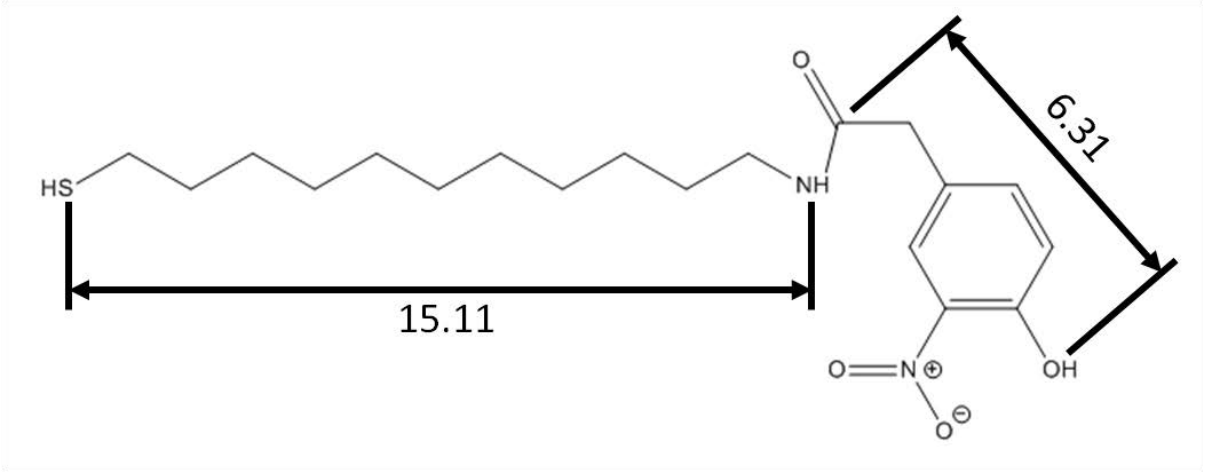

At maximum hinge angle the joined compound would experience the full length addition of the added NP portion, whereas at minimum hinge angle there would be no addition to the length of the joined compound.

8.4 Theoretical SAM Thicknesses for Deposition of Different Molecules

CS	molecule length [nm]	SAM thickness with molecule at 0° tilt angle with surface normal [nm]	SAM thickness with molecule at 30° tilt angle with surface normal [nm]
CS-CH_3	1.609	1.609	1.393
CS-NH_2	1.595	1.595	1.381
CS-COOH	1.581	1.581	1.369
CS-OH	1.583	1.583	1.371
CS-NP 90° hinge angle	1.511 + 0	1.511	1.309
CS-NP 0° hinge angle	1.511 + 0.631	2.142	1.855

The SAM thickness range for CS-NP is determined for two conditions, because it is a combination of two compounds: the ATAT molecule, and the later added NP group. As can be seen from the structure shown in Appendix 8.3.5 (p.220), the added NP group is at a 90° angle with the ATAT molecule when considering an isolated instance in free space. The first condition for which SAM thicknesses for CS-NP were determined is with the added NP group at the 90° angle as it would be in free space. The second condition considers the N to which the NP group attaches as a hinge around which the NP group can rotate, where the maximum overall molecule length would occur when the NP group is at a 180° angle with the ATAT molecule.

8.5 Fundamentals of Ellipsometry

Ellipsometry is a non-destructive optical technique for the analysis of surface and thin films. It is based on the measurement of the change in polarisation state of a light beam that is caused by reflection of the light beam from the sample surface or by the transmission of the light beam through the material. From this change in polarisation state the film thickness and optical properties can be deduced.

The way that light interacts with a certain medium as it propagates is described by the medium's complex index of refraction, $\mathrm{N_i}$; as depicted in Figure A8.5/1 below.

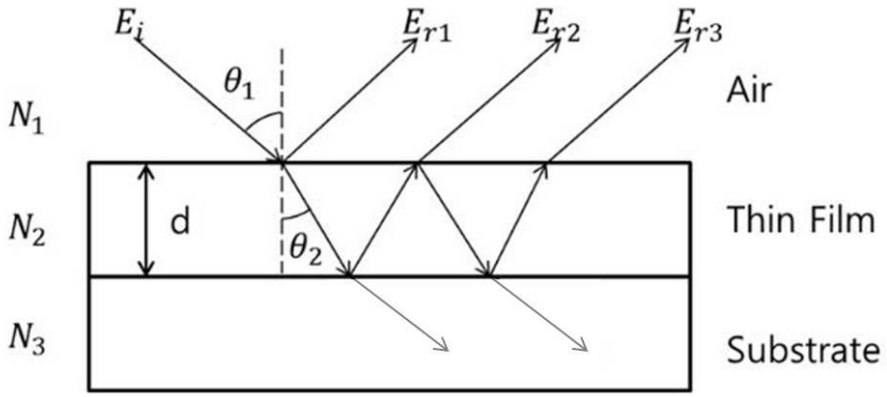

Figure A8.5/1 – Reflections and Transmissions of Light at the Thin-Film Layer. Image Taken From [125].

The complex index of refraction, N, is comprised of a real component, n, the refractive index, and an imaginary component, k, the extinction coefficient; as shown in Equation A8.5/1 below.

$$N_i = n_i - jk_i \qquad \text{Equation A8.5/1}$$

The light incident on samples in ellipsometry is polarised. As depicted in Figure A8.5/2, if two linearly polarised light beams, which are out of phase, are combined, the resultant light beam is elliptically polarised (which is where the name of the technique derives from). In the special case shown in Figure A8.5/2, the two

linearly polarised light beams are out of phase by 90°, and the resultant beam is circularly polarised. The change in state of polarisation of a light beam as it reflects of the sample through a thin film is what is assessed in ellipsometry.

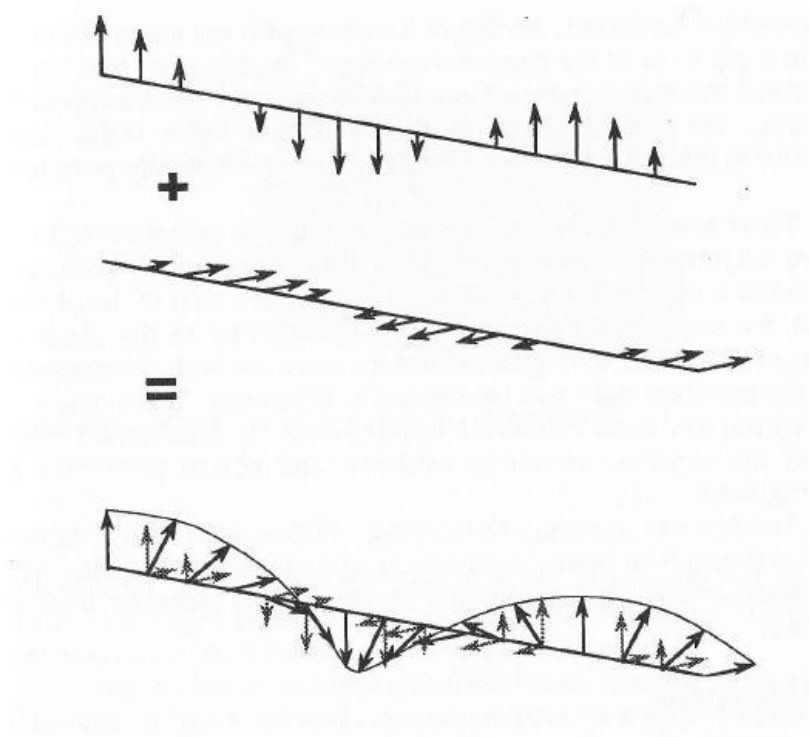

Figure 1-8. If two linearly polarized light beams which are out of phase are combined, the resultant light beam is elliptically polarized. In this particular example, they are out of phase by 90°, hence the resultant beam is circularly polarized.

Figure A8.5/2 – Polarisation of Light. Image Taken From [126].

The parameters measured to assess the change in state of polarisation are the so-called ellipsometric angles Ψ and Δ. These are related to the ratio of the complex Fresnel reflection coefficients r_s and r_p; where r_s is the reflection coefficient for light polarised perpendicular to the plane of incidence, and r_p is the reflection coefficient for light polarised parallel to the plane of incidence.

Considering a plane wave arrives at the sample surface, one part of the wave is reflected, and the other transmitted. The electric field vector of such a wave can be decomposed into two components; one perpendicular to the plane of incidence (E_s),

and one parallel to the plane of incidence (E_p); as shown in Figure A8.5/3 below. Both components show different behaviour during reflection, and, thus, reflection leads to a modification of the light polarisation. This reflection of the components is described by the aforementioned Fresnel coefficients of reflection r_s and r_p.

$$r_s = \frac{E_s^{\,r}}{E_s^{\,i}} = |r_s|e^{i\delta_s} \qquad \text{Equation A8.5/2}$$

$$r_p = \frac{E_p^{\,r}}{E_p^{\,i}} = |r_p|e^{i\delta_p} \qquad \text{Equation A8.5/3}$$

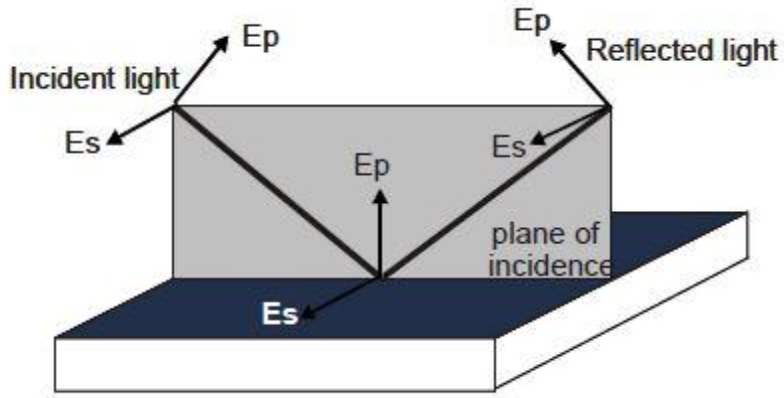

Figure A8.5/3 – Electric Field Vectors of Incident and Reflected Light. Image Taken From [127].

The modules of the coefficients give the amplitude modifications of the electric field components, and their phases give the phase shift caused by the reflection. The ratio of these two coefficients, ρ, is precisely what an ellipsometer measures.

This is expressed in the fundamental equation of ellipsometry, whereby the complex reflectance ratio of a system, ρ, is given as in Equation A8.5/4 below:

$$\rho = \frac{r_p}{r_s} = \tan\Psi e^{i\Delta} \qquad \text{Equation A8.5/4}$$

where

$$\tan\Psi = \frac{|r_p|}{|r_s|} \qquad 0° \leq \Psi \leq 90° \qquad \text{Equation A8.5/5}$$

and

$$\Delta = \delta_p - \delta_s \qquad 0° \leq \Delta \leq 360° \qquad \text{Equation A8.5/6}$$

From the measured parameters Ψ and Δ, optical and structural properties of the sample can be determined through appropriate modelling.

The ellipsometer is set up to acquire data at an angle of incidence of 70°, which is the angle of incidence recommended by the manufacturer for assessing films on metals [127], but furthermore it is very near the Brewster angle for Au ($\theta_{B_{Au}} = 70.295°$)[128]. Acquisitions should be conducted as near as possible to the Brewster angle to maximise sensitivity.[127]

The experimental data that is produced is, as in Figure A8.5/4 below, in n and k, the real and imaginary components of the complex refractive index for the interrogated sample, respectively.

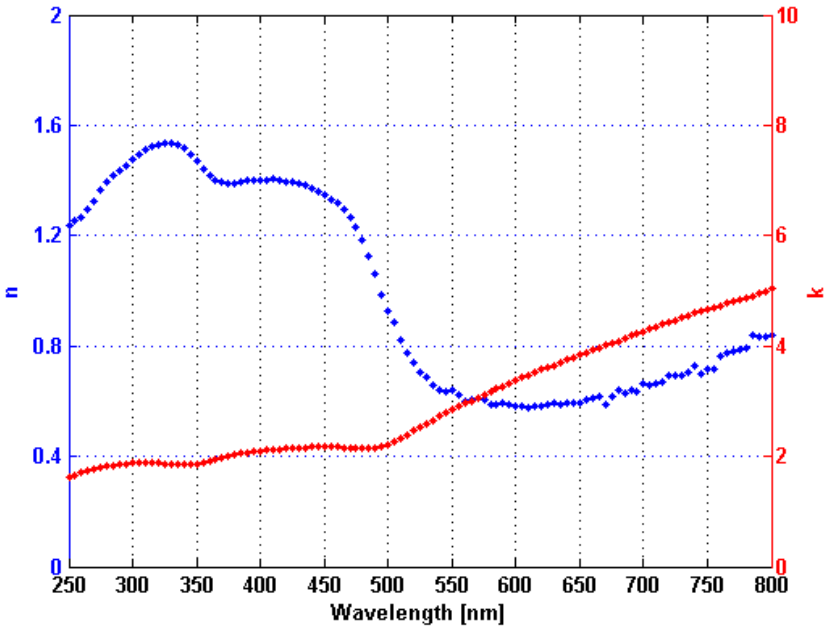

Figure A8.5/4 – Experimental Data

The values of n and k are not simply constants for any given medium, but are in fact functions of the wavelength, λ. It is for that reason, for example, that as light enters a prism, it emerges with the various colours separated. The dependence of the optical constants on wavelength are approximated by the equations below; where n_1, n_2, and n_3, are called the "Cauchy coefficients", and k_1, k_2, and k_3, are called the "Cauchy extinction coefficients"

$$n(\lambda) = n_1 + \frac{n_2}{\lambda^2} + \frac{n_3}{\lambda^4} \qquad \text{Equation A8.5/7}$$

$$k(\lambda) = k_1 + \frac{k_2}{\lambda^2} + \frac{k_3}{\lambda^4} \qquad \text{Equation A8.5/8}$$

The values of Ψ and Δ are always correct [129], and it is subsequently dependent only on the correct use of appropriate models being fitted to the experimental data that determines if unknown parameters such as the film thickness are extracted correctly. This includes specifying parameters based on prior knowledge of the sample, such as, for example, the substrate material and hence its optical properties, and the number of surface layers that are expected to be present.

In order to determine unknown sample parameters from the experimental data, models need to be fitted to the experimental data as closely as possible. However, when plotted against wavelength, the values of Ψ and Δ may contain mirror effects, as well as exhibit asymptotic behaviour. These hinder comparison to theoretical models and assessments of the goodness of fit (GOF) of said models to the experimental data. To prevent this from interfering with model fitting, the trigonometric transformations I_s and I_c, as shown below, are used.

$$I_s = \sin 2\Psi \sin \Delta \qquad \text{Equation A8.5/9}$$

$$I_c = \sin 2\Psi \cos \Delta$$ Equation A8.5/10

Through use of these trigonometric transformations, experimental data as shown in Figure A8.5/5, is transformed to curves as shown in Figure A8.5/6.

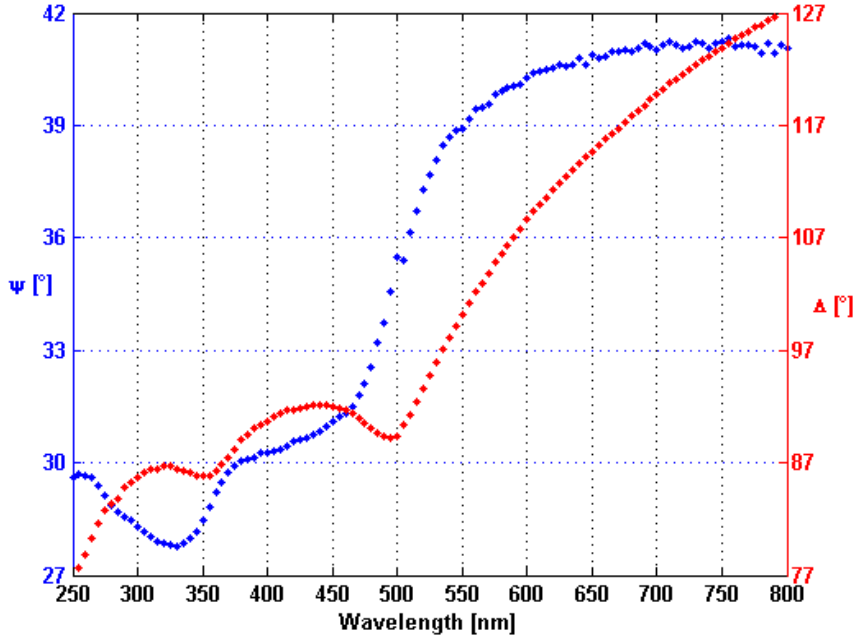

Figure A8.5/5 – Values of Ψ and Δ against Wavelength

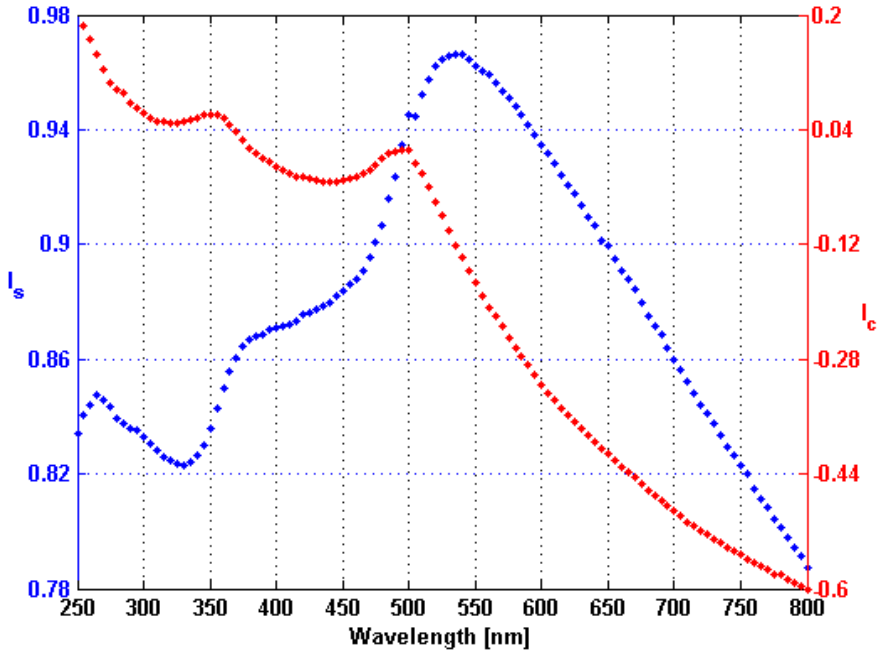

Figure A8.5/6 – Values of I_s and I_c against Wavelength

Subsequent assessments of the goodness of fit (GOF) of models to the experimental data are here made through the parameter χ^2, which is given by Equation A8.5/11 below, and should be as low as possible. For measurements of Ψ and Δ, the χ^2 value compares n pairs of theoretical (Ψ_{th}, Δ_{th}), and experimental (Ψ_{exp}, Δ_{exp}), values; with Γ_i, the standard deviation of each data point, set to 1.

$$\chi^2 = min \sum_{i=1}^{n} \left[\frac{(\Psi_{th} - \Psi_{exp})_i^2}{\Gamma_{\Psi,i}} + \frac{(\Delta_{th} - \Delta_{exp})_i^2}{\Gamma_{\Delta,i}} \right] \qquad \text{Equation A8.5/11}$$

The minimisation algorithm used to determine the (Ψ_{th}, Δ_{th}) pair that produces the lowest χ^2 value is the Levenberg-Marquardt algorithm. The algorithm is allowed to run for a maximum of 100 iterations, and is terminated if the χ^2 value is sufficiently small ($\chi^2 < 10^{-6}$), or if no further improvements in the χ^2 value can be achieved with additional iterations ($\Delta\chi^2 < 10^{-16}$).

8.6 LENNF Application Approval

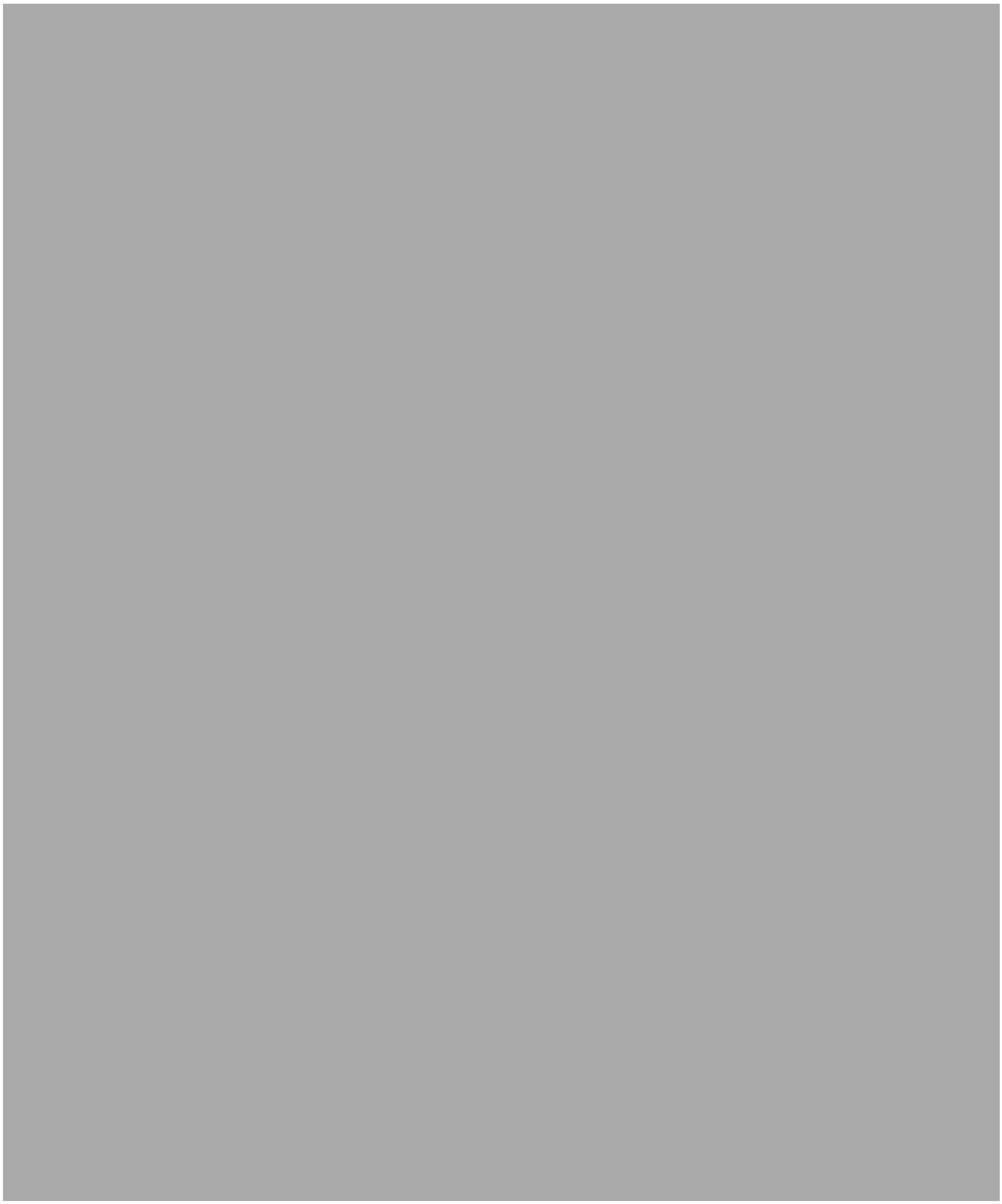

8.7 Consistency of SAM Layer Thicknesses Assessed via Ellipsometry

The table below shows SAM layer thicknesses as determined via ellipsometry; as detailed in §4.1.1. (p.37). The data was produced to assess the consistency with which the different CSs could be prepared; the results are discussed in in §4.2.1.1 (p.43). SAM thickness values are given to 2 decimal places.

		SAM Thickness [nm]		
	Position	Preparation 1	Preparation 2	Preparation 3
CS-CH_3	1	1.85	1.83	2.18
	2	1.76	1.65	2.09
	3	1.58	1.66	1.92
	4			2.00
CS-NH_2	1	4.52	5.41	3.74
	2	4.71	3.73	4.30
	3	4.23	4.45	3.59
	4			3.37
	5			3.65
	6			3.74
CS-COOH	1	1.54	1.55	1.76
	2	1.72	1.59	1.76
	3	1.91	2.27	1.65
	4	1.52		1.61
CS-OH	1	1.77	1.55	1.57
	2	1.62	1.55	1.45
	3	2.18	1.51	1.54
	4		1.73	
	5		1.49	
CS-NP	1	6.26	7.33	5.84
	2	6.26	7.40	4.63
	3	6.12	6.75	4.97

8.8 Images for Contact Angle Analysis

In the table below are the images taken for contact angle analysis, where each of the 5 different CSs was prepared once in three independent groups. Contact angles were measured as described in §4.1.2.1 (p.39) from both left to right (LTR) and right to left (RTL), with averages taken over those two measurements. All values are given in degrees.

	Preparation 1	**Preparation 2**	**Preparation 3**
CS-CH_3	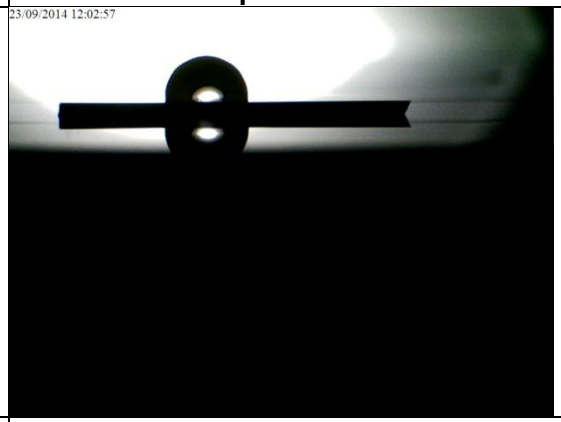	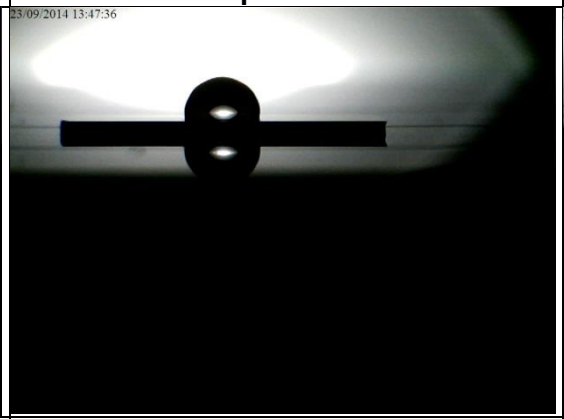	
	LTR: 86.2; RTL: 95.2 Average: 90.7	LTR: 95.4; RTL: 92.8 Average: 94.1	LTR: 93.5; RTL: 92.4 Average: 93.00

$CS\text{-}NH_2$			
	LTR: 68.1; RTL: 69.1 Average: 68.6	LTR: 74.1; RTL: 69.4 Average: 71.8	LTR: 58.1; RTL: 69.1 Average: 63.6
CS-COOH			
	LTR: 28.9; RTL: 27.9 Average: 28.4	LTR: 22.1; RTL: 20.9 Average: 21.5	LTR: 27.2; RTL: 26.3 Average: 26.8

CS-OH			
	LTR: 26.8; RTL: 27.4 Average: 27.1	LTR: 37.7; RTL: 41.8 Average: 39.8	LTR: 39.8; RTL: 34.6 Average: 37.2
CS-NP			
	LTR: 66.5; RTL: 68.6 Average: 67.6	LTR: 73.9; RTL: 68.9 Average: 71.4	LTR: 63.9; RTL: 65.6 Average: 64.8

8.9 Treated AFM Cantilevers Tested Against CSs

The following data was omitted from analysis in §4.2.1 (p.43), because the ellipsometry results in §4.2.1.1 (p.43), as well as the contact angle analysis results in §4.2.1.2 (p.45), showed that the surface modifications of CS-NH_2, and consequently those of CS-NP, were not in the correct conformation. Therefore, the collected data could not be considered representative for interactions of successfully functionalised cantilevers against CSs. The results are here included for completeness, but are not endowed with any weight.

Three treated cantilevers were prepared for the experiment, alongside CS-NP in each of the three independent preparations of all the CSs. The cantilever treated in Preparation 1 (P1) was damaged in preparation of the experiment. The remaining two cantilevers were used in the interrogation of CS-CH_3, CS-NH_2, CS-COOH, and CS-OH, where the cantilever treated in Preparation 2 (P2) was used in the interrogation of CSs from all three preparations, and the cantilever treated in Preparation 3 (P3) was used in the interrogation of the CSs from P1.

Each CS was interrogated three times consecutively, in three non-overlapping 100 µm x 100 µm areas with a grid of 10 x 10 evenly spaced point interrogations.

The following graphs show the interaction forces that were determined in these interrogations.

Interrogation of P1 CSs using cantilever treated in P2.

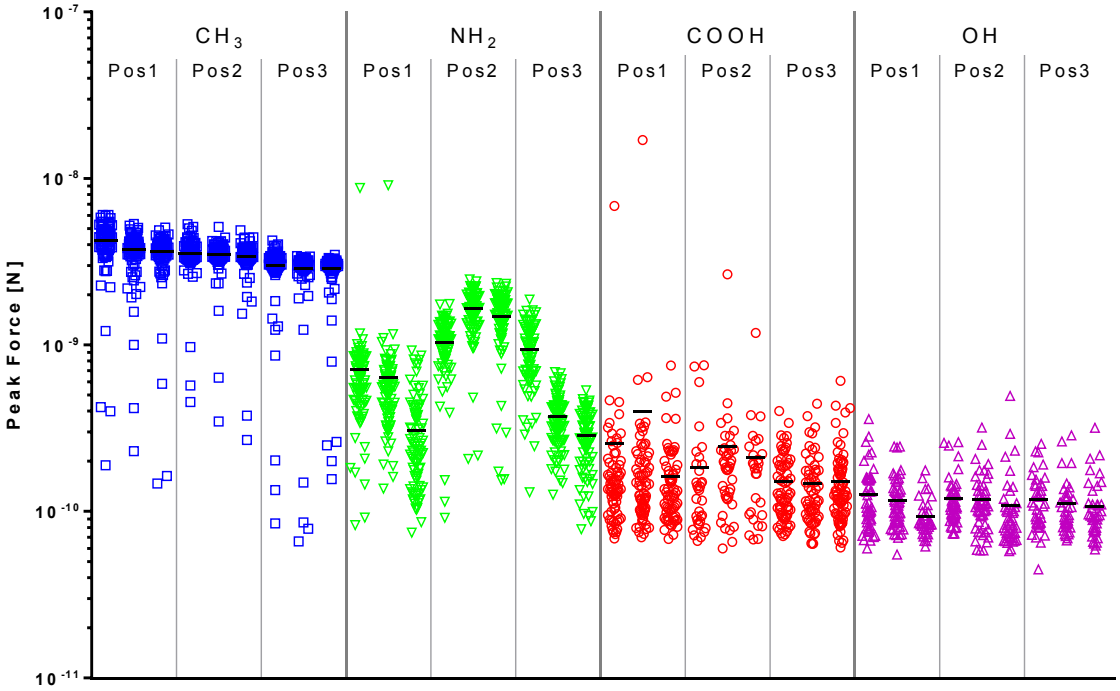

Interrogation of P2 CSs using cantilever treated in P2.

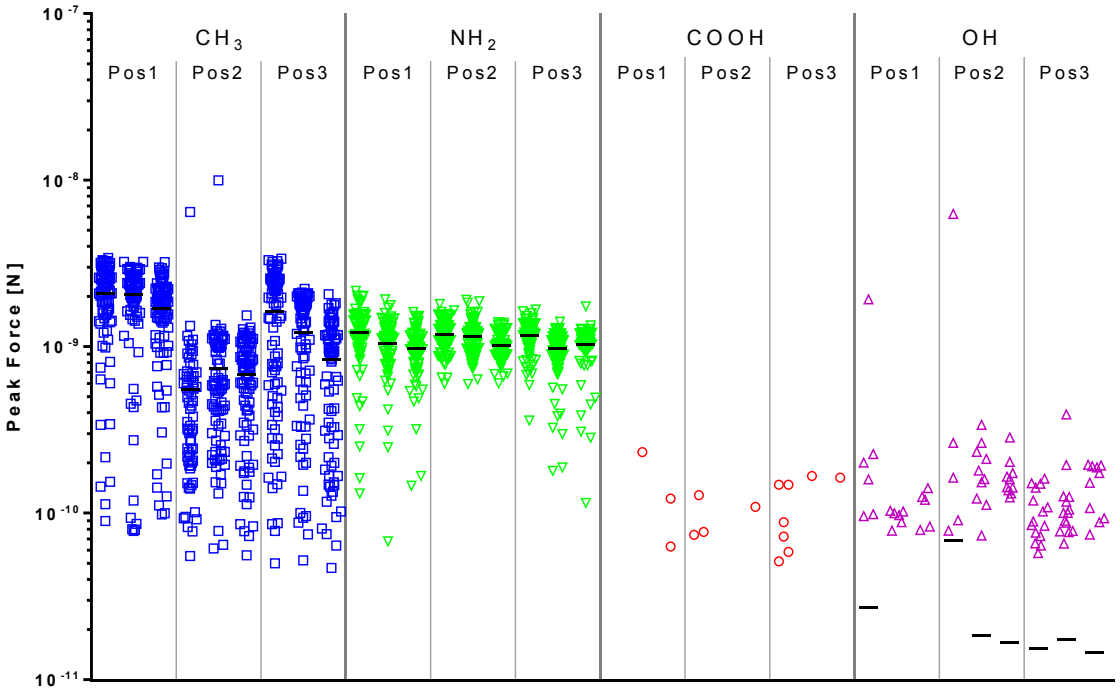

Interrogation of P3 CSs using cantilever treated in P2.

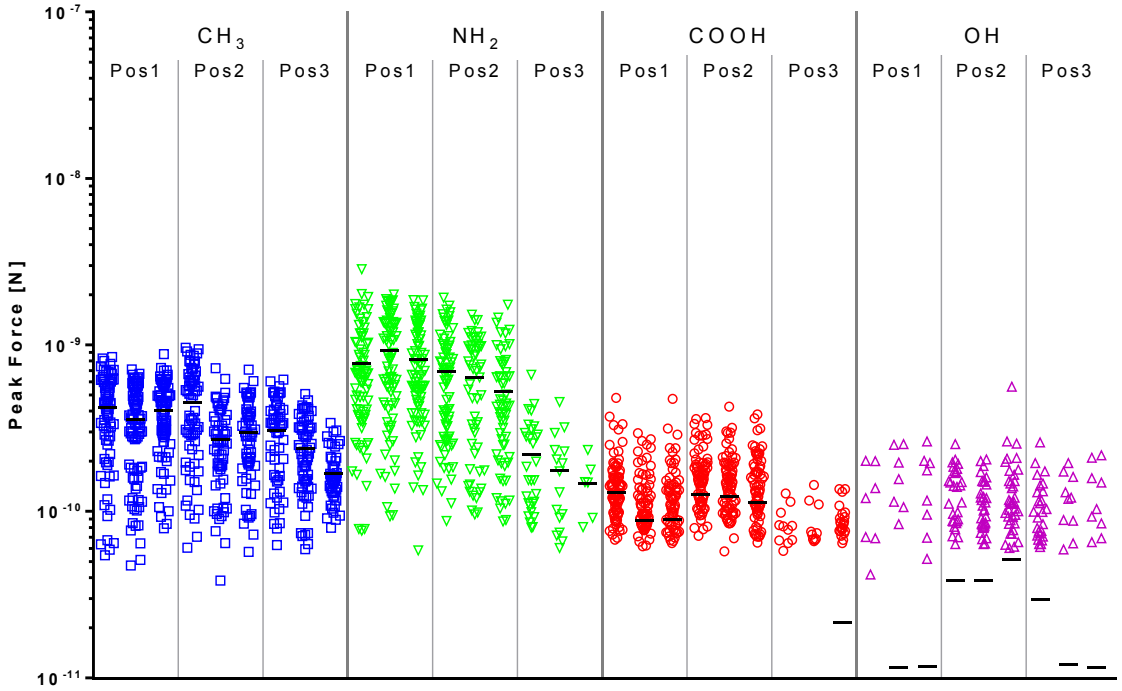

Interrogation of P1 CSs using cantilever treated in P3.

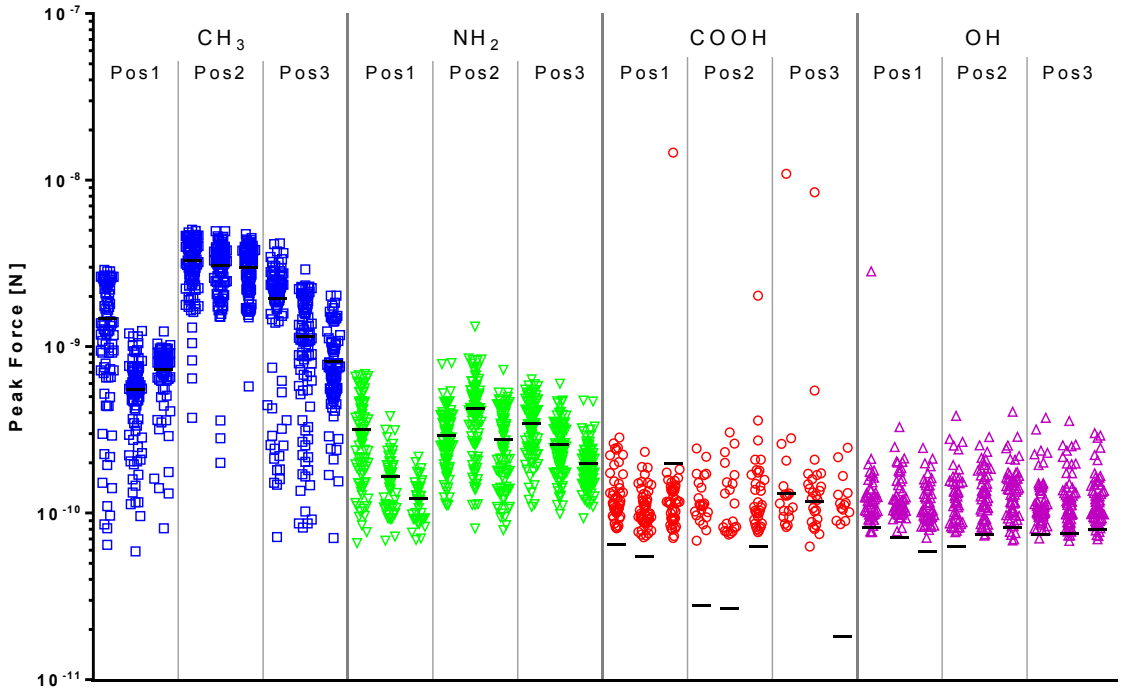

8.10 Electron Binding Energies

Table 1-1. *Electron binding energies, in electron volts, for the elements in their natural forms.*

Element	K 1s	L_1 2s	L_2 $2p_{1/2}$	L_3 $2p_{3/2}$	M_1 3s	M_2 $3p_{1/2}$	M_3 $3p_{3/2}$	M_4 $3d_{3/2}$	M_5 $3d_{5/2}$	N_1 4s	N_2 $4p_{1/2}$	N_3 $4p_{3/2}$
1 H	13.6											
2 He	24.6*											
3 Li	54.7*											
4 Be	111.5*											
5 B	188*											
6 C	284.2*											
7 N	409.9*	37.3*										
8 O	543.1*	41.6*										
9 F	696.7*											
10 Ne	870.2*	48.5*	21.7*	21.6*								
11 Na	1070.8†	63.5†	30.65	30.81								
12 Mg	1303.0†	88.7	49.78	49.50								
13 Al	1559.6	117.8	72.95	72.55								
14 Si	1839	149.7*b	99.82	99.42								
15 P	2145.5	189*	136*	135*								
16 S	2472	230.9	163.6*	162.5*								
17 Cl	2822.4	270*	202*	200*								
18 Ar	3205.9*	326.3*	250.6†	248.4*	29.3*	15.9*	15.7*					
19 K	3608.4*	378.6*	297.3*	294.6*	34.8*	18.3*	18.3*					
20 Ca	4038.5*	438.4†	349.7†	346.2†	44.3 †	25.4†	25.4†					
21 Sc	4492	498.0*	403.6*	398.7*	51.1*	28.3*	28.3*					
22 Ti	4966	560.9†	460.2†	453.8†	58.7†	32.6†	32.6†					

23 V	5465	626.7†	519.8†	512.1†	66.3†	37.2†	37.2†					
24 Cr	5989	696.0†	583.8†	574.1†	74.1†	42.2†	42.2†					
25 Mn	6539	769.1†	649.9†	638.7†	82.3†	47.2†	47.2†					
26 Fe	7112	844.6†	719.9†	706.8†	91.3†	52.7†	52.7†					
27 Co	7709	925.1†	793.2†	778.1†	101.0†	58.9†	59.9†					
28 Ni	8333	1008.6†	870.0†	852.7†	110.8†	68.0†	66.2†					
29 Cu	8979	1096.7†	952.3†	932.7	122.5†	77.3†	75.1†					
30 Zn	9659	1196.2*	1044.9*	1021.8*	139.8*	91.4*	88.6*	10.2*	10.1*			
31 Ga	10367	1299.0*b	1143.2†	1116.4†	159.5†	103.5†	100.0†	18.7†	18.7†			
32 Ge	11103	1414.6*b	1248.1*b	1217.0*b	180.1*	124.9*	120.8*	29.8	29.2			
33 As	11867	1527.0*b	1359.1*b	1323.6*b	204.7*	146.2*	141.2*	41.7*	41.7*			
34 Se	12658	1652.0*b	1474.3*b	1433.9*b	229.6*	166.5*	160.7*	55.5*	54.6*			
35 Br	13474	1782*	1596*	1550*	257*	189*	182*	70*	69*			
36 Kr	14326	1921	1730.9*	1678.4*	292.8*	222.2*	214.4	95.0*	93.8*	27.5*	14.1*	14.1*
37 Rb	15200	2065	1864	1804	326.7*	248.7*	239.1*	113.0*	112*	30.5*	16.3*	15.3 *
38 Sr	16105	2216	2007	1940	358.7†	280.3†	270.0†	136.0†	134.2†	38.9†	21.3	20.1†
39 Y	17038	2373	2156	2080	392.0*b	310.6*	298.8*	157.7†	155.8†	43.8*	24.4*	23.1*
40 Zr	17998	2532	2307	2223	430.3†	343.5†	329.8†	181.1†	178.8†	50.6†	28.5†	27.1†
41 Nb	18986	2698	2465	2371	466.6†	376.1†	360.6†	205.0†	202.3†	56.4†	32.6†	30.8†
42 Mo	20000	2866	2625	2520	506.3†	411.6†	394.0†	231.1†	227.9†	63.2†	37.6†	35.5†
43 Tc	21044	3043	2793	2677	544*	447.6	417.7	257.6	253.9*	69.5*	42.3*	39.9*
44 Ru	22117	3224	2967	2838	586.1*	483.5†	461.4†	284.2†	280.0†	75.0†	46.3†	43.2†
45 Rh	23220	3412	3146	3004	628.1†	521.3†	496.5†	311.9†	307.2†	81.4*b	50.5†	47.3†
46 Pd	24350	3604	3330	3173	671.6†	559.9†	532.3†	340.5†	335.2†	87.1*b	55.7†a	50.9†
47 Ag	25514	3806	3524	3351	719.0†	603.8†	573.0†	374.0†	368.3	97.0†	63.7†	58.3†

Table 1-1. *Electron binding energies (continued).*

Element	K 1s	L_1 2s	L_2 $2p_{1/2}$	L_3 $2p_{3/2}$	M_1 3s	M_2 $3p_{1/2}$	M_3 $3p_{3/2}$	M_4 $3d_{3/2}$	M_5 $3d_{5/2}$	N_1 4s	N_2 $4p_{1/2}$	N_3 $4p_{3/2}$
48 Cd	26711	4018	3727	3538	772.0†	652.6†	618.4†	411.9†	405.2†	109.8†	63.9†a	63.9†a
49 In	27940	4238	3938	3730	827.2†	703.2†	665.3†	451.4†	443.9†	122.9†	73.5†a	73.5†a
50 Sn	29200	4465	4156	3929	884.7†	756.5†	714.6†	493.2†	484.9†	137.1†	83.6†a	83.6†a
51 Sb	30491	4698	4380	4132	946†	812.7†	766.4†	537.5†	528.2†	153.2†	95.6†a	95.6†a
52 Te	31814	4939	4612	4341	1006†	870.8†	820.0†	583.4†	573.0†	169.4†	103.3†a	103.3†a
53 I	33169	5188	4852	4557	1072*	931*	875*	630.8	619.3	186*	123*	123*
54 Xe	34561	5453	5107	4786	1148.7*	1002.1*	940.6*	689.0*	676.4*	213.2*	146.7	145.5*
55 Cs	35985	5714	5359	5012	1211*b	1071*	1003*	740.5*	726.6*	232.3*	172.4*	161.3*
56 Ba	37441	5989	5624	5247	1293*b	1137*b	1063*b	795.7†	780.5*	253.5†	192	178.6†
57 La	38925	6266	5891	5483	1362*b	1209*b	1128*b	853*	836*	274.7*	205.8	196.0*
58 Ce	40443	6549	6164	5723	1436*b	1274*b	1187*b	902.4*	883.8*	291.0*	223.2	206.5*
59 Pr	41991	6835	6440	5964	1511	1337	1242	948.3*	928.8*	304.5	236.3	217.6
60 Nd	43569	7126	6722	6208	1575	1403	1297	1003.3*	980.4*	319.2*	243.3	224.6
61 Pm	45184	7428	7013	6459	—	1471	1357	1052	1027	—	242	242
62 Sm	46834	7737	7312	6716	1723	1541	1420	1110.9*	1083.4*	347.2*	265.6	247.4
63 Eu	48519	8052	7617	6977	1800	1614	1481	1158.6*	1127.5*	360	284	257
64 Gd	50239	8376	7930	7243	1881	1688	1544	1221.9*	1189.6*	378.6*	286	271
65 Tb	51996	8708	8252	7514	1968	1768	1611	1276.9*	1241.1*	396.0*	322.4*	284.1*
66 Dy	53789	9046	8581	7790	2047	1842	1676	1333	1292.6*	414.2*	333.5*	293.2*
67 Ho	55618	9394	8918	8071	2128	1923	1741	1392	1351	432.4*	343.5	308.2*
68 Er	57486	9751	9264	8358	2207	2006	1812	1453	1409	449.8*	366.2	320.2*
69 Tm	59390	10116	9617	8648	2307	2090	1885	1515	1468	470.9*	385.9*	332.6*
70 Yb	61332	10486	9978	8944	2398	2173	1950	1576	1528	480.5*	388.7*	339.7*

Table 1-1. *Electron binding energies (continued).*

Element	N_4 $4d_{3/2}$	N_5 $4d_{5/2}$	N_6 $4f_{5/2}$	N_7 $4f_{7/2}$	O_1 5s	O_2 $5p_{1/2}$	O_3 $5p_{3/2}$	O_4 $5d_{3/2}$	O_5 $5d_{5/2}$	P_1 6s	P_2 $6p_{1/2}$	P_3 $6p_{3/2}$
48 Cd	11.7†	10.7†										
49 In	17.7†	16.9†										
50 Sn	24.9†	23.9†										
51 Sb	33.3†	32.1†										
52 Te	41.9†	40.4†										
53 I	50.6	48.9										
54 Xe	69.5*	67.5*	—	—	23.3*	13.4*	12.1*					
55 Cs	79.8*	77.5*	—	—	22.7	14.2*	12.1*					
56 Ba	92.6†	89.9†	—	—	30.3†	17.0†	14.8†					
57 La	105.3*	102.5*	—	—	34.3*	19.3*	16.8*					
58 Ce	109*	—	0.1	0.1	37.8	19.8*	17.0*					
59 Pr	115.1*	115.1*	2.0	2.0	37.4	22.3	22.3					
60 Nd	120.5*	120.5*	1.5	1.5	37.5	21.1	21.1					
61 Pm	120	120	—	—	—	—	—					
62 Sm	129	129	5.2	5.2	37.4	21.3	21.3					
63 Eu	133	127.7*	0	0	32	22	22					
64 Gd	—	142.6*	8.6*	8.6*	36	28	21					
65 Tb	150.5*	150.5*	7.7*	2.4*	45.6*	28.7*	22.6*					
66 Dy	153.6*	153.6*	8.0*	4.3*	49.9*	26.3	26.3					
67 Ho	160*	160*	8.6*	5.2*	49.3*	30.8*	24.1*					
68 Er	167.6*	167.6*	—	4.7*	50.6*	31.4*	24.7*					
69 Tm	175.5*	175.5*	—	4.6	54.7*	31.8*	25.0*					
70 Yb	191.2*	182.4*	2.5*	1.3*	52.0*	30.3*	24.1*					

Table 1-1. *Electron binding energies (continued).*

Element	K 1s	L_1 2s	L_2 $2p_{1/2}$	L_3 $2p_{3/2}$	M_1 3s	M_2 $3p_{1/2}$	M_3 $3p_{3/2}$	M_4 $3d_{3/2}$	M_5 $3d_{5/2}$	N_1 4s	N_2 $4p_{1/2}$	N_3 $4p_{3/2}$
71 Lu	63314	10870	10349	9244	2491	2264	2024	1639	1589	506.8*	412.4*	359.2*
72 Hf	65351	11271	10739	9561	2601	2365	2108	1716	1662	538*	438.2†	380.7†
73 Ta	67416	11682	11136	9881	2708	2469	2194	1793	1735	563.4†	463.4†	400.9†
74 W	69525	12100	11544	10207	2820	2575	2281	1872	1809	594.1†	490.4†	423.6†
75 Re	71676	12527	11959	10535	2932	2682	2367	1949	1883	625.4†	518.7†	446.8†
76 Os	73871	12968	12385	10871	3049	2792	2457	2031	1960	658.2†	549.1†	470.7†
77 Ir	76111	13419	12824	11215	3174	2909	2551	2116	2040	691.1†	577.8†	495.8†
78 Pt	78395	13880	13273	11564	3296	3027	2645	2202	2122	725.4†	609.1†	519.4†
79 Au	80725	14353	13734	11919	3425	3148	2743	2291	2206	762.1†	642.7†	546.3†
80 Hg	83102	14839	14209	12284	3562	3279	2847	2385	2295	802.2†	680.2†	576.6†
81 Tl	85530	15347	14698	12658	3704	3416	2957	2485	2389	846.2†	720.5†	609.5†
82 Pb	88005	15861	15200	13035	3851	3554	3066	2586	2484	891.8†	761.9†	643.5†
83 Bi	90524	16388	15711	13419	3999	3696	3177	2688	2580	939†	805.2†	678.8†
84 Po	93105	16939	16244	13814	4149	3854	3302	2798	2683	995*	851*	705*
85 At	95730	17493	16785	14214	4317	4008	3426	2909	2787	1042*	886*	740*
86 Rn	98404	18049	17337	14619	4482	4159	3538	3022	2892	1097*	929*	768*
87 Fr	101137	18639	17907	15031	4652	4327	3663	3136	3000	1153*	980*	810*
88 Ra	103922	19237	18484	15444	4822	4490	3792	3248	3105	1208*	1058	879*
89 Ac	106755	19840	19083	15871	5002	4656	3909	3370	3219	1269*	1080*	890*
90 Th	109651	20472	19693	16300	5182	4830	4046	3491	3332	1330*	1168*	966.4†
91 Pa	112601	21105	20314	16733	5367	5001	4174	3611	3442	1387*	1224*	1007*
92 U	115606	21757	20948	17166	5548	5182	4303	3728	3552	1439*b	1271*b	1043†

Table 1-1. *Electron binding energies (continued).*

Element	N_4 $4d_{3/2}$	N_5 $4d_{5/2}$	N_6 $4f_{5/2}$	N_7 $4f_{7/2}$	O_1 5s	O_2 $5p_{1/2}$	O_3 $5p_{3/2}$	O_4 $5d_{3/2}$	O_5 $5d_{5/2}$	P_1 6s	P_2 $6p_{1/2}$	P_3 $6p_{3/2}$
71 Lu	206.1*	196.3*	8.9*	7.5*	57.3*	33.6*	26.7*					
72 Hf	220.0†	211.5†	15.9†	14.2†	64.2†	38*	29.9†					
73 Ta	237.9†	226.4†	23.5†	21.6†	69.7†	42.2*	32.7†					
74 W	255.9†	243.5†	33.6*	31.4†	75.6†	45.3*b	36.8†					
75 Re	273.9†	260.5†	42.9*	40.5*	83†	45.6*	34.6*b					
76 Os	293.1†	278.5†	53.4†	50.7†	84*	58*	44.5†					
77 Ir	311.9†	296.3†	63.8†	60.8†	95.2*b	63.0*b	48.0†					
78 Pt	331.6†	314.6†	74.5†	71.2†	101.7*b	65.3*b	51.7†					
79 Au	353.2†	335.1†	87.6†	84.0	107.2*b	74.2†	57.2†					
80 Hg	378.2†	358.8†	104.0†	99.9†	127†	83.1†	64.5†	9.6†	7.8†			
81 Tl	405.7†	385.0†	122.2†	117.8†	136.0*b	94.6†	73.5†	14.7†	12.5†			
82 Pb	434.3†	412.2†	141.7†	136.9†	147*b	106.4†	83.3†	20.7†	18.1†			
83 Bi	464.0†	440.1†	162.3†	157.0†	159.3*b	119.0†	92.6†	26.9†	23.8†			
84 Po	500*	473*	184*	184*	177*	132*	104*	31*	31*			
85 At	533*	507	210*	210*	195*	148*	115*	40*	40*			
86 Rn	567*	541*	238*	238*	214*	164*	127*	48*	48*	26		
87 Fr	603*	577*	268*	268*	234*	182*	140*	58*	58*	34	15	15
88 Ra	636*	603*	299*	299*	254*	200*	153*	68*	68*	44	19	19
89 Ac	675*	639*	319*	319*	272*	215*	167*	80*	80*	—	—	—
90 Th	712.1†	675.2†	342.4†	333.1†	290*a	229*a	182*a	92.5†	85.4†	41.4†	24.5†	16.6†
91 Pa	743*	708*	371*	360*	310*	232*	232*	94*	94*	—	—	—
92 U	778.3†	736.2†	388.2*	377.4†	321*ab	257*ab	192*ab	102.8†	94.2†	43.9†	26.8†	16.8†

8.11 SAM Layer Thicknesses when Modelling or Pre-Setting Au Substrate Thickness

The table below shows the SAM layer thicknesses as determined via ellipsometry; as detailed in §4.1.1. (p.37). The data was produced to assess the difference in the obtained results, for when the Au layer thickness parameter is set to a fixed value or is modelled along the SAM layer thickness. This is discussed in §4.2.2.1 (p.61). In order for small differences to be discernible, thickness values are given to 3 decimal places.

		Preparation 1				**Preparation 2**				**Preparation 3**			
	Position	**SAM Thickness [nm] Au MODELLED**	**SAM Thickness [nm] Au FIXED**	**absolute difference [nm]**	**percentage difference**	**SAM Thickness [nm] Au MODELLED**	**SAM Thickness [nm] Au FIXED**	**absolute difference [nm]**	**percentage difference**	**SAM Thickness [nm] Au MODELLED**	**SAM Thickness [nm] Au FIXED**	**absolute difference [nm]**	**percentage difference**
$CS\text{-}CH_3$	**1**	1.846	1.847	0.001	0.05	1.828	1.869	0.041	2.22	2.180	2.186	0.006	0.27
	2	1.762	1.786	0.024	1.35	1.650	1.700	0.050	2.99	2.092	2.137	0.045	2.13
	3	1.579	1.577	0.002	0.13	1.659	1.710	0.051	3.03	1.915	2.013	0.098	4.99
	4									1.998	2.092	0.094	4.60
$CS\text{-}NH_2$	**1**	4.524	4.461	0.063	1.40	5.413	5.429	0.016	0.30	3.741	3.770	0.029	0.77
	2	4.709	4.668	0.041	0.87	3.734	3.724	0.010	0.27	4.301	4.327	0.026	0.60
	3	4.233	4.211	0.022	0.52	4.447	4.494	0.047	1.05	3.591	3.550	0.041	1.15
	4									3.370	3.341	0.029	0.86
	5									3.653	3.637	0.016	0.44
	6									3.741	3.780	0.039	1.04

		Preparation 1				Preparation 2				Preparation 3			
	Position	SAM Thickness [nm] Au MODELLED	SAM Thickness [nm] Au FIXED	absolute difference [nm]	percentage difference	SAM Thickness [nm] Au MODELLED	SAM Thickness [nm] Au FIXED	absolute difference [nm]	percentage difference	SAM Thickness [nm] Au MODELLED	SAM Thickness [nm] Au FIXED	absolute difference [nm]	percentage difference
CS-COOH	**1**	1.542	1.596	0.054	3.44	1.546	1.552	0.006	0.39	1.761	1.878	0.117	6.44
	2	1.718	1.718	0.000	0.00	1.593	1.596	0.003	0.19	1.755	1.783	0.028	1.58
	3	1.908	1.911	0.003	0.16	2.274	2.225	0.049	2.18	1.645	1.676	0.031	1.87
	4	1.521	1.512	0.009	0.59					1.608	1.680	0.072	4.38
CS-OH	**1**	1.774	1.863	0.089	4.90	1.549	1.604	0.055	3.49	1.568	1.564	0.004	0.26
	2	1.619	1.778	0.159	9.38	1.552	1.607	0.055	3.48	1.446	1.557	0.111	7.40
	3	2.179	2.202	0.023	1.05	1.511	1.500	0.011	0.73	1.536	1.496	0.040	2.64
	4					1.734	1.819	0.085	4.79				
	5					1.488	1.561	0.073	4.79				
CS-NP	**1**	6.261	6.303	0.042	0.67	7.327	7.602	0.275	3.69	5.837	5.873	0.036	0.61
	2	6.263	6.256	0.007	0.11	7.399	7.590	0.191	2.55	4.629	4.654	0.025	0.54
	3	6.118	6.133	0.015	0.24	6.750	6.921	0.171	2.50	4.973	5.018	0.045	0.90

8.12 Au Layer Thickness

The table below shows the thicknesses of the Au layer of the CS substrates, as determined via ellipsometry, as detailed in §4.1.1. (p.37), when the parameter of Au layer thickness is modelled alongside the SAM layer thickness. This is discussed in §4.2.2.1 (p.63). SAM thickness values are given to 2 decimal places.

		Au Thickness [nm]		
	Position	Preparation 1	Preparation 2	Preparation 3
$CS\text{-}CH_3$	1	29.48	29.15	29.34
	2	29.37	28.93	29.39
	3	30.41	29.27	29.89
	4			29.26
$CS\text{-}NH_2$	1	31.17	29.67	28.72
	2	31.04	29.56	28.57
	3	31.60	29.10	29.40
	4			29.23
	5			29.06
	6			29.01
CS-COOH	1	29.81	30.47	27.75
	2	30.32	30.40	27.37
	3	30.89	31.52	28.24
	4	30.00		28.66
CS-OH	1	25.11	26.59	27.30
	2	25.48	27.14	27.22
	3	26.19	26.26	27.33
	4		26.23	
	5		27.07	
CS-NP	1	30.04	26.78	28.88
	2	30.45	27.63	28.74
	3	30.67	27.55	28.74

8.13 XPS Results for CS-NH_2 Subjected to Sonication

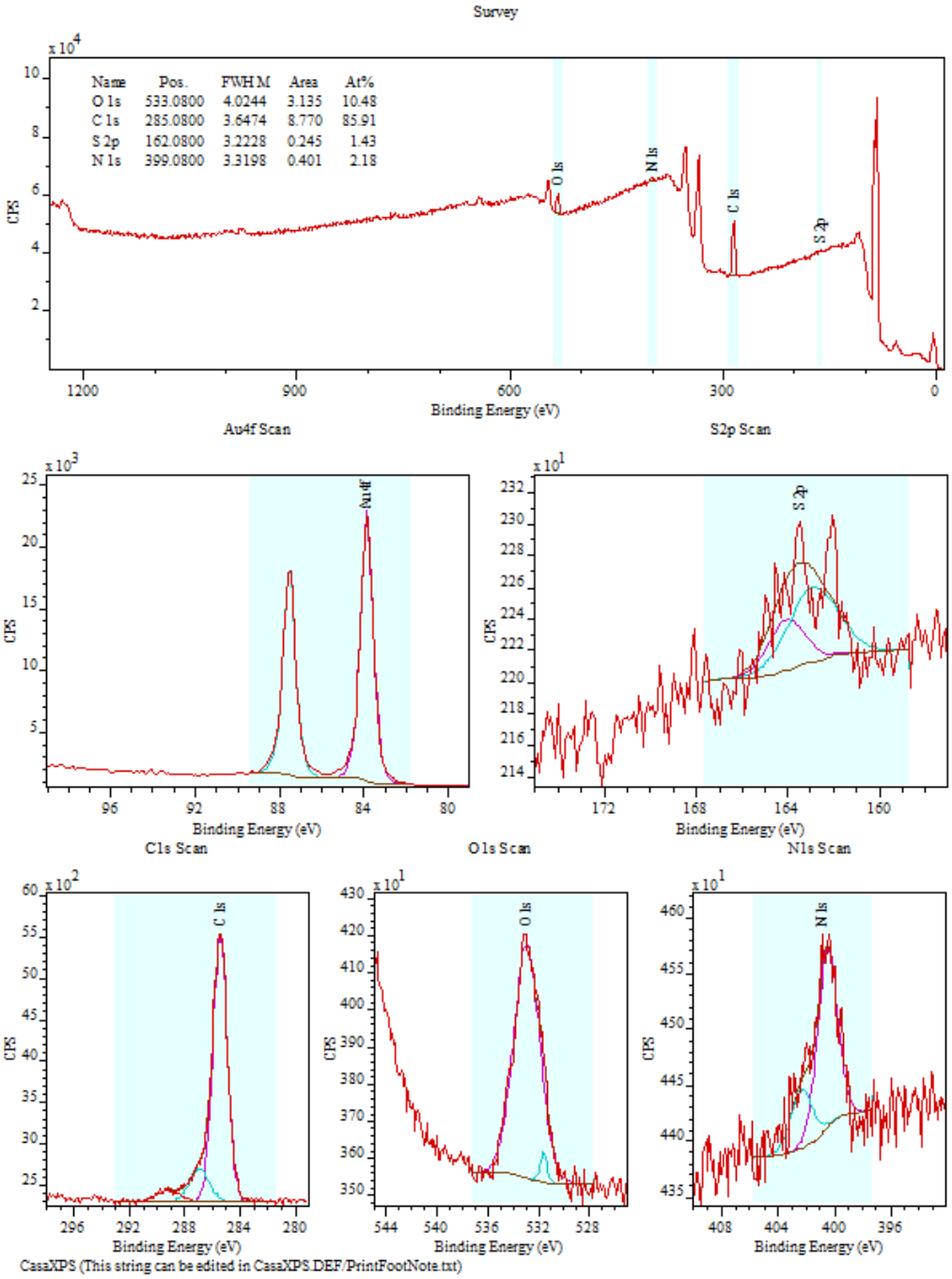

The XPS results for the CS-NH_2 specimen that was subjected to sonication indicate that a better quality SAM was achieved. The signal intensity of the survey spectrum is high, indicating that a thin layer was deposited on the Au substrate. The two characteristic peaks in the Au spectrum demonstrate that the instrument was set up

correctly, and, although low in intensity, the peaks in the S spectrum give indication that the S groups of the deposition molecule bound correctly to the Au substrate.

The C spectrum shows one intense peak, associated with the C in the molecule's C chain, and two smaller shoulders towards higher binding energies, for the (C-S) and (C-N) bonds respectively. Further, the N spectrum confirms the presence of N that is expected as part of the deposition molecule.

As for the CS-NH_2 specimen that was not treated with the sonication step, the XPS results reveal the presence of O in the deposited surface layer.

While the XPS results for the one investigated specimen for the CS-NH_2 preparation with sonication would indicate that sonication does aid in producing better quality SAMs on the samples, the accompanying ellipsometry data shows that the results are too variable; and hence the sonication step was not kept as part of the preparation protocol.

8.14 NH_2 SAM Formation Time Series – Supplemental

In addition to the already presented data shown Figure 28 in §4.2.4 (p.70), the graph below shows the layer thicknesses, as determined via ellipsometry, of a repeated preparation of CSs using deposition solution with added HCl.

While the layer thicknesses of the samples from the repeated preparation are not as low as the values determined for the initial samples, the results show good consistency nonetheless, and a systematic difference between determined values and theoretically expected values is not unexpected when considering that the layer thicknesses of the deposited SAMs are near the detection limit of the instrument.

In order to mitigate against systematic baseline shifts between ellipsometry data from different experiments, control samples need to be included in future experiments on which the SAM formation is known to be consistently of good quality, and use the obtained values to adjust baseline values.

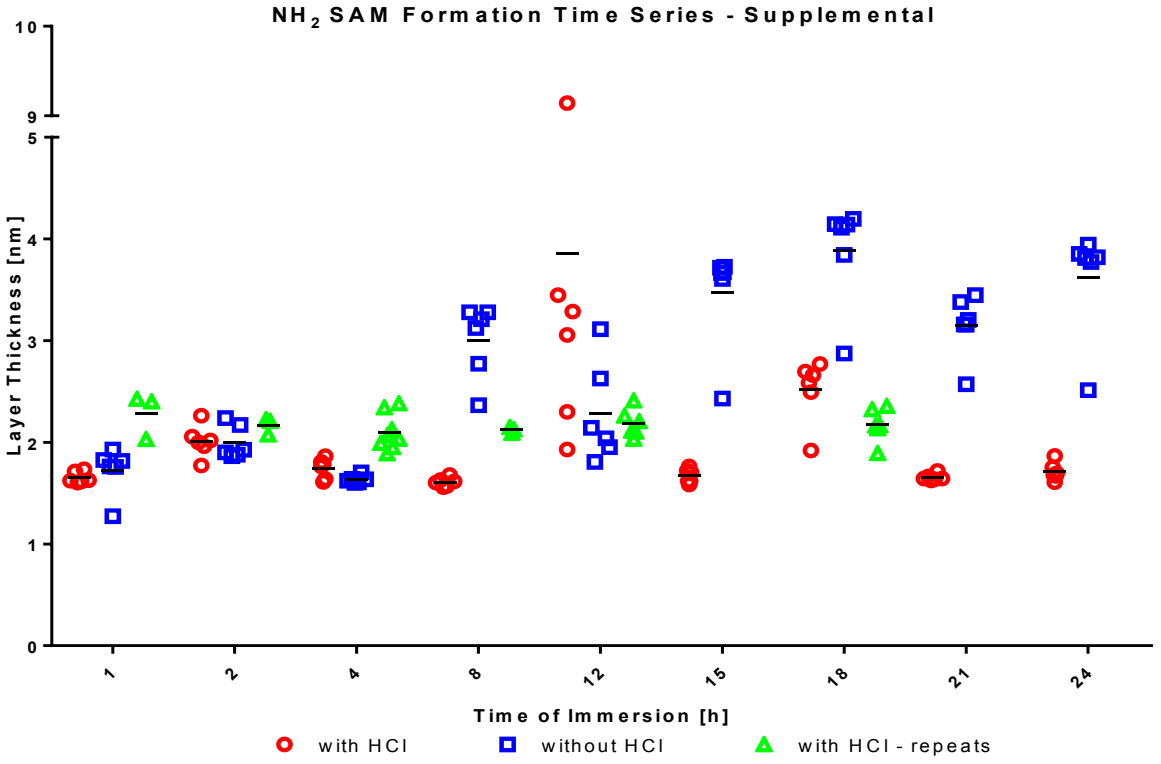

8.15 Hybridoma Technology

The image below is a diagrammatic description of the process for obtaining monoclonal hybridomas.

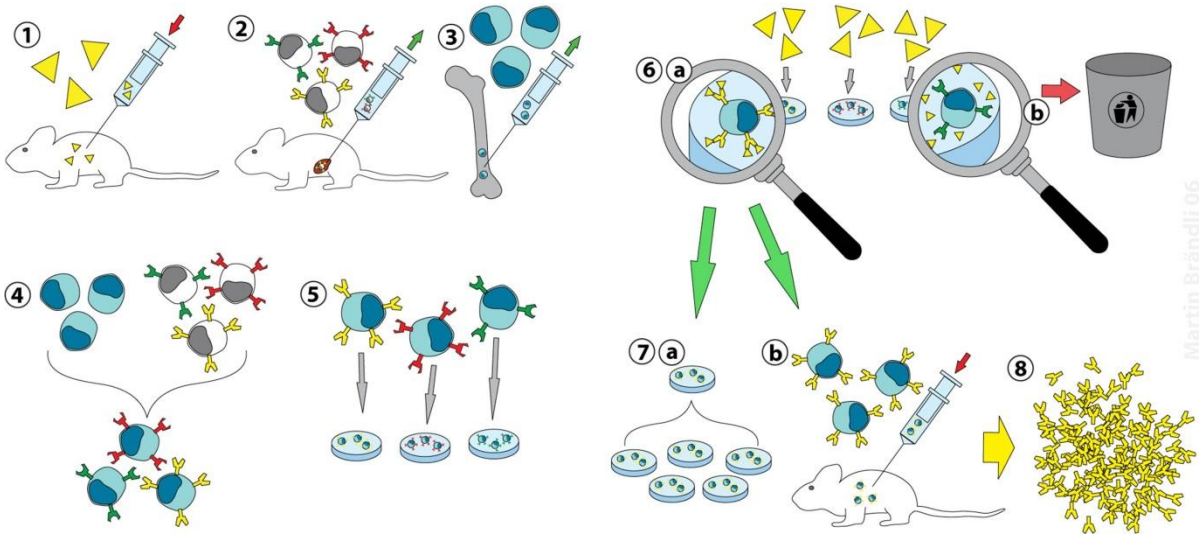

Image source: https://commons.wikimedia.org/wiki/File:Hybridoma_technology.png.

1—Immunisation: A specific antigen is injected into a mouse, triggering an immune response.

2—B cell isolation: Cells that developed to produce antibodies specific towards the initiating antigen are collected from the spleen

3—Cultivation of myeloma cells: Cultures of immortalised myeloma cells are maintained.

4—Fusion: The antibody producing splenocyte is fused with a myeloma cell, equipping the fused hybrid with the antibody producing abilities of the splenocyte and the immortality of the myeloma cell.

5—Cell line separation: The cell suspension containing all different hybridomas is diluted into well plates such that each well contains single cells. Subsequently, cell

populations in each well will be monoclonal; as will the antibody secreted into the supernatant.

6—Screening and selection of suitable cell lines: Collection of the supernatant and testing of the antibodies therein allows for selection of cell lines with the desired properties.

7—In vitro / in vivo multiplication: Cell lines are maintained for expansion of the populations and increased antibody production

8—Harvesting: Periodically, produced antibody can be harvested by collecting the cell culture supernatant, or cells themselves can be harvested.

8.16 Confirming Hybridoma Isotype and Specificity

In order to ensure that the hybridoma cell lines that were maintained in cell culture were indeed of the IgG1 isotype, and were all specific towards the NP antigen, they were tested via flow cytometry.

Cell populations were stained using:

- APC α IgG1 (1/50), (BD Pharmigen, BD Biosciences, USA)

- NP - PE (1/200), (Biosearch Technologies, Inc., USA. Cat.# N-5070-1)

and were subsequently acquired on a Cyan ADP (Beckman Coulter, USA)

Data was analysed using FlowJo (ver. X 10.0.7r2, Tree Star, Inc. USA.)

The diagram below illustrates the gating applied to the investigated cell populations, showing as examples an unstained cell population and cells from the B1.48 cell line.

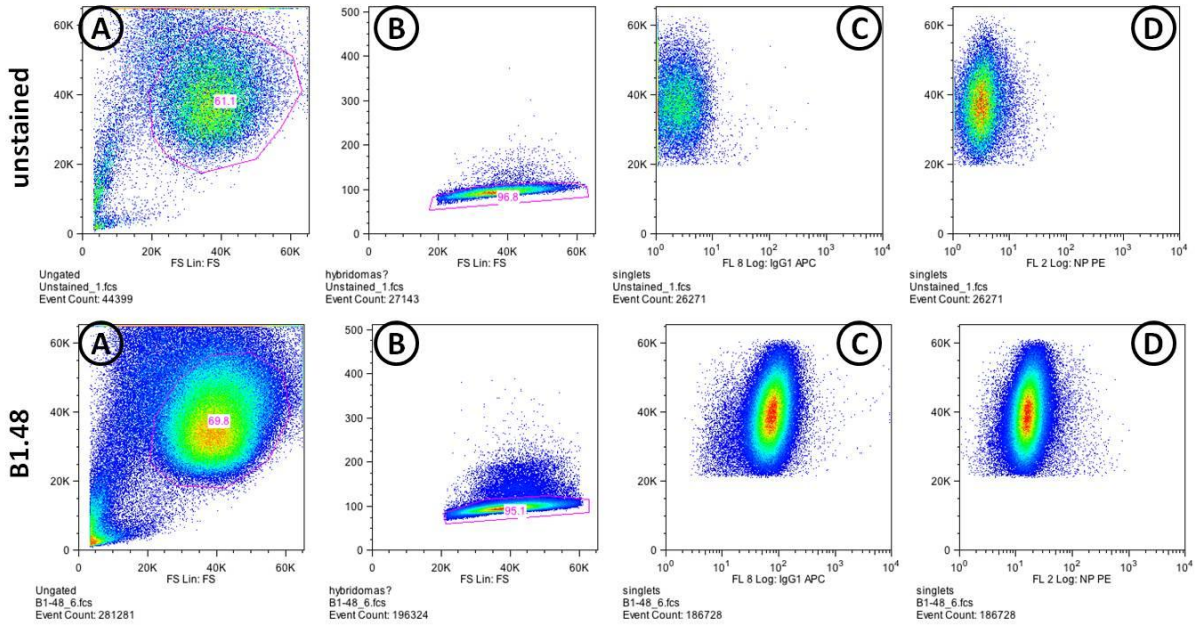

Live cells were gated in (A), followed by singlet selection in (B), allowing for assessment of IgG1$^+$, and NP$^+$, populations in (C) and (D) respectively. Each dot in each of the insets represents one cell. X and Y axes show the intensity of the recorded signal. The colour of the point cloud indicates the frequency of events

detected, showing low point densities in blue, going through green and yellow, to showing high point densities in red.

The histograms below show the distributions of IgG1$^+$, and NP$^+$, populations for all four hybridoma cell lines; for which the percentages of positive cells are shown in the subsequent table.

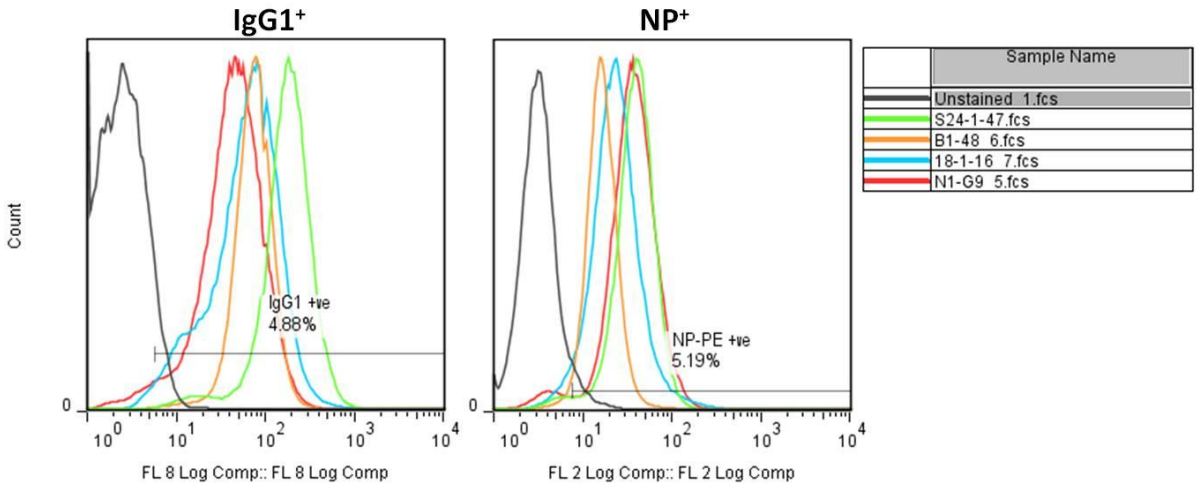

Cell Line	% IgG1$^+$	% NP$^+$
S24.1.47	99.9	97.4
N1.G9	96.6	95.5
B1.48	99.8	97.0
18.1.16	98.5	95.5

8.17 Hybridoma Affinities via SPR

The Biacore instrument (Biacore 3000, Biacore AB, Uppsala, Sweden) makes use of surface plasmon resonance (SPR); a phenomenon through which a dip in intensity in a wedge of light occurs in dependence on the surface it reflects from.

The image below shows a schematic of the principle of SPR as utilised in the Biacore instrument.

- An Au coating on a sensor chip facilitates the immobilisation of antigen
- The sensor chip is attached to a flow cell such that the functionalised surface is exposed
- Antibody specific towards the immobilised antigen is passed through the flow cell
- Dependent on the affinity of the antibody passed through the flow cell, different amounts of antibody are bound to the sensor chip

The addition of mass to the sensor chip influences the SPR angle, at which the dip in intensity in the wedge of light occurs. This shift in angle is quantified by the instrument in resonance units (RU).

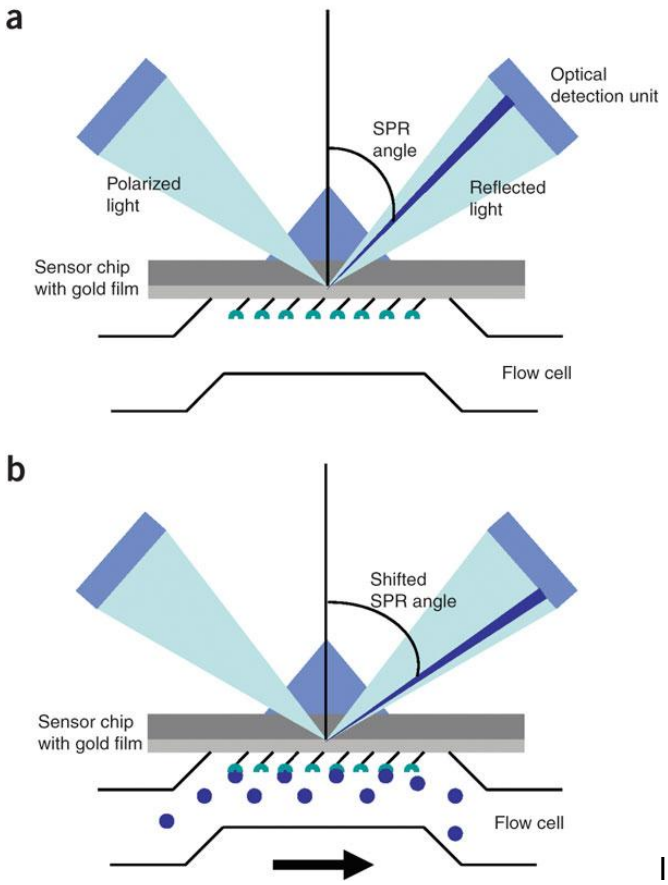

Image taken from [130]

The graph below shows the data obtained in the investigation of purified antibody produced by the different hybridoma strains used in this project.

The first half of each curve represents antibody suspension flowing through the flow cell, and its shape is determined by the amount of antibody that binds to the sensor chip; dependent on the antibody affinity. The second half of each curve represents buffer solution flowing through the flow cell, and its shape is determined by the amount of antibody that is retained on the sensor chip; also dependent on the antibody affinity. For antibodies with high affinity larger amounts bind to the sensor chip during the deposition phase and only small amounts are lost during the rinsing phase; and vice versa.

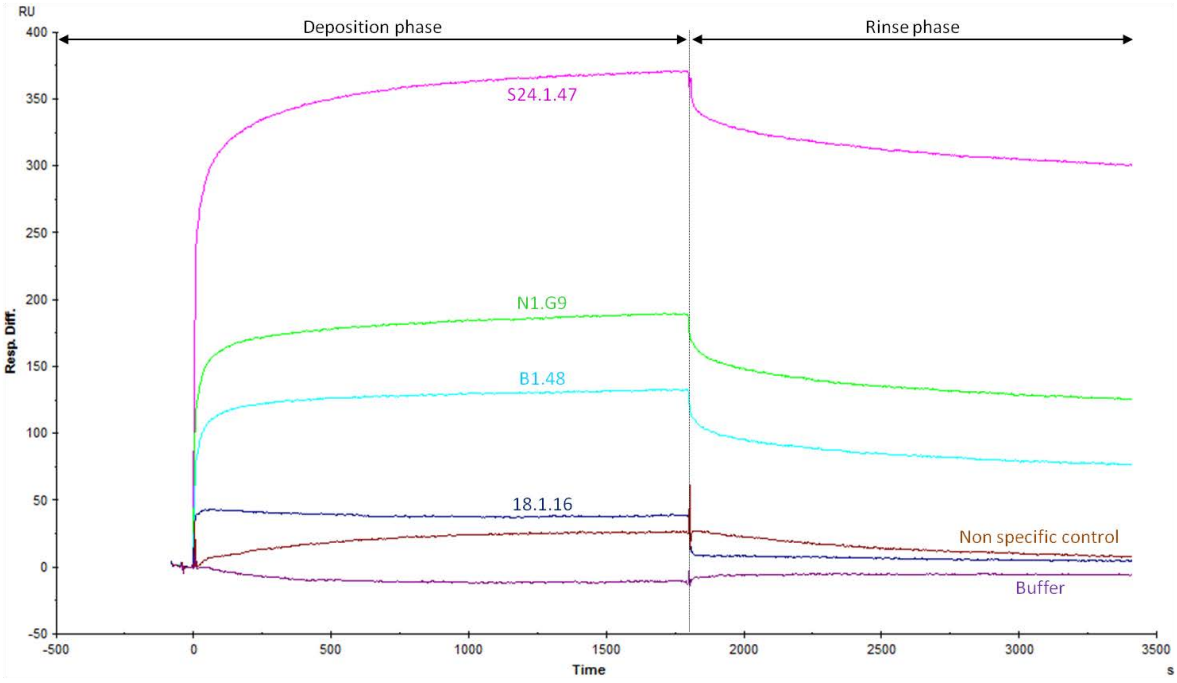

Through fitting of mathematical models to the obtained data, values for k_{on} and k_{off} can be produced from the deposition and the rinsing phase respectively. As detailed in Equation 2 (p.7), the obtained values can subsequently be used to determine values of K_D for the different antibody species.

The table below shows the values of k_{on} and k_{off}, for the different antibody species for which models could be fitted to the experimental data.

	Deposition Phase		Rinse Phase		
Cell Strain	**Fit quality**	**k_{on} [1/Ms]**	**Fit quality**	**k_{off} [1/s]**	**K_D**
S24.1.47	✓	1.11E+02	✗		
N1.G9	✓	1.74E+01	✗		
B1.48	✓	6.35E+00	✓	4.96E-04	7.81E-05
18.1.16	✗		✓	4.80E-04	

Good quality model fitting to both deposition and rinse phase data was only achieved for cell strain B1.48; hence a definite quantitative assessment of the different cell strain affinities could not be made. The qualitative assessment of the data, however, shows quite clearly the relative ranking of the different cell strains in their affinities: Cell strain S24.1.47 is of the highest affinity, with large amounts of antibody quickly attaching to the sensor chip in the deposition phase; the majority of which is retained during the rinse phase. Whereas cell strain 18.1.16 is of the lowest affinity, with only small amounts of antibody attaching during the deposition phase, of which the majority is quickly lost during the rinse phase.

While exact values for the affinities of the antibodies produced by the different cell lines could not be obtained, a qualitative ranking of the cell lines in their affinities could be established to guide expectations for later AFM adhesion measurements:

Cell Strain	Affinity
S24.1.47	High
N1.G9	Medium-High
B1.48	Medium-Low
18.1.16	Low

8.18 Cell Monolayer Preparation Protocol

A. Preparation of coverslips:

1. Prepare a 1 mg/mL solution of poly-l-lysine (Poly-L-lysine hydrobromide, Cat.# P2636, Sigma-Aldrich, USA) in PBS, and pour into a clean glass dish
2. Clean coverslips (13 mm diameter, thickness No. 1,5. Cat.# 631-0150. VWR International, USA) in a small beaker of ethanol, and subsequently in PBS
3. Place the coverslips into the dish containing the poly-l-lysine solutions, such that coverslips are not overlapping
4. Cover the dish with a lid and leave for at least 2 h

B. Equipping coverslips with cells:

1. Determine cell number
2. Resuspend cells in PBS, with 0.1% sodium azide, at $2x10^6$ cells/mL
3. Take coverslips from the poly-l-lysine solution, wash in a beaker of PBS, and place into a 24-well plate (Falcon® 24 well clear flat bottom, Cat.# 353047. Corning GmbH, Wiesbaden, Germany)
4. Add 0.5 mL of RPMI (RPMI-1640 Medium, Cat.# R8758, Sigma-Aldrich, USA) to each well
5. Add 0.5 mL of cell suspension to each well ($1x10^6$ cells)
6. Cover the plate with a lid, and then place into an incubator for 2 h to allow cells to sediment onto the coverslips
7. Remove the coverslips from the wells, and wash gently in a beaker of PBS to remove unbound cells

8. Place coverslips in a glass dish of cold acetone, and keep in the fridge for 20 mins
9. Take a 24 well plate, stuff their bottoms with tissue paper, and soak the paper with PBS or water; creating individual humid chambers for the coverslips
10. Remove the coverslips from the acetone, and place them in the moistened wells

- For samples prepared from hybridoma cells, the cells are harvested from cell culture
- For samples prepared from B cells, a mouse spleen is first obtained, and the B cells isolated using magnetic activated cell sorting according to the Myltenyi Biotec protocol; available at: http://www.miltenyibiotec.com/~/media/Images/Products/Import/0001200/IM0001263.ashx

8.19 Fundamentals of Quantifying Cell Elasticity

Cell elasticity is quantified by the Young's modulus. In general, the Young's modulus is an elastic property of a material, and is defined as the stress of a material divided by the strain, as shown by the Equation A8.19/1 below; which is a normalised measure of the compressibility – the higher the value the stiffer the sample.

$$E = \frac{\sigma}{\varepsilon} \qquad \text{Equation A8.19/1}$$

Where:

$$\sigma = \frac{F}{A} \qquad \text{Equation A8.19/2}$$

$$\varepsilon = \frac{\Delta L}{L} \qquad \text{Equation A8.19/3}$$

Where:

E	=	Young's modulus	[Pa]
σ	=	stress	[Pa]
ε	=	strain	
F	=	force	[N]
A	=	area	[m²]
L		original length	[m]
ΔL		change in length	[m]

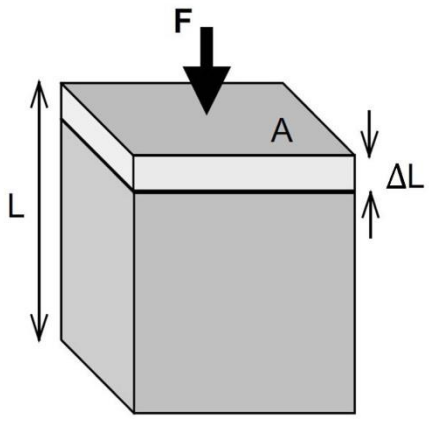

Figure A8.19/1 – Homogenous Uniaxial Compression of a Material. Image Taken From [131].

In the case of homogenous compression, as for the material in Figure A8.19/1, the Young's modulus can readily be obtained. In AFM measurements, however, the surface is indented locally with a specific tip shape. Hence in such experiments a specific indentation geometry needs to be considered. This means that both the stress and the strain, that are required to determine the Young's modulus of a material, are no longer trivial to obtain.

In nanoindentation tests, the size of the impression is too small to be conveniently measured directly. Therefore, the area of contact is instead determined by measuring the depth of penetration of the indenter into the specimen surface. Combined with a known geometry of the indenter, this provides an indirect measurement of contact area at a specific load; from which a mean contact pressure can be estimated. The most well-known scenario, for stresses and deflections arising from contact between two solids, is the contact between a rigid sphere and a flat surface; as illustrated in Figure A8.19/2 below.

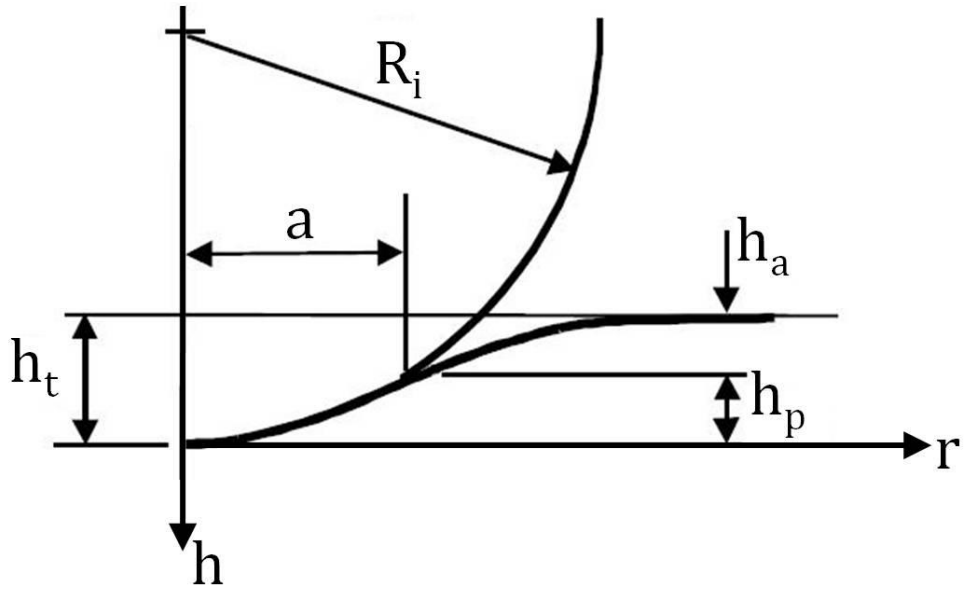

Figure A8.19/2 – Contact Between a Rigid Indenter and a Flat Surface. Image Taken From [132].

Where:

a	=	radius of the circle of contact	[m]
R_i	=	radius of the indenter	[m]
h_t	=	total depth of penetration	[m]
h_a	=	depth of the circle of contact from specimen free surface	[m]
h_p	=	distance from bottom of the contact to contact circle	[m]

As shown by Hertz [133], the radius of the circle of contact a is related to the indenter load F, the indenter radius R, and the elastic properties of the contacting materials E^* by:

$$a^3 = \frac{3}{4}\frac{FR}{E^*} \qquad \text{Equation A8.19/4}$$

The quantity E^* is the combination of the modulus of the indenter and the specimen; which is given by:

$$\frac{1}{E^*} = \frac{(1-v^2)}{E} + \frac{(1-v'^2)}{E'} \qquad \text{Equation A8.19/5}$$

where ν is the Poisson's ratio, the primed terms apply to the indenter properties, and E^* is often referred to as the 'reduced modulus'. In the case of a rigid indenter, E^* is associated only with the specimen, as no 'reductions' in the combined modulus can be incurred if the modulus of the indenter is assumed to be infinite. This may also be assumed for scenarios in which the elastic modulus of the indenter is several orders of magnitude greater than that of the specimen, as here only negligible deformations are incurred in the indenter. Incorporating the assumption of a rigid indenter, Equation A8.19/5 becomes:

$$\frac{1}{E^*} = \frac{(1-v^2)}{E} \qquad \text{Equation A8.19/6}$$

and hence:

$$E^* = \frac{E}{(1 - v^2)}$$ Equation A8.19/7

The deformations at the contact are localised and the Hertz equations are concerned only with these localised deformations, rather than deformations of the bulk or stresses experienced at the supports of the contacting bodies. The deflection profile of the original free surface at the indenter, h, is given by:

$$h(r) = \frac{3}{E^*}\frac{F}{8a}\left(2 - \frac{r^2}{a^2}\right) \qquad r \leq a$$ Equation A8.19/8

It can be shown from Equation A8.19/8 that the depth of the circle of contact beneath the specimen free surface is half of the total elastic displacement; hence, that the distance from the specimen free surface to the depth of the radius of the circle of contact is $\mathrm{h_a} = \mathrm{h_p} = \mathrm{h_t}/2$.

The distance of mutual approach of distant points in the indenter and the specimen, i.e. the distance of approach of points in the indenter and the specimen that are unaffected by deflections caused by penetration of the indenter into the specimen, is calculated from:

$$h^3 = \left(\frac{3}{4E^*}\right)^2 \frac{F^2}{R}$$ Equation A8.19/9

Substituting Equation A8.19/8 into A8.19/4, the distance of mutual approach can be expressed as [132]:

$$h = \frac{a^2}{R}$$ Equation A8.19/10

In the case of a rigid indenter, the distance of mutual approach h is in fact equal to the total depth of penetration of the specimen $\mathrm{h_t}$, as shown in Figure A8.19/2; as no

deformations are incurred in the indenter. Further, the quantity E^* is associated only with the specimen, as shown in Equation A8.19/7. Hence, substituting Equation A8.19/7 into Equation A8.19/9, and rearranging for the load F, yields.

$$F = \frac{E}{1-\nu^2}\frac{4\sqrt{R}}{3}{h_t}^{3/2} \qquad \text{Equation A8.19/11}$$

$$a = \sqrt{Rh_t} \qquad \text{Equation A8.19/12}$$

Equation A8.19/11, and Equation A8.19/10 rearranged for a, as in Equation A8.19/12, are essentially the equations used in the JPK data analysis software [134] that was employed for the evaluation of experimental data.

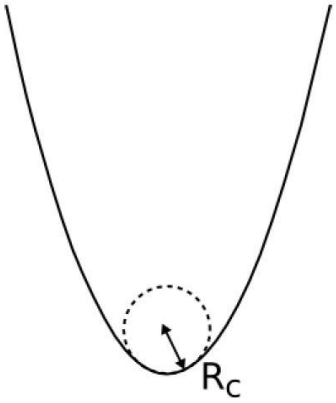

Figure A8.19/3 – Parabolic Indenter with Radius of Tip Curvature R_C. Image Taken From [134].

Adapted to the specific case of a parabolic indenter, as shown in Figure A8.19/3, the radius of the indenter R, is replaced by the radius of the tip curvature R_C.

$$F = \frac{E}{1-\nu^2}\frac{4\sqrt{R_c}}{3}{h_t}^{3/2} \qquad \text{Equation A8.19/13}$$

$$a = \sqrt{R_c h_t} \qquad \text{Equation A8.19/14}$$

Using Equation A8.19/13 allows determination of the specimen Young's modulus E from experimental data. From experimental values for the depth of penetration h, and the applied load F, and specifying reasonable values for the Poisson's ratio ν, and the radius of the tip curvature R_C, a value of E can be determined computationally that

produces the least discrepancy between the employed model and the available experimental data.

From Equation A8.19/14, using the radius of the tip curvature R_C, and the depth of penetration h, the radius of the circle of contact a can be determined; which allows determination of the area of contact. With the area of contact, and the applied load F, available, the mean contact pressure p_m can be determined; which is given by:

$$p_m = \frac{F}{\pi a^2} \qquad \text{Equation A8.19/15}$$

Combining equations A8.19/4 and A8.19/15 subsequently yields:

$$p_m = \left(\frac{4E^*}{3\pi}\right)\frac{a}{R} \qquad \text{Equation A8.19/16}$$

The mean contact pressure p_m can be seen as the 'indentation stress', and the quantity $\frac{a}{R}$ as the 'indentation strain'. This functional relationship between p_m and $\frac{a}{R}$ alludes to the existence of a stress-strain response similar to that commonly obtained from such uniaxial compressions as shown to begin with in Figure A8.19/1.

Using the example of a real data point, the constituent steps to extracting the specimen Young's modulus from force-distance curves, obtained in specimen indentations, are described below.

Figure A8.19/4 shows an individual data point opened in the data processing software, showing the approach curve in magenta, and the retraction curve in blue. All data manipulation required to extract the specimen Young's modulus is performed

on the approach curve. Visibly noticeable, the force distance curves have tilted baselines. This is corrected in the first step of the data analysis.

As shown in Figure A8.19/5, using the ‘subtract baseline’ tool, the baseline tilt is corrected, and the baselines are positioned at 0. This operation is performed on the extension segment of the data point, i.e. the approach curve, and the greater the portion of the baseline used for the operation (the shaded part) the more accurate the results.

The next performed operation is the subtraction of the x-offset. As shown in Figure A8.19/6, the data is shifted such that the contact point is positioned at 0 on the x-axis.

The head height that has been shown on the x-axis until now refers to the measured height of the cantilever support. To be able to determine specimen elasticity, however, the depth of indentation of the tip at the free end of the cantilever into the specimen is required. The next operation takes into account, and corrects for, the bending of the cantilever as it indents the sample. Subsequently, as shown in Figure A8.19/7, the tip-sample separation is displayed on the x-axis. This tip-sample separation is what is used as the depth of penetration h as seen in Equation A8.19/11.

With both the depth of penetration of the indenter h, and the applied load F, available, the next step is the application of the deformation model to extract the specimen elasticity; shown in Figure A8.19/8. Selecting the ‘Paraboloid’ tip shape, the applied deformation model is that detailed in Equation A8.19/11, where for both the depth of penetration of the indenter h, and the applied load F, experimental data is available. Parameters R_C, and ν, are assumed to be prior knowledge, and are specified in the

respective highlighted fields. The radius of the tip curvature R_C is specified as stated by the manufacturer. The Poisson's ratio ν is specified as 0.5, which is the Poisson's ratio of water and is routinely assumed for water based organic materials. At this stage only parameter E remains, for which a value is determined using the Levenberg-Marquardt algorithm by minimising for the discrepancy between theoretical and experimental data. For visual inspection of the obtained fit, only the region in which the tip is in contact with the specimen is of interest (the area encircled by the dashed line).

In Figure A8.19/9 the data window has been adjusted to show in greater detail the region in which the tip is in contact with the specimen, which allows for better visual inspection of the obtained fit (faint green line). As can be seen, the line of the obtained fit deviates from the experimental data after a certain depth of indentation. This is because the Hertzian model fit is based on the assumption of only purely elastic deformations occurring, which only holds for small indentations. Therefore, the region of points considered in the model fit (the shaded area) was restricted to small indentations.

To further indicate that the incurred deformations are not purely elastic, it can clearly be seen that the retraction curve does not overlap with the approach curve. If only purely elastic deformations were occurring, both approach and retraction curve should be identical.

Highlighted in Figure A8.19/9 is the value of the Young's modulus that was obtained through fitting the model, as well as the accompanying residual RMS. The latter is an assessment of the goodness of fit of the model with the experimental data, and its value is an accumulation of the discrepancies between all considered experimental

data and the established fit. The RMS value of 35.69 pN obtained for the examined example data point is low, several orders of magnitude lower than the applied loads, indicating that the established model fits the experimental data well, and hence that the Young's modulus determined for the specimen is reliable.

In the top left corner of the data analysis window, encircled by the dashed line in Figure A8.19/9, a row of icons can be seen. Each icon represents one of the constituent operations that have been performed to extract the specimen Young's modulus. These can be saved as a composite process that can subsequently be applied to batches of data.

The RMS value constitutes a quantitative assessment of the model fit to the experimental data that, especially in the analysis of batches of data, is a readily available tool for the assessment of the reliability of the calculated parameters, which is more reliable and practical as compared to the visual inspection of large data sets.

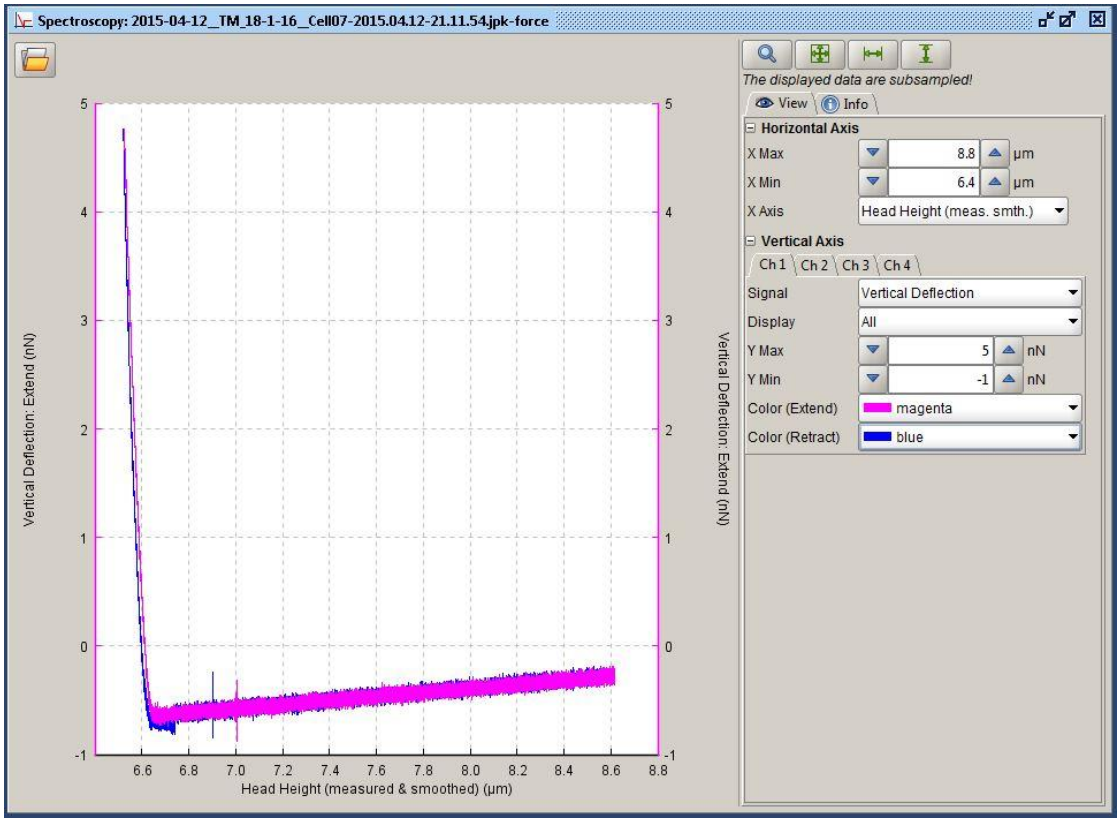

Figure A8.19/4 – Raw Data Opened in JPK Data Processing Software

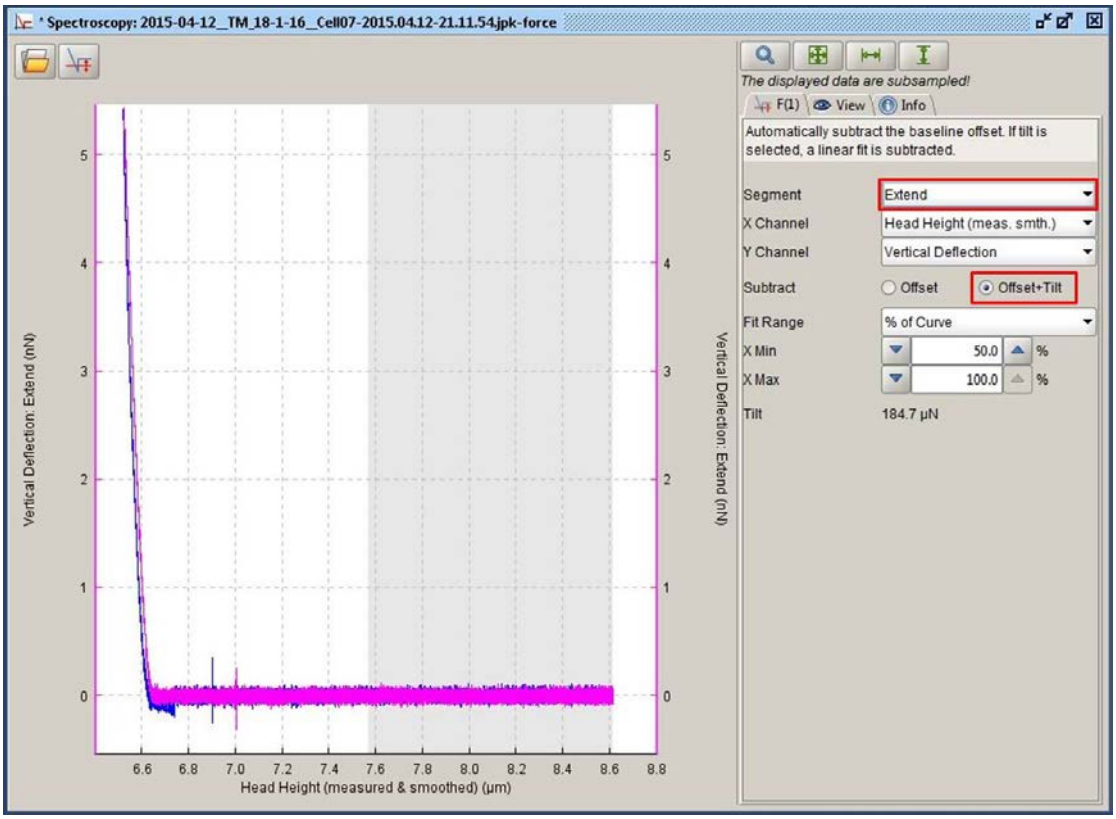

Figure A8.19/5 – Correction of Baseline Offset and Tilt.

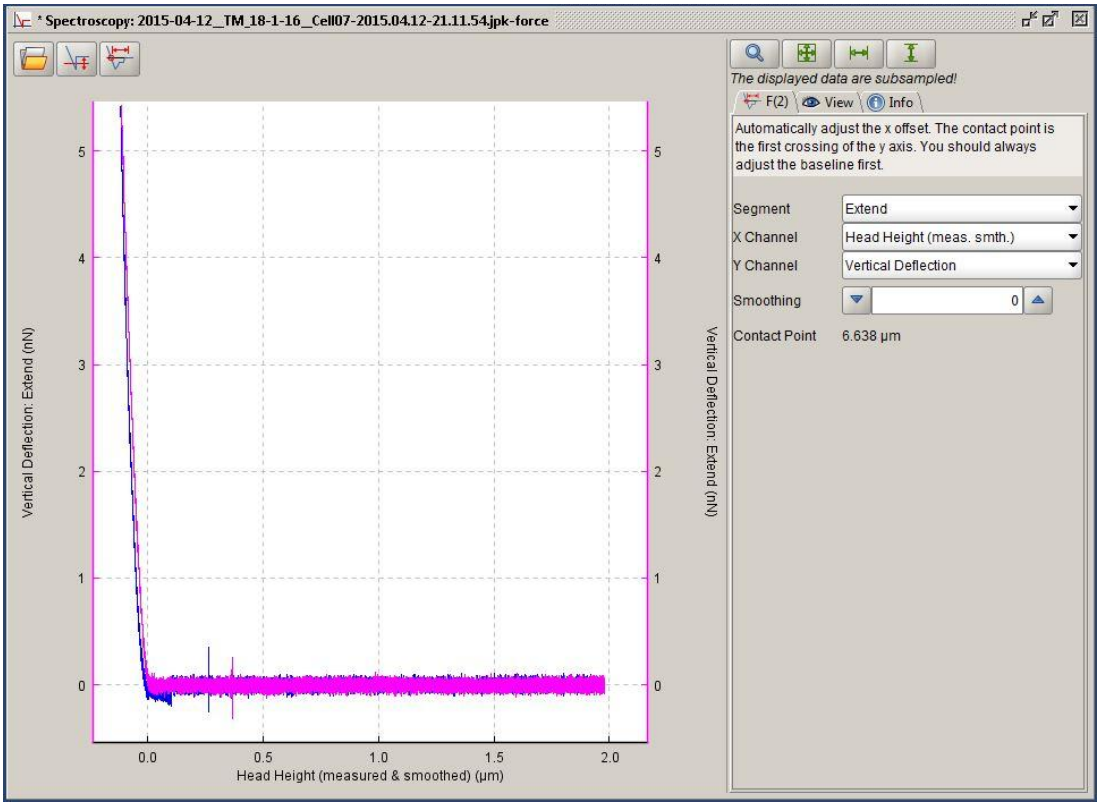

Figure A8.19/6 – Adjusting the Offset in x.

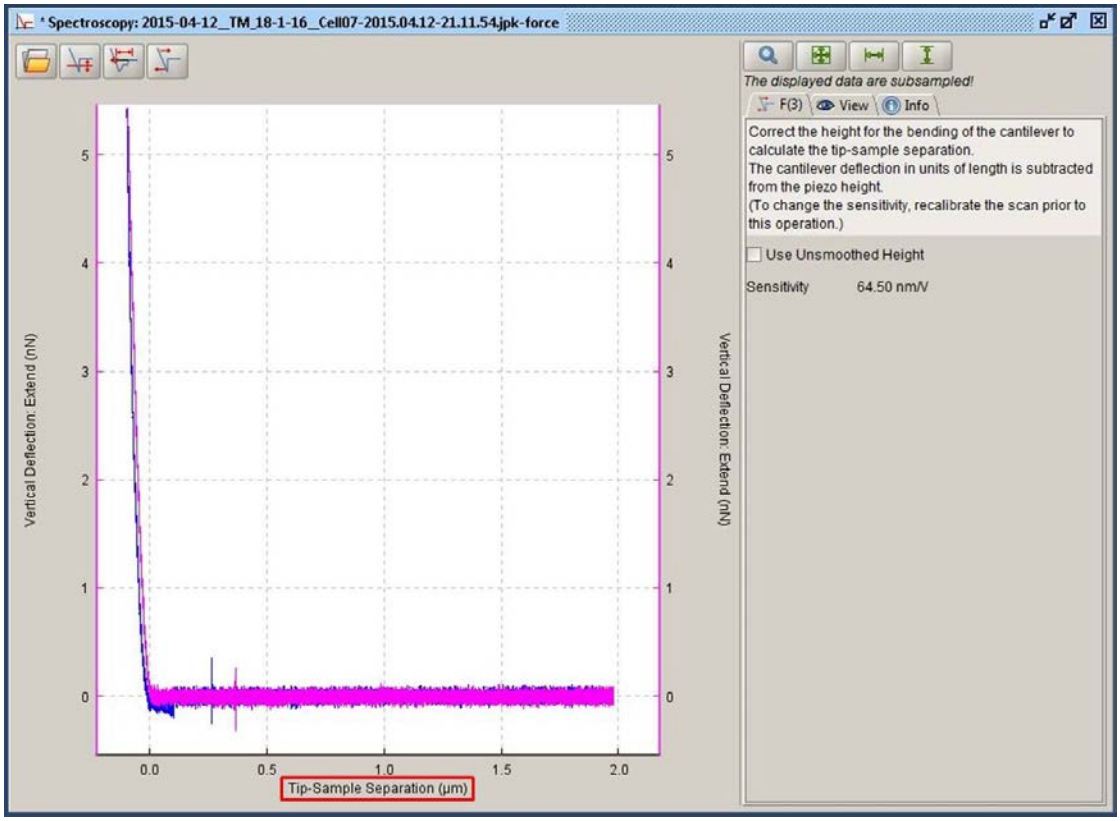

Figure A8.19/7 – Determining Tip Sample Separation

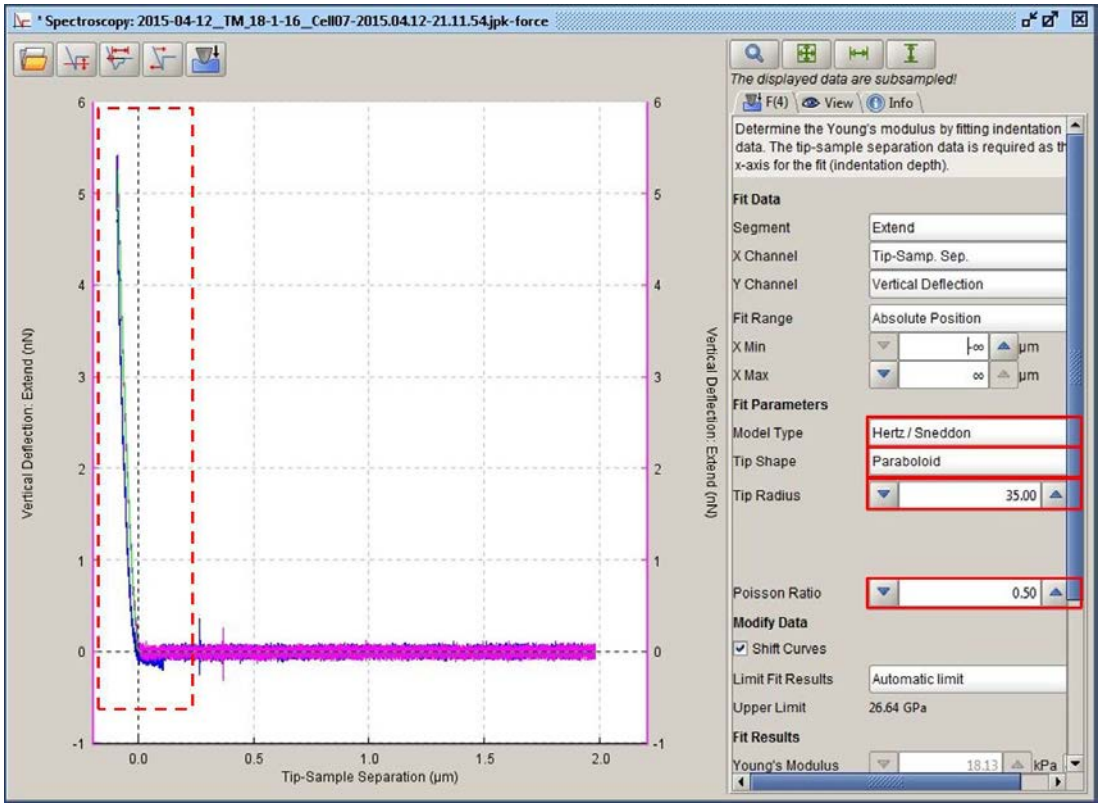

Figure A8.19/8 – Application of Deformation Model for Extracting Specimen Elasticity.

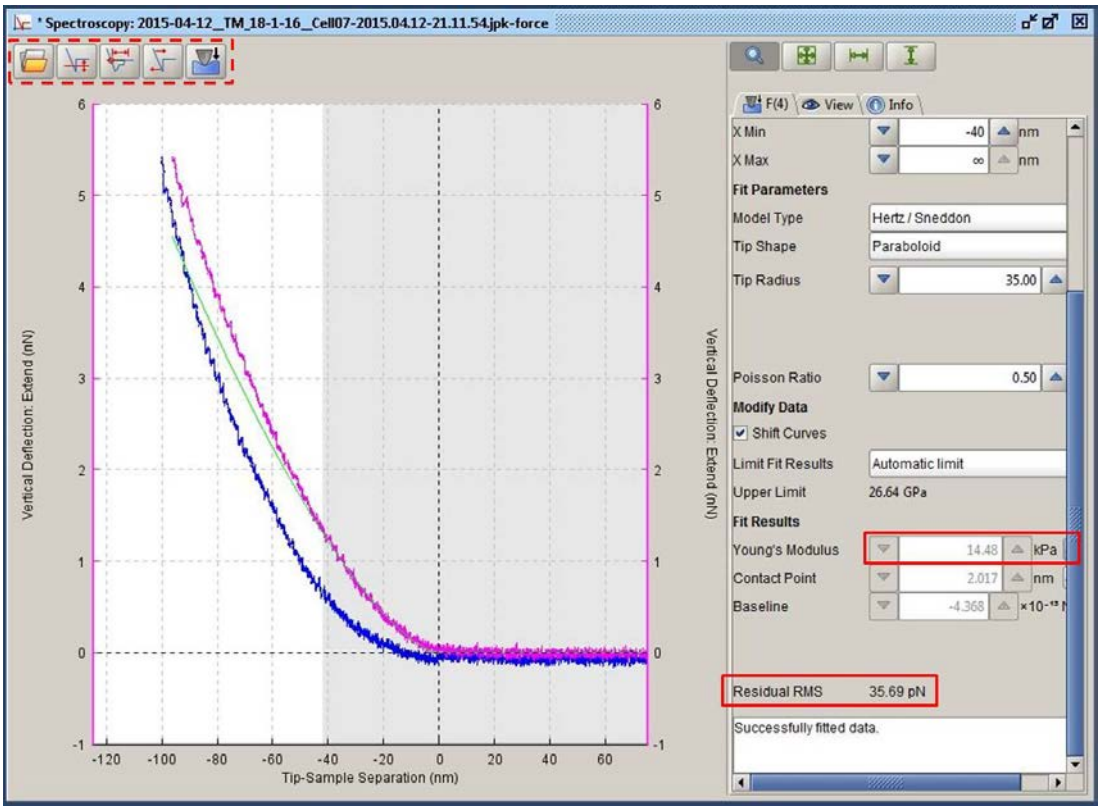

Figure A8.19/9 – Inspection of Area of Interest and Calculated Fit Parameters

To further demonstrate that the employed data analysis strategies produce reliable results, the relationships of the determined Young's moduli with their corresponding RMS values are shown below, for the two data sets presented in §5.5.1.1 (p.105); for which cell elasticity results are first shown. Figures A8.19/10 and A8.19/11 show the results for hybridoma cells interrogated using 3 different cantilever modifications, and B cells interrogated using a NP tip only, respectively.

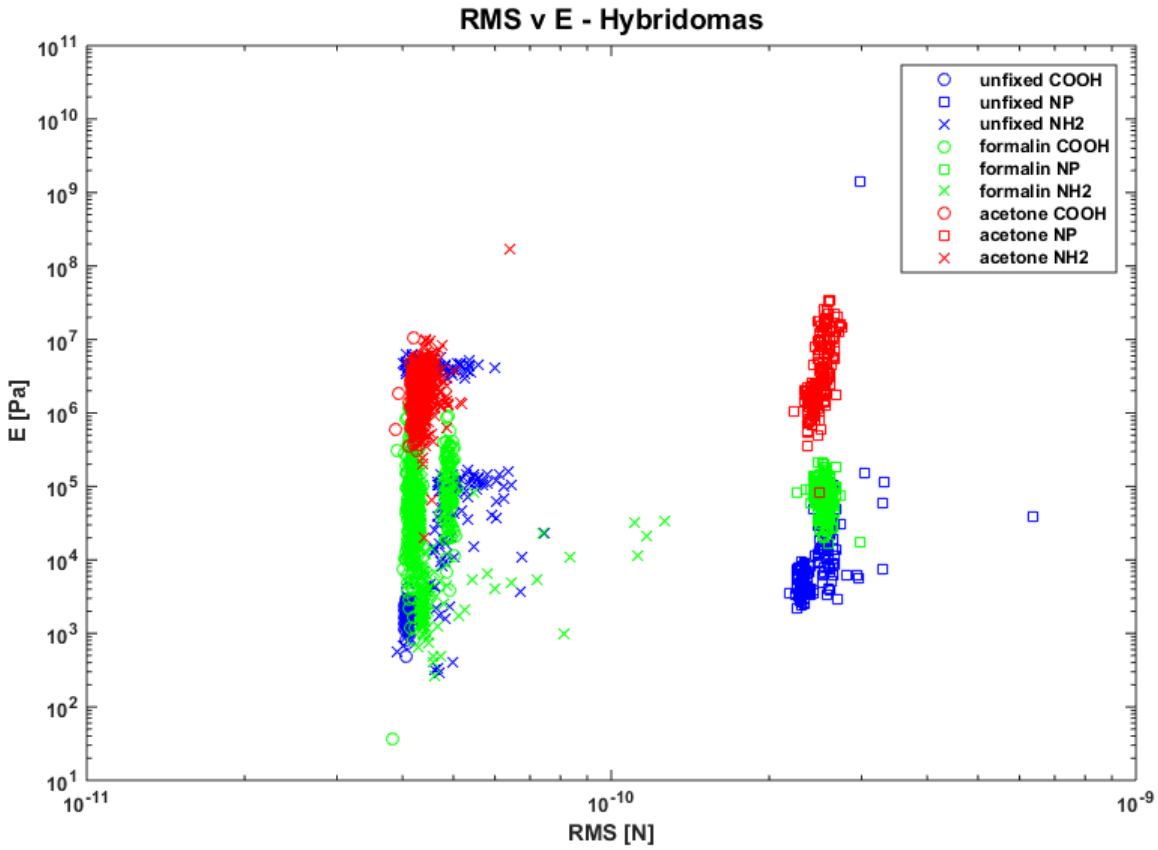

Figure A8.19/10 – RMS v E for hybridoma cells

The results in Figure A8.19/10 show the same variations in elasticity values that can more clearly be inspected in Figure 38 (p.106), but additionally demonstrate that little variation in the RMS values of the separate data sets exist. Clearly discernible is a systematic increase in RMS values associated with measurements conducted using the probe functionalised with NP, however, despite the approximately 5-fold increase

in RMS values, the produced elasticity values remain at the same magnitudes as the ones associated with lower RMS values. A possible reason could be that the greater layer thickness of the NP functionalisation causes increased interference with the laser reflecting off the back of the cantilever, but this was not investigated further.

Similarly, the results presented in Figure A8.19/11 show that the majority of the determined elasticity values, that can in more detailed be examined in Figure 40 (p.109), are associated with low RMS values; and that the elasticity values remain at the same magnitudes even if they are associated with greater RMS values.

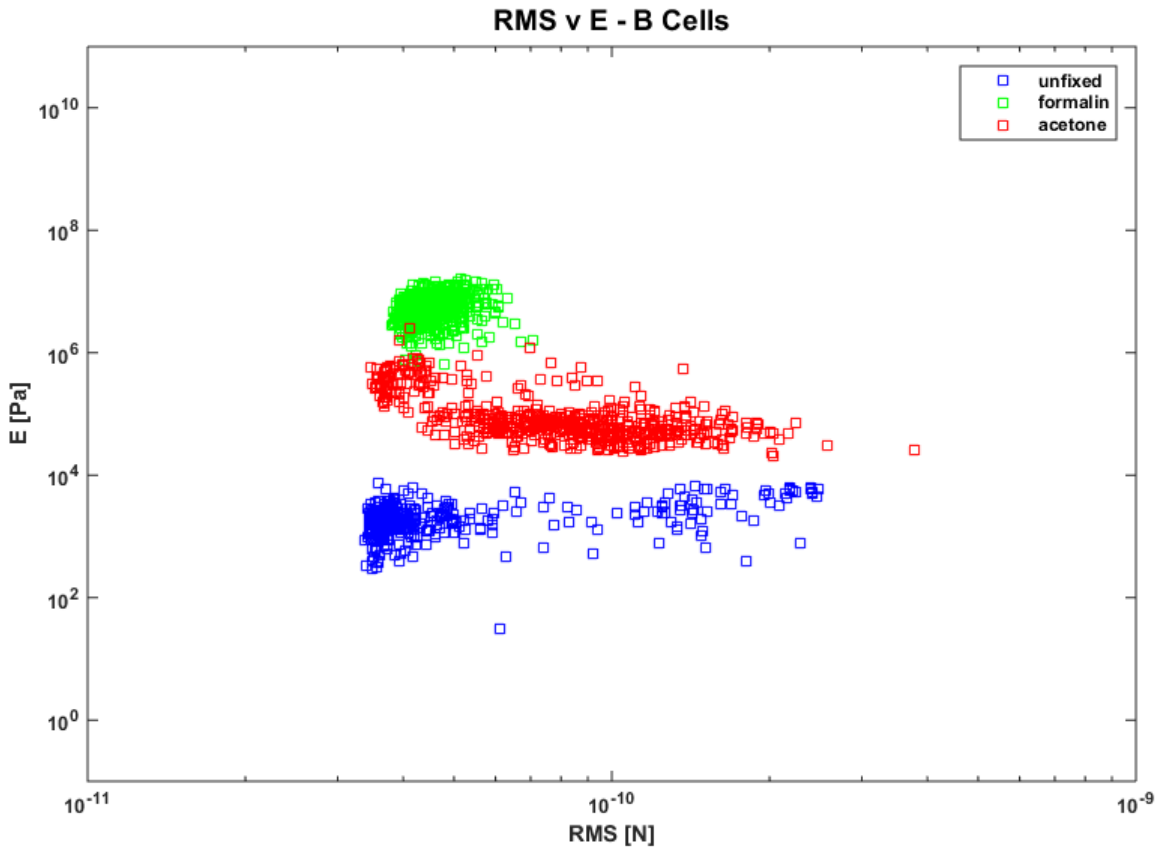

Figure A8.19/11 – RMS v E for B cells

8.20 Hybridoma and B Cell Size Assessment

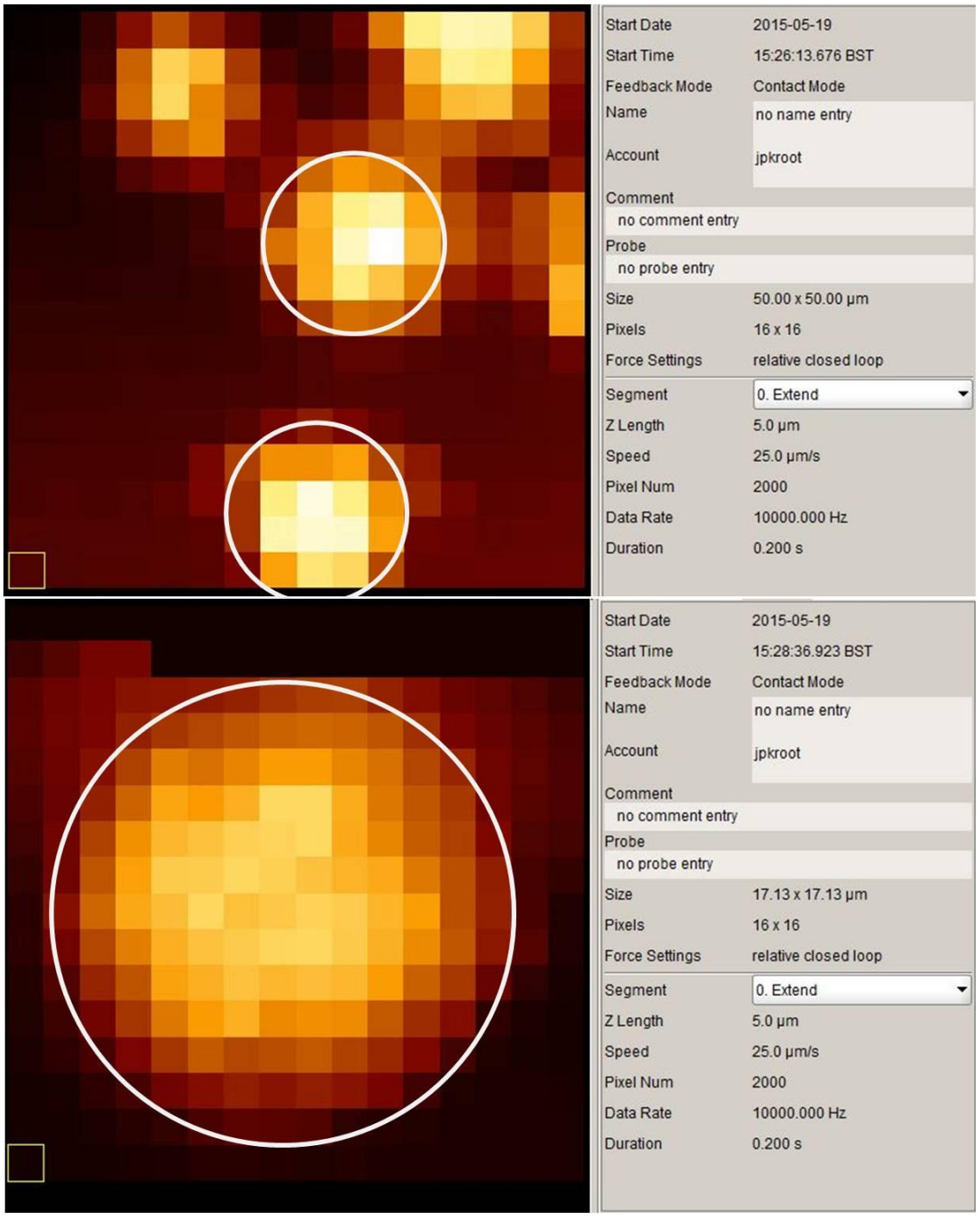

Approximate sizing of hybridoma cell

The size of hybridoma cells as estimated from coarse and fine force scan maps is (5/16 pixel * 50 µm) = **15.6 µm**, and (13/16 pixel * 17.13 µm) = **13.9 µm**, in diameter, respectively.

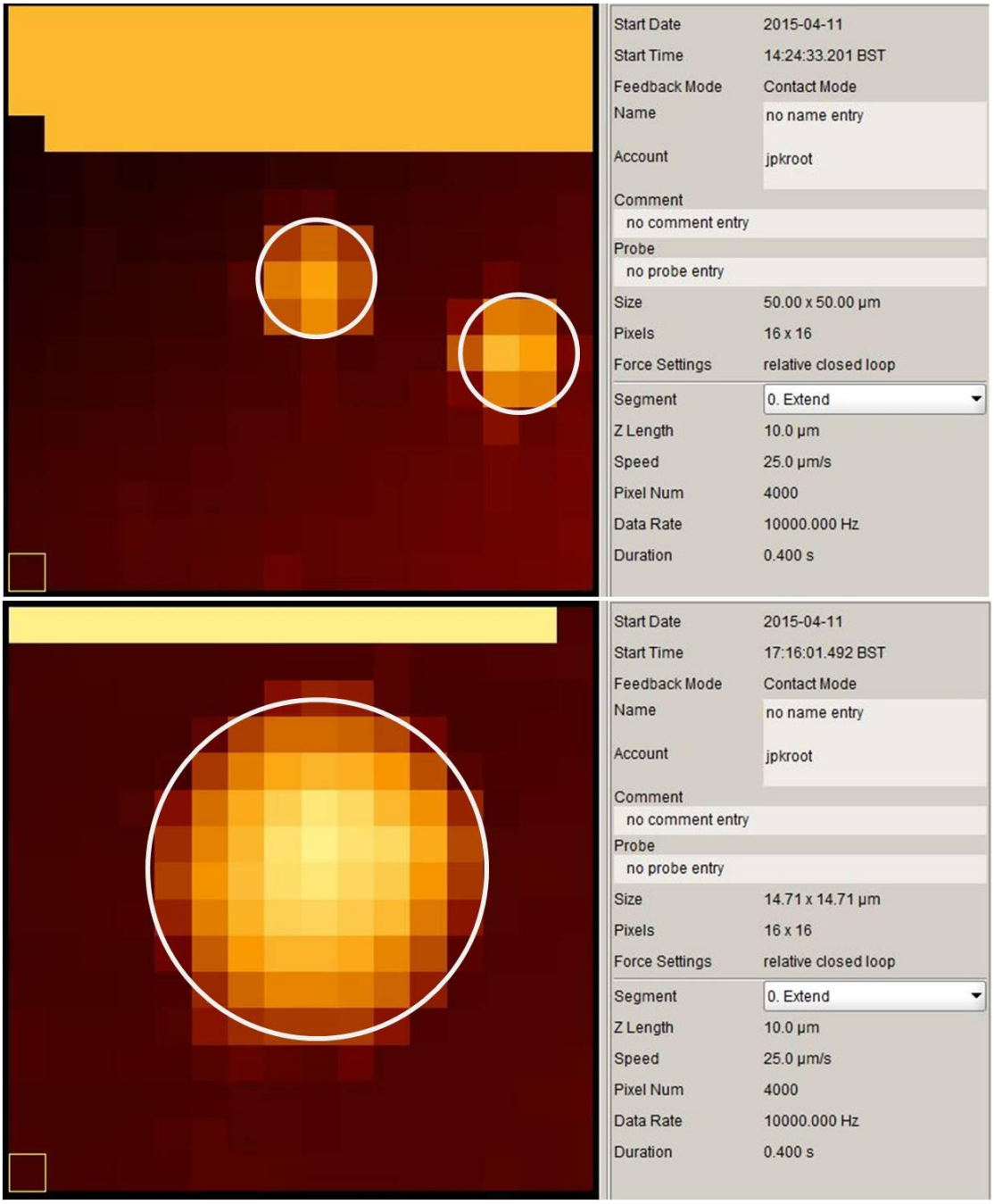

Approximate sizing of B cells

The size of B cells as estimated from coarse and fine force scan maps is (3/16 pixel * 50 µm) = **9.4 µm**, and (9/16 pixel * 14.71 µm) = **8.3 µm**, in diameter, respectively.

8.21 Protocol for Preparation of Tissue Sections

- Spleens were extracted from Cg1-Cre $\kappa^{-/-}$ mice, which were killed 5 days post immunisation with alum-precipitated NP-CGG with *Bordetella* pertussis
- Spleens were immediately snap-frozen in liquid nitrogen after extraction
- Spleens were mounted onto a chuck through a bed of OCT TissueTek compound (Dako, Glostrup, Denmark) and 6μm thick sections were cut on a cryostat (Bright Instruments, Huntington UK)
- Sections were mounted on 22mm diameter coverslips (No.1, 22 mm diameter, Chance Propper Ltd. Smethwick, UK)

Immunohistological staining of tissue sections prior to interrogation via AFM:

The staining applied prior to AFM interrogation was to locate GCs without labelling GCs directly, so as to not occupy the targeted NP-specific receptors. The applied staining labelled:

- $CD3^+$ cells – to identify the T-zone adjacent to GCs
- IgD^+ cells – to identify naïve B cells in the B follicle surrounding GCs

TRIS buffer at pH 7.6, and pH 9.2, was used for the preparation of the staining solutions; the buffers are prepared in the following:

TRIS Buffer pH 7.6:

- 1.0 L of 200 mM TRIS Base
- 1.5 L of 154 mM Physiological NaCl
- 1.0 L of 0.1 M HCl

TRIS Buffer pH 9.2:

As above but at pH 9.2. Initially pH 200 mL of buffer to give pH 9.2 using HCl (dropwise with 1 M or greater) and make up to desired volume with NaCl

The diagram below details the employed staining strategy, including the used antibodies and their dilutions in TRIS buffer at pH 7.6; using:

- IgD-sheep α mouse (The Binding Site, Birmingham, UK)
- HRP-donkey α sheep (Dako, Glostrup, Denmark)
- CD3-rat α mouse (Serotech, Oxford, UK)
- biotin-rabbit α rat (Dako, Glostrup, Denmark)

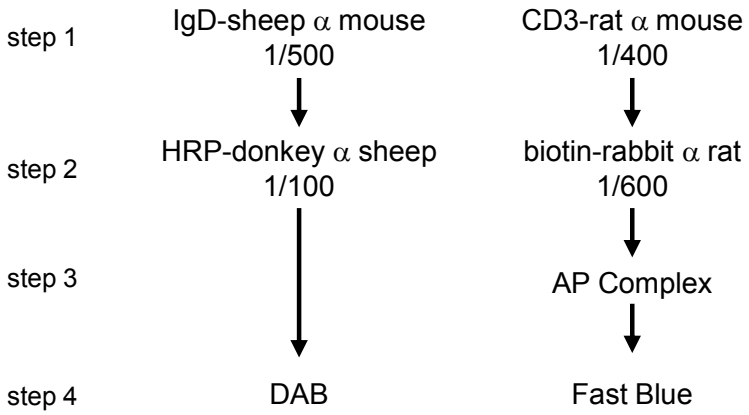

To detect IgD and CD3 on tissue sections a three step staining strategy was used before the stains were developed. Primary antibodies bound to the target directly (step 1), then secondary antibodies conjugated to peroxidase or biotin were applied (step 2). Streptavidin conjugated to alkaline phosphatase (AP) was finally added (step 3) before the brown and blue stains were developed from the reaction with enzymatic substrate (step 4).

- Apply primary antibodies and incubate in humid chamber for ~60 mins
- Wash slides in TRIS buffer (pH 7.6) for 5 mins
- Adsorb secondary antibodies with normal mouse serum, diluted 1:10 prior to addition to the slides

- Apply secondary antibodies and incubate in humid chamber for ~45 mins
- Wash slides in TRIS buffer (pH 7.6) for 5 mins
- Apply Strepavidin-complex with alkaline phosphatase (AP) (Dako, Glostrup, Denmark) and incubate in a humid chamber for ~45 mins
- Wash slides in TRIS buffer (pH 7.6) for 5 mins

After the application of staining antibodies, Horse-Radish Peroxidase (HRP) and AP reagents were developed sequentially using DAB and naphthol AS-MX phosphate with Fast Blue salt, respectively.

For DAB solution:

- Dissolve a single 10 mg 3-3'-diaminobenzidine tetrahydrochloride (DAB) tablet (Sigma Aldrich, Dorset, UK) in 15 mL TRIS buffer; pH 7.6
- Filter using filter paper
- Add 2 drops of 30% hydrogen peroxide (Sigma Aldrich)
- Vortex to mix
- Apply to section

For Fast Blue solution:

- Dissolve 8 mg Levamisole (Sigma Aldrich, Dorset, UK) in 10mL TRIS buffer; pH 9.2
- Dissolve 4 mg naphthol AS-MX phosphate (Sigma Aldrich, Dorset, UK) in 370 μL dimethylformamide in a glass bijoux in a fume hood
- Mix the two solutions and add 10 mg Fast Blue BB salt
- Vortex the solution, then filter using filter paper
- Apply solution to the section

- The DAB stain should be developed first, and usually develops in under 1 min
- Rinse with buffer before developing the Fast Blue; which usually takes ~5 mins to develop
- When both reactions are developed rinse with H_2O

Fluorescent Staining post AFM interrogation:

Post interrogation via AFM, fluorescent staining was applied to the tissue sections to confirm the presence of NP-specificity in the interrogated GCs.

The diagram below details the employed staining strategy, including the used antibodies and their dilutions in PBS; using:

- NP-rabbit (in-house; Chandra Bhati)
- Cy3-donkey α rabbit (Jackson Immuno Research Labs, USA)
- DAPI (Sigma-Aldrich, USA)

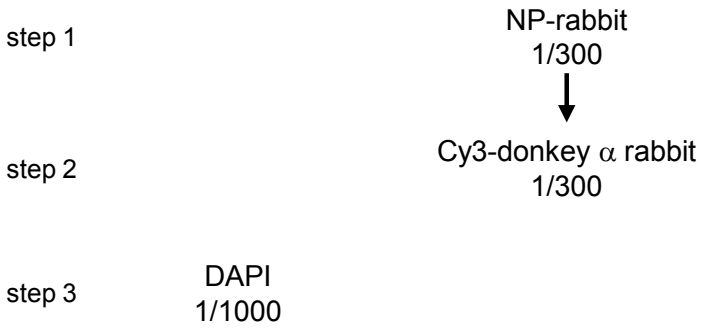

To detect NP specific binding a two-step staining strategy was employed. Primary antibodies conjugated to the target directly (step 1), then secondary antibodies conjugated to fluorophores were applied (step 2). A cell nuclear stain for the identification of individual cells was applied separately (step 3).

- Apply primary antibody and incubate slides in humid chamber for ~50 mins
- Wash slides in PBS

- Apply secondary antibody and incubate slides in the dark for ~45 mins
- Wash slides
- Apply DAPI for nuclear stain for ~1-2 mins
- Wash in PBS
- Mount coverslips onto glass slides using Prolong® Gold antifade reagent (Life Technologies, USA)

8.22 Panels for Individual Scans of GC-I

The following figures show the parameter maps for the individual, consecutive scans of GC-I, where the sum of the parameter maps from the individual scans make up the results shown in Figure 65.

The results from the individual scans do not reveal structure, and isolated points of interrogation producing high signal intensity could at first be interpreted as noise. Through the addition of the individual scans, however, it becomes apparent that interrogation points producing high signal intensity do so repeatedly; highlighting areas of high signal intensity from the background.

Scan 1

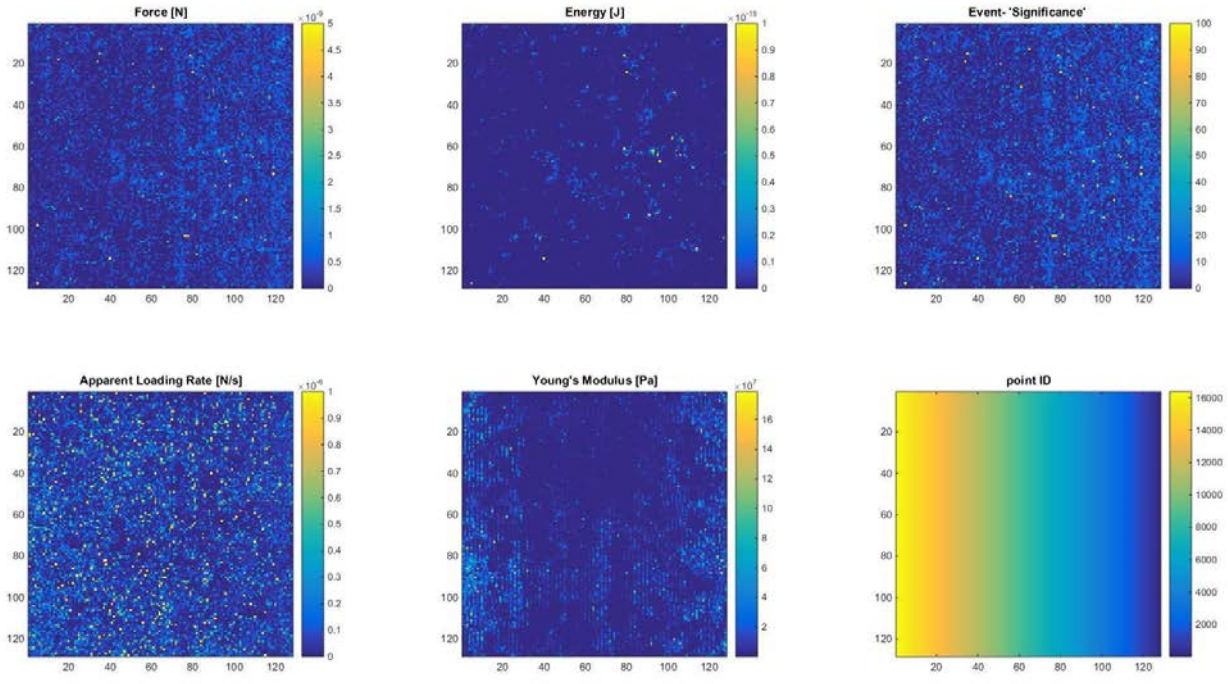

Scan 2

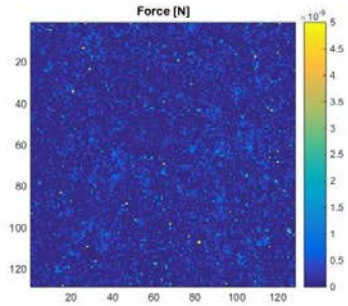
Force [N]

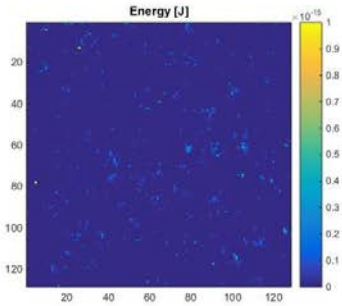
Energy [J]

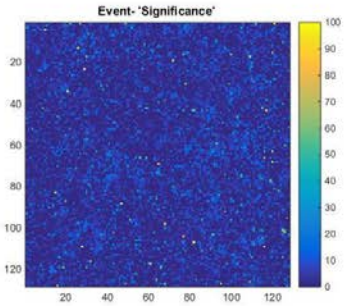
Event- 'Significance'

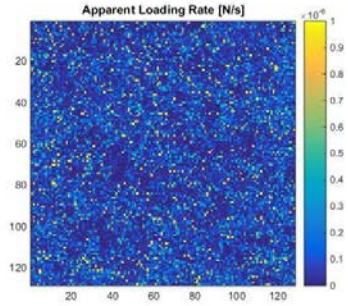
Apparent Loading Rate [N/s]

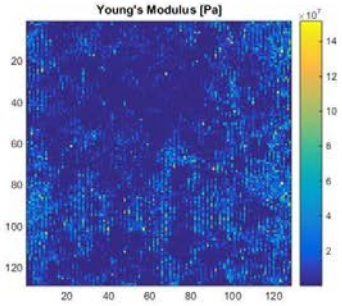
Young's Modulus [Pa]

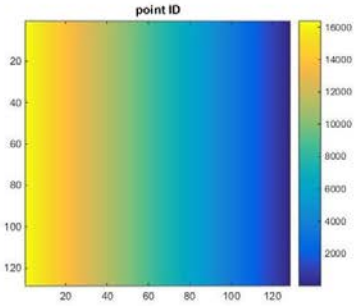
point ID

Scan 3

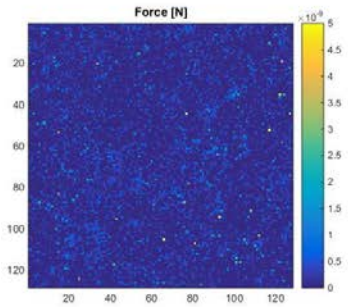
Force [N]

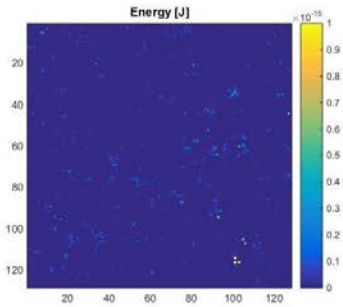
Energy [J]

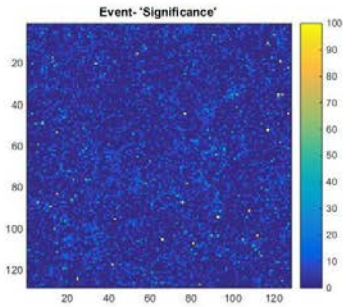
Event- 'Significance'

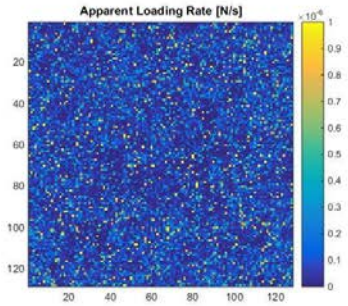
Apparent Loading Rate [N/s]

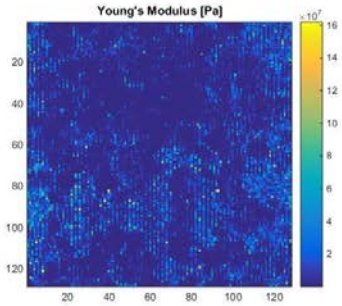
Young's Modulus [Pa]

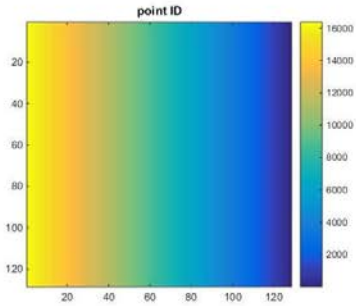
point ID

Scan 4

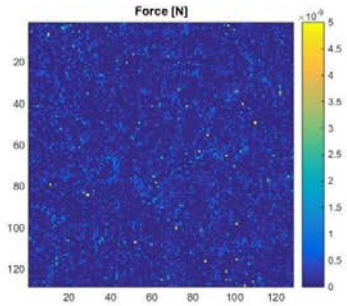
Force [N]

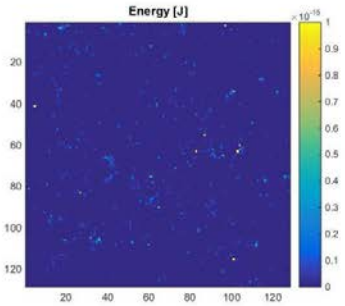
Energy [J]

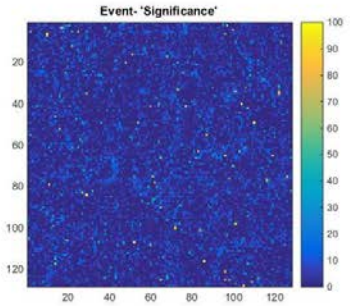
Event- 'Significance'

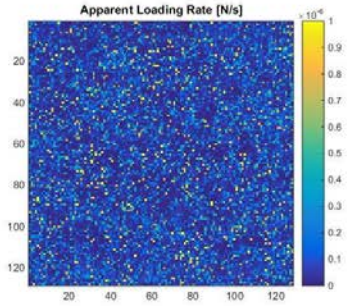
Apparent Loading Rate [N/s]

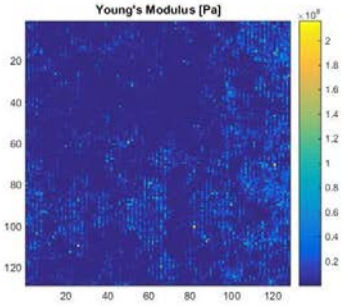
Young's Modulus [Pa]

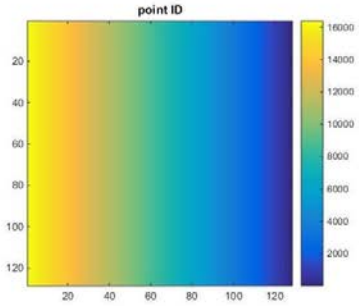
point ID

Scan 5

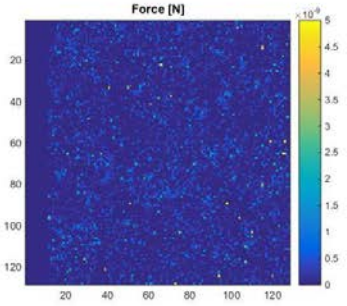
Force [N]

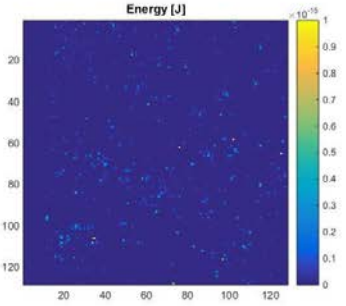
Energy [J]

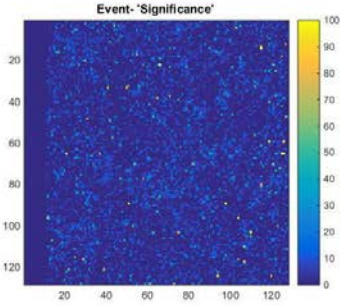
Event- 'Significance'

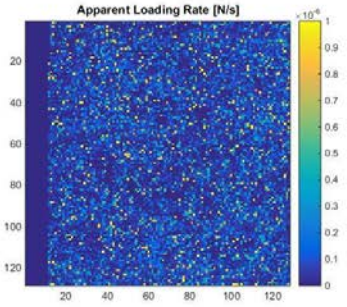
Apparent Loading Rate [N/s]

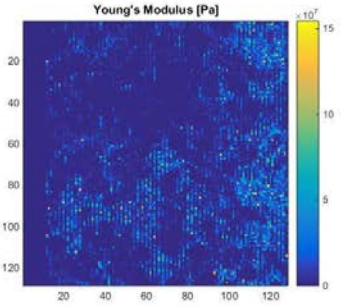
Young's Modulus [Pa]

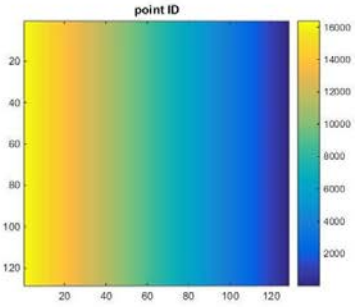
point ID

9 References

1 Flemming, W. *Über die Bildung von Richtungsfiguren in Säugethiereiern beim Untergang Graaf'scher Follikel*. (publisher not identified, 1885).

2 MacLennan, I. C. M. Germinal Centers. *Annual Review of Immunology* **12**, 117-139 (1994).

3 Victora, G. D. & Nussenzweig, M. C. Germinal Centers. *Annual Review of Immunology* **30**, 429-457, doi:10.1146/annurev-immunol-020711-075032 (2012).

4 Janeway, C., Travers, P., Walport, M. & Shlomchik, M. *Janeway's Immunobiology*. (Garland Science, 2012).

5 Victora, G. D. *et al.* Identification of human germinal center light and dark zone cells and their relationship to human B-cell lymphomas. *Blood* **120**, 2240-2248 (2012).

6 Allen, C. D. C., Okada, T., Tang, H. L. & Cyster, J. G. Imaging of Germinal Center Selection Events During Affinity Maturation. *Science* **315**, 528-531 (2007).

7 Victora, G. D. *et al.* Germinal Center Dynamics Revealed by Multiphoton Microscopy with a Photoactivatable Fluorescent Reporter. *Cell* **143**, 592-605 (2010).

8 Allen, C. D. C., Okada, T. & Cyster, J. G. Germinal-Center Organization and Cellular Dynamics. *Immunity* **27**, 190-202 (2007).

9 Zhang, Y. *et al.* Germinal Center B Cells Govern Their Own Fate via Antibody Feedback. *The Journal of experimental medicine* **210**, 457-464 (2013).

10 Parham, P. *The Immune System*. (Garland Science, 2005).

11 Racaniello, V. *Adaptive Immune Defenses: Antibodies*, <http://www.virology.ws/2009/07/22/adaptive-immune-defenses-antibodies/> (2009).

12 Mayer, G. *Immunoglobulins - Antigen-Antibody Reactions and Selected Tests*, <http://www.microbiologybook.org/mayer/ab-ag-rx.htm> (2010).

13 Van Oss, C., Good, R. & Chaudhury, M. Nature of the Antigen-Antibody Interaction: Primary and Secondary Bonds: Optimal Conditions for Association and Dissociation. *Journal of Chromatography B: Biomedical Sciences and Applications* **376**, 111-119 (1986).

14 Reverberi, R. & Reverberi, L. Factors Affecting the Antigen-Antibody Reaction. *Blood Transfusion* **5**, 227 (2007).

15 Kuppers, R., Zhao, M., Hansmann, M. L. & Rajewsky, K. Tracing B Cell Development in Human Germinal Centres by Molecular Analysis of Single Cells Picked from Histological Sections. *The EMBO journal* **12**, 4955-4967 (1993).
16 Georgiou, G. *et al.* The Promise and Challenge of High-Throughput Sequencing of the Antibody Repertoire. *Nature biotechnology* **32**, 158-168 (2014).
17 Hauser, A. E. *et al.* Definition of Germinal-Center B Cell Migration In Vivo Reveals Predominant Intrazonal Circulation Patterns. *Immunity* **26**, 655-667 (2007).
18 Kepler, T. B. & Perelson, A. S. Cyclic Re-Entry of Germinal Center B Cells and the Efficiency of Affinity Maturation. *Immunology Today* **14**, 412-415 (1993).
19 Oprea, M. & Perelson, A. S. Somatic Mutation Leads to Efficient Affinity Maturation When Centrocytes Recycle back to Centroblasts. *The Journal of Immunology* **158**, 5155-5162 (1997).
20 MacLennan, I., Johnson, G., Liu, Y.-J. & Gordon, J. The Heterogeneity of Follicular Reactions. *Research in Immunology* **142**, 253-257 (1991).
21 Kleinstein, S. H. & Singh, J. P. Toward Quantitative Simulation of Germinal Center Dynamics: Biological and Modeling Insights from Experimental Validation. *Journal of Theoretical Biology* **211**, 253-275 (2001).
22 Shlomchik, M., Watts, P., Weigert, M. & Litwin, S. Clone: A Monte-Carlo Computer Simulation of B Cell Clonal Expansion, Somatic Mutation, and Antigen-Driven Selection. *Somatic Diversification of Immune Responses*, 173-197 (1998).
23 Meyer-Hermann, M., Figge, M. T. & Toellner, K.-M. Germinal Centres Seen Through the Mathematical Eye: B-Cell Models on the Catwalk. *Trends in Immunology* **30**, 157-164 (2009).
24 Figge, M. T. *et al.* Deriving a Germinal Center Lymphocyte Migration Model From Two-Photon Data. *The Journal of experimental medicine* **205**, 3019-3029 (2008).
25 Schwickert, T. A. *et al.* In Vivo Imaging of Germinal Centres Reveals a Dynamic Open Structure. *Nature* **446**, 83-87 (2007).
26 Binnig, G. R., H. Scanning Tunnelling Microscopy. *Surface Science* **126**, 236-244 (1983).
27 *All Nobel Prizes in Physics*, <http://www.nobelprize.org/nobel_prizes/physics/laureates> (2015).

28 Binnig, G., Quate, C. F. & Gerber, C. Atomic Force Microscope. *Physical Review Letters* **56**, 930-933 (1986).
29 Hansma, P. K., Elings, V. B., Marti, O. & Bracker, C. E. Scanning Tunneling Microscopy and Atomic Force Microscopy: Application to Biology and Technology. *Science* **242**, 209-216 (1988).
30 Albrecht, T. & Quate, C. Atomic Resolution Imaging of a Nonconductor by Atomic Force Microscopy. *Journal of Applied Physics* **62**, 2599-2602 (1987).
31 Marti, O., Drake, B., Ribi, H., Albrecht, T. R. & Quate, C. F. Atomic Force Microscopy of an Organic Monolayer. *Science* **239**, 50-52 (1988).
32 Bowen, J. & Cheneler, D. A Dynamic Model of the Jump-To Phenomenon during AFM Analysis. *Langmuir* **28**, 17273-17286 (2012).
33 Shahin, V., Ludwig, Y., Schafer, C., Nikova, D. & Oberleithner, H. Glucocorticoids Remodel Nuclear Envelope Structure and Permeability. *Journal of cell science* **118**, 2881-2889 (2005).
34 Clifford, C. A. & Seah, M. P. The Determination of Atomic Force Microscope Cantilever Spring Constants via Dimensional Methods for Nanomechanical Analysis. *Nanotechnology* **16**, 1666-1680, doi:10.1088/0957-4484/16/9/044 (2005).
35 Bowen, J. *et al.* On the Calibration of Rectangular Atomic Force Microscope Cantilevers Modified by Particle Attachment and Lamination. *Measurement Science and Technology* **21**, 115106, doi:10.1088/0957-0233/21/11/115106 (2010).
36 Wong, J., Chilkoti, A. & Moy, V. T. Direct Force Measurements of the Streptavidin–Biotin Interaction. *Biomolecular Engineering* **16**, 45-55 (1999).
37 Ludwig, M., Dettmann, W. & Gaub, H. E. Atomic Force Microscope Imaging Contrast Based on Molecular Recognition. *Biophysical journal* **72**, 445-448 (1997).
38 Allen, S. *et al.* Detection of Antigen-Antibody Binding Events with the Atomic Force Microscope. *Biochemistry* **36**, 7457-7463, doi:10.1021/bi962531z (1997).
39 Harada, Y., Kuroda, M. & Ishida, A. Specific and Quantized Antigen−Antibody Interaction Measured by Atomic Force Microscopy. *Langmuir* **16**, 708-715, doi:10.1021/la990236k (1999).
40 Florin, E.-L., Moy, V. T. & Gaub, H. E. Adhesion Forces Between Individual Ligand-Receptor Pairs. *Science-AAAS-Weekly Paper Edition-Including Guide to Scientific Information* **264**, 415-417 (1994).

41 Fichtner, D. *et al.* Covalent and Density-Controlled Surface Immobilization of E-Cadherin for Adhesion Force Spectroscopy. *PLoS ONE* **9** (2014).
42 Tsapikouni, T. & Missirlis, Y. F. P-Selectin/Ligand Unbinding Force Measured With Atomic Force Microscopy: Comparison of Two Chemical Protocols for the Tethering of Single Molecules. *Journal of Molecular Recognition* **24**, 847-853 (2011).
43 Wildling, L. *et al.* Probing Binding Pocket of Serotonin Transporter by Single Molecular Force Spectroscopy on Living Cells. *The Journal of biological chemistry* **287**, 105-113 (2012).
44 Engel, A. & Gaub, H. E. Structure and Mechanics of Membrane Proteins. *Annual review of biochemistry* **77**, 127-148 (2008).
45 Baclayon, M., Roos, W. H. & Wuite, G. J. L. Sampling Protein Form and Function with the Atomic Force Microscope. *Molecular & Cellular Proteomics* **9**, 1678-1688, doi:10.1074/mcp.R110.001461 (2010).
46 Muller, D. J., Helenius, J., Alsteens, D. & Dufrene, Y. F. Force Probing Surfaces of Living Cells to Molecular Resolution. *Nature chemical biology* **5**, 383-390 (2009).
47 Dufrene, Y. F., Martinez-Martin, D., Medalsy, I., Alsteens, D. & Muller, D. J. Multiparametric Imaging of Biological Systems by Force-Distance Curve-Based AFM. *Nature methods* **10**, 847-854 (2013).
48 Marszalek, P. E. & Dufrene, Y. F. Stretching Single Polysaccharides and Proteins Using Atomic Force Microscopy. *Chemical Society Reviews* **41**, 3523-3534 (2012).
49 Allison, D. P., Mortensen, N. P., Sullivan, C. J. & Doktycz, M. J. Atomic Force Microscopy of Biological Samples. *Wiley Interdisciplinary Reviews: Nanomedicine and Nanobiotechnology* **2**, 618-634 (2010).
50 Eifert, A. & Kranz, C. Hyphenating Atomic Force Microscopy. *Analytical chemistry* **86**, 5190-5200 (2014).
51 Bell, G. I. Models for the Specific Adhesion of Cells to Cells. *Science* **200**, 618-627 (1978).
52 Evans, E. & Ritchie, K. Dynamic Strength of Molecular Adhesion Bonds. *Biophysical journal* **72**, 1541 (1997).
53 Schwesinger, F. *et al.* Unbinding Forces of Single Antibody-Antigen Complexes Correlate with Their Thermal Dissociation Rates. *Proceedings of the National Academy of Sciences* **97**, 9972-9977 (2000).

54 *Atomic Force Microscopy in Biomedical Research*. (Humana Press, 2011).
55 Natkanski, E. *et al.* B Cells Use Mechanical Energy to Discriminate Antigen Affinities. *Science* **340**, 1587-1590 (2013).
56 Tolar, P. Discussing "B Cells Use Mechanical Energy to Discriminate Antigen Affinities". *MRC Centre, London* (2014).
57 *NP-O-Succinimide*, <http://pubchem.ncbi.nlm.nih.gov/compound/126530> (
58 Sunday, M. E., Weinberger, J., Benacerraf, B. & Dorf, M. Hapten-Specific T Cell Responses to 4-Hydroxy-3-Nitrophenyl Acetyl. *The Journal of Immunology* **125**, 1601-1605 (1980).
59 Nossal, G. J., Karvelas, M. & Pulendran, B. Soluble Antigen Profoundly Reduces Memory B Cell Numbers Even When Given After Challenge Immunization. *Proceedings of the National Academy of Sciences* **90**, 3088-3092 (1993).
60 Dammer, U. *et al.* Binding Strength Between Cell Adhesion Proteoglycans Measured by Atomic Force Microscopy. *Science* **267**, 1173-1175, doi:10.1126/science.7855599 (1995).
61 Grandbois, M., Beyer, M., Rief, M., Clausen-Schaumann, H. & Gaub, H. E. How Strong is a Covalent Bond? *Science* **283**, 1727-1730 (1999).
62 Teulon, J. M. *et al.* Single and Multiple Bonds in (Strept) Avidin–Biotin Interactions. *Journal of Molecular Recognition* **24**, 490-502 (2011).
63 Allison, S. D. *et al.* Effects of Drying Methods and Additives on Structure and Function of Actin: Mechanisms of Dehydration-Induced Damage and its Inhibition. *Archives of Biochemistry and Biophysics* **358**, 171-181 (1998).
64 Ulman, A. Formation and Structure of Self-Assembled Monolayers. *Chemical reviews* **96**, 1533-1554 (1996).
65 Baio, J. *et al.* Amine Terminated SAMs: Investigating why Oxygen is Present in these Films. *Journal of Electron Spectroscopy and Related Phenomena* **172**, 2-8 (2009).
66 Wang, H., Chen, S., Li, L. & Jiang, S. Improved Method for the Preparation of Carboxylic Acid and Amine Terminated Self-Assembled Monolayers of Alkanethiolates. *Langmuir* **21**, 2633-2636, doi:10.1021/la046810w (2005).
67 Wang, M. S., Palmer, L. B., Schwartz, J. D. & Razatos, A. Evaluating Protein Attraction and Adhesion to Biomaterials with the Atomic Force Microscope. *Langmuir* **20**, 7753-7759, doi:10.1021/la049849+ (2004).

68 Love, J. C., Estroff, L. A., Kriebel, J. K., Nuzzo, R. G. & Whitesides, G. M. Self-Assembled Monolayers of Thiolates on Metals as a Form of Nanotechnology. *Chemical reviews* **105**, 1103-1170 (2005).
69 Spori, D. M. *Structural Influences on Self-Cleaning Surfaces* Diplom Werkstoff Ingenieur thesis, ETH Zurich, (2010).
70 Toworfe, G., Composto, R., Shapiro, I. & Ducheyne, P. Nucleation and Growth of Calcium Phosphate on Amine-, Carboxyl-and Hydroxyl-Silane Self-Assembled Monolayers. *Biomaterials* **27**, 631-642 (2006).
71 Troughton, E. B. *et al.* Monolayer Films Prepared by the Spontaneous Self-Assembly of Symmetrical and Unsymmetrical Dialkyl Sulfides from Solution onto Gold Substrates: Structure, Properties, and Reactivity of Constituent Functional Groups. *Langmuir* **4**, 365-385 (1988).
72 Fujiwara, H. *Spectroscopic Ellipsometry: Principles and Applications*. (John Wiley & Sons, 2007).
73 *X-Ray Photoelectron Spectroscopy*, <http://www.elettra.trieste.it/lightsources/labs-and-services/surface-lab/x-ray-photoelectron-spectroscopy.html> (2012).
74 Balachander, N. & Sukenik, C. N. Monolayer Transformation by Nucleophilic Substitution: Applications to the Creation of New Monolayer Assemblies. *Langmuir* **6**, 1621-1627 (1990).
75 Thompson, A. *et al.* X-Ray Data Booklet (2009). doi:http://xdb.lbl.gov/xdb.pdf.
76 ThermoFisherScientific_XPS. *XPS Reference - Table of Elements*, <http://xpssimplified.com/periodictable.php> (2013).
77 *LaSurface.com*, <http://www.lasurface.com/database/elementxps.php?nrj=1270> (
78 Lee, S.-H. *et al.* Photooxidation of Amine-Terminated Self-Assembled Monolayers on Gold. *The Journal of Physical Chemistry C* **114**, 10512-10519, doi:10.1021/jp101426h (2010).
79 Wallwork, M. L., Smith, D. A., Zhang, J., Kirkham, J. & Robinson, C. Complex Chemical Force Titration Behavior of Amine-Terminated Self-Assembled Monolayers. *Langmuir* **17**, 1126-1131 (2001).
80 Fears, K. P., Creager, S. E. & Latour, R. A. Determination of the Surface p K of Carboxylic-and Amine-Terminated Alkanethiols Using Surface Plasmon Resonance Spectroscopy. *Langmuir* **24**, 837-843 (2008).

81 Yeung, C. L. *et al.* Different Formation Kinetics and Photoisomerization Behavior of Self-Assembled Monolayers of Thiols and Dithiolanes Bearing Azobenzene Moieties. *Physical Chemistry Chemical Physics* **15**, 11014-11024 (2013).
82 Li, L., Chen, S. & Jiang, S. Molecular-Scale Mixed Alkanethiol Monolayers of Different Terminal Groups on Au (111) by Low-Current Scanning Tunneling Microscopy. *Langmuir* **19**, 3266-3271 (2003).
83 Köhler, G. & Milstein, C. Continuous Cultures of Fused Cells Secreting Antibody of Predefined Specificity. *Nature* **256**, 495-497 (1975).
84 Shaw, R. K., Daniell, S., Ebel, F., Frankel, G. & Knutton, S. EspA Filament-Mediated Protein Translocation into Red Blood Cells. *Cellular Microbiology* **3**, 213-222 (2001).
85 Shaw, R. K., Daniell, S., Frankel, G. & Knutton, S. Enteropathogenic Escherichia Coli Translocate Tir and Form an Intimin–Tir Intimate Attachment to Red Blood Cell Membranes. *Microbiology* **148**, 1355-1365 (2002).
86 MIKROMASCH. *HQ:CSC17/CR-AU*, <http://www.spmtips.com/afm-tip-hq-csc17-cr-au> (2016).
87 OLYMPUS. *OMCL-TR400PB / OMCL-TR800PB / OMCL-RC800PB*, <http://probe.olympus-global.com/en/product/omcl_tr400pb_1/> (2016).
88 Kiernan, J. A. Formaldehyde, Formalin, Paraformaldehyde And Glutaraldehyde: What They Are And What They Do. *Microscopy Today* **1** (2000).
89 Baker, A. *et al.* Reaction of N-Acetylglycyllysine Methyl Ester with 2-Alkenals: An Alternative Model for Covalent Modification of Proteins. *Chemical research in toxicology* **11**, 730-740 (1998).
90 Thorsten, C. Some Fixatives & Preservatives for Microscopy. *CRS CR Scientific LLC*.
91 Bancroft, J. Histochemical Techniques Butterworth's. *London and Boston* (1975).
92 Lin, D. C., Shreiber, D. I., Dimitriadis, E. K. & Horkay, F. Spherical Indentation of Soft Matter Beyond the Hertzian Regime: Numerical and Experimental Validation of Hyperelastic Models. *Biomechanics and modeling in mechanobiology* **8**, 345-358 (2009).
93 Dimitriadis, E. K., Horkay, F., Maresca, J., Kachar, B. & Chadwick, R. S. Determination of Elastic Moduli of Thin Layers of Soft Material Using the Atomic Force Microscope. *Biophysical journal* **82**, 2798-2810 (2002).

94 Dokukin, M. E., Guz, N. V. & Sokolov, I. Quantitative Study of the Elastic Modulus of Loosely Attached Cells in AFM Indentation Experiments. *Biophysical journal* **104**, 2123-2131 (2013).
95 Lin, D. C., Dimitriadis, E. K. & Horkay, F. Robust Strategies for Automated AFM Force Curve Analysis—I. Non-Adhesive Indentation of Soft, Inhomogeneous Materials. *Journal of Biomechanical Engineering* **129**, 430-440 (2007).
96 Darling, E. M., Zauscher, S., Block, J. A. & Guilak, F. A Thin-Layer Model for Viscoelastic, Stress-Relaxation Testing of Cells Using Atomic Force Microscopy: Do Cell Properties Reflect Metastatic Potential? *Biophysical journal* **92**, 1784-1791 (2007).
97 Goga, Y., Chiba, M., Shimizu, Y. & Mitani, H. Compressive Force Induces Osteoblast Apoptosis via Caspase-8. *Journal of Dental Research* **85**, 240-244 (2006).
98 Knight, M. *et al.* Cell and Nucleus Deformation in Compressed Chondrocyte–Alginate Constructs: Temporal Changes and Calculation of Cell Modulus. *Biochimica et Biophysica Acta (BBA)-General Subjects* **1570**, 1-8 (2002).
99 Mathur, A. B., Collinsworth, A. M., Reichert, W. M., Kraus, W. E. & Truskey, G. A. Endothelial, Cardiac Muscle and Skeletal Muscle Exhibit Different Viscous and Elastic Properties as Determined by Atomic Force Microscopy. *Journal of Biomechanics* **34**, 1545-1553 (2001).
100 Peeters, E., Oomens, C., Bouten, C., Bader, D. & Baaijens, F. Mechanical and Failure Properties of Single Attached Cells Under Compression. *Journal of biomechanics* **38**, 1685-1693 (2005).
101 Takai, E., Costa, K. D., Shaheen, A., Hung, C. T. & Guo, X. E. Osteoblast Elastic Modulus Measured by Atomic Force Microscopy is Substrate Dependent. *Annals of Biomedical Engineering* **33**, 963-971 (2005).
102 Lulevich, V., Zink, T., Chen, H.-Y., Liu, F.-T. & Liu, G.-y. Cell Mechanics Using Atomic Force Microscopy-Based Single-Cell Compression. *Langmuir* **22**, 8151-8155 (2006).
103 Jamur, M. C. & Oliver, C. Permeabilization of Cell Membranes. *Methods in molecular biology (Clifton, N.J.)* **588**, 63-66 (2010).
104 Pekker, M. & Shneider, M. The Surface Charge of a Cell Lipid Membrane. *arXiv:1401.4707 [physics.bioph]* (2014).
105 Neumann, T. Determining the Elastic Modulus of Biological Samples Using Atomic Force Microscopy. *JPK Instruments Application Report* (2008).

106 McPhee, G. M. *Elasticity as an Indicator of Cell Responses to Topography and Chemically Modified Surfaces: an Atomic Force Microscopy Approach*, University of Glasgow, (2012).
107 Mueller, S. & Sandrin, L. Liver Stiffness: a Novel Parameter for the Diagnosis of Liver Disease. *Hepatic Medicine: Evidence and Research* **2**, 49 (2010).
108 Masuzaki, R. *et al.* Assessing Liver Tumor Stiffness by Transient Elastography. *Hepatology international* **1**, 394-397 (2007).
109 Li, Q., Lee, G., Ong, C. & Lim, C. AFM Indentation Study of Breast Cancer Cells. *Biochemical and Biophysical Research Communications* **374**, 609-613 (2008).
110 Lekka, M. *et al.* Elasticity of Normal and Cancerous Human Bladder Cells Studied by Scanning Force Microscopy. *European Biophysics Journal* **28**, 312-316 (1999).
111 Faria, E. C. *et al.* Measurement of Elastic Properties of Prostate Cancer Cells Using AFM. *The Analyst* **133**, 1498-1500 (2008).
112 Cotter, T. G. & Al-Rubeai, M. Cell Death (Apoptosis) in Cell Culture Systems. *Trends in Biotechnology* **13**, 150-155 (1995).
113 Shapiro-Shelef, M. & Calame, K. Regulation of Plasma-Cell Development. *Nature Reviews Immunology* **5**, 230-242 (2005).
114 Kendall, K., Cambridge University, (1969).
115 Roberts, A. D., Cambridge University, (1969).
116 Johnson, K., Kendall, K. & Roberts, A. in *Proceedings of the Royal Society of London A: Mathematical, Physical and Engineering Sciences.* 301-313 (The Royal Society).
117 Awada, H., Castelein, G. & Brogly, M. Quantitative Determination of Surface Energy Using Atomic Force Microscopy: The Case of Hydrophobic/Hydrophobic Contact and Hydrophilic/Hydrophilic Contact. *Surface and Interface Analysis* **37**, 755-764 (2005).
118 Clear, S. C. & Nealey, P. F. Chemical Force Microscopy Study of Adhesion and Friction Between Surfaces Functionalized with Self-Assembled Monolayers and Immersed in Solvents. *Journal of Colloid and Interface Science* **213**, 238-250 (1999).
119 Shih, T.-A. Y., Roederer, M. & Nussenzweig, M. C. Role of Antigen Receptor Affinity in T Cell–Independent Antibody Responses In Vivo. *Nature Immunology* **3**, 399-406 (2002).
120 Johnson, K. *Contact Mechanics* (Cambridge University Press 1985).
121 Noy, A. & Friddle, R. W. Practical Single Molecule Force Spectroscopy: How to Determine Fundamental Thermodynamic

Parameters of Intermolecular Bonds with an Atomic Force Microscope. *Methods* **60**, 142-150 (2013).
122 Christ, A. F. *et al.* Mechanical Difference Between White and Gray Matter in the Rat Cerebellum Measured by Scanning Force Microscopy. *Journal of Biomechanics* **43**, 2986-2992 (2010).
123 Berg, J. M., Tymoczko, J. L. & Stryer, L. *Biochemistry*. 5th edn, (New York: WH Freeman, 2002).
124 Bowen, J. *NanoAdhesion: Investigating Nanoscale Adhesion Using Self-Assembled Monolayers* PhD thesis, Univerity of Birmingham, (2005).
125 Kwon, S., Kim, N., Jo, T. & Pahk, H. J. Critical Dimension Measurement of Transparent Film Layers by Multispectral Imaging. *Optics Express* **22**, 17370-17381 (2014).
126 Tompkins, H. *A User's Guide to Ellipsometry*. (Dover Publications Inc., New York, 2006).
127 HORIBA. *Spectroscopic Ellipsometry - User Guide*. (HORIBA-JOBIN YVON, 2008).
128 Rakić, A. D., Djurišić, A. B., Elazar, J. M. & Majewski, M. L. Optical Properties of Metallic Films for Vertical-Cavity Optoelectronic Devices. *Applied Optics* **37**, 5271-5283 (1998).
129 Tompkins, H. G. Spectroscopic Ellipsometry: What it is, what it will do, and what it won't do. *27th International Conference on the Physics of Semiconductors: Tutorials* (2004).
130 Madeira, A. *et al.* Coupling Surface Plasmon Resonance to Mass Spectrometry to Discover Novel Protein–Protein Interactions. *Nature protocols* **4**, 1023-1037 (2009).
131 JPK. Data Processing Software Manual. *JPK Instruments AG* **4.0** (2011).
132 Fischer-Cripps, A. C. *Introduction to Contact Mechanics*. (Springer, 2000).
133 Hertz, H. Über die Berührung Fester Elastischer Körper. *Journal für die Reine und Angewandte Mathematik* **92**, 156-171 (1882).
134 JPK. Data Processing Software Manual. *JPK Instruments AG* **5.0** (2015).